

Dissertation  
submitted to the  
Combined Faculty of Mathematics, Engineering and Natural Sciences  
of Heidelberg University, Germany  
for the degree of  
Doctor of Natural Sciences

Put forward by

Hazal, Göksu

born in: Yalova, Turkey

Oral examination: 18.12.2024



The Southern Wide-field Gamma-ray Observatory:  
The Lake Approach and  
the Pulsar Wind Nebula HESS J1825-137

Referees: Prof. Dr. James A. Hinton  
Prof. Dr. Stefan Wagner



*Everything starts somewhere, although many physicists disagree.*

— Terry Pratchett

Dedicated to my family.



## ABSTRACT

---

In this thesis I describe the motivations behind and design of the lake concept, an alternative detector technology idea for the future Southern Wide-field Gamma-ray Observatory (SWGGO), a planned gamma-ray observatory in the Andes. In the lake concept, light-tight bladders that form optically separated water Cherenkov detector (WCD) units would be deployed in a natural or artificial lake. This technology option offers potential cost savings compared to tank-based approaches. In this work I focus on the double-layered WCD design, where a lower layer with reflective lining is used for muon identification in addition to the upper layer that is used for calorimetric detection of gamma-ray initiated extensive air showers. I present simulations of the lake option, showing that the presence of water around the double-layered WCD units provides a shielding advantage for the lower chamber. Furthermore I present a discussion of the water waves that pose a challenge for the lake concept.

In collaboration with colleagues from MPIK, I have designed, evaluated, tested and simulated a full scale prototype detector unit for the lake concept. This detector is designed for the lake idea, however it also provides the first experimental verification of the double-layered design for SWGGO and in addition allowed tests of materials. After the evaluation of early prototypes, a final double-layer WCD prototype was built. A flexible inner chamber that forms the lower chamber, named the matryoshka, was inserted into a larger commercially produced single cell bladder, forming the first double-layered WCD prototype for SWGGO. A setup utilizing photomultiplier tubes and a full electronics chain, where the WCD prototype was located between two muon tagger detectors, was used to take coincidence data of through-going particles. The data were compared with simulations and a good agreement between the detector simulation and data was seen. The materials used for the prototyping of unit detectors were tested for reflectivity and water degradation. These tests inform the simulations performed to evaluate the double-layer WCD prototype.

Among the sources that would be transiting the field of view of SWGGO at low zenith is HESS J1825-137, a middle aged pulsar wind nebula (PWN) that appears to be among the largest sources known in the gamma-ray sky and is one of the most powerful emitters at TeV and ultra-high energies. In this thesis I present an analysis of HESS J1825-137 with the recently revised data from the HAWC observatory, a wide-field gamma-ray observatory in Mexico and find a spectrum consistent with other instruments. Similar to previous observations by H.E.S.S. and Fermi-LAT we observe an energy-dependent morphology of HESS J1825-137 up to hundreds of TeV. The PWN decreases in size with increasing energy, which can be used to constrain particle transport mechanisms, once the morphology at higher energies is resolved better with SWGGO. As PWNe are currently the dominant source class in TeV energies, they form one of the important science goals with SWGGO.

## ZUSAMMENFASSUNG

---

In dieser Arbeit beschreibe ich die Beweggründe und das Design des Seenkonzpts, einer alternativen Detektortechnologie für das zukünftige Southern Wide-field Gamma-ray Observatory (SWGGO), ein geplantes Gammastrahlenobservatorium in den Anden. Bei dem Seenkonzpt würden lichtdichte Blasen, die optisch getrennte Wasser-Tscherenkov-Detektoreinheiten (WCD) bilden, in einem natürlichen oder künstlichen See eingesetzt. Diese Technologieoption bietet potenzielle Kosteneinsparungen im Vergleich zu tankbasierten Ansätzen. In dieser Arbeit konzentriere ich mich auf das zweischichtige WCD-Design, bei dem eine untere Schicht mit reflektierender Auskleidung für die Myonen-Identifizierung zusätzlich zur oberen Schicht verwendet wird, die für die kalorimetrische Detektion von durch Gammastrahlen ausgelösten ausgedehnten Luftschauern eingesetzt wird. Ich präsentiere Simulationen der See-Option, die zeigen, dass das Vorhandensein von Wasser um die doppelagigen WCD-Einheiten einen Abschirmungsvorteil für die untere Kammer bietet. Außerdem erörtere ich die Wasserwellen, die eine Herausforderung für das Seekonzpt darstellen.

In Zusammenarbeit mit Kollegen vom MPIK habe ich einen Prototyp einer Detektoreinheit in Originalgröße für das Seekonzpt entworfen, bewertet, getestet und simuliert. Dieser Detektor ist für das Seekonzpt konzipiert, bietet aber auch die erste experimentelle Verifizierung des zweischichtigen Designs für SWGGO und ermöglichte darüber hinaus Materialtests. Nach der Bewertung der ersten Prototypen wurde ein endgültiger zweischichtiger WCD-Prototyp gebaut. Eine flexible Innenkammer, die die untere Kammer bildet und Matroschka genannt wird, wurde in eine größere, kommerziell hergestellte Einzelzellenblase eingesetzt und bildete den ersten doppelagigen WCD-Prototyp für SWGGO. Ein Aufbau mit Photomultipliern und einer vollständigen Elektronikette, bei dem der WCD-Prototyp zwischen zwei Myonen-Tagger-Detektoren angeordnet war, diente zur Aufnahme von Koinzidenzdaten der durchgehenden Teilchen. Die Daten wurden mit Simulationen verglichen und es zeigte sich eine gute Übereinstimmung zwischen der Detektorsimulation und den Daten. Die Materialien, die für den Prototyp der Einheitsdetektoren verwendet wurden, wurden auf ihr Reflexionsvermögen und den Wasserabbau getestet. Diese Tests dienten als Grundlage für die Simulationen, die zur Bewertung des doppelschichtigen WCD-Prototyps durchgeführt wurden.

Zu den Quellen, die das Gesichtsfeld von SWGGO bei niedrigem Zenit durchqueren würden, gehört HESS J1825-137, ein Pulsar-Wind-Nebel (PWN) mittleren Alters, der zu den größten am Gammastrahlenhimmel bekannten Quellen zu gehören scheint und einer der stärksten Emitter bei TeV und ultrahohen Energien ist. In dieser Arbeit präsentiere ich eine Analyse von HESS J1825-137 mit den kürzlich revidierten Daten des HAWC-Observatoriums, einem Großfeld-Gammastrahlenobservatorium in Mexiko, und finde ein Spektrum, das mit anderen Instrumenten übereinstimmt. Ähnlich wie bei früheren Beob-

achtungen von H.E.S.S. und Fermi-LAT beobachten wir eine energieabhängige Morphologie von HESS J1825-137 bis zu Hunderten von TeV. Die Größe der PWN nimmt mit zunehmender Energie ab, was zur Eingrenzung der Teilchentransportmechanismen genutzt werden kann, sobald die Morphologie bei höheren Energien mit SWGO besser aufgelöst ist. Da PWNe derzeit die dominierende Quellenklasse bei TeV-Energien sind, bilden sie eines der wichtigen wissenschaftlichen Ziele von SWGO.

*Diese Übersetzung wurde mithilfe von DeepL erstellt.*



## ACKNOWLEDGMENTS

---

I would like to thank my supervisor Prof. Dr. Jim Hinton for everything. For responding to that very first email so enthusiastically, and giving me this opportunity; for all the inspiring ideas and discussions; for being so understanding and thoughtful during the strange circumstances of a pandemic, and the aftermath of a broken leg. The support and encouragement I got has been essential to this process.

I would also like to thank Prof. Dr. Werner Hofmann for his support, his guidance, his ideas and all the fruitful discussions, and for reading part of this thesis.

Dr. Felix Werner has been immensely helpful with his support and guidance during this process, and for reading multiple chapters of this thesis.

I would like to thank Prof. Dr. Stefan Wagner for agreeing to referee this thesis and being part of my thesis committee during these years. I would like to also thank Prof. Dr. Joerg Jaeckel and Dr. Teresa Marrodan Undagoitia for agreeing to be part of my examination committee.

I would like to thank our colleagues in SWGO and HAWC for helpful discussions and all the opportunities. The future will be exciting.

I am thankful to the members of the MPIK workshop, Stefan Schmidt, Peter Gaa, Christian Neureuther and Frank Garrecht. Frank, I really enjoyed being Piggeldy.

I would like to thank Dr. Fabian Haist for his help with electronics, bladder and water related matters, for reading part of this thesis, and for all the fun collaboration meetings.

I would like to thank Dr. Samridha Kunwar for all his help, especially for simulations, and for reading parts of this thesis. I am also very grateful for his friendship, and the many discussions on history.

I would like to thank Dr. Quentin Remy, Dr. Simon Sailer, Dr. Davide Deapoli for their support, friendship, and reading parts of this thesis. Quentin and Simon, thank you for being the wise masters.

A big thank you goes to Dr. Laura Olivera-Nieto for supporting me in multiple ways, always being there for me and reading multiple chapters of this thesis. Thank you also for all the fun times and for encouraging me always.

I am grateful to be part of such a supportive group in MPIK. I would like to thank everyone in our group, and especially to the eternal members of *Gasolina*.

I would like to thank my previous supervisors and instructors, especially Dr. Rémi Adam, Prof Dr. Adrian Biland, Prof Dr. Stephan S. Meyer and Irakli Minashvili.

I also would like to thank Dr. Alison Oğuz and Sibel Almas for believing in me back in highschool, and fascinating me with Physics and Biology. Your encouraging words follow me everywhere I go.

My thanks also go to my other friends in Heidelberg, Sin Min Chan, Miguel Molina-Hernandez, Simon ter Maat, Claire Aubry and others, for all the happy days and evenings, for the support at strange times, and the dances. You have made this process much more fun.

I should also mention, I am very thankful to Claire, Simon I & III and Laura for letting me stay at their places during these extraordinary times. You have made my life much easier these days.

A huge thanks to Zeynep Özarda for always answering my calls and always being there for me, to ZıHBıPıN, and my other friends from Turkey, Switzerland, Chicago and Paris for their support.

I am also grateful for Gemma the Gamma, and all the other random characters that came into existence during these years.

En büyük teşekkürü de aileme etmek istiyorum. Annem, babam, benim için yaptığınız her şey için size minnettarım. Sayenizde bugünlere geldim, bir şeyler yazdım. Sevginizle büyüdüm. Canım kardeşim Arda, sen bu evrendeki en sevdiğim insansın. İyi ki varsın. Hep yanımda olduğunuz için teşekkür ederim. Ez ji we pir hez dikim.



## CONTENTS

---

1	Production of Gamma-rays and Particle Interactions	1
1.1	Gamma-Rays and Cosmic Rays	1
1.1.1	Acceleration Mechanisms	2
1.2	Gamma-Ray Production Mechanisms	4
1.2.1	Synchrotron Radiation	5
1.2.2	Inverse Compton Scattering	6
1.2.3	Bremsstrahlung	7
1.2.4	Hadronic Interactions	8
1.3	Pulsar Wind Nebulae	8
1.3.1	Pulsars	8
1.3.2	Pulsar Wind Nebulae	10
1.4	Particle Detection	13
1.4.1	Ionization Losses	13
1.4.2	Cherenkov Radiation	14
1.4.3	Interactions of Photons	16
1.5	Summary	17
2	Gamma-ray Astronomy with Ground Particle Arrays	19
2.1	Introduction	19
2.2	Extensive Air Showers	20
2.3	Water Cherenkov Detector Arrays for Gamma Ray Astronomy	22
2.3.1	Water Cherenkov Detectors	23
2.3.2	Photomultiplier Tubes	25
2.3.3	Data Reconstruction with WCD Arrays	26
2.3.4	Ground Particle Array Experiments	28
2.3.5	HAWC Observatory	32
2.3.6	SWGO	34
2.4	Summary	38
3	Lake Concept	39
3.1	Detectors for SWGO	39
3.1.1	Double-Layered Detector Unit Design	39
3.1.2	Detector Technology Options	40
3.2	The Lake Concept	41
3.2.1	Advantages	42
3.2.2	Challenges	43
3.2.3	Survival under Wave Motion	44
3.2.4	Pond Option	50
3.3	Simulated Performance for the Lake Concept	51
3.3.1	Overburden	52
3.3.2	Shielding	53
3.3.3	Vertical Interactions at Boundaries	56
3.4	Summary	56
4	Evaluation of the Lake Option	59

4.1	Bladder Materials	59
4.1.1	Requirements of Bladder Materials	59
4.1.2	Bladder Material Production Plans	60
4.1.3	Reflectivity Measurements	61
4.1.4	Water Quality Monitoring	69
4.1.5	Summary of Water Quality Measurements	73
4.1.6	Conclusion of Water Quality Tests	78
4.1.7	Future Material Tests	78
4.2	Prototyping Tests with a Lake Simulation Tank	78
4.2.1	Small Bladder Tests	79
4.2.2	The Test Setup	80
4.2.3	Muon Taggers	81
4.2.4	Double Chamber Prototype Tests	84
4.2.5	Tests and Modifications	86
4.2.6	Comparison of Data with Simulations	98
4.3	Summary and Outlook	104
4.3.1	SWGO Prospects for the lake concept	104
5	Emission from Pulsar Wind Nebula HESS J1825-137 with the HAWC Observatory	107
5.1	Introduction	107
5.1.1	The Region	107
5.1.2	Overview of Observations of the Region	108
5.2	Analysis	110
5.2.1	Analysis with Gammapy	111
5.2.2	HAWC Data	112
5.2.3	Significance Maps	114
5.2.4	Modeling the Region	115
5.2.5	Fitting	116
5.2.6	Alternative Models and Fits	117
5.2.7	Flux Points	118
5.2.8	Energy Dependent Morphology	120
5.3	Discussion	122
5.3.1	Particle Acceleration Mechanism	122
5.3.2	PWN Halo	124
5.4	Further Analysis Using HAWC Data	125
5.5	Prospects of the Region with SWGO	126
5.5.1	Energy Dependent Morphology	128
5.5.2	SWGO prospects for PWN HESS J1825-137	129
5.6	Summary	130
6	Conclusion	131
A	Appendix A: Matryoshka Deployment	133
B	Reflectivity Measurements	137
B.1	Integrating Spheres as Devices for Measuring Reflectivity	137
C	Conductivity Measurements of Test Samples	141
C.1	Conductivity Measurements	141
D	Counts Maps for SWGO Sensitivity	143

E	Planned Tests in a Wave Basin	145
E.1	Facility	145
E.2	Test Setup	146
E.3	Test Plan	146
	Bibliography	149

## LIST OF FIGURES

---

- Figure 1.1 Cosmic ray differential energy spectrum from air shower measurements. The spectrum is shown multiplied by  $E^{2.6}$  to display the features; namely the three 'kinks' in the spectrum due to changes in spectral index. Figure taken from [34]. 3
- Figure 1.2 A Hillas diagram showing potential cosmic accelerators, with magnetic field strength on the y-axis and source radius  $R$  on the x-axis, for acceleration of UHECR to  $10^{20}$  eV. Figure taken from [26]. 4
- Figure 1.3 An example spectral energy distribution showing the different gamma-ray production mechanisms. Depending on the environment and nature of the source, different mechanisms would dominate. Figure taken from Jardin-Blicq [96]. 5
- Figure 1.4 The dependence of total Klein-Nishina cross-section divided the Thomson cross-section on  $h\nu/m_e c^2$ . Below  $h\nu/m_e c^2 \approx 1$ , the two cross sections are roughly equal. At energies above  $h\nu/m_e^2$ , IC scattering mechanism gets suppressed. Figure taken from [167]. 7
- Figure 1.5 Sketch of a pulsar. The magnetic field axis and rotation axis are misaligned. Particles accelerated along the open magnetic field lines may escape and form pulsar winds. Figure taken from Mitchell and Gelfand [130]. 9
- Figure 1.6 Spectral energy distribution of the Crab nebula, from radio to PeV energies, taken from Dirson and Horns [57]. 10
- Figure 1.7 The three evolutionary stages of PWNe. Initially the PWN is confined within the SNR with a forward shock (FS) and a contact discontinuity (CD). At the second stage the PWN is crushed by the inward moving reverse shock (RS). Lastly the pulsar escapes from the SNR. The escaped electron positron pairs may then form a pulsar halo. Figure taken from Giacinti et al. [68]. 11
- Figure 1.8 Energy loss for increasing  $\beta\gamma$  for different absorbers. Figure from PDG (2022) [175]. 14
- Figure 1.9 A charged particle emits Cherenkov radiation if its velocity is more than the speed of light in that medium. Figure taken from [96]. 15

- Figure 1.10 *Left:* Energy loss mechanisms for electrons. At higher energies, bremsstrahlung takes over from ionization losses, where the takeover energy  $E_c$  is material dependent. Figure taken from [175]. *Right:* Interactions of high energy photons with matter. The photon interaction cross section in Nitrogen is shown. Figure taken from [98]. 16
- Figure 2.1 Extensive air showers (EAS) produced by a gamma-ray and a cosmic ray. *Left:* Gamma-ray induced electromagnetic air shower with a sequence of pair production and bremsstrahlung processes. *Right:* Cosmic rays producing a hadronic EAS with electromagnetic components. Figure taken from [178]. 20
- Figure 2.2 *Left:* Longitudinal shower development, where shower size vs atmospheric depth is shown. More energetic showers reach lower altitudes.  $s = 1$  shows the shower maximum. Figure taken from [178]. *Right:* PMT recorded hit times for a photon from the Crab nebula for HAWC. Figure taken from [5]. 22
- Figure 2.3 Figures made using HAWCSim(based on GEANT4) showing a 1 GeV electron(*left*) and a 1 GeV muon (*right*) passing through a double-layer WCD. The electron decays quickly while the muon goes into the lower chamber. 24
- Figure 2.4 A PMT schematic. An incident photon strikes the photocathode. Photoelectrons from the photocathode travel through the vacuum and get amplified at each dynode. Taken from [144]. 25
- Figure 2.5 Distribution of fraction of the total energy that reaches ground ( $x_{gr} = E_i/E_{gr}$ ), at an altitude of 5000 m. For, gamma induced showers, most energy is photon dominated, while for proton showers muons dominate. Figure taken from [151]. 27
- Figure 2.6 The pool used for Milagro. Two layers of PMTs are seen, one layer directly connected to the PVC pipes, and the other later suspended above via ropes. Image taken from [148]. 29
- Figure 2.7 The surface detector element of Pierre Auger Observatory. The rotomolded tanks are lined with liners that reflect the Cherenkov light from the passing by particle to the downward facing PMTs. Figure taken from [122]. 31
- Figure 2.8 *Left:* The HAWC experiment layout with its 300 steel tanks.*Right:* Diagram of a HAWC tank shows the three eight-inch PMTs surrounding the ten-inch PMT. 32

- Figure 2.9 A proton (*Left*) and a gamma (*right*) induced shower on the HAWC array. The proton shower has energy deposited further away from the core, enabling gamma/hadron separation. Figure taken from [61] 33
- Figure 2.10 Sketch of the SWGO array concept. Figure credit: Richard White. 35
- Figure 2.11 SWGO sensitivity for the A<sub>4</sub> configuration for one year of observation, compared with CTA South and LHAASO. Plot made by Jim Hinton. 37
- Figure 2.12 The Gamma-ray sky as seen by HAWC and expected to be seen by SWGO. Many interesting regions such as the Galactic Center and the Fermi Bubbles will be within SWGO FOV. Image from Richard White. 37
- Figure 3.1 The double-layered WCD design for SWGO uses two chambers and a double PMT support. 40
- Figure 3.2 The technology options for SWGO WCDs. *Left*: Corrugated steel tanks and rotomolded high-density polyethylene (HDPE) tanks. *Middle*: A bladder in an artificial lake. *Right*: A bladder in a natural lake. Figure by Felix Werner, featured in [173]. 41
- Figure 3.3 A 2D representation of a plain water wave in Airy Wave Theory.  $\lambda$  is wavelength,  $H$  is wave height and  $\eta$  is the free surface elevation. Figure taken from [132]. 45
- Figure 3.4 Water particle movement under a wave with  $T = 2$  s. Red circles depict the water particle trajectories varying with depth according to Airy Wave Theory. Two bladders are depicted following the particle trajectories for illustration, the reality is more complicated. 47
- Figure 3.5 Velocity vectors and pressure anomaly for a wave with period 2 s. Image is taken from [28]. 48
- Figure 3.6 The hydrodynamics and ocean engineering tank at LHEEA, France. The segmented wavemaker is seen in the background. Figure taken from [91]. 50
- Figure 3.7 Sketch of the gap between two artificial ponds. Field nodes are placed on land and there is a 45° angle at the edge of each pond. Figure made by Felix Werner. 51
- Figure 3.8 Impact of water depth above a WCD on the probability of detection of one or more photoelectrons as a function of particle energy. *Left*: For gammas. *Right*: For electrons. 52
- Figure 3.9 An array of 20 double-layered WCDs placed in a circular pond, simulated using HAWCSim. The secondary gammas (in dark blue) and electrons (in yellow) coming from a vertical gamma-ray initiated shower are seen. 53

- Figure 3.10 The central double-layered WCD in the array depicted in Figure 3.9 when a gamma-ray shower is thrown to towards the center of the array, with an angle of  $30^\circ$ . The blue points represent the water hits, or the point of first interaction in the water volume within the double-layered WCD. *Left:* Double-layered WCD array is in air. The shielding from the neighboring tanks is seen. *Right:* The double-layered WCD array is in water. A more uniform shielding is seen. 54
- Figure 3.11 A double-layered WCD at the edge of the array depicted in Figure 3.9 when a gamma-ray shower is thrown to towards the center of the array, with an angle of  $30^\circ$ . *Left:* Double-layered WCD array is in air. The double-layered WCD at the edge of the array has no shielding to sideways entry. *Right:* The double-layered WCD array is in water. A uniform shielding is seen. 54
- Figure 3.12 *Top:* Signal amplitude distribution in the air (left) and lake (right) cases for the central double-layered WCD for the  $30^\circ$  gamma shower. *Bottom:* Signal amplitude distribution in the air (left) and lake (right) cases for the edge double-layered WCD. 55
- Figure 3.13 Fraction of events recorded by upper and lower chambers of a single double-layered WCD, for vertically thrown gammas and electrons. The top plots are for gammas and bottom are for electrons. *Left:* Particles thrown 1 cm outside the WCD. *Middle:* Particles thrown around the boundary of the WCD. *Right:* Particles thrown outside and inside the WCD. 57
- Figure 4.1 *Left:* The Auger liner, three separate laminates welded together using custom made impulse sealer. Figure from [142]. *Right:* Sketch of the LHAASO muon detector liner. Two circular laminates are welded together from the outside. Figure from [123]. 60
- Figure 4.2 Figures taken from Kunwar et al [108]. 62
- Figure 4.3 Input flux hitting the inside of an integrating sphere. Figure taken from [110]. 63
- Figure 4.4 *Left:* The integrating sphere used in the measurements. *Right:* The measurement cap covered with a sample of Tyvek. Samples of other materials are seen around it. 64
- Figure 4.5 The sphere wall reflectance,  $\rho_w$ , as measured, compared with the nominal values from the Labsphere manual [110] 65

- Figure 4.6 Measurements for the tyvek samples in MPIK. While 1082D stands out as the type with the greatest reflectivity, all Tyvek types show a reflectivity above 80% in the wavelengths of interest. 66
- Figure 4.7 The reflectivity measurements of a SWGO custom film sample, carried out by the National Institute of Astrophysics, Optics and Electronics [INAOE], in Mexico, and initiated by Michael Schneider. 67
- Figure 4.8 *Left:* Measurements for the HAWC liner and the liner of our first prototype bladder. *Right:* Measurements for our first custom-made SWGO liner. Tyvek is laminated to the black side of this liner. Measurements from INAOE are shown for comparison. 68
- Figure 4.9 *Left:* Measured diffuse reflectivity spectrum for VM2000, A4 printing paper and household aluminum. *Right:* Figure taken from [95], showing reflectivity measurements. 68
- Figure 4.10 *Left:* Reflectivity of half tyvek-covered material sample. *Right:* The half tyvek-covered measurement cap. The measurements were done by rotating this cap by 90° each time. 69
- Figure 4.11 Different absorption length spectra possibilities for a water sample measured to have  $\lambda_{abs} = 18$  m at 410 nm. The absorption spectra measured are by Segelstein in 1981 [153], Querry, Cary, and Waring in 1978 [147], Pope and Fry in 1997 [143] and Sogandares and Fry in 1997 [157]. The Quantum Efficiency of PMT R5912 used in the simulations with HAWCSim is plotted in red. 71
- Figure 4.12 The setup to measure water transmission. The C-star transmissometer is on the left, connected to a power source and a laptop, and on the right are four of the buckets that house materials being tested. 72
- Figure 4.13 Water quality measurements for the PVC bladder material. *Top:* Measurements using reverse osmosis water. *Bottom:* Measurements using filtered water. 74
- Figure 4.14 Water quality measurements for the HAWC bladder material. *Top:* Measurements using reverse osmosis water. *Bottom:* Measurements using filtered water. 75
- Figure 4.15 Water quality measurements for the GeoFlex and Enviro liners that were produced by the Layfield company. The outer layer of our double-layered WCD prototype is made of GeoFlex (See Section 4.2). 75

- Figure 4.16 *Top:* Water quality measurements of Tyvek samples. *Bottom:* Water quality measurements for Tyvek 1082D, started earlier than the other samples. This is the Tyvek used for the lower chamber for the double-layered WCD prototype (see Section 4.2). 76
- Figure 4.17 *Top:* Water quality measurements for the A4 and A2 stainless steel screws. *Bottom:* Water quality measurements for two different PMTs along with their control barrels. 77
- Figure 4.18 *Left:* The custom hot air welding machine made by MPIK workshop and the first bladder made using it. *Right:* Commercially ordered array of three 60 cm high PVC bladders, attached with floaters. 79
- Figure 4.19 The test facility at MPIK: A lake simulation tank that is 10m in diameter, 7 m in height, shown with two bladders deployed. Two PhD students are shown for scale. 80
- Figure 4.20 The muon taggers were used to get known particle paths during the prototyping tests. 82
- Figure 4.21 *Left:* The first single chamber prototype bladder, made of PVC, with a floating hatch and two floaters attached. *Right:* The sketch of the single-chamber prototype tests. The bladder made of PVC floats in between two muon taggers. The PMT unit is hanging from the hatch at the top of the bladder. 83
- Figure 4.22 The signal times of the three-channel runs taken with the one-chamber PVC bladder, triggering on the coincidence between the top and bottom muon taggers. "Bottom" and "top" denote the bottom and top muon taggers. Time correlation between all channels is seen. The offset in the axis is due to the differences in cable length. 85
- Figure 4.23 The three design options for a double-layered WCD. From left to right: A) Bladder with an internal divider, B) Two independent volumes, C) the matryoshka, or nested bladders 86
- Figure 4.24 The prototyping of a muon matryoshka. *Left:* Muon matryoshka passing through a bladder's hatch. *Middle:* Muon matryoshka in closed position. *Right:* Muon matryoshka in open position, how it would sit inside the larger bladder. 87
- Figure 4.25 The pool tests for the matryoshka 88
- Figure 4.26 Deployment of the matryoshka. 89

- Figure 4.27 The two configurations used while data taking. The setup is shown from the top and from the side. For "Center", the top tagger, shown with orange, was placed close to the hatch. For "Edge", the top tagger was moved to the edge of the bladder, shown in dark green.  $a = 139$  cm.  $b = 64$  cm.  $c = 67$  cm.  $d = 27$  cm.  $e = 55$  cm  
90
- Figure 4.28 The signal in the lower chamber vs the signal in the upper chamber for the two datasets that were obtained by triggering on the coincidence between the two muon taggers, obtained by integrating over the full waveforms after making quality cuts. The left dataset was taken when the top tagger was placed close to the center of the bladder, while the right one was taken when the top tagger was near the edge of the bladder. 91
- Figure 4.29 Example SPE pulses, for the lower chamber PMT Hamamatsu R5912, at a voltage of 1.76 kV 92
- Figure 4.30 Ratio of integrated pulses over pulse maxima. *Left*: Center run. *Right*: Edge run. We see that for smaller pulses, the ratio gets larger for the reflective lower chamber. This effect gets amplified for the edge run where there are more reflections. 93
- Figure 4.31 The integral distributions of the waveforms for the SPE runs of the lower chamber (*Left*) and the upper chamber (*Right*). 93
- Figure 4.32 Data calibration using integration 94
- Figure 4.33 Normalized charge distribution histograms for the 'center' and 'edge' case in units of photoelectrons (p.e.). Green shows the calibration that was done with the values from the fit made using all five SPE runs, while blue shows the one made using the three SPE runs with the highest voltages. We see that the lower chamber signal appears higher in the second case, while for the upper chamber there is no difference. 95
- Figure 4.34 Peak amplitude distributions obtained by looking at all waveforms, and those that come only after the peak that caused a trigger. 96
- Figure 4.35 Integral distributions obtained by looking at all pulses, and those that come only after the peak that caused a trigger. 97
- Figure 4.36 *Left*: Example fit performed on an integral distribution of the pulses after the triggered peak, using gaussian-kde. *Right*: The maxima for each fit vs voltage setting for the upper chamber. Two exponential fits are performed as before. 97

- Figure 4.37 Visualisation of a GEANT4 simulation of the test facility in Heidelberg, where the lower chamber that is immersed into the larger bladder is depicted as a separate bladder with a smaller radius. 99
- Figure 4.38 The measured signal distribution (histogram) compared with selected simulations made with HAWCSim. 101
- Figure 4.39 Simulations with the bottom tagger's position varied relative to the double-layered WCD. 102
- Figure 4.40 Time distributions of data and the simulations with different parameters for the lower chamber. The combination  $\lambda = 10 \text{ m}$   $R \approx 0.92$  is the most realistic one that matches the data. 103
- Figure 5.1 *Left:* The excess map from H.E.S.S. paper, taken from [77]. The two PWN (J1826-130 and J1825-137, along with their associated PSR are shown) *Right:* The HAWC detection of the region from 2021, taken from [20] 108
- Figure 5.2 HAWC angular resolution before (Pass 4) and after (Pass 5) the recent data reconstruction improvements as a function of FHit bin. Plot taken from Albert et al. [22]. 112
- Figure 5.3 The HAWC energy bins. The bins used in this analysis are shown in white. 113
- Figure 5.4 Significance map of the region, made by assuming a model and convolving it with the PSF of the instrument. Individual structures are resolved. 114
- Figure 5.5 The flux points for PWN HESS J1825-137 extracted with a log-parabola model and an exponential cut-off power-law model. There is a marginal preference for the exponential cut-off power-law model. 117
- Figure 5.6 The spectra extracted for the three sources in the region. LS5039 has a preferred power-law spectrum, while HESS J1826-130 has log-parabola. The PWN HESS J1825-137 is plotted with the marginally preferred exponential cut-off power-law spectrum. 118
- Figure 5.7 Spectral Points taken from Fermi-LAT [145], H.E.S.S. [77], HAWC [20], and LHAASO [46]; compared with our analysis and best fit model. 119
- Figure 5.8 Significance maps with different energy bands using HAWC data. Contours from the H.E.S.S. publication [77] are shown in white. *Left:* [1 – 10] TeV. *Middle:* [10 – 56] TeV. *Right:* [56 – 316] TeV. 120
- Figure 5.9 The radial extent of the PWN vs energy. The radial extent values for HAWC obtained from the three separate fits are shown in orange. The H.E.S.S. [77] and Fermi-LAT [145] points have a different definition of radial extent. The H.E.S.S. points are taken from Analysis A and include the systematic errors. 121

- Figure 5.10 *Left:*An example electron spectrum that is in equilibrium between injection and losses, by Breuhaus et al. [43]. *Right:* Steady-state gamma-ray spectra, with increasing values of  $\Xi$ , from an electron spectrum with  $E^{-2}$  with an exponential cutoff at 10 PeV. The IC emission is able to account for higher energy emissions with increasing values of  $\Xi$ . Figure is taken from Breuhaus et al. [41]. 123
- Figure 5.11 The model of IC emission valid in radiation environments from [42], which is able to describe the UHE emission seen from HESS J1825-137 with the HAWC data. 124
- Figure 5.12 The number of hours per day HAWC and SWGO would see sources in the sky depending on their declination. The declination of HESS J1825-137 is shown with pink. 126
- Figure 5.13 The spectral energy distribution of HESS J1825-137 with the two SWGO predictions. Simulating a two component model and fitting with a single component model gives the flux points in dark red, while simulating a single energy dependent component model and fitting with a single model gives the flux points in black. 128
- Figure 5.14 The potential for SWGO for seeing the energy dependent size of HESS J1825-137. The radial extent of the nebula was found using simulated data obtained from IRFs that are given up to 317 TeV. SWGO is expected to probe energies higher than shown here. 129
- Figure A.1 The matryoshka is attached to a hallow ring via eight ropes, and the PMT support that the matroyaska is attached to has three ropes suspending it. The ropes of the PMT support and the hallow ring are all attached to a pivot point, which is suspended in air via a crane. The ropes shown in orange are not controlled directly by the winch 133
- Figure A.2 The matroyshka is lowered into the bladder, two persons waited near the bladder to ensure it went in smoothly. 134
- Figure A.3 Fully opened matryoshka inside the larger bladder,SWGO Unit Prototyping ready for data taking. 135
- Figure B.1 Input flux hitting the inside of an integrating sphere. Figure taken from [110] 137
- Figure C.1 Some conductivity measurements. 141
- Figure C.2 Some conductivity measurements. 142
- Figure D.1 The counts maps for different energy bins 143
- Figure E.1 The hydrodynamics and ocean engineering tank at LHEEA, France. The segmented wavemaker is seen in the background. Figure taken from [91]. 145

Figure E.2 Sketch of the one-bladder setup for the upcoming wave basin tests in France. Figure credit: Werner Hofmann. 146

## LIST OF TABLES

---

Table 1.1	Radiated gamma-ray spectra and energy losses, assuming a parent particle population with a powerlaw spectrum $N(E_e) \propto E_e^{-s}$ . Adapted from [135] 5
Table 2.1	The Science benchmarks for SWGO along with their respective design drivers. Adapted from [53] 38
Table 4.1	The diameters of the three port openings of the integrating sphere. 65
Table 4.2	The results of an analysis of the two water types used in our water quality measurements, compared with regular tap water from MPIK. The analysis was performed externally. 73
Table 4.3	SPE values acquired using integration around the highest pulses. 96
Table 4.4	SPE values found by integrating around the pulses that are after the trigger peak to check for bias. 98
Table 5.1	The best fit parameters for HESS J1825-137 for the three spectral models tested. The amplitude is in units of $10^{-13} \text{ TeV}^{-1} \text{ s}^{-1} \text{ cm}^{-2}$ with $E_0 = 10 \text{ TeV}$ . 117



## PREFACE

---

The work described in this thesis was possible with the help and guidance of many people and institutions. In this section I will summarize my personal contributions.

### CHAPTER 3: LAKE DESIGN

The presentation of the Lake design in this chapter is written by me, although the ideas are a product of the discussions and written exchanges, with Werner Hofmann, Felix Werner and Jim Hinton, and members of the SWGO collaboration.

I have performed the simulations using the HAWCSim software in order to evaluate the aspects of the lake design that may differ from the other technologies, including overburden and shielding capabilities of the lake design. I have contributed to the paper that evaluated the double-layered water Cherenkov detector design, Kunwar et al. [108]. I have contributed to the text and used EXPACS/PARMA and HAWCSim to perform the simulations for the HAWC tanks.

### CHAPTER 4: LAKE EVALUATION

Several people contributed to the evaluation and prototyping of the lake concept. The workshop at the Max-Planck-Institute for Nuclear Physics (MPIK), Felix Werner, Jim Hinton, Werner Hofmann and Fabian Haist were the main people that have contributed to this work. Below I give a list of my own contributions.

- I have performed the **reflectivity tests** and analyzed them.
- Together with Fabian Haist, I have performed the **water quality tests**.
- I have tested, and evaluated the **muon taggers**, with input from Werner Hofmann and help from the workshop.
- I have performed the **mechanical tests with small bladders** with input from Werner Hofmann and help from the workshop.
- The single layer bladders were commercially acquired. The bladder deployment process collaborative. I have taken data with the bladders after deployment, and performed the analysis of the data for the single layer bladders.
- The **matryoshka** was envisioned during our discussions with Felix Werner and Werner Hofmann. Several tests, miniatures, mini prototypes were conducted with the help of the workshop. These tests presented us with new challenges that we overcame with adjustments to the design. The

design details, for example the addition of the ring, were thought by me, however additions such as using the PMT weight came out of discussions with Werner Hofmann and Jim Hinton.

- I have contributed, along with the people mentioned before, to the deployment and testing of the matroshka and forming of the first double-layered water Cherenkov detector for SWGO. I have led the planning for this process.
- I have taken coincidence data using the double-layered bladder, with input from Fabian Haist and Felix Werner, and I have performed the calibration and analysis of this data.
- I have performed extensive simulations using HAWCSim in order to compare the data taken with the double-layered bladder and analyzed the results.

#### CHAPTER 5: HESS J1825-137 USING HAWC DATA

I have tested HAWC data reconstruction algorithms that were fixed by Chad Brisbois and Andrews Smith among others, such as a curvature correction algorithm, and reproduced core correction parameters found by Andrew Smith. Furthermore, I have applied the HAWC realignment corrections that were produced by Andrew Smith and others to the data level 3 scripts used for generating GDAF data for analysis with *gammapy*. I have also performed a verification of realignment of these corrections using the Crab nebula.

With the support of Quentin Remy and Jim Hinton, I have performed the modeling and analysis of the HESS J1825-137 region, but by taking the models of Quentin Remy as a basis. I have created significance maps, tested models for the sources in the region and performed fits. I have also performed the energy dependent morphology analysis with the HAWC data. The instrument response functions (IRFs) for the SWGO study was provided by Laura Olivera-Nieto. I have used these IRFs to simulate SWGO data for this region with *Gammapy*. I have performed the preliminary SWGO analysis.

## PRODUCTION OF GAMMA-RAYS AND PARTICLE INTERACTIONS

---

Astrophysical research using different wavelengths is crucial for our understanding of the Universe and the physical processes guiding its evolution. Observations in different wavelengths of the electromagnetic spectrum work together to give a complete view of a source or a physical phenomenon. At the highest energy end of the electromagnetic spectrum are gamma-rays, photons with energies larger than 100 keV, revealing the extreme and very high energy universe. While lower energy photons can be emitted due to thermal radiation following a black body spectrum, gamma-rays are only emitted due to processes that charged particles go through.

Gamma-rays originate from very energetic particles in various sources such as supernovae or pulsars, through non-thermal mechanisms involving magnetic fields and ambient photons and matter. Unlike the particles themselves, gamma-rays are chargeless, so they mostly point back to their origin, enabling studies of acceleration sites and mechanisms. Gamma-ray astronomy plays a very important role in exploring the non-thermal universe, as it covers a diverse range of topics in astrophysics [19], including the origin of cosmic rays, acceleration and radiation processes in extreme astrophysical environments, cosmological topics, beyond standard model physics and dark matter.

Section 1.1 introduces cosmic rays, gamma-rays and their acceleration mechanisms. Section 1.2 describes gamma-ray production mechanisms, while Section 1.3 explores pulsar wind nebulae (PWN) as gamma-ray sources. Finally, Section 1.4 describes the interaction of photons and charged particles with matter, namely the processes that may be used for detection of gamma-rays.

### 1.1 GAMMA-RAYS AND COSMIC RAYS

Cosmic rays, defined here as charged particles of extraterrestrial origin, were discovered over a hundred years ago. The presence of ionizing radiation in air was noticed by Rutherford in 1903 through an electroscope discharging completely despite being in vacuum [121], but at that time it was assumed that this radiation came from the Earth crust entirely. In 1911, Victor Hess made measurements with balloons at high altitudes up to 5 km and saw that the ionizing radiation in fact increased with altitude, showing the extraterrestrial origin of the radiation. The development of the cloud chamber in 1912 by Wilson made it possible to follow the tracks of these ionizing particles, eventually named by Robert A Millikan as "cosmic rays" (CR) [55, 75].

CRs are mainly protons ( $\sim 90\%$ ), helium nuclei ( $< 10\%$ ), heavier elements ( $< 1\%$ ) and electrons ( $< 1\%$ ) [121]. The energy spectrum of CRs is known

to extend up to very high energies, up to  $10^{20}$  eV and higher, approximately following a power law.

$$\frac{dN}{dE} \propto E^{-\alpha} \quad (1.1)$$

The spectral index  $\alpha$  undergoes a number of changes with increasing particle energy, giving the spectrum the distinct features seen from Figure 1.1. The figure shows the spectrum of CRs that is made by the measurements from different experiments, multiplied by  $E^{2.6}$  to display the changes in spectral index. These are in particular the spectral steepening at the *knee*, at around  $10^{15}$  eV, and the spectral flattening at the *ankle* at around  $10^{18}$  eV. Different speculations exist on the origin of these features, but general, the transition from CR with a galactic origin to CR with extragalactic origin is believed to happen around the ankle region [2, 87]. The second *knee* in the plot is a more recent observation, for example as seen by the TALE experiment [11].

Chemically, the composition of CR particles is similar to that of the sun, with the exceptions of lithium, beryllium and boron (present in high abundance in CR compared to terrestrial values) [55, 121]. Charged CR arrive in our solar system after being deflected by galactic and extragalactic magnetic fields, losing information on their origin.

As CR are charged particles, their trajectories get randomized by the magnetic fields in the universe, while gamma-rays (and neutrinos), being uncharged, propagate undeflected through space, without being influenced by any intergalactic or interstellar magnetic fields. Consequently they point towards their origins. As gamma-ray production occurs around the same places as CR production, they provide insight on the locations of CR production as well.

### 1.1.1 Acceleration Mechanisms

The mechanisms by which CR get accelerated and travel through space have been important research topics in astroparticle physics. The origin of highest-energy cosmic rays is still under debate. They may be produced as secondaries from the decay of heavy particles, or accelerated directly into relativistic energies within regions of intense magnetic fields [19]. In order to be a source of ultrahigh-energy cosmic rays (UHECR) there are several conditions an astrophysical object needs to satisfy.

The Hillas condition states that particles can be accelerated to ultrahigh energies given that they are confined within the acceleration region, meaning their Larmor radius would need to be smaller than the size of the accelerator:

The maximum energy achievable for a source with size  $R$  and magnetic field strength  $B$  is

$$E_{max} = \eta^{-1} \beta_{sh} e B R \Gamma \quad (1.2)$$

where  $\Gamma$  is the Lorentz factor of motion of the source,  $\beta_{sh} = \frac{u_{sh}}{c}$  is the shock velocity in units of speed of light, and  $e$  and  $\eta$  are acceleration efficiency parameters, where  $\eta = 1$  is the maximum achievable efficiency [26].

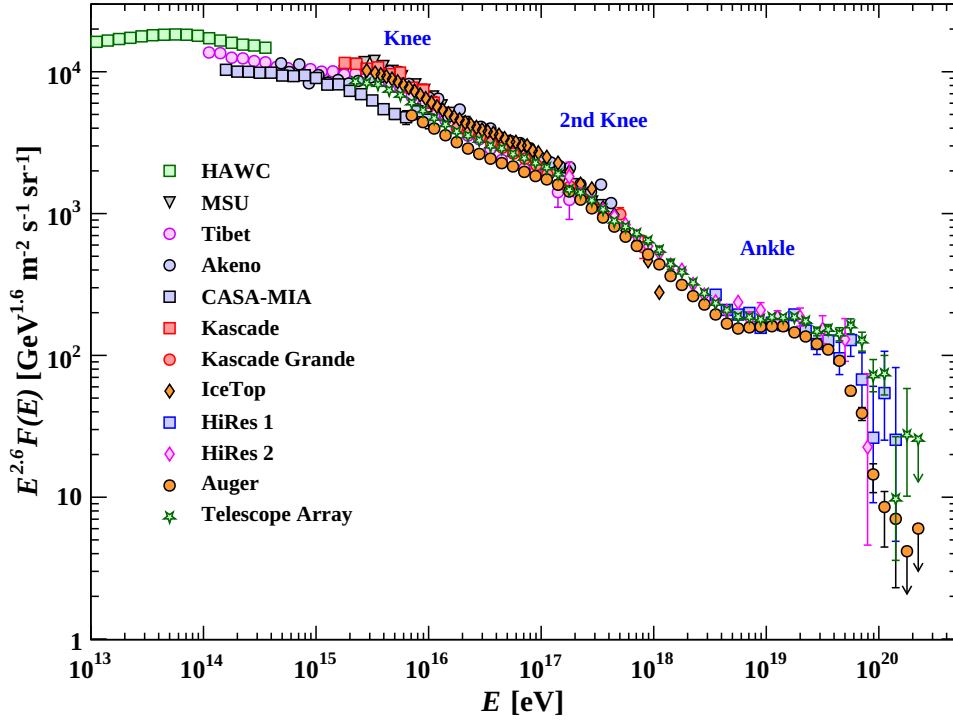


Figure 1.1: Cosmic ray differential energy spectrum from air shower measurements. The spectrum is shown multiplied by  $E^{2.6}$  to display the features; namely the three 'kinks' in the spectrum due to changes in spectral index. Figure taken from [34].

Figure 1.2 shows a Hillas diagram that shows astrophysical objects that are potential CR accelerators, with the vertical axis the magnetic field strength  $B$  of the source and the horizontal axis as the radial size  $R$ , equal to the comoving size multiplied by  $\Gamma$ , for  $\eta = 1$  limit. The solid lines indicate the minimum  $BR$  required to accelerate protons and iron nuclei to  $10^{20}$  eV energies in the case of a fast shock, while the dashed lines are for the case of a slower shock. Objects to the left of the lines are those that do not satisfy the Hillas condition and thus would be unable to accelerate protons or iron nuclei to  $10^{20}$  eV.

Another condition is that the source should be able to provide the necessary energy for the acceleration of UHECR. Moreover, the radiation energy losses and the energy losses coming from the interaction with other particles should be less than the gained energy within the acceleration area [44].

As seen from the Hillas diagram, sources that can accelerate CRs include active galactic nuclei (AGN), Galaxy clusters, gamma ray bursts (GRB) and neutron stars/ magnetars. CR acceleration is possible also from pulsar wind nebulae (PWNe), supernova remnants (SNRs), binary system and the Galactic center.

An early attempt to explain the acceleration of CRs was **second-order Fermi acceleration**, proposed by Enrico Fermi in 1949. This mechanism postulates that particles get accelerated to high energies by colliding with interstellar clouds that act as magnetic mirrors. This mechanism manages to generate

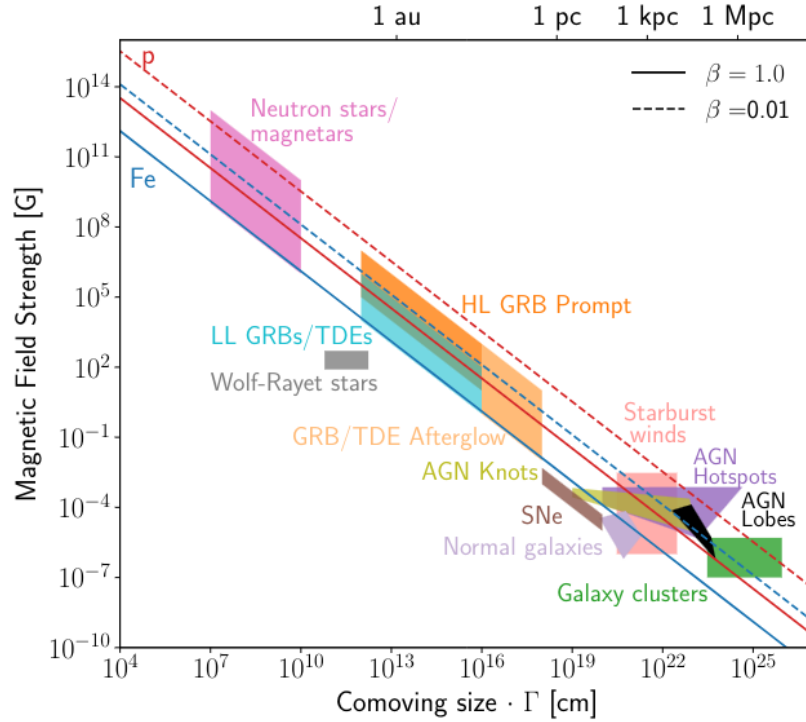


Figure 1.2: A Hillas diagram showing potential cosmic accelerators, with magnetic field strength on the y-axis and source radius  $R$  on the x-axis, for acceleration of UHECR to  $10^{20}$  eV. Figure taken from [26].

a power law spectrum for CR acceleration, however it is quite inefficient. These interstellar clouds are replaced in newer theories by turbulent astrophysical plasmas. **First-order Fermi acceleration**, proposed in 1970s, is a more efficient acceleration mechanism where the acceleration sites are instead in shocks. Shocks are discontinuities in temperature, pressure and density of a medium [121]. In this mechanism, also referred to as diffusive shock acceleration, particles gain energy as they diffusively cross the shock repeatedly, for example in SNRs or shocks from pulsar winds [84].

## 1.2 GAMMA-RAY PRODUCTION MECHANISMS

The interaction of charged particles with matter and radiation fields result in the emission of gamma-rays that may eventually be detected by gamma-ray detectors on satellites or the ground. These processes include different emission mechanisms that may emit in different wave bands, and energy loss mechanisms that are utilized in the gamma-ray detectors themselves. In this section we briefly go over the relevant radiation processes. An example gamma-ray spectrum that is formed from the processes is shown in Figure 1.3, taken from [96]. The energy losses of the parent particles along with the radiated spectra are summarized in Table 1.1, adapted from Naurois [135].

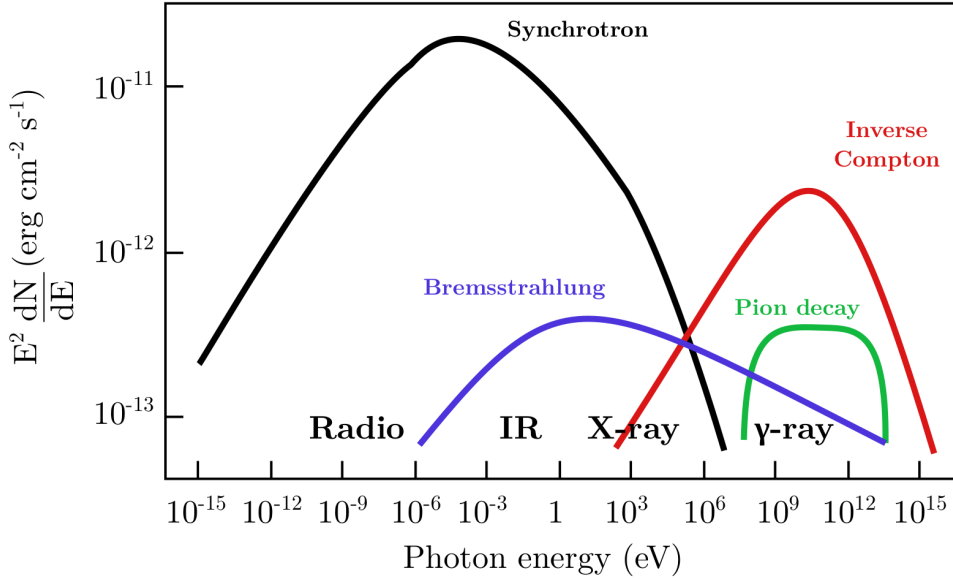


Figure 1.3: An example spectral energy distribution showing the different gamma-ray production mechanisms. Depending on the environment and nature of the source, different mechanisms would dominate. Figure taken from Jardin-Blicq [96].

Process	Energy Losses (dE/dt)	Radiated Spectrum
Synchrotron	$\propto E^2$	$I(E_\gamma) \propto E_\gamma^{(1-s)/2}$
Inverse Compton (Thomson)	$\propto E^2$	$E_\gamma^{(1-s)/2}$
Bremsstrahlung	$\propto E$	$E_\gamma^{-s}$
Hadronic Interaction	$\propto E$	$E_\gamma^{-s}$

Table 1.1: Radiated gamma-ray spectra and energy losses, assuming a parent particle population with a power law spectrum  $N(E_e) \propto E_e^{-s}$ . Adapted from [135].

### 1.2.1 Synchrotron Radiation

Charged particles in accelerated motion radiate energy. Under the influence of a magnetic field, charged particles undergo an accelerated motion perpendicular to their velocity, radiating photons. The emission can be shown to depend with mass of the particle as  $\propto 1/m^4$ , hence synchrotron emission is more significant for lighter particles, being more prominent in electrons than protons.

For a population of electrons with a power law spectrum  $N(E_e) \propto E_e^{-s}$ , the spectrum of radiated energy has the form  $\propto E_\gamma^{\frac{1-s}{2}}$ .

Energy loss of an electron by synchrotron radiation is given by

$$\frac{-dE}{dt} = \frac{4}{3} \sigma_{TC} U_B \beta^2 \gamma^2 \quad (1.3)$$

where  $U_B = B^2/8\pi$  is the magnetic energy density,  $\sigma_T = \frac{8\pi}{3}r_e^2$  is the Thomson cross-section,  $\gamma = \frac{1}{\sqrt{1-\beta^2}}$  is the Lorentz factor for the parent particle (electron) and  $\beta = \frac{v}{c}$ . We see that the emission is proportional to  $\gamma^2$  and  $B^2$ , electron energy and magnetic field. The spectrum of synchrotron radiation for an electron is distributed around a critical frequency  $\nu_c = \frac{3}{4\pi}\gamma^2\frac{qB}{mc}\sin\theta$  where  $\theta$  is the pitch angle,  $q$  is the charge of the particle, and  $\gamma$  is the Lorentz factor of the particle [38], and peaks at a frequency  $\nu_{max} = 0.29\nu_c$  [14, 135].

The electron cooling time is proportional to  $\propto 1/\gamma B^2$ , hence cooling time is longer in regions of smaller magnetic fields and for lower energy particles [133].

Synchrotron emission can span a range from radio to X-ray emission, as shown in Figure 1.3. For example, in the case of the Crab nebula, synchrotron emission from radio energies up to gamma-ray energies is observed, as shown in Figure 1.6 [57, 84].

### 1.2.2 Inverse Compton Scattering

Electrons moving at relativistic speed can scatter low energy photons, such as those of the Cosmic Microwave Background (CMB), to high energies, resulting in Inverse-Compton (IC) radiation, which is the primary mechanism for high energy radiation from electrons. In Compton scattering, it is the high energy photons that scatter off lower energy electrons, giving them energy (see Section 1.4.3).

For a single electron the energy loss from IC mechanism is expressed as

$$-\frac{dE}{dt} = \frac{4}{3}\sigma_T c U_R \beta^2 \gamma^2 \quad (1.4)$$

where  $U_R$  is the target photon energy density. While synchrotron emission depends on both electron distribution and magnetic field, IC emission is independent of magnetic field, but dependent on the target photon energy density.

When the energy of the incoming photon ( $\hbar\omega$ ) is  $\hbar\omega \lesssim m_e c^2$ , the process is similar to Thomson scattering where the energy transfer is negligible and Thomson cross section applies. Above this regime, Klein-Nishina (KN) cross-section applies and the energy transfer is large. The scattering is deeply inelastic. The total Klein-Nishina cross section  $\sigma_{K-N}$  is shown in Figure 1.4, with its dependence on energy. Above the energies  $\hbar\omega \approx m_e c^2$ , the cross section decreases. At high energy, the drop in the cross section is seen as

$$\sigma_{K-N} = \frac{3}{8}\sigma_T \frac{1}{x} \left( \ln 2x + \frac{1}{2} \right) \quad (1.5)$$

where  $x = \hbar\omega / m_e c^2$ .

This drop at high energies has the effect that IC scattering gets exponentially attenuated as shown in Figure 1.4. This suppression of IC radiation happens at electron energies of around 100 TeV, 10 TeV and 30 GeV respectively for the cases of CMB photons, infrared from dust, and visible light [84]. Due to this

suppression effect, UHE emission used to be thought of as evidence of emission from hadronic interaction mechanisms.

In addition, at these high energies electron cooling becomes less efficient, meaning electrons survive longer. Thus, in the KN regime, when IC losses dominate in radiation dominated environments, harder, cooled spectra are expected [84].

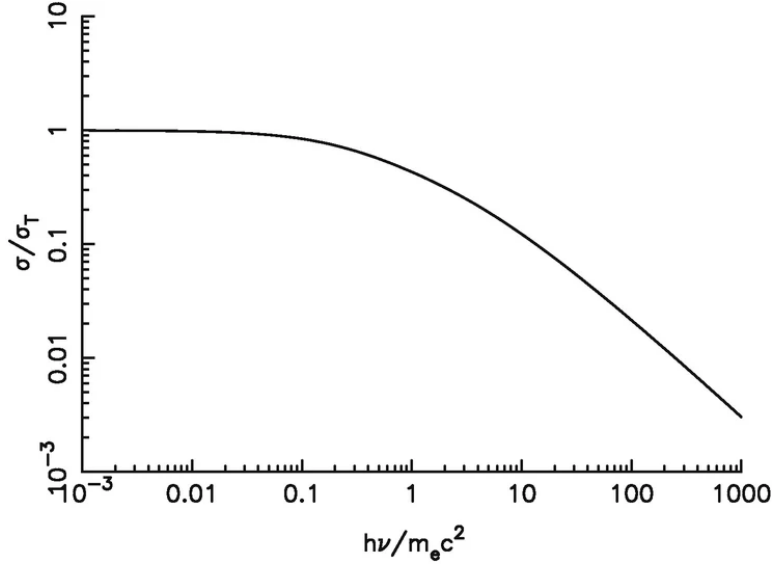


Figure 1.4: The dependence of total Klein-Nishina cross-section divided the Thomson cross-section on  $h\nu/m_e c^2$ . Below  $h\nu/m_e c^2 \approx 1$ , the two cross sections are roughly equal. At energies above  $h\nu/m_e^2$ , IC scattering mechanism gets suppressed. Figure taken from [167].

The IC spectrum has the same shape as synchrotron spectrum,  $\propto E_\gamma^{\frac{1-s}{2}}$ . In the KN regime this becomes  $\propto E_\gamma^{1-2}$  [84].

In the Thomson regime the ratio of synchrotron emission over IC emission is  $\frac{P_{IC}}{P_{sync}} = \frac{U_r}{U_b}$ .

### 1.2.3 Bremsstrahlung

When a charged particle is in the Coulomb field of a nucleus or ion, it is deflected, radiating bremsstrahlung photons [75]. The direction of the emitted photons is in the original direction of the charged particle. The emitted photon takes about half of the kinetic energy of the parent particle. For a parent particle population with  $N(E_e) \propto E_e^{-s}$ , the emission spectrum shape takes the form  $\propto E^{-s}$  [133].

Bremsstrahlung radiation rate is inversely proportional to the square of mass. For this reason, although bremsstrahlung happens for all charged particles, for electrons, due to their low mass, it is the dominating process. For example muons radiate  $(m_e/m_\mu)^2 \sim (1/200)^2$  less than electrons. Hence, electrons and positrons lose energy primarily via bremsstrahlung, until a critical energy  $E_c$  is reached. At energies lower than  $E_c$ , electrons and positrons primarily lose

energy mainly by ionization (see the left plot of Figure 1.10). While ionization varies logarithmically with electron energy, bremsstrahlung losses are nearly proportional to energy. The bremsstrahlung mechanism becomes relevant for particles passing through matter, such as water or atmosphere, especially for electrons.

#### 1.2.4 Hadronic Interactions

CR protons or nuclei can interact hadronically with matter and radiation, eventually generating gamma-rays through pion decay. Gamma-ray emission produced this way traces the CR acceleration and propagation sites. Through inelastic collisions of high energy protons with the target matter, pions  $\pi^+$ ,  $\pi^-$  and  $\pi^0$  get produced in roughly the same amount. While  $\pi^0$  decay into gamma-rays, causing high energy gamma-ray emission,  $\pi^+$  and  $\pi^-$  decay into charged muons, neutrinos and electrons [99].

$$pp \rightarrow \pi^0 \rightarrow \gamma\gamma$$

$$pp \rightarrow \pi^\pm \rightarrow \mu^\pm + \nu_\mu/\bar{\nu}_\mu \rightarrow e^\pm + \nu_e/\bar{\nu}_e + \nu_\mu + \bar{\nu}_\mu$$

For a power law distribution of CR protons with  $N(E_p) \propto E_p^{-s}$ , the gamma-ray emission spectrum from pion decay has the same index. The cooling in this case is almost independent of energy.

### 1.3 PULSAR WIND NEBULAE

Pulsars are highly magnetized rapidly rotating neutron stars. Pulsar wind nebulae (PWNe) are bubbles of shocked relativistic particles that form when a pulsar ejects winds that interact with the environment [67]. PWNe are able to exhibit emission from radio wavelengths up to TeV energies.

From surveys of instruments such as H.E.S.S.<sup>1</sup>, MAGIC<sup>2</sup> and HAWC<sup>3</sup>, we see that PWNe are the dominant source population at TeV energies [101, 165].

Chapter 5 presents a study of the PWN HESS J1825-137 using HAWC data and simulated SWGO data. This PWN exhibits asymmetric extended emission and energy dependent morphology. At a distance of  $\sim 4$  kpc, it is one of the largest sources known in the gamma-ray sky and one of the most powerful TeV emitters. We take a closer look at pulsars and PWNe in this section.

#### 1.3.1 Pulsars

Pulsars are highly magnetized rapidly rotating neutron stars emitting periodic radio pulses detectable from Earth. They were discovered due to their radio

<sup>1</sup> The High Energy Stereoscopic System (H.E.S.S.) is a system of five Imaging Atmospheric Cherenkov Telescopes (IACT) in Namibia.

<sup>2</sup> Major Atmospheric Gamma Imaging Cherenkov Telescopes (MAGIC) is a system of two IACTs in La Palma, Spain.

<sup>3</sup> High Altitude Water Cherenkov (HAWC) Observatory is a wide field gamma-ray observatory in Mexico.

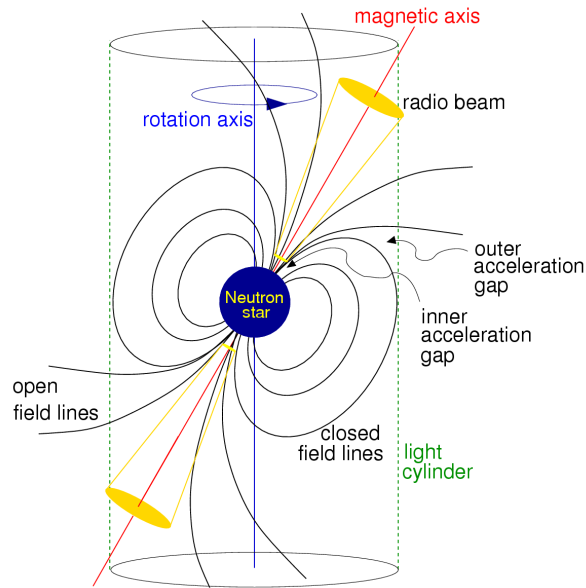


Figure 1.5: Sketch of a pulsar. The magnetic field axis and rotation axis are misaligned. Particles accelerated along the open magnetic field lines may escape and form pulsar winds. Figure taken from Mitchell and Gelfand [130].

pulsations in 1967 [121] and can rotate up to one-third the speed of light. Neutron stars have a mass of around 1.5 solar masses ( $M_{\odot}$ ) and radius around  $\sim 12$  km, being one of the densest forms of matter in the universe.

At the end of its life cycle, the core of a massive star (mass above  $8M_{\odot}$ ) runs out of nuclear fuel and gravitationally collapses. After having burnt all elements within its composition through different nuclear reactions, the star is left with its iron core. Thermal high energy gamma-rays in the core that were produced during earlier fusion reactions acquire enough energy to photodisintegrate iron nuclei into protons and neutrons. Through inverse  $\beta$ -decay, free energetic electrons interact with protons to form neutrons. A large neutrino luminosity and a large release of energy follows. A Type II Supernova (SN) explosion occurs, and if the progenitor star's mass is not more than  $\approx 20M_{\odot}$ , the compact remnant of this explosion evolves into a neutron star [47, 112].

Pulsars have a high speed and high magnetic field. When a star with around  $\sim 10^6$  km radius shrinks to  $\sim 20$  km radius, in the process of gravitational collapse, angular momentum conservation makes the pulsar rotate rapidly. Magnetic flux conservation causes the high magnetization of pulsars, where the magnetic field direction is most of the time not parallel to the rotation axis. This misalignment results in a dipole that rotates, as can be seen from Figure 1.5.

As the magnetic field lines rotate rapidly with the star, a very strong electric field is induced. This strong electric field is able to pull charged particles away from the surface of the neutron star. A pair production cascade occurs, where an accelerated electron emits synchrotron radiation, and the synchrotron photons have enough energy to pair produce. This plasma of charged particles rotates

with the pulsar's magnetic field lines and its escape forms the pulsar wind. The light cylinder is the cylinder where the matter rotating along the field lines would need to rotate at the speed of light. Particles that are produced along the open field lines that go beyond the light cylinder are the ones that are able to escape [130].

The spin period of a pulsar increases with time, meaning a decrease in rotational kinetic energy. The spin down luminosity of a pulsar is the rate at which rotational kinetic energy is dissipated, given by

$$\dot{E} = 4\pi^2 I \frac{\dot{P}}{P^3} \quad (1.6)$$

where  $P$  is the spin period, which can be found from observations, and  $I$  is the moment of inertia of the neutron star. This is the rate at which the pulsar dissipates energy, supplying the emission from PWNe, via magnetized particle winds of electron-positron pairs [67].

The age of a pulsar can also be inferred from this quantity, along with its magnetic field strength.

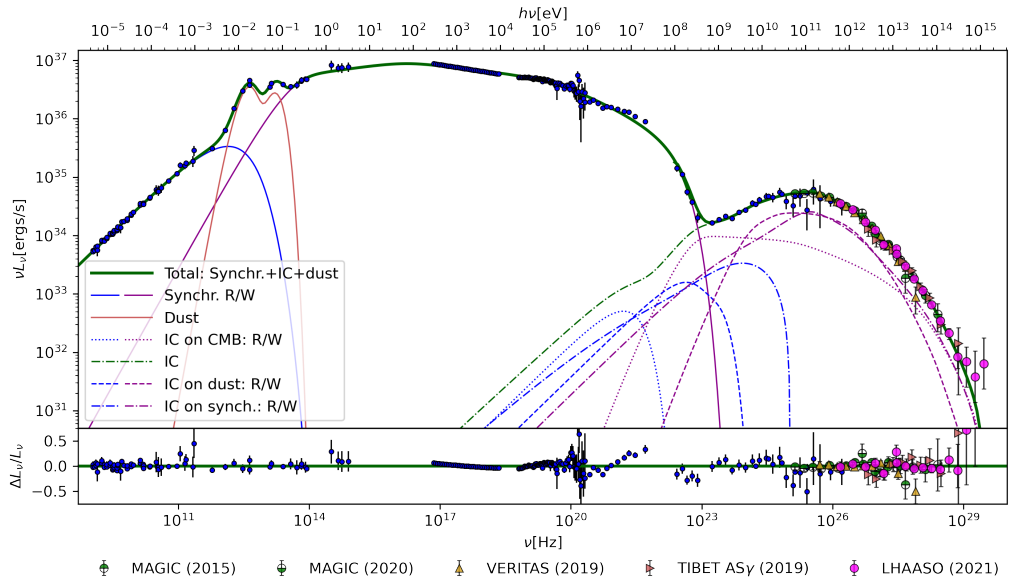


Figure 1.6: Spectral energy distribution of the Crab nebula, from radio to PeV energies, taken from Dirson and Horns [57].

### 1.3.2 Pulsar Wind Nebulae

PWNe are bubbles of escaped relativistic particles that emit radiation. They are formed when a pulsar's escaping relativistic wind interacts with and becomes confined by the surrounding medium. PWNe emission has been detected across multiple wavelengths, from radio emission to gamma-ray emission. The Crab nebula is a prominent example of a source that emits across wavelengths ranging from radio to gamma-ray energies, as shown in the broadband spectrum from Dirson and Horns, shown in Figure 1.6 [57].

The outflow of particles from the pulsar is initially highly relativistic and low pressure, and it is converted to a lower bulk velocity high pressure plasma. A wind termination shock is produced with the deceleration of this outflow, where the ram pressure of the wind is balanced by the external medium.

At the termination shock, much of the magnetic energy of the wind is converted to particle energy, causing the plasma to be a particle dominated environment [67, 130]. The acceleration of particles may be due to magnetic reconnection at this termination shock which releases energy. The high energy emission from PWNe comes from this plasma that is made up of electrons and positrons, hence the primary mechanisms are synchrotron and IC emission.

The expansion of the PWN into the supernova ejecta may produce instabilities that are observed as filamentary structures in UV/optical. Furthermore, particles accelerated at the wind termination shock form a toroidal structure, generating synchrotron radiation that is seen in X-ray bands [67].

The movement of the pulsar wind is not well understood, although many models exist. A common one is the striped wind model that has alternating stripes of wind coming out of the pulsar with opposite polarity as it rotates. According to the model, the reconnection of these alternating fields near the shocks may accelerate particles.

#### 1.3.2.1 PWNe Evolution

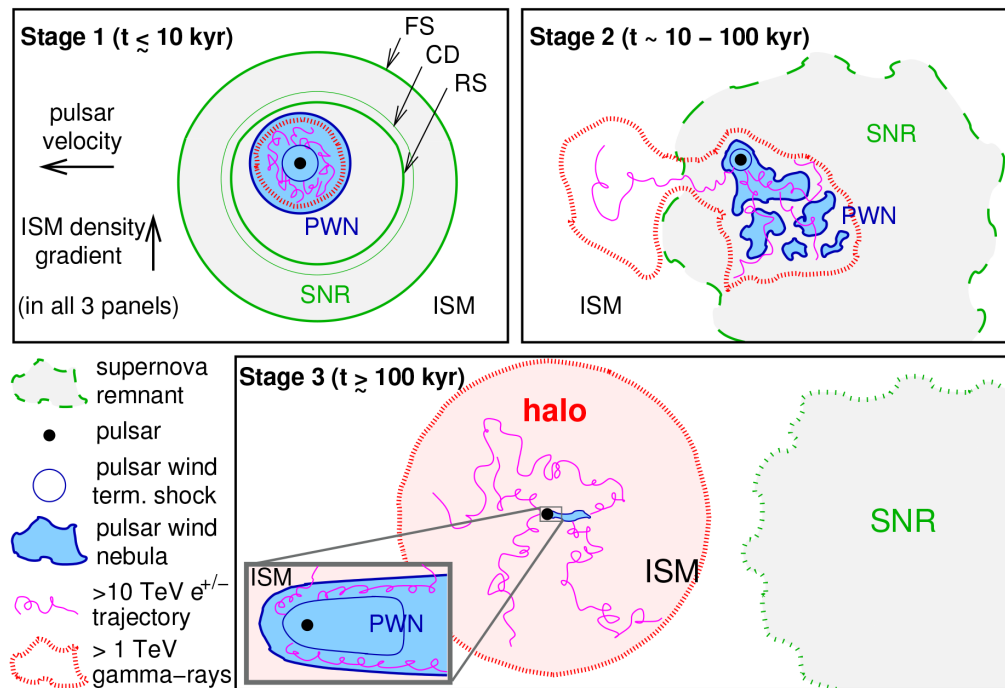


Figure 1.7: The three evolutionary stages of PWNe. Initially the PWN is confined within the SNR with a forward shock (FS) and a contact discontinuity (CD). At the second stage the PWN is crushed by the inward moving reverse shock (RS). Lastly the pulsar escapes from the SNR. The escaped electron positron pairs may then form a pulsar halo. Figure taken from Giacinti et al. [68].

PWNe physical characteristics change significantly through their lifetime. Depending on their age, the stage of their development and the interstellar medium (ISM) surrounding them, PWN show emission on different wavebands and different characteristics. For these reasons it is important to go over the evolution or lifetime of PWNe, shown in the panels of Figure 1.7.

During **stage one** ( $t < 10$  kyr after the SN explosion), the PWN undergoes an expansion near the center of the SNR, and the pulsar wind is confined. The SNR formed by the expansion of the supernova ejecta into the surrounding interstellar matter creates a forward shock, and at the same time surrounds the PWN with slow moving, high density, pressure-less material [67, 68]. The expansion's slowing down creates a second shock, the reverse shock. A contact discontinuity region separates the two shocks (see Figure 1.7). The PWN is entirely confined, along with the high energy electrons and positrons accelerated within. The Crab nebula is an example of a PWN thought to be in this stage. It is a young system with X-ray and TeV emission coming from similar regions.

At the end of this stage, the reverse shock moves inwards, reaching some regions of the PWN earlier than others, and crushes the PWN.

**Stage two** ( $t \sim 10$ -100 kyr) starts once the PWN is interacting with the material in the SNR. This happens when the PWN collides with the reverse shock, getting crushed. The electrons previously confined inside the PWN are able to escape into the surrounding SNR, and possibly propagate into the ISM. This may enable the extent of the TeV emission to be greater than the nebula [68]. The Vela nebula seems to be at this stage. This is due to its age, and the difference observed between the location of its X-ray and TeV emission. X-ray emission is produced from the high energy electrons through synchrotron emission that stay close to the source, while TeV emission can be produced from older, lower energy electrons that are further away from the source through IC emission.

**Stage three** ( $t > 100$  kyr) occurs once the pulsar fueling the PWN has escaped from the SNR, moving supersonically with respect to its surroundings. As the SNR slowly expands and fades away, the pulsar propagating within the ISM forms a **bow-shock PWN**, where a shocked PWN tail is trailing behind the pulsar, and a relic PWN is left behind. High-energy electrons and positrons are able to escape into the surrounding ISM, demonstrated by the observations of X-ray filaments around such PWNe [68]. In this case, the high energy particles from the PWN can diffuse in the ISM and emit TeV gamma-rays in regions larger than the PWN. Geminga for example, can be classified as a bow-shock PWN in Stage three. In this classification of three stages, the PWN studied in this thesis, HESS J1825-137, is suggested by Giacinti et al. to be in a hybrid stage due to its asymmetric morphology and characteristic age of  $\sim 21.4$  kyr [68].

### 1.3.2.2 Pulsar Halos

After the detection of extended gamma-ray emission around some middle-aged pulsars by wide field of view instruments Milagro and HAWC, a new source class termed TeV halos was proposed by Linden et al. [120], with a different morphology. They argue that the significantly more extended TeV

emission from PWNe, compared to X-ray PWN, may point at a unique origin and dynamic evolution. They point out that this feature may help identify radio quiet PWNe. Giacinti et al. [68], meanwhile, define pulsar halos as regions of escaped particles where there is an overdensity of relativistic electrons in a zone where the source (PWNe, or other) no longer dominates the dynamics of the surrounding medium. This means propagation dominated by diffusion, and not advection. While in the Linden et al. definition TeV emission further away from the extend of a PWN during Stage two may count as a TeV Halo, this would not be the case for the definition posited by Giacinti et al. As we will see in more detail in Chapter 5, PWN HESS J1825-137 has such extended TeV emission.

#### 1.4 PARTICLE DETECTION

Interactions of particles with matter and their emission of photons are mechanisms utilized in gamma-ray detectors on satellites or on the ground. Electromagnetic Air Showers (EAS) start when a primary gamma-ray interacts in earth's atmosphere and pair produces an electron positron pair. From thereon, in addition to bremsstrahlung of electrons, pair production is the main mechanism with which gamma-rays lose their energy in the atmosphere (see Chapter 2 for more detail). These gamma-ray initiated EAS can be detected on the ground by wide-field gamma-ray observatories when their secondaries pass through water Cherenkov detectors (WCDs), through their interactions with the water medium. In this section we go over the processes that are relevant in particular for the detection of EAS by wide-field gamma-ray observatories and identification of charged particles for background elimination.

##### 1.4.1 Ionization Losses

The average value of energy lost by a charged particle going through matter, per length traversed, is given by Bethe-Bloch formula<sup>4</sup> in the region  $0.1 \gtrsim \beta\gamma \gtrsim 1000$ . This formula is valid for heavy ( $m_{particle} \gg m_{electron}$ ), charged particles including protons, pions and muons. The formula can be approximated as

$$-\frac{dE}{dx} = Kz^2 \frac{Z}{A} \frac{1}{\beta^2} \left[ \frac{1}{2} \ln \frac{2m_e c^2 \beta^2 \gamma^2 T_{max}}{I^2} - \beta^2 - \frac{\delta}{2} \right] \quad (1.7)$$

where  $K \sim 0.307 \text{ MeV}/(\text{g}/\text{cm}^2)$ ,  $T_{max}$  is the maximum energy transfer to an electron,  $z$  is the charge of the incident particle,  $Z$  and  $A$  are the atomic number and mass number of the absorber/material the particle is going through and  $\beta = v/c$  is the velocity of the incident particle and  $\gamma = (1 - \beta^2)^{-2}$  is the Lorentz factor [175].

This formula, derived from relativistic quantum theory using Rutherford cross-section, shows that energy loss rate depends on the velocity of the in-

<sup>4</sup> The Bethe-Bloch formula describes only the average energy loss which has a Landau distribution. At higher energies radiative losses take over.

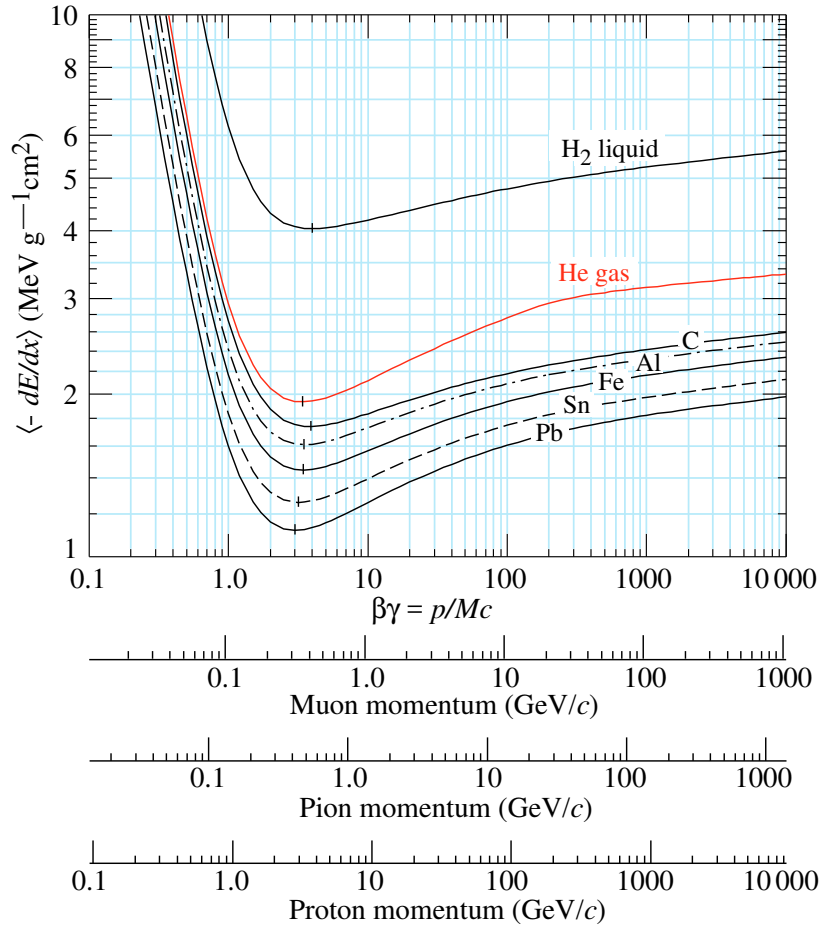


Figure 1.8: Energy loss for increasing  $\beta\gamma$  for different absorbers. Figure from PDG (2022) [175].

coming particle and its charge. Figure 1.8 shows  $dE/dx$  with increasing  $\beta\gamma$ , for different materials. For materials other than hydrogen, the curve is relatively similar. We see that at lower energies the energy loss decreases with energy, with a dependence  $\beta^{-2}$ , then it reaches a minimum ionization level at  $\beta\gamma \approx 3.5$  and afterwards relativistic takeover happens, causing a logarithmic increase in energy loss. Particles at  $\beta\gamma \approx 3.5$  are called minimum ionizing particles (MIP). The energy loss of MIPs by ionization in air is approximately  $1.8 \text{ MeV}/(\text{g}/\text{cm}^2)$  and in water, or ice, is  $2 \text{ MeV}/(\text{g}/\text{cm}^2)$ .

The energy loss is around MIP level for the muon momenta that would be observed in high energy physics and cosmic rays, roughly from around 1 GeV to 100 GeV.

#### 1.4.2 Cherenkov Radiation

When a charged particle passes through a medium, that medium is polarized. These polarized particles emit photons as they return back to their ground state. These photons form the spherical wavefronts, spreading with speed of light in

that medium. If the particle's velocity is faster than the speed of light in that medium,  $c_n = c/n$ , the polarized medium gets depolarized after the particle passes. This means that the wavefront moves slower than the particle, and an effect similar to the breaking of the sound barrier occurs, as shown in Figure 1.9. As a consequence, a cone of light is emitted in the direction of the particle, and the opening angle of the cone,  $\theta$ , is related to the speed of the particle as

$$\theta = \cos^{-1}\left(\frac{1}{n\beta}\right) \quad (1.8)$$

where  $n$  is the index of refraction of the medium and  $\beta$  is the speed of that particle. Figure 1.9 shows the spreading of the Cherenkov cone in the direction of the particle. In water, this angle is  $41^\circ$  and in air it varies depending on atmospheric depth from  $\approx 0.8^\circ$  to  $\approx 1.5^\circ$ .

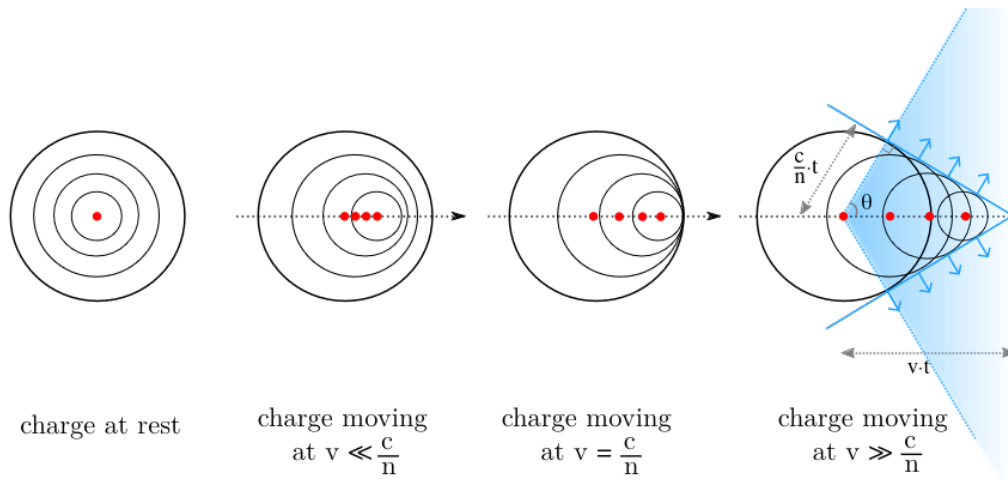


Figure 1.9: A charged particle emits Cherenkov radiation if its velocity is more than the speed of light in that medium. Figure taken from [96].

The Cherenkov light yield of a charged particle traversing through a material is given by

$$\frac{d^2N}{d\lambda dx} = \frac{2\pi\alpha}{\lambda^2} \times \sin^2\theta_C \quad (1.9)$$

where  $\alpha$  is the fine structure constant,  $dx$  is unit path length and  $d\lambda$  is unit wavelength [97]. The number of photons produced by the particle per unit length can thus be found by integrating over 400-800 nm.

This is the main process used to detect charged particles and air showers, as described in Chapter 2. WCDs utilize Cherenkov radiation from charged secondary particles passing through their purified water to detect extensive air showers on ground level. Equation 1.4.2 can be used to predict energy deposition of secondaries. The process is explained in more detail in Section 2.3.

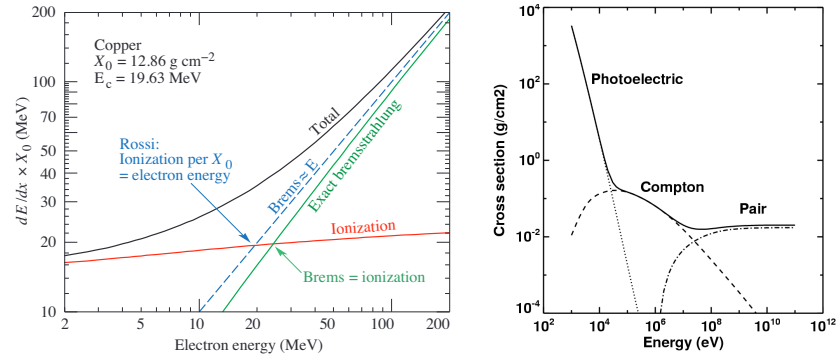


Figure 1.10: *Left*: Energy loss mechanisms for electrons. At higher energies, bremsstrahlung takes over from ionization losses, where the takeover energy  $E_c$  is material dependent. Figure taken from [175]. *Right*: Interactions of high energy photons with matter. The photon interaction cross section in Nitrogen is shown. Figure taken from [98].

### 1.4.3 Interactions of Photons

While electrons lose energy more continuously through processes of bremsstrahlung and ionization (see the left plot of Figure 1.10), depending on their energy; photons tend to lose their energy via processes that result in more abrupt changes, such as the complete absorption or annihilation of a photon. The three mechanisms of high energy photon interaction are shown in Figure 1.10. Lowest energy photons, below several hundred keV, interact via photoelectric effect, while in MeV energies Compton scattering dominates, and then finally, at highest energies, starting with above 10 MeV, pair production. Processes like Rayleigh scattering occur in lower energies and have smaller cross sections.

#### 1.4.3.1 Photoelectric Effect

Photoelectric effect occurs when a material absorbs a photon and ejects an electron, called a photoelectron. When the energy of the incident photons,  $\hbar\omega$ , is greater than the energy of an atomic energy level  $E_I$ , an electron can be ejected from that level with the kinetic energy  $\hbar\omega - E_I$ . As the incident photon energy gets higher, the cross section for photoelectric effect decreases as  $\approx \omega^{-3}$  [121].

The absorption cross sections for photoelectric effect have a strong dependence on atomic number  $Z$  and are derived for different atomic shells. Figure 1.10 shows an example cross section curve for Nitrogen.

Photomultiplier tubes (PMT), vacuum tubes commonly used in gamma-ray ground particle arrays to detect Cherenkov light, have photocathodes that use photoelectric effect to convert incident photons to photoelectrons (see Section 2.3.2 for more information).

#### 1.4.3.2 Compton Scattering

Compton scattering is the collision between a photon and an electron that results in energy transfer from the photon to the electron. During Compton scattering, the incoming photon transfers part of its energy to the electron, getting deflected with a certain angle  $\theta$ . The inverse of this mechanism, where high energy electrons upscatter low energy photons, is responsible for gamma-ray acceleration by electrons, as described in Section 1.2.

#### 1.4.3.3 Pair Production

Pair production is the creation of a subatomic particle and its antiparticle from a neutral boson, in this case the creation of an electron-positron pair from a photon. For photons with energies above  $\sim 10$  MeV in the presence of matter, pair production is the dominant mechanism of interaction. If a photon has energy greater than  $2m_e c^2$  ( $\sim 1$  MeV) is near the field of a nucleus, pair production can take place. Due to energy conservation, pair production can occur for a photon that has at least the total rest mass energy of the two particles being created. Furthermore, due to momentum conservation the photon needs to be near the Coulomb field of a nucleus, such that the nucleus receives some recoil due to the initial momentum of the photon [75, 121].

### 1.5 SUMMARY

Gamma-ray astronomy is an important part of non-thermal astrophysics. We discussed cosmic rays and the production mechanisms of gamma-rays. Cosmic rays may be accelerated via different mechanisms from different sources, emitting gamma-rays. Gamma-ray production may occur through electrons interacting with magnetic fields and photon populations, in addition to hadronic channels. Pulsar wind nebulae are a dominant population of TeV gamma-ray emitters that form when the escaped wind from pulsars are confined. Depending on their evolutionary stage they may exhibit emission in different wavelengths. Gamma-rays can be detected from the ground via different mechanisms utilizing the processes of Cherenkov radiation, ionization losses, photoelectric effect, and pair production. We will see in the next chapter how these processes are used by water Cherenkov detectors for gamma-ray detection.



## GAMMA-RAY ASTRONOMY WITH GROUND PARTICLE ARRAYS

---

Gamma rays coming from space interact with our atmosphere and produce extensive air showers (EAS), which get detected by ground based instruments on earth. The usage of ground particle arrays is an established method for detecting gamma-rays hitting the ground. As this thesis is focused on an upcoming ground-particle array for gamma-ray astronomy, SWGO, along with data analysis from a latest generation ground-particle array, HAWC, in this chapter we will have an overview of this field. The first part of the chapter is about EAS, followed by a discussion of the water Cherenkov technique. Finally, we give an overview of water Cherenkov detector (WCD) arrays that have been developed over time, focusing on the detection techniques and detector units. We conclude our discussion with a focused look on HAWC and SWGO.

### 2.1 INTRODUCTION

The detection of gamma-rays between energies of 100 keV up to 100 GeV using space-based instruments is done directly, employing laboratory particle physics methods in order to detect energetic gamma-rays when they undergo pair production.

Above energies of 100 GeV, the limited size of the space based instruments is not sufficient for getting enough flux of gamma-rays, and the need for larger areas is compensated via ground based instruments. On ground, detection of gamma-rays is done via the detection of secondary particles that are products of extensive air showers initiated by primary gamma-rays. The two main techniques are Imaging Atmospheric Cherenkov Telescopes (IACT) and wide-field ground based particle detector arrays, including WCD arrays [75, 121]. (For a review of space-based instruments see [162])

Gamma-rays above energies of 100 GeV interact with our atmosphere and produce EAS, essentially turning our atmosphere into an inhomogeneous calorimeter. The longitudinal development of these air showers can be detected by IACTs that collect the Cherenkov light produced by the secondaries of the gamma rays during their travel through the atmosphere (See [88] for a review of IACTs). If the gamma-ray entering the atmosphere has enough energy, its air shower secondaries will reach ground level and can be detected directly via ground-based particle detector arrays.

Ground-based particle detector arrays can function as particle counters, especially in case of scintillator arrays or RPCs, or via using water Cherenkov technique, in which case the energy of the secondaries is also measured.

## 2.2 EXTENSIVE AIR SHOWERS

When gamma rays reach our atmosphere, they interact with the Coulomb fields of the atoms and start pair production, gradually forming many secondary particles and resulting in EAS. These showers form by a continuous sequence of pair production and bremsstrahlung, and ionization. [19] (see Chapter 1 for a review of these three processes).

When gamma-rays reach earth's atmosphere and approach the Coulomb field of a nucleus, pair production occurs, creating an electron-positron pair, as shown on the left panel of Figure 2.1. These electron-positron pairs emit gamma-rays through bremsstrahlung. Pair production occurs again for the newly produced gamma-rays, meanwhile the electron-positron pairs continue losing energy via bremsstrahlung. This process continues, forming an electromagnetic cascade and as the number of particles increases, their average energy decreases [7], until the electron-positron pairs reach a critical energy, where the shower reaches its maximum. At this energy the radiative losses equal the collisional losses and the shower begins dying out.

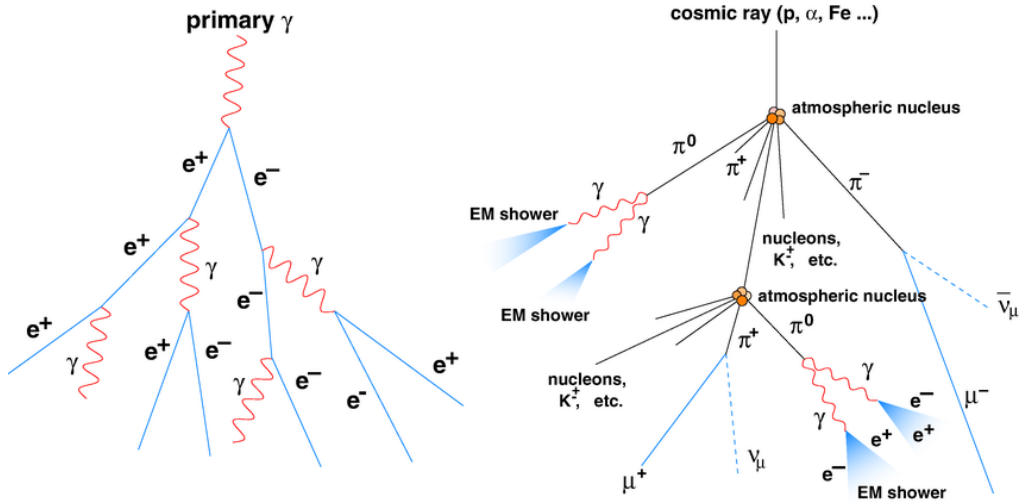


Figure 2.1: Extensive air showers (EAS) produced by a gamma-ray and a cosmic ray. *Left:* Gamma-ray induced electromagnetic air shower with a sequence of pair production and bremsstrahlung processes. *Right:* Cosmic rays producing a hadronic EAS with electromagnetic components. Figure taken from [178].

**Radiation length**  $X_0$  is the amount of matter an electron needs to transverse in order to lose all but  $1/e$  of its total energy ( $E(x) = E_0 e^{x/X_0}$ ).  $X_0$  depends on the medium, and in air it is  $X_0 \sim 37 \text{ g/cm}^2$ . The mean free path for pair production of gammas,  $\lambda_{pair}$ , is close to radiation length ( $\lambda_{pair} \approx \frac{9}{7} X_0$ ). **Critical energy**,  $E_c$  is defined as the energy at which ionization energy loss is equal to the bremsstrahlung energy loss. The loss by bremsstrahlung is nearly proportional to electron energy while ionization loss rate has a logarithmic dependence to electron energy. Hence,  $E_c$  is the cross-over energy, below which ionization losses dominate. An alternative definition by Rossi defines  $E_c$  as the energy at which ionization loss rate per radiation length is equal to electron

energy [175]. The approximation  $|dE/dx_{brems}| \approx E/X_0$  makes the two definitions equal.  $E_c$  under both of these definitions is shown in Figure 1.10. The **Heitler model** presents a simplified treatment of EAS, assuming the radiation length for bremsstrahlung and the mean free path for pair production to be the same. Under this assumption, after every  $X_0$ , each particle produces two more particles sharing its energy so that after a distance  $x$ , the number of particles in the EAS is given as

$$N(x) = 2^{x/X_0}$$

with energies

$$E(x) = E_0 2^{-x/X_0}$$

As the number of particles is doubled with each interaction, their energy is halved. The process continues until the secondary particles reach the critical energy after which ionization losses dominate. At this energy electrons would lose their energy in a length scale smaller than one radiation length. The ionizing energy loss for electrons is  $2.2 \text{ MeV/g/cm}^2$ , hence the critical energy is  $E_c \sim 81 \text{ MeV}$  in air and when  $\beta\gamma \leq 1$  particles stop. Electrons stop around  $40 \text{ gm/cm}^2$ , which is around one  $X_0$ . After  $E_c$  is reached, the shower dies out [63].

The approximate depth of shower maximum is given as

$$X_{max} \sim \frac{\ln(E_{\text{primary}}/E_c)}{\ln(2)} \quad (2.1)$$

with the approximate number of particles at the shower maximum given as  $\sim E_{\text{primary}}/E_c$ .

For a shower from a primary gamma-ray of energy  $\sim 1 \text{ TeV}$ , the shower maximum would occur at around  $\sim 13X_0$ , with an approximate number of secondaries of  $N \sim 10,000$ .

At sea level, the overburden of air is around  $28 X_0$ . The left plot of Figure 2.2 shows the atmospheric depth at which EAS from primary gamma-rays of different energies reach their maxima, when  $s = 1$ , where  $s$  is a parameter for shower age. The larger the energy of the primary gamma-ray, the deeper in the atmosphere the shower maximum occurs.

**HADRONIC SHOWERS** Cosmic rays (CR) are the dominant background contribution in the observation of gamma-ray induced EAS [90]. CRs reach earth and interact with earth's atmosphere, generating EAS with electromagnetic and hadronic components. Hadronic showers are less uniform than electromagnetic showers, more spread out, and include muons and secondary hadrons. In hadronic EAS, in addition to the bremsstrahlung and pair production processes of the electromagnetic component of the shower, there are additional hadronic processes that create nuclear fragments, pions, kaons, muons and neutrinos, etc. Hadronic interaction lengths are longer than electromagnetic processes; for protons, around  $\sim 80 \text{ g/cm}^2$ , for pions, around  $\sim 120 \text{ g/cm}^2$  [139]. All

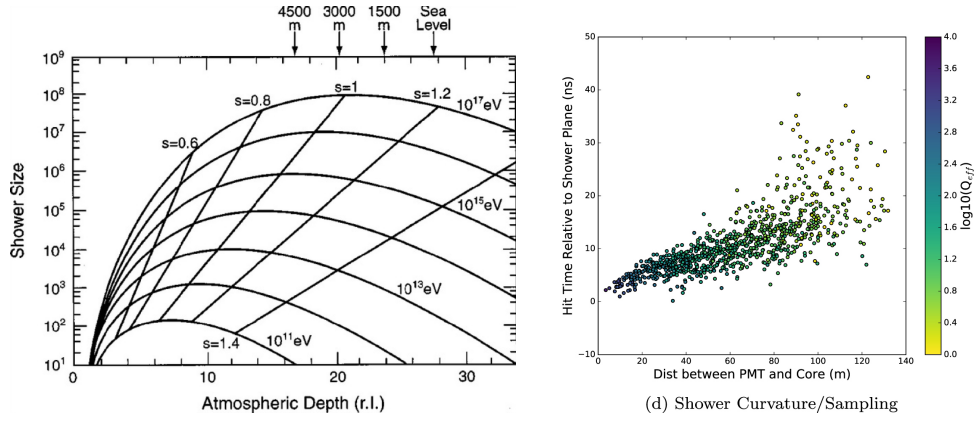


Figure 2.2: *Left*: Longitudinal shower development, where shower size vs atmospheric depth is shown. More energetic showers reach lower altitudes.  $s = 1$  shows the shower maximum. Figure taken from [178]. *Right*: PMT recorded hit times for a photon from the Crab nebula for HAWC. Figure taken from [5].

final states tend to be in form of pions ( $\pi_+$ ,  $\pi_-$ ,  $\pi_0$ ). Neutral pions decay into gammas, while charged pions decay into muons and neutrinos.

At sea level, **muons** are the most numerous charged particles with extraterrestrial origin. Their mean energy at sea level is  $\sim 4$  GeV, with an integral intensity of vertical muons above 1 GeV/c of  $\approx 70 \text{ m}^{-2} \text{ s}^{-1} \text{ sr}^{-1}$  [34]. The critical energy for muons is  $\sim 200$  times larger than for electrons due to their greater mass, hence their energy loss is dominated by ionization losses and is about 2 MeV per  $\text{g}/\text{cm}^2$ . Most muons get produced at a height of about  $\sim 15$  km in the atmosphere, hence they lose about 2 GeV before reaching sea level, which suggests original muon energies around  $\sim 6$  GeV.

For a ground-level of 5000 km above sea level (asl), the mean energy distributions of photons, electrons and muons on ground level were found by Schoorlemmer & Hinton [151] to be around  $\sim 6$  MeV, 20 MeV, and 2-3 GeV, respectively. In the study, as expected, muons are the most numerous charged particles on the ground level, dominating the total energy left over from hadronic showers.

### 2.3 WATER CHERENKOV DETECTOR ARRAYS FOR GAMMA RAY ASTRONOMY

The longitudinal development of EAS shows that at high altitudes (above  $\sim 4000$  m asl) a significant number of secondaries of EAS will reach ground level and can be detected with arrays of surface detectors. For example, the right plot of Figure 2.2 shows the PMT recorded hit times for a photon from the Crab nebula for the HAWC detector [178]. The plot shows the spread of secondary particles of an EAS at a height of 4000 m asl has a radius of around  $\sim 100$  m, arriving on ground within a few nanoseconds [63]. We see that the shower front has a cone like shape, as due to the geometry of the shower, particles at the edges have to travel longer distances to reach the shower plane. These secondaries can be detected with an array of detectors, with increasing detection efficiency with increasing total area, often achieved by an array of

smaller detectors, namely scintillating counters, Resistive Plate Counters (RPCs) or water Cherenkov detectors (WCDs).

**SCINTILLATORS** Scintillators are materials that emit light when excited by ionizing radiation, as a small portion of the excitation energy is released as optical photons. Electrons with energies of a few MeV produce scintillating light while passing through scintillating counters [63]. The heavier muon also produces photons proportional to its total path length in the scintillator.

**RPCS** RPCs are gaseous parallel plate avalanche detectors filled with gas, supporting a very good spatial and time resolution [63]. They consist of two metal plates and two high-resistance plates that are gas filled. A high voltage is applied between the metal plates and a charged particle passing through ionizes the gas in between [63].

### 2.3.1 Water Cherenkov Detectors

The two wide-field gamma-ray observatories this work is focused on, HAWC and SWGO, are both arrays of WCDs. A WCD measures the total number of Cherenkov photons that are emitted when a charged particle passes through the water enclosed within its volume. The number of detected photons is proportional to the energy that particle deposits in the detector. The height of the WCD, which can be several radiation lengths, compared to the scintillators and RPCs, allows electromagnetic cascade development within the detector volume. The process is as follows:

1. A charged particle with a relativistic speed enters the WCD.
2. Particle emits Cherenkov light as it passes through the purified water inside the detector volume.
3. The Cherenkov light reaches the light sensors (PMTs in our case) in the WCD.
4. PMTs convert photons to photoelectrons that are amplified and their voltage signal is digitized as waveforms.

Stages (1) and (2) are shown on Figure 2.3 with a vertical electron shown in yellow and a vertical muon shown in green, both secondaries with an energy of 1 GeV, passing through a double-layered WCD, a planned unit design for SWGO. The electron quickly loses its energy while the muon is seen to penetrate deeper into the lower layer of the detector, which is intended for muon counting purposes (see Kunwar et al. [108] for a study of this design, and Section 3.1.1).

Secondary electrons that enter a WCD volume have a radiation length of  $X_0 \sim 36$  cm in purified water, and hence would lose their energy within a few radiations lengths in the WCD volume in most cases. If the entering electron has an energy above the critical energy ( $E_c \approx 80$  MeV for water), the dominating mechanism will be bremsstrahlung, followed by ionization losses once the

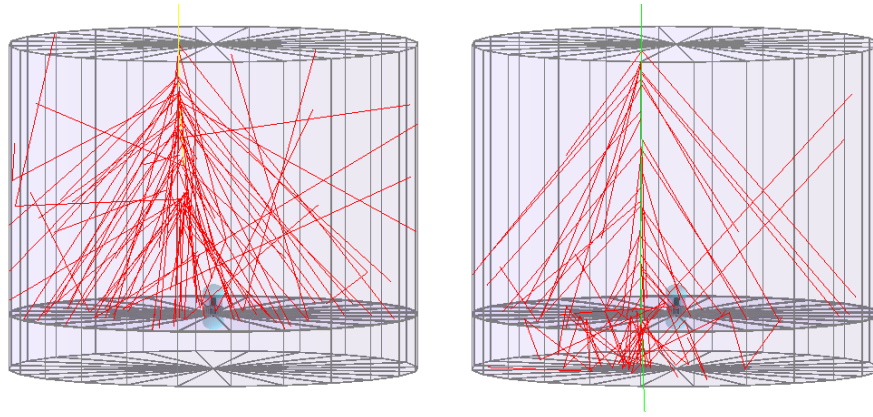


Figure 2.3: Figures made using HAWCSim (based on GEANT4) showing a 1 GeV electron (*left*) and a 1 GeV muon (*right*) passing through a double-layer WCD. The electron decays quickly while the muon goes into the lower chamber.

energy falls below  $E_c$  (see the left plot of Figure 1.10). The energy loss by electrons by ionization at this point is 2 MeV/cm, hence the electron loses all its energy and falls below its Cherenkov threshold energy of  $\sim 0.8$  MeV within one  $X_0$  [87]. For a double layered WCD as in Figure 2.3, unless energetic enough to continue bremsstrahlung through the depth of the upper chamber, an electron will deposit all its energy in the upper layer only.

In case of secondary gammas, pair production is the dominant mechanism of interaction above energies of  $\sim 10$  MeV (see the right plot of Figure 1.10). As described in Section 1.4.3, photons do not lose their energy continuously, but abruptly, by complete annihilation in case of pair production. With a mean free path that is close to electron radiation length ( $\lambda_{pair} \approx \frac{9}{7} X_0$ ), secondary gammas lose their energy within a few radiation lengths of the WCD volume. In case of a double layered WCD, they would give signals only on the upper layer, similar to electrons.

Meanwhile muons, being minimally ionizing particles, will pass through, making it to lower layer of the WCD shown in Figure 2.3, or into buried muon detectors of experiments such as LHAASO.

Electrons fall below the Cherenkov threshold much earlier than muons, and their total energy deposited can thus be measured via their **Cherenkov yield**. The Cherenkov yield of a charged particle transversing through a material is given by equation 1.4.2. The opening angle for Cherenkov emission is  $\theta_C = 41^\circ$  in water. The light yield for electrons, in the 300-600 nm range, is found by integrating over the wavelengths as  $\approx 320$  photons/cm, or 160 photons per MeV energy loss [87].

The Cherenkov yield in terms of photons can be multiplied by the quantum efficiency (QE) of the PMT to obtain the yield in terms of photoelectrons. The QE of the PMT Hamamatsu R5912, as given by Hamamatsu, is plotted in Figure 4.11.

### 2.3.2 Photomultiplier Tubes

The WCD units of LHAASO, HAWC and future SWGO use photomultiplier tubes (PMTs) as their light sensors to inside their WCDs. These PMTs detect and record arrival times and voltage pulses (or waveforms) from the Cherenkov light emitted by the secondary particles passing through the WCDs. Understanding the operating principles and failure modes of PMTs is therefore essential for understanding WCDs.

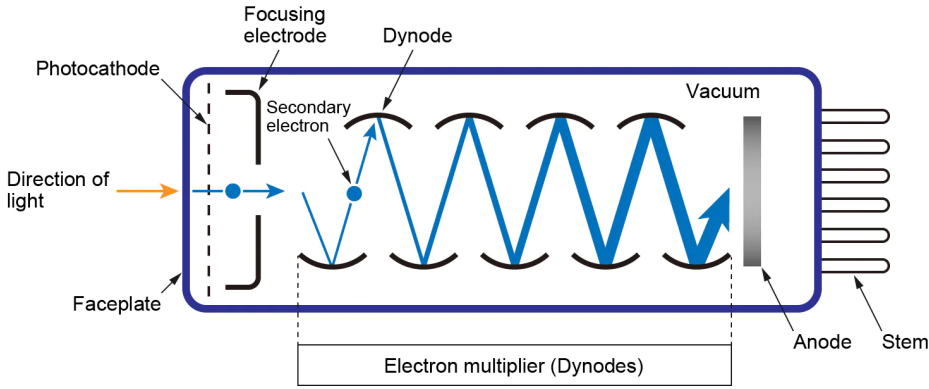


Figure 2.4: A PMT schematic. An incident photon strikes the photocathode. Photoelectrons from the photocathode travel through the vacuum and get amplified at each dynode. Taken from [144].

Inside a PMT, there is a photocathode followed by a series of dynodes and a final anode as shown in Figure 2.4. If an incident photon with sufficient energy strikes the photocathode, an electron might be emitted due to photoelectric effect (see Chapter 1). These electrons are called **photoelectrons** (p.e.). The electrons are emitted into the vacuum of the PMT as photoelectrons with a probability  $\eta_{QE}$ , where  $QE$  stands for the **quantum efficiency**, which is the production probability of one photoelectron due to an incoming photon after it hits the photocathode of the PMT. It can be expressed as

$$\eta_{QE} = (1 - R) \frac{P_e(\lambda)}{k} \frac{1}{1 + 1/kl} P_s \quad (2.2)$$

where  $\lambda$  is the wavelength of the photon,  $k$  is the absorption coefficient of photons,  $R$  is a reflection coefficient of the incident light,  $P_e(\lambda)$  is the probability of the absorption of a photon exciting an electron of sufficient energy,  $P_s$  is the probability that an electron reaching the surface escapes into the vacuum, and  $l$  is the mean escape length of electrons. The wavelength dependence of the QE for the Hamamatsu R5912 PMTs used in our experiments is shown in Figure 4.11.

The photoelectrons are accelerated to the first dynode of the PMT, with the assistance of a focusing electrode. Multiple secondary electrons are struck out by these electrons, and the process continues onto the following dynodes. The electric field inside the vacuum tube directs these electrons towards the dynodes, which function as electron multipliers, because each dynode is held

at a more positive voltage. After the last dynodes, all secondary electrons are collected on the anode, which forms a spike in current. This current pulse is then processed through a preamplifier and shaper, passing onto analog to digital converters (ADC).

The probability that the photoelectron reaches the first dynode is **collection efficiency**. This process creates an electron cascade with exponentially increasing number of electrons. Each electron produces a certain number of secondary electrons depending on the **multiplication factor** [79].

The **gain** of a PMT is the number of electrons produced at the anode for every photoelectron coming from the photocathode (typically  $10^7$  for PMT R5912 for example [109]), hence it is equal to the ratio of the anode current to the photocathode current.

PMTs placed inside WCDs detect the Cherenkov light that reaches them in the form of current pulses, or waveforms, which go through a signal processing chain, including preamplifiers, signal shapers and analog to digital converters (ADCs). Waveforms obtained from a PMT inside a double-layer WCD, after going through a signal processing chain, are shown in Figure 4.29 in Chapter 4.

### 2.3.3 Data Reconstruction with WCD Arrays

The signals from the PMTs inside the WCDs are processed through the data acquisition system of the observatory. Time of detection and charge are recorded, depending on the data processing and triggering chain of the observatory. After the data is recorded, on the array level, the shower parameters are reconstructed, namely the direction and energy of the primary particle, and gamma/hadron separation.

The **energy of the primary particle** can be determined by particle counting and the deposited electromagnetic energy. The air shower core is the intersection point of the primary particle trajectory and the detector plane. Most of the air shower secondaries are distributed around the shower axis. Hence, the core location can be estimated by considering all the particle densities that are detected by the individual WCD units of the array. The **direction of the primary particle** can be determined from an analysis of the arrival times of the signal on the array of WCDs. The shower front is curved since the secondaries closer to the core travel a shorter distance and are subjected to less multiple scattering, which can be seen from the right plot of Figure 2.2. Hence, particles at the edge of the shower arrive later and have a broader time distribution. Depending on the direction of the primary particle, this curved shower front arrives at the detector plane and initiates signals at the WCDs on different times, as can be seen from Figure 2.2. Thus, particle type, arrival time information of the particles of the shower front, along with the core location estimation, can be used to find the direction of the primary gamma-ray.

**Gamma/hadron separation** is crucial, as hadronic showers form the majority of the background for wide-field gamma-ray observatories. As we saw, electromagnetic and hadronic showers have differences that can be exploited for this purpose, such as shower secondary products and topology of showers.

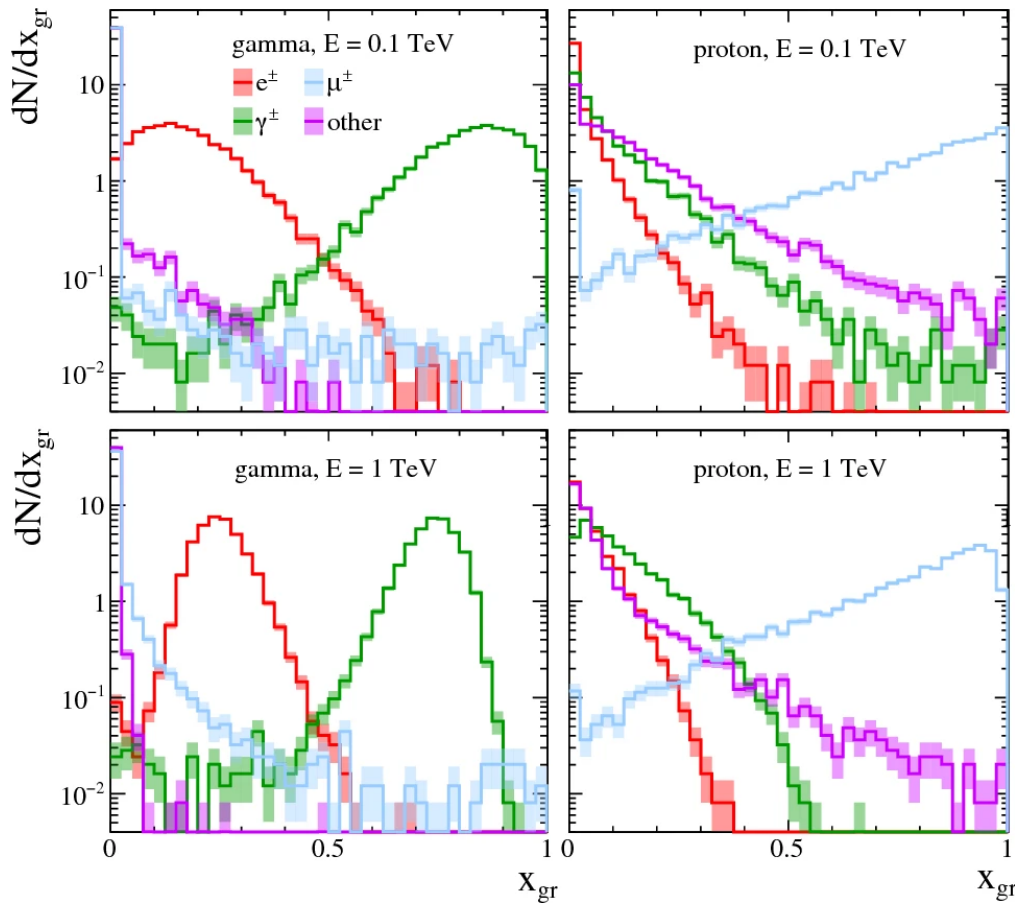


Figure 2.5: Distribution of fraction of the total energy that reaches ground ( $x_{gr} = E_i/E_{gr}$ ), at an altitude of 5000 m. For, gamma induced showers, most energy is photon dominated, while for proton showers muons dominate. Figure taken from [151].

**Shower topology** can be used to distinguish the two types of showers as hadronic showers tend to spread over larger areas and have a more complex composition due to subshowers. Methods exploiting shower topology were developed by Milagro observatory, the pioneer for water Cherenkov approach for wide-field gamma-ray observatories, which were improved upon by the later HAWC observatory. Section 2.3.4 gives an overview of these observatories along with the gamma/hadron separation methods they utilized.

**Muon identification** is another effective way for gamma/hadron separation (See [52, 87, 151]). Figure 2.5 taken from the study of Schoorlemmer et al. shows the distribution of the fraction of total energy arriving at the ground for gamma and proton induced showers, where the ground is at 5000 m asl. For gamma induced showers, photons carry most of the energy as expected, although muons also carry a small fraction of energy [151]. For proton induced showers, muons emerge as the most dominant particle, carrying most of the energy of the shower. The number of muons arriving on ground level is found to be one to two orders of magnitude lower for gamma-rays [87]. Separately buried muon detectors and WCDs have been used by ground particle arrays

previously for muon identification. An alternative method is to incorporate muon counting into every element in the detector array, in the form of an optically separated lower compartment within the WCDs themselves, hence provide discrimination within each WCD unit. This motivates the design for a double-layered WCD for SWGO, detailed in Section 3.1.1 and [108].

#### 2.3.4 Ground Particle Array Experiments

We give an overview of ground particle array experiments, with a focus on WCD arrays. Initially, for ground-based particle detector arrays, small plastic scintillators distributed over large areas were used, and later on gradually, starting with purposes of muon identification, the use of WCDs increased. SWGO and HAWC, the main focus of this thesis, are WCD arrays that benefit from the experience from the experiments mentioned in this section.

##### 2.3.4.1 Historical Overview

The idea of using ground based detectors for detecting cosmic air showers took ground in the early 1900s. B. Rossi made the first detection of EAS by discovering the correlated arrival times of particles that were detected with separated Geiger counters in 1934 [171]. Afterwards, two groups in Germany made systematic studies using separated Geiger counters (50 cm, up to 75 m). Pierre Auger and his collaborators used further separated counters (over 300 m) in 1939 along with cloud chambers, discovering that penetrating particles were associated with the showers. Several studies followed, a review of which can be found in [171]. Geiger counters were an integral part of exploring EAS, until well into 1950s and were replaced gradually by scintillators and WCDs. In 1958, using Geiger counters, Kulikov and Khristiansen saw the steepening of the number spectrum of showers, what is now called *the knee*. Scintillation counters were invented by S.C. Curran in 1944 and were subsequently used by the group of Rossi in MIT for studying air showers, in the form of liquid scintillation counters. More arrays in Bolivia and New Mexico were constructed using plastic scintillators.

Pontecorvo, after working with Pierre Auger, moved to the UK, and, being informed about the liquid scintillator work at MIT, asked J.V. Jelley to investigate the efficiency of light output with the quantity used. Jelley found that light can be detected via Cherenkov radiation in liquids including distilled water, and afterwards, Neil Porter developed in 1958 the first water Cherenkov detector [171]. Eventually this also led to the discovery of Cherenkov light from the atmosphere, and the use of WCDs for detection of EAS, such as in the case of the Haverah Park experiment, operated by the University of Leeds, was a 12 km<sup>2</sup> array of 1.2 m deep WCDs [31].

For detecting gamma-ray induced EAS, the largest early examples of scintillator arrays are the case of CASA-MIA [39], where buried muon counters along with plastic scintillators were used, and CYGNUS [23], which also used scintillators along with five Water Cherenkov detectors (3 m deep) for muon

detection. These experiments had high-energy thresholds close to 100 TeV and did not make significant detections.

Tibet Air Shower gamma experiment (Tibet-AS $\gamma$ ) located at 4300 m asl in Tibet, China, has also been using plastic scintillator counters. This joint Chinese-Japanese experiment has been operating since 1990 [161]. It consists of 1000 plastic scintillation counters of 0.5 m<sup>2</sup> forming a 65,000 m<sup>2</sup> surface array in addition to 3,400 m<sup>2</sup> water Cherenkov muon detectors.

WCDs and detection of particles via Cherenkov light are methods also used in neutrino astronomy, see [158] for a review of the methods and important experiments.

#### 2.3.4.2 Milagro Gamma-Ray Observatory

Milagro was the first large-scale water Cherenkov gamma-ray observatory. It was located in New Mexico, at an altitude of 2630 m asl and operated between 2000-2008. It consisted of a 4800 m<sup>2</sup> (80 m  $\times$  60 m  $\times$  8 m) pool with a light tight cover, which was 8 m deep. The pool was equipped with two layers of 8-inch PMTs (Hamamatsu R5912), the first layer placed under 1.2 m of water, with 3 m spacing in between, and the second layer under 6 m water [156]. Figure 2.6 shows the light tight pool lined with the PMTs. The bottom of the pool had, on top of a black liner separating the water from the soil, a grid of PVC pipes onto which the PMTs were attached. This observatory had no optical isolation between PMTs. In 2004, 175 plastic tanks were added outside the pool, each with a height of 1 m and a diameter of 3 m. These tanks had Tyvek linings and a single PMT at the top of each plastic tank.

In the pool, the top layer of the PMTs was intended for triggering and reconstructing the direction and energy of the primary gamma-ray, while the bottom layer was mostly intended for background rejection.



Figure 2.6: The pool used for Milagro. Two layers of PMTs are seen, one layer directly connected to the PVC pipes, and the other later suspended above via ropes. Image taken from [148].

Gamma/hadron separation was done using a technique that exploits the different shower topologies of hadronic and gamma initiated showers and by

the presence of muons. The bottom layer of PMTs of Milagro were seen to have different signals depending on the type of EAS: The energy deposited by hadronic air showers in the bottom layer of PMTs was in the form of clumps of deposited energy, due to the presence of deeply penetrating muons, while the energy deposited by electromagnetic air showers was more uniform, and had a lower level of illumination with a peak at the shower core position. This difference was captured in the form of a single parameter called *compactness*, which enabled the collaboration to reject  $\sim 90\%$  of background events and retain  $\sim 50\%$  of the gamma-ray events [30, 156].

Milagro managed to detect the Crab nebula in 2003 with three years of data [30], and by 2008 it had detected gamma-ray emission around Geminga, and dozens of other gamma-ray sources. Milagro also detected galactic diffuse emission near 10 TeV for the first time [1]. The successes of Milagro established the WCD array method as a viable approach, and the background rejection techniques developed and lessons learned through Milagro were crucial for future developments.

#### 2.3.4.3 *ARGO-YBJ Experiment*

This experiment consisted of a single layer of RPCs with a modular configuration and operated from 2007 until 2013, at an altitude of 4300 m in Tibet [93]. In addition to the main central carpet of RPCs, a partially instrumented portion extended the total area to  $\sim 11,000 \text{ m}^2$ . Thanks to its small pixel size it was able to have high density sampling and good angular resolution. This experiment had great spatial resolution, however poorer gamma/hadron separation abilities compared to Milagro.

#### 2.3.4.4 *Pierre Auger Observatory*

The Pierre Auger Observatory in Argentina, at an altitude 1400 m, has an array of 1600 surface detectors along with 28 fluorescence detectors at the edges. Covering an area of  $3000 \text{ km}^2$ , it is the largest cosmic-ray experiment in the world [122, 142]. Its surface detectors consist of an array of WCDs, each with a diameter of 3.6 m and equipped with solar panels, a GPS receiver and radio receiver, being self-contained. Each WCD has a reflective inner surface (more information on reflective surfaces in Section 4.1.3.3) and contains pure water. Figure 2.7 shows a sketch of a charged particle passing through the WCD, producing Cherenkov light shown with dashed lines that is reflected through the inner liner of the WCD. The light is collected by the three 9-inch PMTs facing downwards. These surface detectors maximize signal efficiency by using the reflective walls.

The cylindrical tanks are manufactured commercially via rotational molding ("rotomolding") of high-density polyethylene (HDPE). This rotomolded tank design of the Auger Observatory is viewed as a candidate detector unit design for the upcoming SWGO observatory (see Chapter 3).

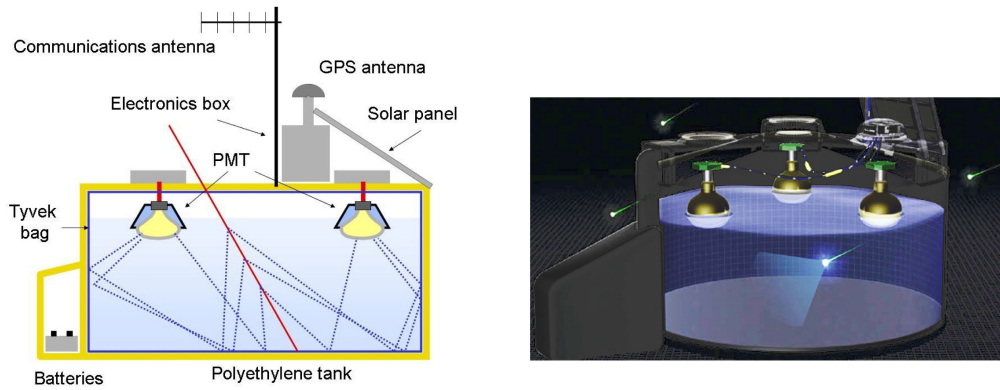


Figure 2.7: The surface detector element of Pierre Auger Observatory. The rotomolded tanks are lined with liners that reflect the Cherenkov light from the passing by particle to the downward facing PMTs. Figure taken from [122].

#### 2.3.4.5 ALPACA

Andes Large-area PARTICle detector for Cosmic-ray physics and Astronomy (ALPACA) is one of the upcoming particle sampling arrays that is a collaboration between Bolivia, Mexico and Japan. This experiment is located at the Chacaltaya plateau in La Paz, Bolivia (4740 m asl), not so far from the SWGO site of Pampa la Bola in Chile [103]. This experiment utilizes an air shower array of 400 scintillation counters that are based on the earlier Tibet AS $\gamma$  design, in addition to an underground WCD muon array (each 1 m deep), with a total area of  $\sim 83,000 \text{ m}^2$ . The prototype-array ALPAQUITA, with 97 scintillation counters, has been operating since 2022 [102]. The experiment is aiming to survey the Southern sky, similar to SWGO. The scientific motivations of ALPACA include the study of gamma-rays from 5 TeV to 1 PeV from the Southern hemisphere, investigation of cosmic ray anisotropy with energies above 5 TeV and examination of the cosmic ray energy spectrum in the knee region [160].

#### 2.3.4.6 LHAASO

Large High Altitude Air Shower Observatory (LHAASO) is a large experiment located at an altitude of 4400 m asl in the Tibetan plateau, made up of four separate built and planned detectors. There is a central water Cherenkov detector array (WCDA), surrounded by a larger ground particle detector called Kilometer Squared Array (KM2A). KM2A is made up of an array of electromagnetic particle detectors (ED) and buried muon detector (MD) components. Within the KM2A, The ED are made up of plastic scintillator plates and wavelength shifting fibers. The MD are buried muon detectors that are made up of concrete tanks lined with bladders that have a diameter of 6.8 m and height of 1.2 m each. An 8-inch PMT is at the top of the liner looking downwards, resembling the Auger plastic tank setup [123]. The WCDA is made up of three separate buildings containing 4.4 m deep pools (Two with an area  $150 \times 150 \text{ m}$ , one with area  $300 \times 110 \text{ m}$ ). The 3120 total WCDs within the pools are separated by black plastic curtains. The water purification system used for the WCDA array aims to

guarantee an attenuation length of 15 m. The water purification system includes a storage filter, a multi-media filter, a stage of filters of 5-3-1-0.1  $\mu\text{m}$ , an ozone mixing pool, carbon filtration and a sterilization area with UV lamps [116]. As light sensors, this array uses both 8-inch and 20-inch PMTs, along with smaller PMTs next to them for increasing the dynamic range.

### 2.3.5 HAWC Observatory

The HAWC observatory is a second-generation wide field TeV gamma-ray observatory located at Sierra Negra, Mexico at an altitude of 4,100 m asl [5]. It consists of 300 WCDs that are continuously operated, providing a wide field of view and nearly 100% duty cycle.

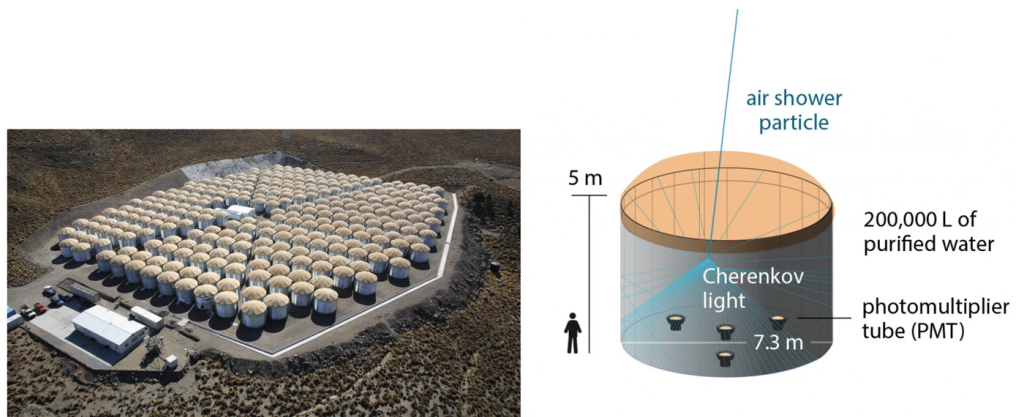


Figure 2.8: *Left:* The HAWC experiment layout with its 300 steel tanks. *Right:* Diagram of a HAWC tank shows the three eight-inch PMTs surrounding the ten-inch PMT.

HAWC was built based on the success and lessons from previous wide-field observatories, in particular of Milagro as a WCD array. An improvement from Milagro was building the observatory at a higher altitude, closer to the maxima of lower energy showers (see Figure 2.2). Another improvement was to optically isolate the PMTs, achieved by placing them into separated WCD units in form of tanks. When detector elements are not optically isolated, muons passing by at an angle can illuminate many PMTs and trigger the detector, hence optical isolation helps reduce the trigger rate, while improving the energy resolution. Furthermore, a larger detector array was made in order to increase muon detection area, in order to achieve a better gamma/hadron separation [155].

The layout of the WCDs can be seen in Figure 2.8. This main array covers an area of over 22000  $\text{m}^2$ . An outrigger array of smaller WCDs deployed around this main array increases the total area by a factor of four [125]. The central WCDs of HAWC are aluminum tanks that are 5 m in height and 7.3 m in diameter. Each WCD houses water proof, light-tight custom bladders filled with purified water. The bladders have a black inner layer and each one has four PMTs facing upwards inside, where the one at the center is the 10-inch high quantum efficiency PMT (Hamamatsu R7081, 30% QE), and three 8-inch

PMTs (Hamamatsu R5912) are surrounding it in a triangular form, as pictured in the right of Figure 2.8 [9]. The PMTs were inserted into this position after filling the bladders with purified water, using an integrated mounting fixture for each PMT and a pulley system (see [9] for details).

As the opening angle of the Cherenkov cone for incoming charged particles is  $41^\circ$ , all particles entering a WCD are expected to be detected by at least one PMT in the setup. The large water volume ensures effective calorimetry, where, the secondary gammas entering pair produce due to the presence of water molecules, and the electrons/positrons deposit all their energy within the volume of the tank, while radiating Cherenkov light. The black walls with low reflectivity minimize the reflected light, ensuring that all the Cherenkov light detected can help with time reconstruction, since most of the light detected by the PMTs would be prompt Cherenkov emission, as opposed to reflected light with time delays.

Gamma/hadron separation techniques from Milagro were improved on for the HAWC observatory. The *compactness* parameter of Milagro is being used in HAWC as well, where muons are identified as localized charge depositions, similar to the Milagro method. A second variable for gamma/hadron separation again utilizes the shower topology: The *PINC* variable (Parameter for Identifying Nuclear Cosmic rays) is based on the lateral distribution of showers, where the hadronic showers tend to have isolated high-charge hits further away from the shower core due to the hadronic subshowers and muons, while gamma-ray showers are axially smoother [5]. Figure 2.9 depicts a gamma induced and a proton induced shower as seen from the HAWC array charge deposition. As expected, the proton shower has a larger spread, with energy deposited further away from the core, while the gamma shower is more compact.

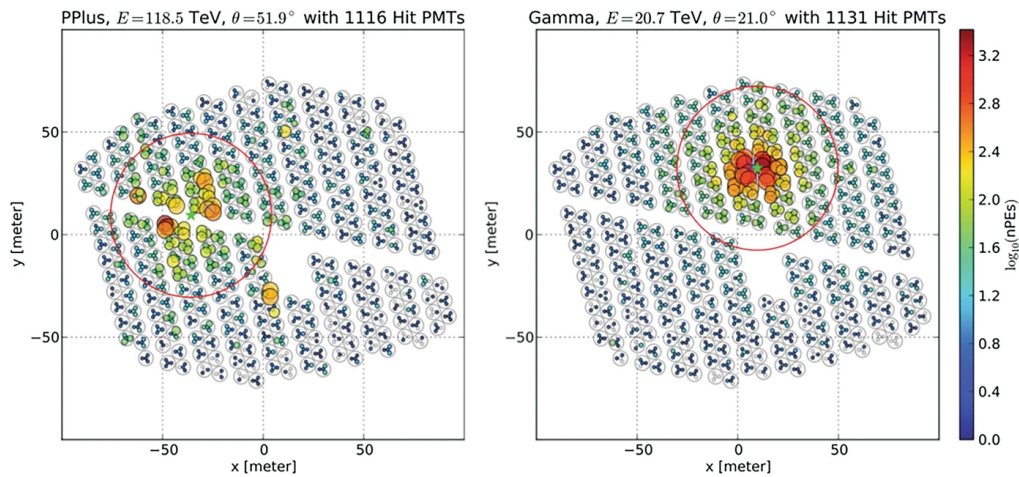


Figure 2.9: A proton (*Left*) and a gamma (*right*) induced shower on the HAWC array. The proton shower has energy deposited further away from the core, enabling gamma/hadron separation. Figure taken from [61]

HAWC recently went through a revision of its data reconstruction which increased its angular resolution for sources above a zenith of  $30^\circ$  and corrected

a systematic pointing error (more information on this revision is given in Section 5.2.2).

**SCIENCE WITH HAWC** HAWC detects gamma-rays from energies of 100 GeV up to 100 TeV, and it can also detect emission above 100 TeV energies, albeit with reduced gamma/hadron separation capabilities [5, 7]. Throughout its years of operation, HAWC has provided important detections on the gamma-ray sky. HAWC has detected extended gamma-ray emission from the locations of Geminga and PSR B0656+14 pulsars, demonstrating that they are local accelerated lepton sources [4, 83]. HAWC has also detected gamma-ray emission powered by the jets of the microquasar SS 433, which is a binary system with a supergiant star and a compact object. The two jets emanating from this system terminate inside a supernova remnant W50 where particle acceleration is expected. HAWC detections have managed to spatially resolve the lobes of W50 by detecting localized TeV emission from the region [6]. These gamma-ray emission detections provide evidence for various particle acceleration mechanisms and offer insight into complex physical processes occurring in these sources. HAWC has also contributed to multimessenger astronomy, by detecting gamma-ray flares in the direction of a blazar TXS 0506+056, as part of a multimessenger campaign involving several collaborations, led in particular by IceCube [92]. After the last major data reconstruction revision, HAWC was able to provide spatially resolvable detections for regions that transit through its field of view above 30° zenith, such as the galactic center and the region of the PWN HESS J1825-137. This thesis describes an analysis of this PWN with HAWC data in Chapter 5.

### 2.3.6 SWGO

Southern Wide-field Gamma Ray Observatory (SWGO) will be a next generation gamma-ray particle array observatory in the southern hemisphere [90]. Building on the experience of the previous and current ground particle array observatories, SWGO will utilize a large area, high altitude and a southern location for a galactic focused science program. The absence of any WCD array instruments on the southern hemisphere makes SWGO crucial for observations of a key portion of the gamma-ray sky. Figure 2.10 shows a concept array for SWGO. The previous experiments HAWC and LHAASO have proven the effectiveness of the WCD approach for detecting and characterizing EAS secondary particles, and large arrays with optically separated units are effective for gamma/hadron separation. SWGO aims to improve sensitivity by an order of magnitude in the region overlapping with the HAWC observatory through advancements in detector unit design, layout, and reconstruction. As an ambitious and multinational project, the building of SWGO is preceeded by an extensive optimization phase.

The SWGO collaboration has been involved in an extensive R&D phase to evaluate different design choices and layouts to optimize the performance and cost of the observatory, based on a number of science goals, considering existing

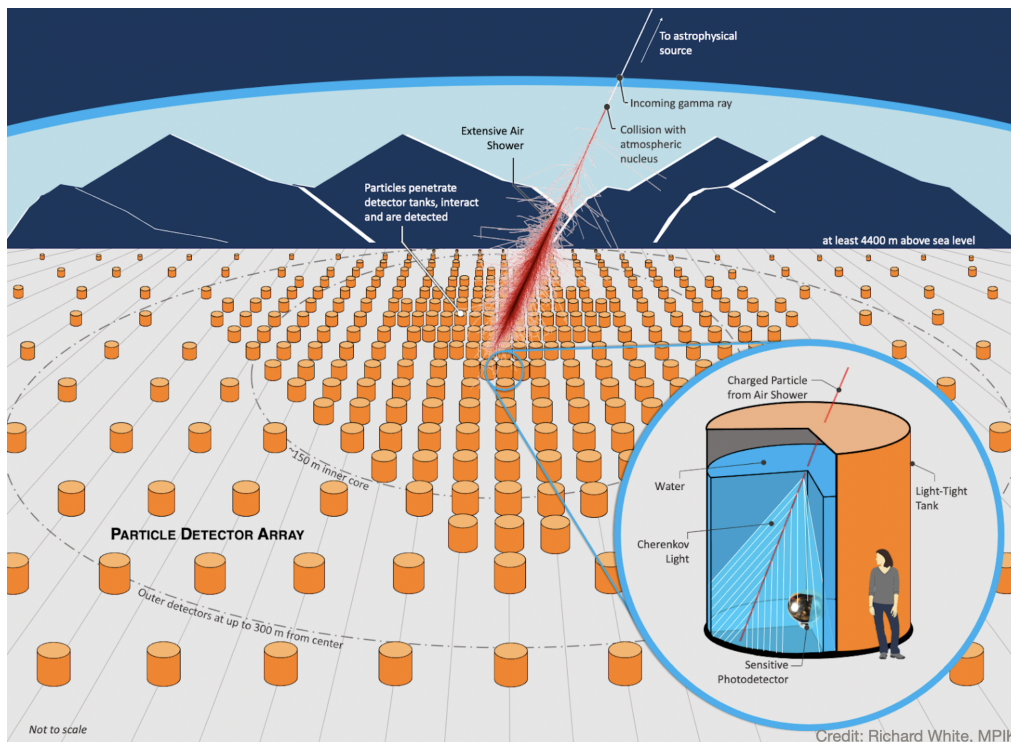


Figure 2.10: Sketch of the SWGO array concept. Figure credit: Richard White.

options along with innovative designs and ideas. Different working groups within the collaboration work on these different areas, following a plan that is anticipated to culminate in the construction of SWGO within a few years.

#### 2.3.6.1 Detector and Site Choices

The choice of the technology and form of the detector unit that forms the whole array is an integral part of the performance of SWGO. The Detector group is responsible for the technology options for the detector units, including light sensors and the building and design of the detectors. Chapter 3 presents a discussion of the detector unit designs for SWGO, focusing on tank and lake based options.

Several sites in South America were considered for SWGO by the Site group, collaborating with local authorities and representatives. All of the sites have a minimum altitude requirement of 4400 m asl, since a higher altitude allows for a lower energy threshold (see Figure 2.2). Recently, Pampa la Bola in the Atacama Astronomical Park, Chile, at an altitude of 4770 m asl was chosen [149].

#### 2.3.6.2 Detector Designs and Array Layout Configurations

The candidate detector unit designs include four designs encompassing a double-layer design with different light sensors and sizes, one innovative design, and one single layer design inspired by HAWC and LHAASO-WCDA detectors. The double layer design is detailed in Chapter 3 along with first results in Chapter 4.

There are seven layouts that are under evaluation by the collaboration. These evaluate choices of fill factor, overall area. A denser layout would help reconstruct lowest energy showers with higher efficiency, while a sparse layout would increase the effective area to record highest energy showers as those have a larger footprint on the ground. The reference layout, layout 1, has two zones of different coverage (80% fill factor in a central portion and % fill factor in an outer region, 88000 m<sup>2</sup> in total). The other layout options are designed to evaluate the effects of larger sparse zones, three zone arrays, clustering of tanks and more.

### 2.3.6.3 *Analysis & Simulations*

The different layout and design choices are being evaluated by the Analysis & Simulations group, who also are responsible with creating the Instrument Response Functions (IRFs), in collaboration with the Science group.

The IRFs are generated via a chain that starts with using CORSIKA [82], HAWCSim<sup>1</sup>, and then pyswgo<sup>2</sup>, which reduces the output to event level parameters and cut values, after which IRFs are generated. The IRFs are important for knowing the response and capabilities of SWGO depending on different array layouts and altitudes, for different science cases. The sensitivity curve for one of the candidate designs, the A4 configuration, is shown in Figure 2.11, along with the sensitivity of CTA South in 50 hours and the LHAASO one year sensitivity. A preliminary study using SWGO IRFs generated for A4 configuration, in the case of the PWN HESS J1825-137, is described in Section 5.5.

### 2.3.6.4 *Science Cases for SWGO*

SWGO addresses several scientific possibilities, as shown in Figure 2.12. The total sky coverage of SWGO will be  $\sim 8$  steradians and it will be able to observe a large number of sources simultaneously. The scientific potential of SWGO was explored in the white paper from 2019 utilizing a strawman design [90], using HAWC performance parameters scaled to a larger array at a higher altitude. Since then, the benchmark science cases for SWGO have been defined by the collaboration, along with the requirements the observatory would need to meet (see [10, 81, 85] for example). The six core cases are defined in Table 2.1 along with their design drivers.

SWGO will be able to search for gamma-ray emission from 12 Geminga-like PWNs, study the nature of extended sources such as Fermi bubbles, measure Galactic diffuse emission and more. While the transient sources observation case places a requirement for a low energy threshold, hence high altitude, the galactic accelerator benchmarks place demands on energy and angular resolution. These benchmarks hence inform the R&D work of the other working groups. The Science working group evaluates the potential of SWGO for achieving these

<sup>1</sup> This is a simulation package made by the HAWC collaboration based on GEANT4 [13]

<sup>2</sup> A higher-level analysis tool written in Python3 developed by the Analysis& simulations group [53].

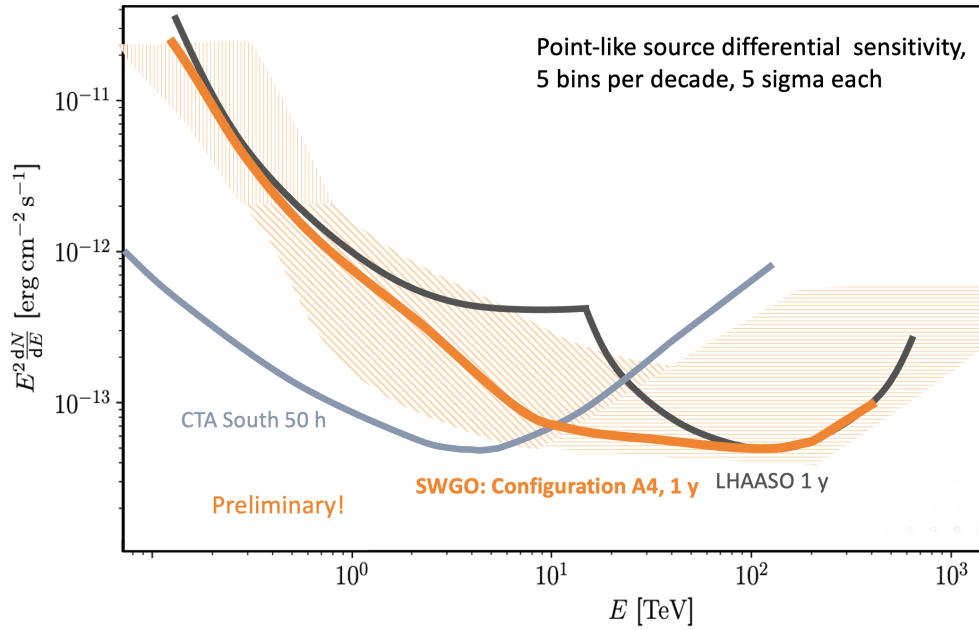


Figure 2.11: SWGO sensitivity for the A4 configuration for one year of observation, compared with CTA South and LHAASO. Plot made by Jim Hinton.

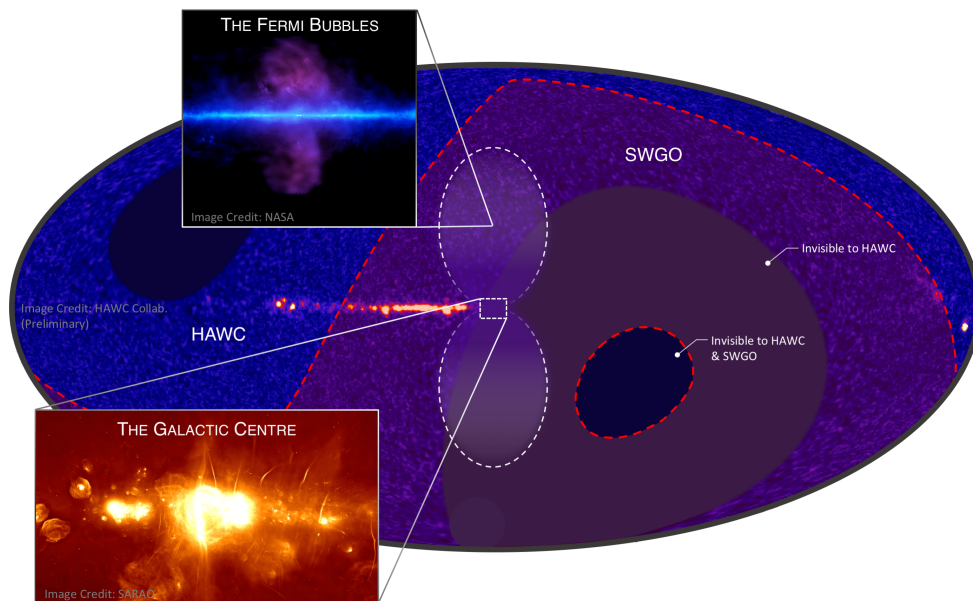


Figure 2.12: The Gamma-ray sky as seen by HAWC and expected to be seen by SWGO. Many interesting regions such as the Galactic Center and the Fermi Bubbles will be within SWGO FOV. Image from Richard White.

science goals given the findings of the Analysis& Simulations group through the IRFs provided.

<b>Core Science Case</b>	<b>Design Drivers</b>
Transient sources: Gamma-ray Bursts.	Low energy threshold
Galactic Accelerators: PeVatron Sources	High energy sensitivity
Galactic Accelerators: PWNe and TeV Halos	Extended source sensitivity
Diffuse Emission: Fermi Bubbles	Background rejection
Fundamental Physics: Dark matter from galactic center halo	Mid-range Energy sensitivity
Cosmic-rays: Mass-resolved dipole Multi-pole anisotropy	Muon counting capability

Table 2.1: The Science benchmarks for SWGO along with their respective design drivers. Adapted from [53]

#### 2.4 SUMMARY

Wide-field gamma-ray observatories have contributed and continue to contribute to science. Extensive electromagnetic air showers initiated by cosmic gamma-rays can be detected from ground with the usage of wide-field arrays, and in particular water Cherenkov detector units provide a cost effective method for measuring the energies. This chapter reviewed aspects of extensive air showers and showed the working principles of WCDs. We went over important developments in the field, culminating our discussion in HAWC and SWGO.

## LAKE CONCEPT

---

The Lake concept is one of the alternative designs for the Southern Wide-Field Gamma-ray Observatory (SWGGO). Bladders filled with clean water are deployed near the surface of a natural lake, where each bladder is a light-tight stand-alone unit containing one or more photosensors. The lake design was shown as a poster during the 37th and 38th International Cosmic Ray Conferences (ICRC) in 2021 and 2023. The corresponding proceedings articles outline the design and prototyping steps [70, 71].

Section 3.1 gives an overview of the detector unit design candidates for SWGGO. The advantages and challenges of the lake concept are given in Sections 3.2.1 and 3.2.2. Section 3.2.3 presents an overview of the impact of wave motion. Section 3.2.4 describes artificial lakes as an alternative to natural lakes. Simulations for the detector units placed into a lake are described in Section 3.3. More details on the later stages of the prototyping are given in Chapter 4.

### 3.1 DETECTORS FOR SWGGO

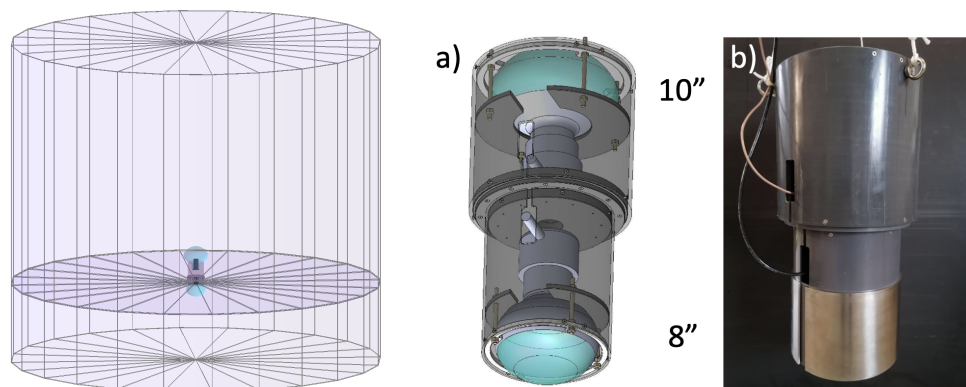
SWGGO will employ a large array of water Cherenkov detectors (WCDs) (around an order of 6000 units) in order to record extensive air showers (EAS) from gamma-rays at ground level (see Section 2.3.1). As described in Section 2.3.6, different WCD designs and array layout options are being considered. The baseline layout used during the extensive simulations has been the A4 layout, where a dense core detector with up to 80% fill factor is surrounded by a sparse array of outriggers with  $\sim 5\%$  fill factor. SWGGO is in the process of choosing a detector unit concept along with its components such as the light sensors, as part of the R&D phase. A combination of prototyping activities and simulation work is expected to help the collaboration find the most optimal detector array configuration, along with the most convenient and effective detector unit design, as described in Section 2.3.6.

#### 3.1.1 *Double-Layered Detector Unit Design*

The SWGGO collaboration has considered several different detector unit designs for the WCDs. Among them, four are double-layered designs with different sizes, one is a large HAWC-like chamber, and another is a smaller structure with three photomultiplier tubes (PMTs) called the Mercedes design [24, 29].

In the double-layer design, shown in Figure 3.1, the top cell is an electromagnetic volume for timing and energy, and the bottom cell helps with muon identification and saturation recovery. Each cell has a photomultiplier tube (PMT) that detects the Cherenkov light inside the bladder. The two PMTs form

a mechanical unit such as shown in Figure 3.1, with one facing downwards and the other one facing upwards. The importance of muon identification for background identification was explained in Chapter 2, as muons are a signature of hadronic showers. An investigation of the double-layer WCD design for SWGO was made in a previous paper titled *A Double-Layered Water Cherenkov Detector Array for Gamma-ray Astronomy* [108]. The upper chamber would have low reflectivity, with an inner liner such as polyethylene, and would provide timing and energy information for incoming particles. The lower chamber would have a lining with high reflectivity to be able to detect the through going muons with maximum efficiency, working for muon tagging. The optimal aspect ratio of the two chambers is evaluated in Kunwar et al. along with the influence of reflectivity on time and charge resolution [108]. In general, the depth of the upper chamber has to be at least a few radiation lengths to be able to contain the electromagnetic component (see Section 2.2). For the lower chamber, the minimum height that still gives reliable signals is found in this paper to be 0.5 m.



(a) Sketch of a double-layered WCD made using GEANT4 [13]. The larger upper chamber is for electromagnetic signals, the lower chamber is for muon identification. (b) Double photo-multiplier assembly ready for installation in a WCD: a) mechanical design, b) prototype with a 10-inch Hamamatsu R7081 PMT facing up and an 8-inch R5912 PMT facing down.

Figure 3.1: The double-layered WCD design for SWGO uses two chambers and a double PMT support .

### 3.1.2 Detector Technology Options

The different detector unit designs considered can be built utilizing different detector technologies. The different technology options for the WCDs of SWGO are shown in Figure 3.2. The first category of technologies is to use tanks that are made of plastic or corrugated steel, while the other category is to put bladders into a natural or artificial lake. For all technology options, PMTs are housed inside bladders made of multilayered flexible materials and filled with purified water. Section 4.1 presents a discussion of the properties required of bladder materials in more detail.

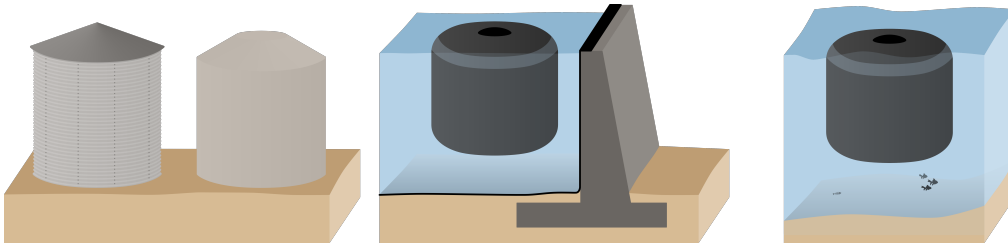


Figure 3.2: The technology options for SWGO WCDs. *Left*: Corrugated steel tanks and rotomolded high-density polyethylene (HDPE) tanks. *Middle*: A bladder in an artificial lake. *Right*: A bladder in a natural lake. Figure by Felix Werner, featured in [173].

An array of tanks similar to HAWC [9] or the Pierre Auger Observatory [142] may be used to make up the WCD array for SWGO. Tanks made up of corrugated steel sheets, similar to those of HAWC, could make carrying easier and would need to be built on site. The tanks could be made to have large sizes as was demonstrated by the HAWC observatory and could support a single or double-layer structure. More information on the tank design of SWGO can be found in [35], where it is explained that corrugated steel tanks would be custom produced by an Australian company called Aquamate<sup>1</sup>. The steel tanks are suitable and tested for housing double-layered WCD designs. In the other tank option, rotomolded high-density polyethylene (HDPE) tanks similar to those of Auger are combined with a shallow single chamber tank design. In this solution the WCD unit size is reduced, less water is needed to fill the WCD units, and less labor at high altitude is needed since the tanks would be produced away from site. Furthermore, the smaller size of the tanks (in context of the Mercedes design) require less water to be carried on site. This also brings about more difficulties for their transportation, compared to the corrugated steel tank option. Discussions of the usage of rotomolded HDPE designs can be seen in [24].

In the lake option, tanks as structural support for the bladders are abandoned, and instead, the bladders are placed in a larger body of water. The bladders have a cylindrical shape, with an access hatch at the top and are attached to circular floater units. The array of bladders may be placed in a natural high altitude lake, or alternatively in an artificial lake, or pond, that is constructed for this purpose.

All of the different detector unit designs being considered can be adapted to the tank or lake technology options, with the exception of the Mercedes design, which utilizes the rotomolded HDPE tank option.

### 3.2 THE LAKE CONCEPT

Placing bladders inside a lake is a new approach in context of ground particle arrays for gamma-ray astronomy, however lakes have been used in astroparticle

<sup>1</sup> Aquamate is a commercial company that installs geomembranes and corrugated steel tanks, based in Australia [27].

physics before. Neutrino astronomy has been using lake based detectors, for example in the case of the deep underwater detector in Lake Baikal [36]. Using acoustic detection in large lakes in order to detect EAS was also a project pursued in the 1980s, however it was not brought to life due to high acoustic background in such lakes [73, 100]. For the purposes of a ground-particle array for gamma-ray astronomy, ponds have been used before where water was the detecting medium, in case of Milagro Observatory [176] and currently for the WCDA of LHAASO [123] (see Section 2.3.4).

In case of the lake solution for SWGO, the purified-water-filled bladders form optically separated WCD units that float in an artificial or natural lake. The baseline idea is to use double-layered WCD bladders supported with floaters, with a double PMT structure produced in the Max-Planck-Institute for Nuclear Physics (MPIK), as shown in Figure 3.1, hung via three ropes from the hatch at the top of the bladder. The details of this design can be modified based on needs. The lake approach is attractive as the external water volume can provide mechanical support for the WCDs with little to no cost, and would mean a more flexible array. However it also comes with challenges, discussed in the following section.

### 3.2.1 Advantages

Deploying bladders into an artificial or natural lake is a method that has not been tried in the context of gamma-ray ground particle arrays before, but it has particular advantages that make it attractive, the anticipated reduced cost being possibly the most attractive one. In general, the lake concept offers the promise of extended flexibility, with an array that can be tuned for scientific needs, combined with reduced costs due to absence of tanks.

Specific advantages are:

- The material cost of a lake-based unit is reduced due to the absence of a water container or tank. The additional needs in terms of flotation are modest in comparison to tanks. However, additional costs may be introduced due to the deployment requirements that may arise. In the event of using an artificial lake or pond, the costs are increased, but are not expected to exceed those of tanks as discussed in Section 3.2.4. A reduction in transportation cost is also expected as there is less material to transport and no need for transporting water to the site.
- The lake approach ensures a flexible array configuration that can be modified according to the changing needs of the observatory over time; for example a higher energy or a lower energy focused configuration. The individual WCDs can be readily repositioned without removing water or sensors, since they are not housed inside stationary tanks, unlike the case of arrays like HAWC.
- As there are no tanks or enclosures to account for, the individual detector units can be optimized entirely based on physics requirements, as opposed

to taking into account other factors such as the size of commercially available tanks.

- The presence of water around each detector unit will suppress sideways entry of electromagnetic particles, even compared to high fill factor arrays, likely improving the quality of muon tagging using the lower chamber, in particular for showers coming at an angle. This effect is demonstrated with simulations in Section 3.3.2.
- Logistics are potentially simplified, as the amount of material to ship or transport to the remote site is expected to be less than compared to tank solutions.

### 3.2.2 Challenges

As this is a new technology, no previous experience exists for large-scale deployment of lake detectors. This means every complication that could occur needs to be evaluated, by working with realistic prototypes and mini-arrays. Specific challenges include:

- The mechanical stability of detector units under water motion needs to be ensured. In the presence of wave loads, the bladders are expected to move and they should be able to withstand the forces such movements would bring. Small movements of bladders against one another over time could also potentially damage them over long periods. The continuous movements and forces from the waves can initiate fatigue<sup>2</sup> in the bladder materials, which may cause fractures over time. Single and small array bladder units should be tested in a controlled environment against wave motion. Section 3.2.3 presents a more detailed look on this challenge.
- The absence of an outer container increases the requirements on the bladder, in terms of durability, tolerance to long-term UV exposure and light-tightness. In case of the tank solutions, additional light barriers may be used, and the bladders are not expected to be subject to continuous movement. Bladders suspended inside a lake, however, would be experience more UV exposure, and more stretching due to water waves. Additional material requirements such as light tightness, not contaminating the water they have inside, hold for all technology solutions. Section 4.1 gives an overview of the material requirements for the lake bladders.
- Since the units will be floating in water and will be subjected to disturbances, the geometry calibration is more complex than for the static tank case. Strategies for monitoring the position of the bladders and of the PMT positions inside each bladder need to be developed. These could be

---

<sup>2</sup> Fatigue is the degradation of mechanical properties of a material leading to an eventual failure under cyclic loading [140].

data-driven position calibration methods that are augmented by specific instrumentation.

- Challenges exist regarding the identification of a suitable site. If a natural lake is preferred, this greatly reduces the choice of sites. Several high altitude lakes exist in Peru and Bolivia, however cultural and environmental concerns may arise in these sites. If an artificial lake is preferred, this brings about extra engineering efforts and costs. Restrictions on array geometry are also expected, since in addition to the dense array, outriggers would need to be arranged.

### 3.2.3 *Survival under Wave Motion*

Wave loads are not a concern for the tank design, and likely not for the pond design, but in case of a natural lake, waves are expected depending on the size of the lake and the wind conditions in the area. The pressure oscillations occurring due to waves exert a mechanical load on the bladders, which can have a negative influence on measurements, and over time damage the bladders themselves. Wave loads would also vary the position of the bladders and the photosensors inside them. For these reasons, the influence of waves has to be determined and accounted for.

The hydrodynamical problem of determining the influences of a wave on a flexible bladder material is complex. A full treatment of this problem needs to be done via specialized simulation programs such as smoothed particle hydrodynamics (SPH) and a real life demonstration. In this section we mainly look at a simplified version of the problem.

#### 3.2.3.1 *Linear Wave Theory*

Behavior of water waves is explained to a linear approximation via the Linear Wave theory, developed by Airy in 1845, also called Airy wave theory. This theory gives a reasonable approximation for water waves for many parameters, although a more complete description would need summation of many approximations and additional terms, using "finite amplitude theories" [62]. Here we use the Airy wave theory in order to understand a basic description of waves that may occur in a lake and their impact on bladders.

Surface waves are mostly introduced by winds inducing friction, and gravity functioning as the force restoring equilibrium. At every point  $(x,z)$  where  $z$  is the distance from the still water line (SWL) to the sea bottom (see Figure 3.3), the fluid velocity is expressed as  $v(x,z,t) = u(x,z,t)i_x + w(x,z,t)i_z$  with the velocity vectors in  $x$  and  $z$  directions  $u = \frac{\partial\Phi}{\partial x}$  and  $w = \frac{\partial\Phi}{\partial z}$ .

Airy wave theory makes the assumption that the fluid flow is irrotational, so that the water particles do not rotate, having only normal forces. Moreover, it assumes the case of an ideal fluid that is homogenous and incompressible, hence the Laplace equation governs the flow beneath the waves at the surface.

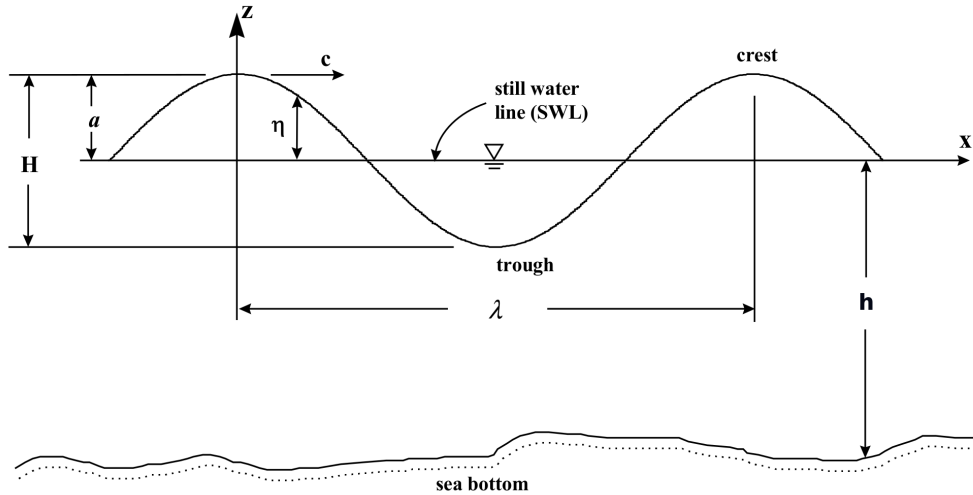


Figure 3.3: A 2D representation of a plain water wave in Airy Wave Theory.  $\lambda$  is wavelength,  $H$  is wave height and  $\eta$  is the free surface elevation. Figure taken from [132].

$$\frac{\partial^2 \Phi}{\partial x^2} + \frac{\partial^2 \Phi}{\partial z^2} = 0 \quad (3.1)$$

As for the water surface, the Airy wave theory makes the assumptions that surface tension can be neglected, that the pressure at surface is uniform and constant, the surface is always made up of the same particles, and that the floor bed is an impermeable boundary – meaning that the vertical velocity at the bottom is zero. (Discussion of these assumptions in [62, 107].)

With these assumptions, the theory is able to describe the free surface elevation of water waves as a regular sine wave dependent on position  $x$  and time  $t$ , as

$$\eta(x, t) = a \cos(kx - \omega t) \quad (3.2)$$

where  $\omega$  is the wave frequency and  $k = 2\pi/\lambda$  is the wave number [40, 62], with  $\lambda$  as the wavelength. The parameter  $\eta$  is the displacement of water surface relative to the still water line, shown in Figure 3.3. Wave frequency  $\omega$  is related to wave number  $k$  via the dispersion relation, which states that waves with a given frequency must have a certain wavelength.

$$\omega^2 = gk \tanh(kh) \quad (3.3)$$

Phase velocity is defined as the speed at which a waveform propagates,  $C = \omega/k$ . Group velocity is the velocity of a group of waves and the speed at which the wave energy travels.

There are two cases, shallow water is defined when  $h/L < 1/2$ , and deep water is defined if  $h/L > 1/2$ . We look in this chapter to the deep water case,

where the wavelength  $L$  is much smaller than water depth, which simplifies our discussion. In this case, the dispersion relation becomes  $\omega = \pm\sqrt{gk}$ .

Under the free surface, the local fluid velocity components are found by using the dispersion relation. When the deep water approximation is made, it is seen that the fluid particles follow closed circular orbits with radii that decrease with distance from the water surface, as

$$R = ae^{2\pi z/\lambda} \quad (3.4)$$

where  $z$  is the distance from water surface, or still water level, starting at SWL with  $z = 0$  and reaching  $z = -h$  at the flat-assumed sea bottom. As the distance from the still water level increases, there is an exponential decay of magnitude of the velocity components. In deep water, diameter is reduced to 4% of the value of the surface, at a depth of  $\lambda/2$ . The fluid under the wave crest moves in direction of wave propagation, and returns during the trough, hence we see oscillatory fluid motion from Airy wave theory.

Figure 3.4 depicts the motion of fluid particles. The red circles indicate the oscillatory particle trajectories, becoming smaller with depth. The figure is made assuming equation 3.4 and 3.2 for a wave with a period of  $T = 2$  s and using the deep water approximation for the dispersion relation. We see that the radius for particle trajectories is around 20 cm at SWL, and drops down to 7 cm 1 m below SWL. Two 'bladders' are drawn in the figure for illustrating the scale of our bladders, around 3 m depth and 3 m diameter. Hence, the bladders would experience little to no disturbance at their bottom side, and maximum disturbance at the top. Compared to the forces associated with water motion, the elastic forces of the bladders are small, hence the bladder is expected to essentially follow the water flow as shown in Figure 3.4.

The reality is more complicated as many of the assumptions may not hold. For example, there is also a slight displacement of particles along the propagation direction of the wave, called the Stokes drift [107]. The forces on the bladders and the stretching they would cause is also not depicted in the figure.

### 3.2.3.2 Wave Load on Bladders

Similar to the fluid particle oscillations, there is also a pressure oscillation that varies with distance from water surface, depicted in Figure 3.5 for a wave with a period  $T = 2$  s. The pressure under the free water surface is a sum of static pressure that occurs due to mean water level variation (increases from zero at water surface to  $\rho gh$  at the bottom, where  $h$  is the mean water height) and dynamic pressure that is induced due to waves. Wave-induced pressure oscillations differ under crests and troughs of waves, and similar to the water particle movement, reduces exponentially with depth below water surface.

$$P = \rho ga \frac{\cosh(k(h+z))}{\cosh(kh)} \quad (3.5)$$

where  $h$  is the height of water surface above ground. In the deep water approximation,  $\cosh(k(h+z)) \approx e^{kz}$ , so the dynamic pressure equation can be approximated as

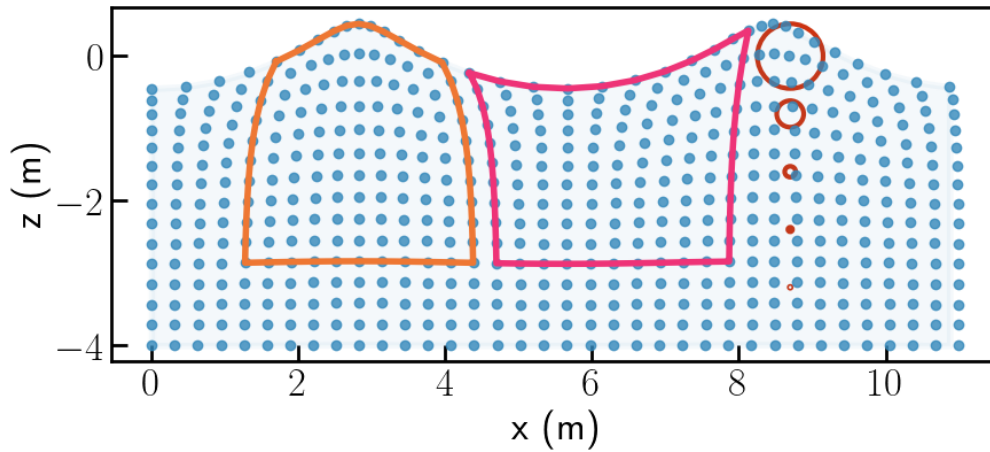


Figure 3.4: Water particle movement under a wave with  $T = 2$  s. Red circles depict the water particle trajectories varying with depth according to Airy Wave Theory. Two bladders are depicted following the particle trajectories for illustration, the reality is more complicated.

$$p = \rho g a e^{kz} \quad (3.6)$$

The dynamic pressure induced by a traveling wave of height 0.5 m and period 2 s, as the one depicted on Figure 3.4, would vary between  $\approx 5 \times 10^3 \text{ N/m}^2$  and  $\approx 200 \text{ N/m}^2$ , at a height of 10 cm below surface, to 300 cm, within the scale of our bladders. The exponential decay in the dynamic pressure is evident, and would result in differing amounts of stress and stretching for the bladders. The bladders are expected to move along with the waves as depicted in Figure 3.4. During these movements, the bladder material should be able to stay within its elastic range<sup>3</sup>. In addition to instantaneous forces, the movement of water may also cause bladders to rub against one another over years, causing fatigue and eventual damage.

A proper treatment of the forces acting on a flexible body such as our bladders needs taking into account the drag force and inertial force is beyond the scope of this thesis. Furthermore, as our bladders are made up of flexible materials and also would have independent water volumes inside them, the question becomes very complex. Calculating the forces acting on a bladder, made up of HDPE layers, filled with purified water requires consideration of fluid-structure interaction, the deformable nature of the bladder, and the dynamic forces from waves and currents. Advanced numerical simulations such as smooth particle hydrodynamics (SPH) or computational fluid dynamics (CFD) would need to be used.

For a comprehensive study on this subject, refer to the PhD Thesis titled *Wave loading on bodies in free surface using smoothed particle hydrodynamics (SPH)* [138].

<sup>3</sup> Elastic range is the range in which the distortion of the material due to a force disappears once the force is removed, such that the material turns to its original form [146].

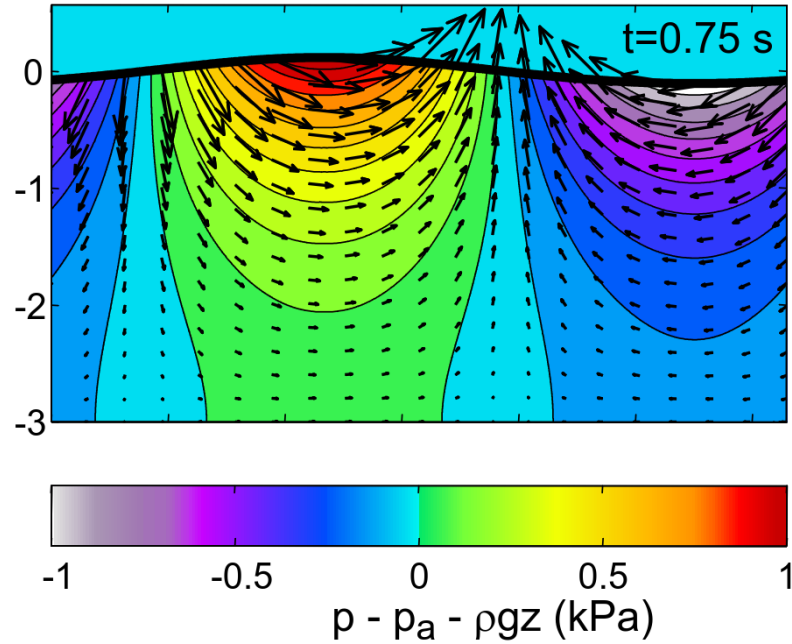


Figure 3.5: Velocity vectors and pressure anomaly for a wave with period 2 s. Image is taken from [28].

### 3.2.3.3 Wind Speed, Fetch and Wave Spectra

We saw that the forces exerted on a body inside water depend on the dynamic pressure, which depends on the height and period of the water waves. The height and period of wind-excited waves in turn depend on the characteristics of the wind in the area and the fetch. Fetch is the distance over which wind interacts with wind surface. In general, higher wind speed and larger fetch corresponds to a larger wave height and period, hence for our purposes small lakes are favored [40].

Waves are irregular and chaotic, however their statistical properties vary slowly, so it is possible to describe the water surface by using a variance density spectrum. These wave spectra assume that each wave is a sum of several sinusoidal terms and give the distribution of wave energy over different wave frequencies  $\omega$ . They give information of the superposition of waves generated with different wind speeds at different times, called 'swells', and the wave being generated by the wind at that time.

One of the simplest spectra is the Pierson-Moskowitz (PM) spectrum. This spectrum, developed in 1964, makes the assumption that the wind blew steadily for a long enough time over a large enough area, such that the waves are in equilibrium with the wind. Pierson and Moskowitz obtained the spectrum by choosing data taken with weather ships that had wind blowing steadily for some time, and calculating wind spectra for various wind speeds [159].

$$S(\omega) = \frac{\alpha g^2}{\omega^5} \exp\left[-\beta\left(\frac{\omega_0}{\omega}\right)^4\right] \quad (3.7)$$

where  $\alpha$  and  $\beta$  are coefficients and  $\omega_o = \frac{g}{U_{19.5}}$ ,  $U_{19.5}$  being the wind speed at 19.5 m above sea level. The JONSWAP spectrum derived in 1973 multiplies the PM spectrum by a 'peak enhancement' factor.

The variance of the free surface elevation  $\eta$  is given by the integral of these spectrum, and the different moments of the spectrum express different parameters, including significant wave height and period. Significant wave height is derived as  $H_s = 4\sqrt{m_0}$  where

$$m_n = \int_0^{\infty} \omega^n S(\omega) d\omega \quad (3.8)$$

Significant wave height  $H_s$  is defined as the average of the highest third of the waves. Formulas for significant wave height and period can thus be derived from PM and JONSWAP spectra, where in both cases there is a dependence on wind speed  $U$ , and in the JONSWAP case fetch also has an influence.

Several empirical formulas that connect wind speed and fetch with significant wave height and period exist (Carter, 1982 [48], Hanson & Larson, 2008 [80], Shore Protection Manual (SPM) method, 1984 [154]). We use the SPM method, used also in a technical document on floating fish farms in Norway for estimates [45, 134]. In this parameterization, the wind speed  $U$  [m/s] is measured 10 m above water. Significant wave height  $H_s$  [m] and wave period  $T_p$  [s] are given as a function of fetch  $F$  [m] as

$$\begin{aligned} U_A &= 0.71U^{1.23} \\ H_s &= 5.112 \times 10^{-4} U_A F^{1/2} \\ T_p &= 6.238 \times (10^{-2} U_A F)^{1/3} \end{aligned} \quad (3.9)$$

Where  $U_A$  is the adjusted wind speed. This parameterization takes into account only the wind waves (not swells) and any particular site conditions such as reflections from steep features. We use these formulas to estimate that for a lake with a fetch of  $F \approx 800$  m and average wind speeds around  $U \approx 27$  m/s, we get  $H_s \approx 0.6$  m,  $T_p \approx 2$  s and  $\lambda = 1/T_p \approx 6$  m. This is similar to the conditions we have used for Figure 3.4.

Prior to deployment in any natural lake, depth surveys and an analysis of the weather conditions is necessary. In general, smaller lakes are favored due to their smaller fetch, which also favors the use of artificial lakes.

#### 3.2.3.4 Tests of Bladders in a Wave Basin

In order to evaluate the behaviour of our bladders and the PMT units inside them under wave conditions that may be expected in lakes, tests will be conducted in an indoor wave basin in the Research Laboratory in Hydrodynamics, Energetics and Atmospheric Environment (LHEEA) [91], located in Nantes, France.

The segmented wave maker of the wave basin, shown in Figure 3.6, will be used to generate waves of varying frequencies and heights. The bladders placed inside the wave basin will have fully-functional PMT units and readout



Figure 3.6: The hydrodynamics and ocean engineering tank at LHEEA, France. The segmented wavemaker is seen in the background. Figure taken from [91].

installed to them, monitoring light tightness. Furthermore, each bladder will be equipped with inertial sensors to track PMT motion and the anchoring forces on the springs connected to the bladder floaters will be monitored.

Scheduled to take place for early 2025, these tests will reveal the behavior of bladders and the PMTs inside them under wave conditions, and also test the overall scheme including deployment and recovery of bladders, interconnections, anchoring and PMT deployment. The planned wave basin tests are described in more detail in Appendix E.

#### 3.2.4 Pond Option

Ponds can be used for a ground particle array in two ways, firstly as a light tight volume filled with purified water, namely a 'closed pond', secondly as an artificial lake that would house bladders, as an 'open pond'.

The option of a light tight closed pond with purified water, housing photosensors optically decoupled via curtains is not pursued by SWGO in light of the experiences of LHAASO and Milagro observatories. The difficulties in making such a large closed pond light tight, maintaining the water quality in such a large volume, and the increased possibility of leaks coupled with the difficulties of humidity control make the option of closed pond unattractive.

The open pond option, on the other hand, emerges as a promising solution to some of the challenges of the lake option. As outlined in Section 3.2.2, some of the challenges of deploying bladders in a natural lake are the difficulty of finding a suitable high altitude lake, and the question of survival under wave motion. It is easier to find a site suitable for pond construction, hence there is more freedom for site selection. Moreover, since the pond size would be optimized for the array, large waves can be avoided, and access to the individual detectors may be easier. It may also be possible to provide additional light barriers to protect from UV light exposure.

The pond option would require more civil engineering work compared to the natural lake option, as a hole would need to be dug for providing material for the walls and a membrane would need to be inserted into the pond to minimize water leakage; the details of pond construction would need to be

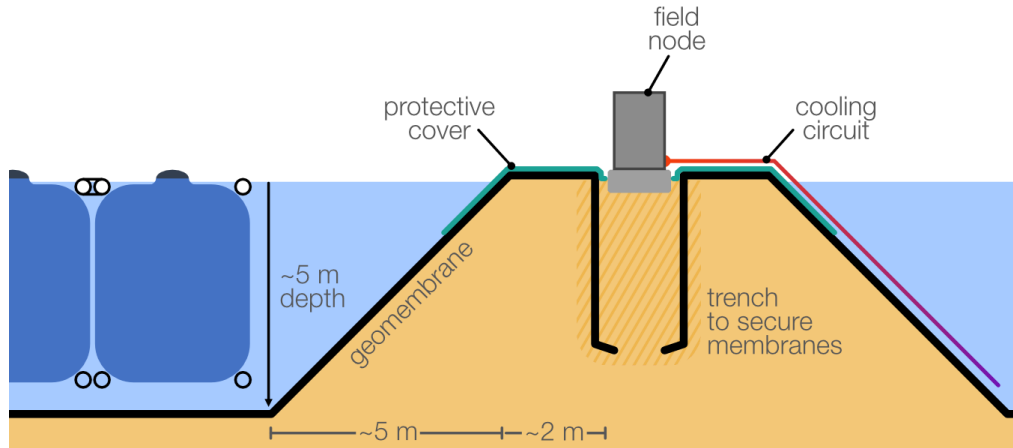


Figure 3.7: Sketch of the gap between two artificial ponds. Field nodes are placed on land and there is a  $45^\circ$  angle at the edge of each pond. Figure made by Felix Werner.

determined by external companies. Furthermore, the site of the pond should have a steady water supply nearby, such as a river, to ensure that the pond's water level remains stable, which places a restriction on sites.

The design and cost assignment for ponds would be provided by an experienced engineering company. This company would need to run a geotechnical study of the site and the soil and give a cost estimate. A smaller test pond would need to be built as well. The pond would need to be designed such that it can be used once it is out of commission by the local community for water storage, fish farming etc.

The detector units would be grouped together into hexagonal grids inside several adjacent ponds. The cables from these detectors would be collected together at field nodes placed on land as shown in Figure 3.7 in between ponds, where pond water can be used for cooling. The ponds would be 1-2 m deeper than the WCD depth. The borders of the ponds need to have a slope of  $\sim 45^\circ$  for stability as shown in the figure. The geomembranes of the ponds can be anchored in the space between each pond. These considerations may be altered based on external company recommendations.

### 3.3 SIMULATED PERFORMANCE FOR THE LAKE CONCEPT

The performance of a single detector unit immersed in water is in principle similar to a single detector unit on land, housed inside a tank. A detailed investigation of double-layered WCDs as individual detectors and as arrays was made in Kunwar et al. [108], considering different chamber dimensions and liners, on single detector and array levels. In this section, only the properties that would differ for double-layered WCD detectors inside a body of water are evaluated; namely overburden and shielding. A simulation framework based on GEANT4 [13], called HAWCSim, is used, similar to in [108]. The WCD used in these simulations has a diameter of 3.6 m, and upper chamber to lower chamber height ratio of 2.5 m:0.5 m. The two photosensors used are Hamamatsu

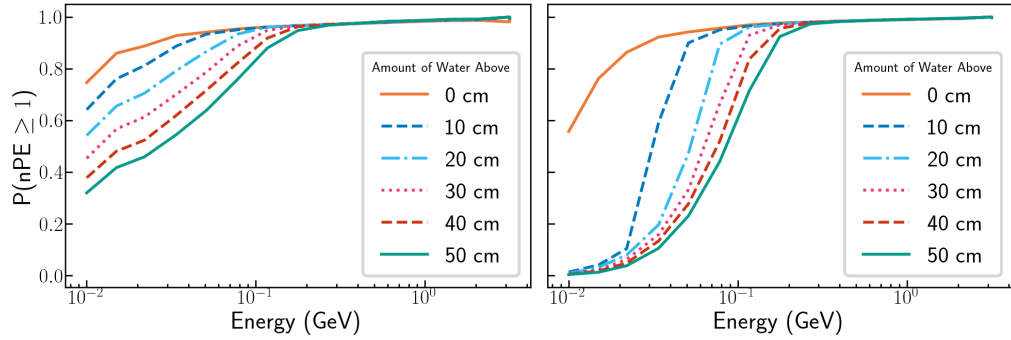


Figure 3.8: Impact of water depth above a WCD on the probability of detection of one or more photoelectrons as a function of particle energy. *Left:* For gammas. *Right:* For electrons.

R5912 [109] and the water absorption length is 18 m at 410 nm, following a spectrum from the study by Segelstein [153] (see Section 4.1). The reflectivity of polyethylene which is the inner liner for the upper chamber is assumed to be 0.1 while reflectivity of Tyvek which is the inner liner for the lower chamber is assumed to be 0.92, at 410 nm (For more information on water absorption length and reflectivity, refer to Section 4.1).

### 3.3.1 Overburden

In the lake configuration, the top of the detector may be partially immersed in water. The detector units are expected to have a shape described in Section 3.1, which would mean that they could have  $\sim 30$  cm water above, depending on local conditions and design choices. To test for the possible overburden from this partial immersion, a single double-layered WCD is simulated, immersed into a body of water such that there is increasingly more water above it, starting from 0 cm water above and going up to 50 cm. At each level, vertical gammas and electrons are thrown to the double-layered WCD, with energies ranging from 10 MeV up to a few GeV. Figure 3.8 shows the detection probability as a function of energy of the incoming particle. For all cases, detection probability approaches 1 as the particle energy reaches GeV energies, hence we see that around GeV energies overburden does not have a significant affect for gammas or electrons.

In the case of low energy electrons, the detection probability drops sharply with overburden, while for gammas it does not go below 40%, as expected. As described in Section 2.3.1, electron interaction in water is dominated by bremsstrahlung when they are above the critical energy of  $E_c \approx 80$  MeV, after which they lose energy primarily via ionization (see Figure 1.10). In the right plot of Figure 3.8, we see that below this critical energy, electron detection probability quickly drops to zero, as ionization losses dominate. At that point electrons lose  $\approx 2$  MeV/cm in water, so for low energy electrons 10 cm water above would mean they lose most of their energy. Meanwhile gammas interact mainly via pair production, with a mean free path of around  $\sim 40$  cm (see

Section 1.4.3). From this study we see that overburden makes a difference for low energy particles, below 100 MeV, especially for electrons.

### 3.3.2 Shielding

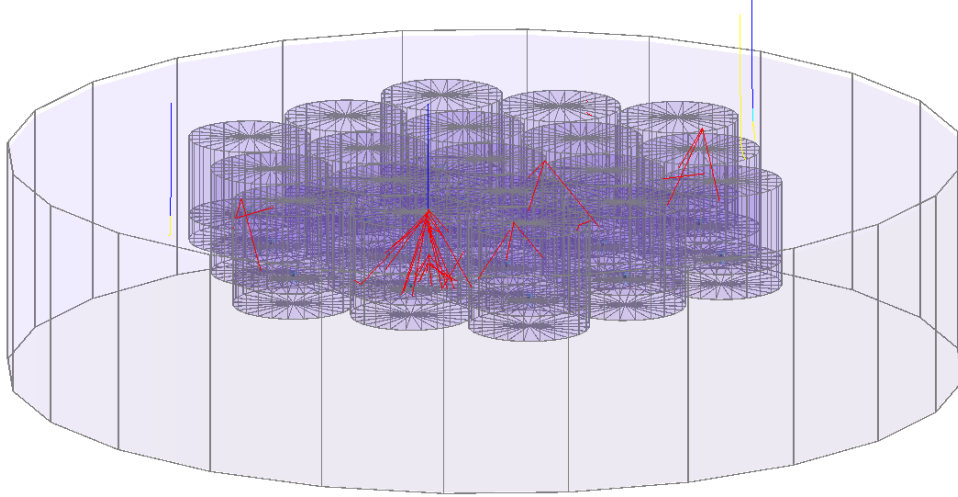


Figure 3.9: An array of 20 double-layered WCDs placed in a circular pond, simulated using HAWCSim. The secondary gammas (in dark blue) and electrons (in yellow) coming from a vertical gamma-ray initiated shower are seen.

In the double chamber design, as described in Section 3.1 and in Kunwar et al. [108], the lower chamber functions to tag incoming muons, however electrons or gammas may still be able to enter this chamber from the sides, bypassing the upper chamber entirely. This would cause an electron to be misidentified as a muon, likely worsening the gamma/hadron separation. If the double-layered WCD is immersed in water, this effect would be avoided, as the outside would be surrounded by water that can stop sideways entry, providing shielding.

Shielding is tested by injecting gamma-ray initiated EAS to a small (20 units) array of double-layered WCDs, where EAS are simulated using the CORSIKA simulation package [82]. Figure 3.9 shows the mini array made up of identical double-layered WCDs. In this figure, the array is immersed in a larger water tank, or a pond, filled with water. The blue lines indicate some of the secondary gamma-rays coming from an EAS, while the yellow line is an electron. The red lines indicate the Cherenkov photons inside the double-layered WCDs. The CORSIKA showers are directed to the center of the array and have primary particle energies from 100 GeV to 5 TeV with an energy spectrum  $E^{-2}$ . The different angle combinations tested are the Zenith angle 0, and combinations of  $\theta = 30^\circ$  and  $\phi = 60^\circ$ .

For gamma showers from zenith, the sideways entry into the lower chamber is quite small (around 0.1% for air, for the central tank, and around 0.5% for the edge tank), however as in the figure, for showers that are around angles of  $30^\circ$ , the difference grows. Figure 3.10 and Figure 3.11 compare double-layered

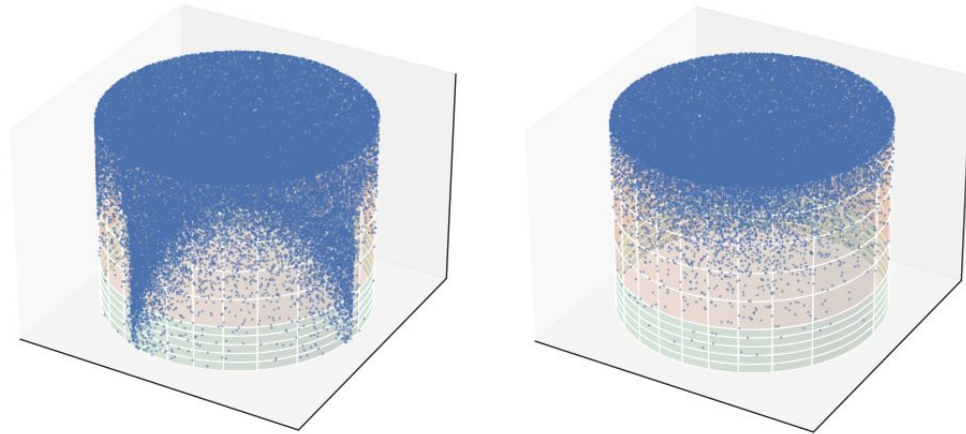


Figure 3.10: The central double-layered WCD in the array depicted in Figure 3.9 when a gamma-ray shower is thrown towards the center of the array, with an angle of  $30^\circ$ . The blue points represent the water hits, or the point of first interaction in the water volume within the double-layered WCD. *Left:* Double-layered WCD array is in air. The shielding from the neighboring tanks is seen. *Right:* The double-layered WCD array is in water. A more uniform shielding is seen.

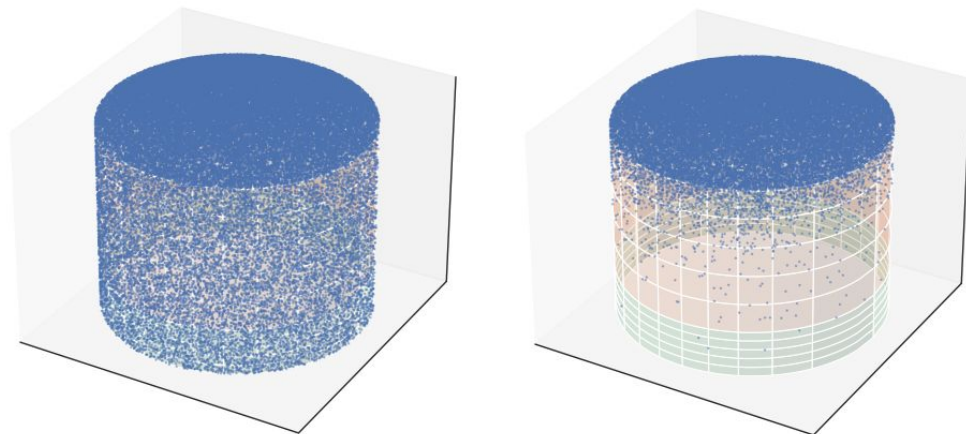


Figure 3.11: A double-layered WCD at the edge of the array depicted in Figure 3.9 when a gamma-ray shower is thrown towards the center of the array, with an angle of  $30^\circ$ . *Left:* Double-layered WCD array is in air. The double-layered WCD at the edge of the array has no shielding to sideways entry. *Right:* The double-layered WCD array is in water. A uniform shielding is seen.

WCD units that are part of the small array of double-layered WCDs, for the case of  $30^\circ$  inclined gamma-ray showers, where on the left side the array is in air, which would be the case for an array of tanks, and on the right side the array is immersed in a body of water. The blue points represent the point of first contact with the water inside the double-layered WCD. In Figure 3.10,

depicting the double-layered WCDs at the center of the array, for the air case, we can see the ‘shadow’ of the neighboring tanks, shielding the central tank, while when the detector units are immersed in water, shown on the right, the shielding is more uniform, giving a sideways entry into the lower chamber of less than 0.1%. In Figure 3.11 a tank at the edge of the array is depicted, where in the case of air we see there is no shielding, and the sideways entry into the lower chamber is around 5%. Meanwhile, the water immersed case still has the expected more uniform shielding, with a sideways entry of less than 1%. We see that when the showers have an angle, the presence of water around the double-layered WCDs makes a difference.

The effect of shielding can also be seen by looking at the signal amplitude distributions for these cases, shown in Figure 3.12. On the left side we see the double-layered WCDs in air and on the right side in water. The top plots are for the double-layered WCDs at the center of the array while the bottom plots are for those on the edge. In the air case, the frequency of large signals are similar for upper and lower chambers, meanwhile in the water case, large signals are suppressed for the lower chamber.

The influence of this shielding of sideways entry on gamma/hadron separation and signal quality remains to be evaluated with full array simulations.

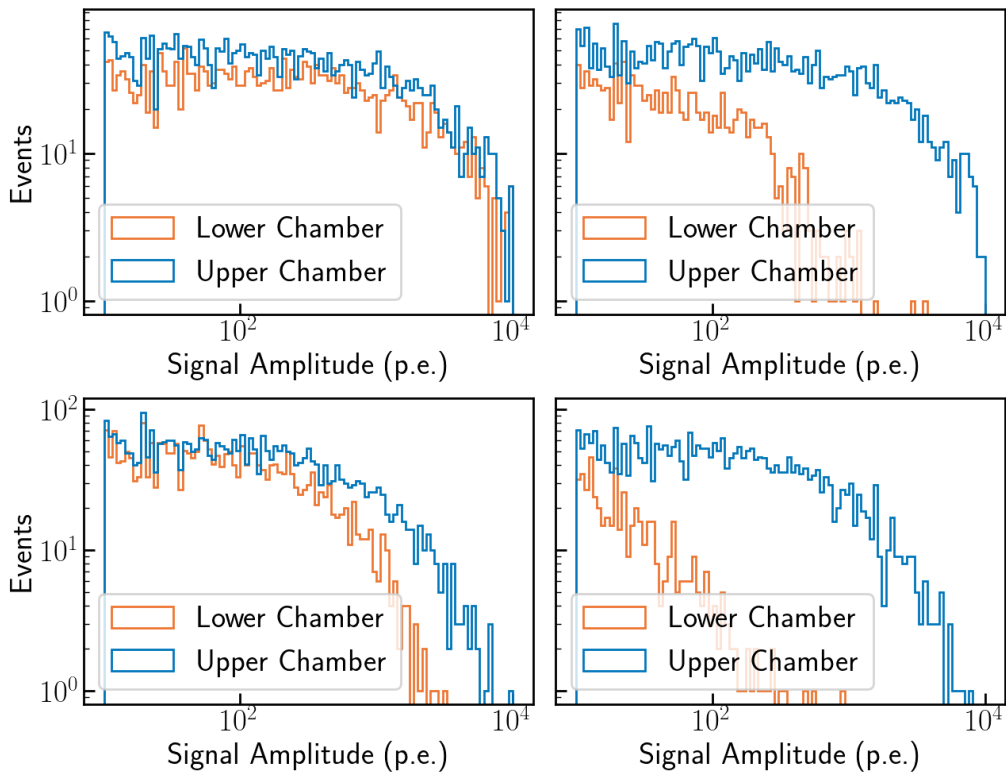


Figure 3.12: *Top*: Signal amplitude distribution in the air (left) and lake (right) cases for the central double-layered WCD for the 30° gamma shower. *Bottom*: Signal amplitude distribution in the air (left) and lake (right) cases for the edge double-layered WCD.

### 3.3.3 *Vertical Interactions at Boundaries*

The secondary particles from EAS follow different directions depending on their interactions, and in rare cases, a secondary particle may reach the detectors at a vertical angle. In this section, this case is evaluated by throwing vertical gammas and electrons at the boundaries of double-layered WCDs, with energies from 50 MeV to 1 GeV.

Three cases are considered. The first case is when vertical gammas and electrons are injected right outside the double-layered WCD, between a distance 1 cm to 5 cm away from the boundary of the double-layered WCD. The second case is when vertical gammas and electrons are directed on the boundary. Lastly, gammas and electrons are injected towards the inside and outside of the tank, around the boundary.

We see that in this case the lake solution gives marginally more signal. Figure 3.13 shows the results for gamma-rays at the top and for electrons at the bottom. In all cases, we see more signal when the WCD is immersed in a lake. The leftmost plots show the case when the particles are thrown right outside the WCD. For the lake case we see that 20% of the events give low threshold signals, and as the signal increases the fraction approaches zero. The air case has no signal for gamma-rays and very small signal for electrons. The middle plots show the case at the boundary of the WCD, where we see a slight increase for the lake case and fractions above zero for the air case, but again we approach zero with higher signal. For both particles, we see that as expected the upper chamber signal is higher. Since gamma-rays tend to pair produce later on and electrons interact much quicker, we see a greater difference between lower and upper chambers for electrons. Finally, for the last case where particles are injected towards inside and outside the WCD, we see higher signal, with fractions starting around 40% for both the lake and air cases.

For the rare event that a vertical particle comes near the boundary of a WCD, we see that the lake case is able to pick up signals from these particles as well, picking up more shower energy. Since interactions in water are more likely than in air, gamma-rays are more likely to pair produce while passing through lake water, occasionally depositing signals in the lower chamber. In general we see from Section 3.3.2 that this affect does not influence the superior shielding capabilities of the lake concept.

## 3.4 SUMMARY

In this Chapter we described the lake concept as a detector technology option for SWGO as a potentially cost saving alternative to the more traditional tank approaches. We saw that immersing an array of light tight bladders into a natural or artificial lake may have cost saving advantages, and in addition provide a more flexible configuration. Evidently, the performance of flexible bladders that make up the detector units in water motion should be evaluated thoroughly. We also saw that the immersion of double-layered WCD units in a lake provides a uniform shielding against sideways entry of secondary particles

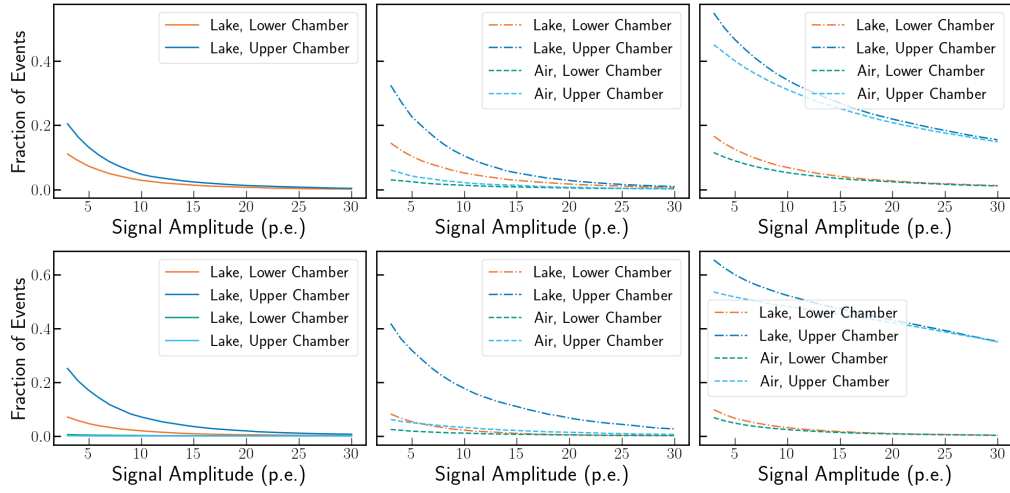


Figure 3.13: Fraction of events recorded by upper and lower chambers of a single double-layered WCD, for vertically thrown gammas and electrons. The top plots are for gammas and bottom are for electrons. *Left*: Particles thrown 1 cm outside the WCD. *Middle*: Particles thrown around the boundary of the WCD. *Right*: Particles thrown outside and inside the WCD.

to the lower chamber, while without a lake only the neighboring double-layered WCDs provide shielding. The influence of this effect on gamma/hadron separation remains to be studied.



## EVALUATION OF THE LAKE OPTION

---

The deployment of individual bladders into a natural or artificial lake for the Southern Wide-field Gamma-ray Observatory (SWGGO) was proposed as a promising approach in Chapter 3. As outlined in Section 3.2, this design represents a new application in the context of gamma-ray astronomy, with no prior experimental precedent.

In this chapter, prototyping efforts for the lake-based design are presented. Section 4.1 begins by evaluating the materials used in each detector unit, focusing on reflectivity and water quality. This is followed in the next section by the development and testing of a detector unit for the lake design, progressing from small-scale bladders to the construction and assessment of the first double-layered detector unit for SWGGO.

### 4.1 BLADDER MATERIALS

The efficiency of signal and timing obtained from the detector units of a ground particle array depend on several parameters, such as the geometry of the detector units, the properties of photosensors used for signal detection, the quality of water as a detecting medium, and the reflectivity of the inner walls. Factors such as the aspect ratio, the form of the detector array, the number of detectors, the location of the observatory, the photosensors being used all have an influence on the performance of the observatory as a whole. In this section we focus on the material related aspects; we go over the general requirements for the bladder materials, and we discuss the reflectivity and water quality tests being performed at the Max Planck Institute for Nuclear Physics (MPIK).

#### 4.1.1 *Requirements of Bladder Materials*

The bladders that make up the detector unit units of our array need to fulfill several requirements. These include

- **Strength & Durability** of materials is crucial to keep the detector units intact over several years. The materials should be resistant to punctures and folds occurring during transportation. An additional requirement for the lake case is that the material should stay within its elastic range under the forces coming from wave motion and should withstand fatigue, as described in Section 3.2.3.
- **Flexibility** of bladder materials goes together with their strength. The material should be flexible and foldable during transportation as well.

- **Light tight** materials should be used in order to construct detector units, this is one of the essential requirements for an array of WCDs. Optically independent light-tight units are needed.
- **Water purity** inside the detector units is important. The bladder materials should not degrade the quality of the highly purified water inside them over the years. The liners should be resistant against any biological activity or chemicals and release little or no extractables <sup>1</sup> into the purified water.
- **Withstanding UV radiation** is required especially for the lake case, as the bladders are expected to be under direct sunlight at high altitudes for prolonged amounts of time.
- **Reflectivity of the lower chamber's inner lining** should be high in order to maximize muon signals.

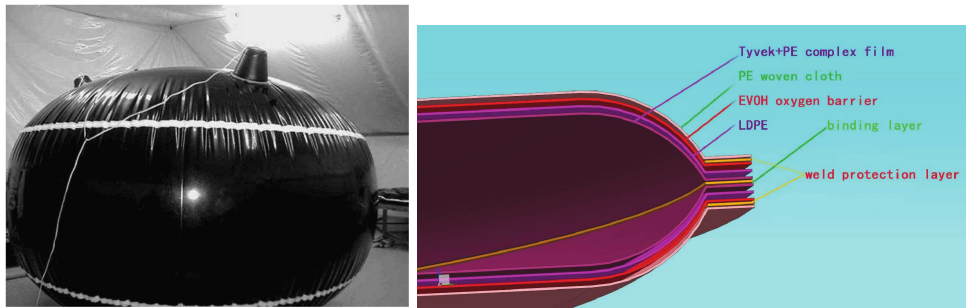


Figure 4.1: *Left*: The Auger liner, three separate laminates welded together using custom made impulse sealer. Figure from [142]. *Right*: Sketch of the LHAASO muon detector liner. Two circular laminates are welded together from the outside. Figure from [123].

#### 4.1.2 Bladder Material Production Plans

Custom bladder liners for SWGO are planned to be made up of several layers in order to address all of these requirements properly. Surface detector arrays such as Pierre Auger Observatory [142], HAWC [9] and LHAASO [123] have used composite materials for their detector units.

The flexible plastic liners for the Pierre Auger Observatory are housed inside plastic tanks (See Section 2.3.4). Their tanks are already providing the primary light protection, while the liners act as secondary barriers against outside light. Their liner is also resistant against damage due to ice formation since the temperature change experienced by their tanks varies greatly. Their liner is composed of a three-layer low-density polyethylene (LDPE) film providing strength and flexibility that is bonded to a layer of Tyvek 1025-BL that provides diffuse reflectivity. The LDPE layer has a thicker carbon black loaded LDPE component that provides light tightness, placed between two thinner layers

<sup>1</sup> Extractables are organic and inorganic chemical compounds that may be released from a material [174].

of LDPE. The reflective Tyvek liner is bonded to the LDPE layers by titanium-dioxide ( $\text{TiO}_2$ ) LDPE film [142].  $\text{TiO}_2$  could have benefits as it has antibacterial properties and reduces UV degradation [136].

The bladders for HAWC are housed inside steel tanks covered with an extra film cover and are much larger than Auger bladders, with a diameter of 7 m and heights of 5 m. These bladders are also made of LDPE and do not have Tyvek inner lining. The  $\approx 0.4$  mm thick liners are composed of the layers of a film with three substrates, bonded via a co-extrusion process [9].

In case of LHAASO, their muon detector (MD) array which functions to identify muons for the KM2A (see Section 2.3.4), is made up of wide cylindrical bladders housed inside concrete tanks that are buried in soil. The bladder liners of the MD are also mechanically supported by the tank surrounding it. Similar to the liners for Auger, this liner is a composite using LDPE and Tyvek. In this case, Tyvek 1082D is used along with a layer of PE, and a layer of ethylene vinyl alcohol copolymer (EVOH) is added after the LDPE layer for protection against oxygen permeability [123].

In light of the experiences of these ground particle arrays, the SWGO bladders will also be composite materials utilizing LDPE and Tyvek. The presence of carbon black for light tightness is crucial, but the flexibility of the material should not be reduced at any cost. Companies specialized in composite film production will handle the production of these materials.

Once the bladder liners are produced, they needed to be welded together in order to complete making of the bladder. Custom prototype bladders for SWGO are already being produced by the company Aquamate<sup>2</sup>. Our design has a top layer that has a hole for the hatch, the cylindrical side layer, a middle membrane with a hole in the middle for the double-PMT, and finally a bottom layer. The Auger liners were first manufactured as three separate sections from their custom film, namely the bottom, side strip and the top. Afterwards these were sealed together by welding the layers together under pressure using custom made impulse heat sealing machines [142] (see Figure 4.1). The welding process for the LHAASO MD bladders appears to be somewhat simpler as two circular liners are welded together from the outside, as shown in Figure 4.1.

#### 4.1.3 Reflectivity Measurements

The effects of reflectivity of the inner liners of a WCD on signal efficiency and timing are discussed in Kunwar et al [108], which investigates double-layered WCDs for SWGO. The influence of reflectivity of the inner lining on signal efficiency and timing is shown in the plots of Figure 4.2, taken from the same study. The left figure shows the probability of detecting one or more photoelectrons for vertical gamma-rays injected across the top of the upper chamber of a double-layered WCD. Here "white" denotes a Tyvek-covered inner surface with high reflectivity ( $\sim 92\%$  at 450 nm), while "black" denotes low reflectivity ( $\sim 10\%$  at 450 nm) bladder materials, such as polypropylene

<sup>2</sup> Aquamate is a commercial company that installs geomembranes and corrugated steel tanks, based in Australia [27].

or polyethylene. The right figure shows the arrival time distribution for the different cases.

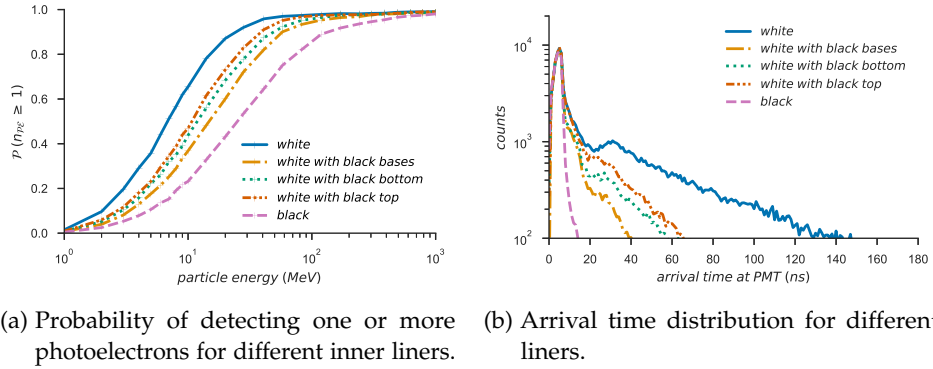


Figure 4.2: Figures from Kunwar et al [108].

As shown in this figure, reflective inner walls increase particle detection efficiency as they help redirect the Cherenkov light spreading from the particle passing through towards the photosensor. At the same time, we see a much wider spread in the arrival time distribution for an upper chamber with entirely white walls, reducing time resolution.

As seen from these plots, the reflectivity of inner liners is an important parameter for WCD performance that needs to be known for a proper characterization of the detector units of a ground particle gamma-ray observatory. At MPIK it is possible to measure the diffuse reflectivity of different materials using an integrating sphere.

#### 4.1.3.1 Integrating Spheres as Devices for Measuring Reflectivity

An integrating sphere is a device that spatially integrates radiation that is incident on it. It has a spherical cavity covered with a diffuse reflective coating, with entrance and exit ports. Through multiple reflections on its diffuse spherical surface, it provides a uniform radiance. Integrating spheres can be used to measure the flux from different illumination sources, as a large area source with uniform radiance that can be used for calibrating electronic imaging devices, and for measuring the transmittance and reflectance of different materials [110].

In an integrating sphere, a fraction of the radiant flux that is received by a region within the sphere, is the fractional surface area that the region covers within the sphere [110]. This fact can be used to measure the reflectivity of different materials. During the tests in MPIK, one port opening was used to provide an input flux, another port opening for measuring the resulting radiance, and a final larger port opening for placing the material of interest.

Figure 4.3 shows some of these different ports.  $A_i$  is the input port area,  $\Phi_i$  is the input flux and  $A_e$  is the area of an exit port, which can be used for measurements.

Assuming uniform reflected flux over a solid angle  $\pi$ , the radiance  $L$  (flux density per unit solid angle) of a diffuse surface is

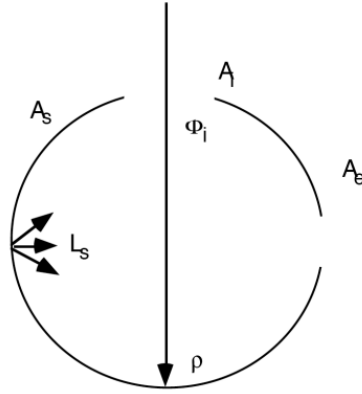


Figure 4.3: Input flux hitting the inside of an integrating sphere. Figure taken from [110].

$$L = \frac{\Phi_i \rho}{\pi A} \quad (4.1)$$

where  $\Phi_i$  is the input flux,  $\rho$  is reflectance and  $A$  is the total area illuminated. For an integrating sphere, the port openings cause losses in this total area, and at the same time, there are multiple surface reflections. The total amount of flux incident on the sphere surface is  $\Phi_{received} = \Phi_i \rho F_{sphere}$ , where  $F_{sphere}$  is the fraction of the flux received on the surface of the sphere:

$$F = \frac{A_s - A_i - A_e}{A_s}$$

$A_i$  is the input port area,  $A_e$  is the exit port area, which can be the output or measurement port area, and  $A_s$  is the total area of the inner sphere surface. Below, the common notation  $F = 1 - f$  is used for this term, where  $f$  is the port fraction. After one reflection, the flux incident on the sphere is  $\Phi_{received1} = \Phi_i \rho (1 - f)$ . After several reflections, expanding the equation for the total amount of flux incident on the sphere surface to a power series, the radiance of the sphere is obtained:

$$L_{sphere} = \frac{\Phi_i \rho (1 - f)}{\pi A (1 - (1 - \rho))} \quad (4.2)$$

The latter term is called "sphere multiplier",  $M$ , and it accounts for the increase in radiance due to multiple reflections.

When the input flux  $\Phi_i$  is not known, comparing the radiance measurements of reference materials with that of the sample of interest can give the reflectance of that sample. To achieve this, the radiance can be measured three times, where the 'material port' is covered by first the material of interest, then by a reference cap that has the same coating as the inner surface of the integrating sphere, and finally by a material with minimal reflectance (or left open, if the environment is dark). Equation 4.2 shows that for each measurement, the

reflectance terms and the port openings are absorbed in the sphere multiplier, hence the sphere multipliers can be compared to obtain measurements of reflectivity. The calculations detailed in Appendix B are performed, giving the equation to find the reflectivity of our sample being measured,  $\rho_x$ :

$$\rho_x = \rho_w \left[ \frac{1 - \frac{M_{black}/M_{ref}}{M_x/M_{ref}}}{1 - (M_{black}/M_{ref})} \right] \quad (4.3)$$

where  $\rho_w$  is the sphere wall reflectance, expressed with equation B.6.

In the following, the radiance for different materials is measured and equation 4.3 is used to obtain values for reflectivity.

#### 4.1.3.2 MPIK Lab Setup

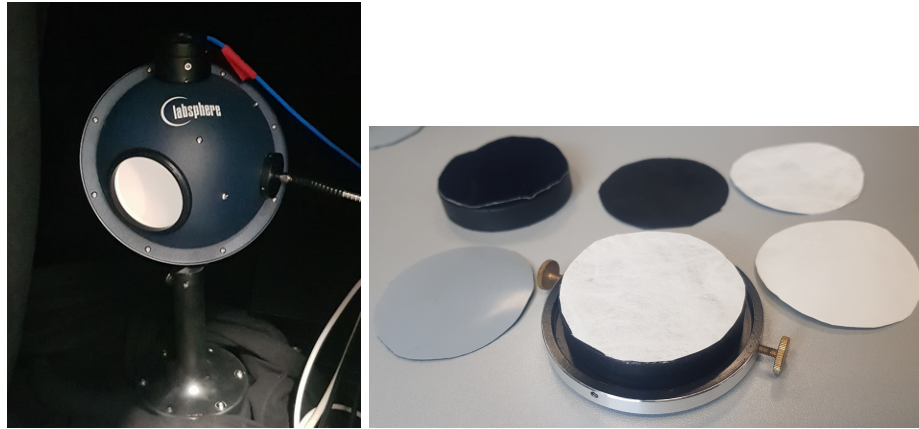


Figure 4.4: *Left:* The integrating sphere used in the measurements. *Right:* The measurement cap covered with a sample of Tyvek. Samples of other materials are seen around it.

During the measurements, an integrating sphere from the company Labsphere was used, pictured on the left image of Figure 4.4. Integrating spheres measure the integral reflectivity, over all angles. The sphere has three ports, the input port  $f_i$ , the measurement port  $f_m$  and the sample material port  $f_x$ . As seen in the picture, the input port is facing a portless side of the sphere wall. The material port is on the left of the input port, hence there is no direct light incident on the samples being tested before any reflections. A baffle between the input port and the sample material port, not visible in the picture, ensures there are no direct hits from the input port to the sample material port. The relevant dimensions of the sphere elements are shown in Table 4.1.

The sample materials are glued on circular caps that can be screwed to a removable cap that is attached to the integrating sphere (6.4 cm). The right image of Figure 4.4 shows the removable measurement cap, along with sample materials such as different types of tyvek and bladder liners.

For input, the setup uses a Xenon arc lamp (Muller Elektronik, 75 W) with a monochromator (Digicrom CM112) as a light source. At the measurement

Element	Diameter (cm)
Full Sphere	13.5
Sample Port	6.4
Input Port	2.5
Measurement Port	2.5

Table 4.1: The diameters of the three port openings of the integrating sphere.

port,  $f_m$ , there is a reference diode (Newport 818-UV) that is read out by a powermeter (Newport 2835). The light from the monochromator strikes the inner wall of the sphere and undergoes multiple reflections. The remotely controllable monochromator allows tests for reflectivity within the range of interest, around 400 nm. For each measurement, a predetermined range of wavelengths, usually from 200 nm to 700 nm, is run through.

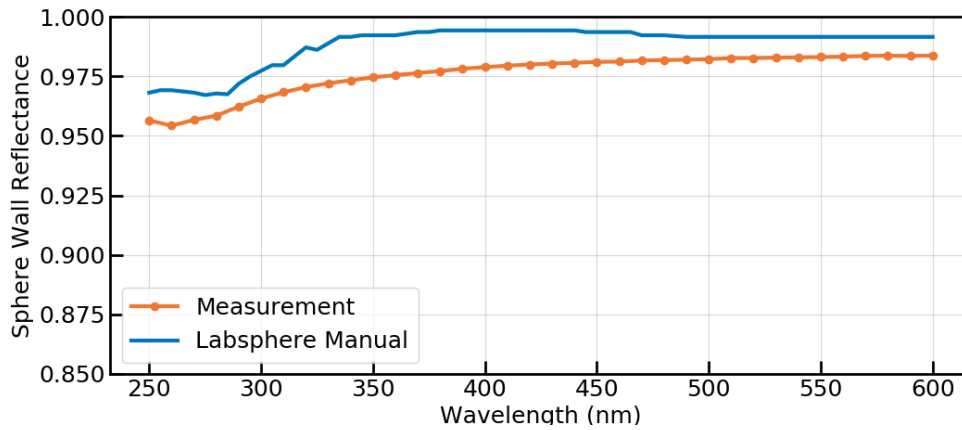


Figure 4.5: The sphere wall reflectance,  $\rho_w$ , as measured, compared with the nominal values from the Labsphere manual [110]

The inner sphere wall is coated with spectralon, which is a thermoplastic resin that gives the highest diffuse reflectance of any known material over UV and visible wavelengths [111]. The sphere wall reflectance  $\rho_w$  can be obtained using equation B.6 and making measurements of radiance using the reference cap (corresponding to  $M_{ref}$ ) and using a black reference ( $M_{black}$ ). A measurement done with our setup from 250 nm to 600 nm is shown in Figure 4.5, compared with the nominal values from the Labsphere manual [110]. We see a difference of around 1 – 2% between the measured and nominal values. Nevertheless, the measured reflectivity of spectralon for our integrating sphere is above 95% for the range 250 – 600 nm.

#### 4.1.3.3 Measurements and Results

Different bladder liner candidates were measured along with other kinds of materials for testing. For each of the tests for a particular material, one

measurement with a completely black material ( $f_{bl}$ ), one measurement with the material in question ( $f_x, \rho_x$ ), and a final measurement where the port is closed off with the reference cap was taken. Afterwards, using equation 4.3 gives the measurement of reflectivity for the material.

**TYVEK MEASUREMENTS** Tyvek, a trademark of the company DuPont, is a family of sheet products made of high-density polyethylene (HDPE) [60]. Its versatility, low price (200 to 450 Euros for a roll that is 1.5 m in width and 25 m in length, depending on the kind), durability in water and high diffuse reflectance make Tyvek an ideal candidate for the inner reflective liners of our WCDs. Different types of Tyvek are being used in the Auger and LHAASO experiments already. LHAASO uses Tyvek1082D [119], while Auger uses Tyvek 1025B.

Tyvek is made by spinning continuous HDPE fibers into a sheet by bonding them with heat and pressure. Depending on this bonding, it may be paper-like (hard structure) or textile-like (soft structure). Moreover, Tyvek can have different surface treatments. Some Tyvek types are antistatic and corona treated, designated with the letter D or R. Those types designated with the letter B have no such surface treatment, while the D types underwent surface treatment. Antistatic treatment reduces the buildup of static, while corona treatment improves adhesion to surfaces [60].

Figure 4.6 shows the reflectivity measurements for all the Tyvek samples that were received from DuPont. On the left are the Tyvek types that underwent surface treatment. We see that 1082D has the highest reflectivity around the wavelengths we are interested in. This material was used for the inner lining of the small muon taggers and the Tyvek-only lower chamber custom produced in MPIK (Section 4.2.4.2). To make several more detector units, an external company is producing custom-made liners for SWGO, and this company has chosen Tyvek 1025D for the lamination of Tyvek into the inner surface of the lower layer of bladders. This decision is based on availability, costs, and surface properties.

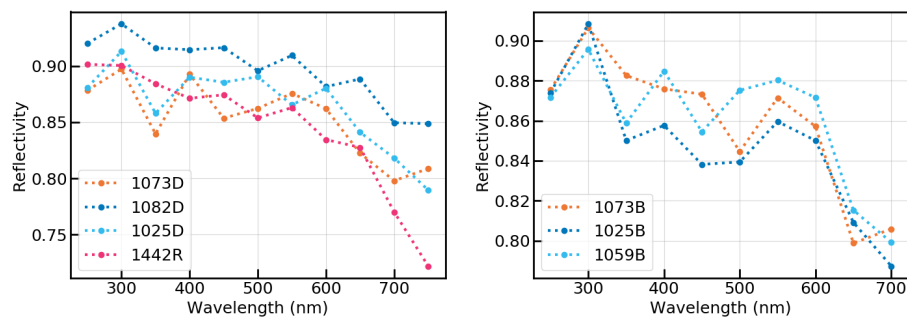


Figure 4.6: Measurements for the tyvek samples in MPIK. While 1082D stands out as the type with the greatest reflectivity, all Tyvek types show a reflectivity above 80% in the wavelengths of interest.

**BLADDER LINERS** Knowing the reflectivity of any liner that is at the inner surface of the detector units is important, as this parameter influences the timing resolution and signal efficiency, shown in Figure 4.2.

A sample of the HAWC bladder liners, a multi-layer liner made of flexible polyethylene [9], was measured. Furthermore, the reflectivity of the GeoFlex material that the outer bladder of our double-layered WCD prototype is made from was measured. This material is produced by the Canadian company Layfield [113] and was used by Aquamate [27] to make single-layer bladders for our prototyping efforts. Figure 4.8, left plot, shows that the white side of the HAWC bladder has a high reflectivity of around 75%, while the black side of the HAWC material and the GeoFlex material is around 10% only.

The external company working on our custom liner production has sent us initial samples for our prototype detectors. The samples we received are a liner with a white and black side, and another liner with a white and a Tyvek-laminated side. Using the setup in MPIK, the reflectivities of the white side, black side and the Tyvek-laminated sides of these samples were measured.

A separate measurement of this custom liner was simultaneously carried out by the National Institute of Astrophysics, Optics and Electronics [INAOE], in Mexico, initiated by Michael Schneider. The measurements were done using a Gretag Macbeth Color Eye 7000A Spectrocolorimeter, at five random locations. Figure 4.7 shows their results.

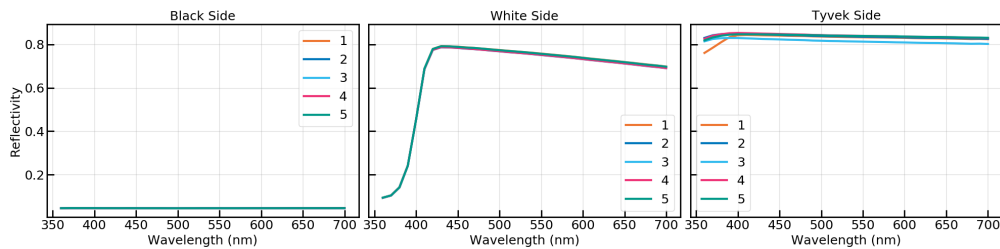


Figure 4.7: The reflectivity measurements of a SWGO custom film sample, carried out by the National Institute of Astrophysics, Optics and Electronics [INAOE], in Mexico, and initiated by Michael Schneider.

Figure 4.8 shows a comparison of the averaged INAOE measurements with the measurements done in our local setup. We see that the Tyvek-laminated film has a reflectivity above 80% in our range of interest, while the black side of the material has a reflectivity lower than 10%. Comparing the MPIK measurements with INAOE, we see a discrepancy of only about 2%, reminiscent of the discrepancy from Figure 4.5.

**OTHER MATERIALS** The reflectivity setup was also used to measure the reflectivity of other materials that are not planned to be used by SWGO. VM2000 is a multilayer specular reflector foil produced by the company 3M. It was used for example in the GERDA experiment for neutrinoless double- $\beta$  decay [12]. Along with VM2000, measurements using regular A4 printing paper and household aluminum foil were made. Comparing in particular the measurements for VM2000 with an independent measurement from Janecek [95] shows agreement,

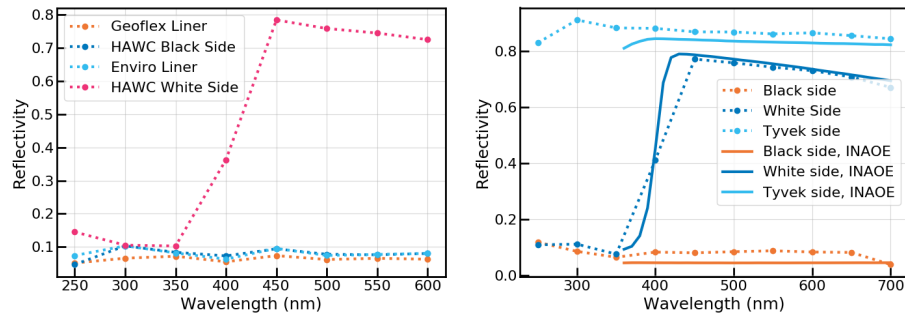


Figure 4.8: *Left*: Measurements for the HAWC liner and the liner of our first prototype bladder. *Right*: Measurements for our first custom-made SWGO liner. Tyvek is laminated to the black side of this liner. Measurements from INAOE are shown for comparison.

further verifying the reflectivity setup and measurements. This measurement was done by Martin Janecek under Lawrence Berkeley National Lab (LBNL), Berkeley, CA (United States). This independent measurement includes Tyvek and aluminum foil as well, where we do not see such a good agreement with the aluminum foil. This could be due to different types of foils being used in the measurements. As for Tyvek, although we do not know which kind they used, we can see agreement with the MPIK measurements from Figure 4.6.

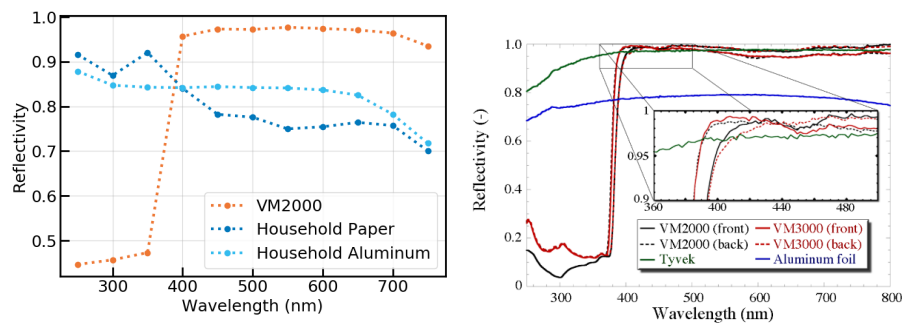


Figure 4.9: *Left*: Measured diffuse reflectivity spectrum for VM2000, A4 printing paper and household aluminum. *Right*: Figure taken from [95], showing reflectivity measurements.

**MEASUREMENTS WITH HALF-COVERED PORT** As a further test of the MPIK setup, in these measurements, half of the port was covered with Tyvek 1082D material and the other half with the 'black' material, as shown on the right in Figure 4.10. The measurement port was rotated so that the Tyvek covered half is first at the top, then left, then bottom, and finally on the right. The plot in Figure 4.10 shows the measurement results. We see that the four different directions are almost identical, verifying that there is no preferred direction, as expected. Moreover, we see that the half Tyvek covered measurements have reflectivity values about half of the full Tyvek measurement (Figure 4.6), verifying that the MPIK setup works as expected. The measurements are in line with the  $\sim 2\%$  uncertainty observed from Figure 4.5 above 300 nm. Below this

wavelength, the discrepancy between the measurements appears to increase, up to  $\sim 10\%$ .

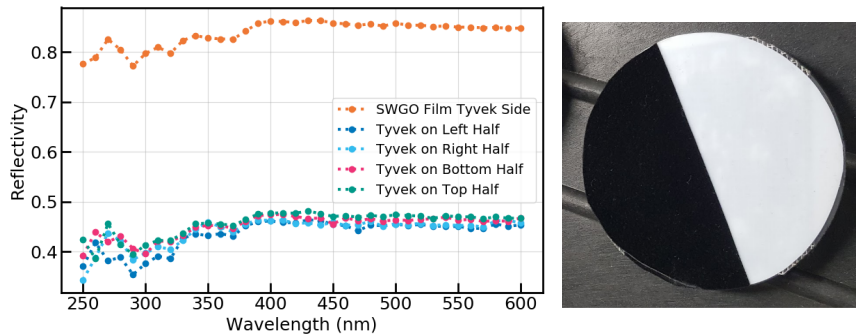


Figure 4.10: *Left*: Reflectivity of half tyvek-covered material sample. *Right*: The half tyvek-covered measurement cap. The measurements were done by rotating this cap by  $90^\circ$  each time.

#### 4.1.3.4 Summary of Reflectivity Measurements

Using a monochromator and an integrating sphere, the reflectivity of various materials across different wavelengths, a factor influencing the performance of our WCDs, was measured. The measurements indicate that most Tyvek types exhibit reflectivity above 80% in the relevant wavelength range from  $\sim 300$  nm to  $\sim 650$  nm. Specifically, Tyvek 1082D, used for in initial prototypes (Section 4.2.4.2), demonstrated the highest reflectivity among samples tested. However, due to its availability and adhesive properties, Tyvek 1025B is being used for the SWGO custom liner in the SWGO bladder production. The other liners have a reflectivity below 10%, suggesting that they would support no more than one or two reflections of incoming Cherenkov light. These reflectivity measurements are used as input parameters for simulations of the test setup of the WCD prototypes (Section 4.2.6).

Furthermore, the first custom SWGO liner we received was measured independently in MPIK and in INAOE, yielding nearly identical results. As expected, the black side of the material exhibited much lower reflectivity ( $\sim 10\%$ ) compared to the white side. The side laminated with Tyvek has the best reflectivity at the wavelengths of interest.

#### 4.1.4 Water Quality Monitoring

Cherenkov light emitted by charged particles within the detector units travels through purified water to reach the photomultiplier tubes (PMTs). Water attenuation length describes the loss of light over a given distance; a higher attenuation length allows Cherenkov light to travel farther and be detected more effectively. Maintaining high water quality with a long attenuation length is essential for WCD arrays, as low attenuation length reduces the light intensity reaching the PMTs. Moreover, contamination in water can also damage detector components over time. Simulations in Section 4.2.6 confirm that lower

attenuation length results in signal reduction. In this section we examine the impact of different materials on attenuation length.

#### 4.1.4.1 Attenuation Length

Attenuation length is related to absorption length and scattering length as

$$\frac{1}{\lambda_{att}} = \frac{1}{\lambda_{abs}} + \frac{1}{\lambda_{scat}} \quad (4.4)$$

Absorption length is the distance after which the probability of a photon not being absorbed is  $1/e$  and scattering length is the change in a photon's direction due to random motion of molecules, dispersing the photons and reducing the intensity of light over a distance. Scattering coefficient of pure water is very low [32, 59]. In purified water, within our wavelengths of interest, the scattering length has a negligible effect on attenuation length, hence the focus will be on absorption length for the rest of this study.

Attenuation length, absorption length and scattering length are wavelength dependent. Measuring these at different wavelengths require dedicated setups that we do not possess in MPIK. Instead, the measurements give only the attenuation coefficient of the water sample being measured only at one wavelength, namely 410 nm. Water absorption length is particularly important if reflective walls are relied on for maximum efficiency.

The two existing gamma-ray WCD arrays, HAWC and LHAASO, have developed different methods to monitor the water quality in their WCDs. The HAWC collaboration performs tests both on-site and in a reference laboratory for the water inside their WCDs, also incorporating a commercial device (a C-star device, similar to what is used for SWGO at MPIK currently) into their measurements [9]. The studies performed by the HAWC collaboration show attenuation lengths varying between 5 m and 16 m for 405 nm [3].

The LHAASO collaboration developed a custom water attenuation measurement device in order to measure the attenuation length of the water for their MD, using an 8 m long tank that water is filled into, different light sources and two PMTs [115, 170]. They reported a mean water attenuation length of  $\sim 70$  m for the ultra-pure water of the MDs. The collaboration also developed methods based on principles of photon propagation to measure water absorption length, liner reflectivity by changing the height of water and reflective liner area, which are valid in the case of tens of reflections of the Cherenkov light [119]. The water housed inside the MD array has a requirement to have a water transparency of above 30 m at 400 nm, and is housed in sealed liners from Figure 4.1, expected to stay ultra-pure for at least 10 years [123]. For the WCDA, the LHAASO collaboration has a system monitoring and recirculating the water in the three pools continuously. The water attenuation length is measured with another custom device that compares the light intensity reduction ratio at different paths [116]. Their requirement based on experiments with their prototype WCDA is an absorption length longer than 15 m for around 400 nm [116, 123].

## 4.1.4.2 Water Absorption Length Spectra

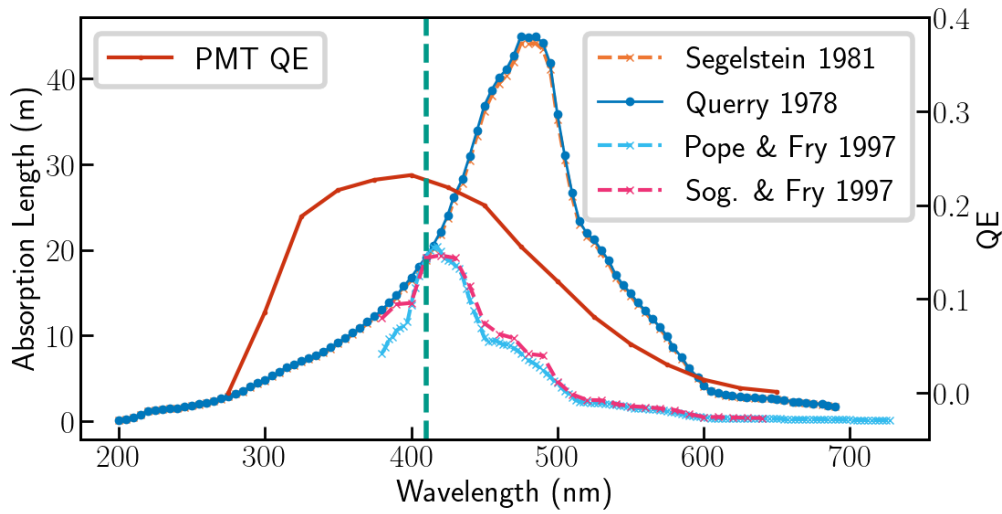


Figure 4.11: Different absorption length spectra possibilities for a water sample measured to have  $\lambda_{abs} = 18$  m at 410 nm. The absorption spectra measured are by Segelstein in 1981 [153], Query, Cary, and Waring in 1978 [147], Pope and Fry in 1997 [143] and Sogandares and Fry in 1997 [157]. The Quantum Efficiency of PMT R5912 used in the simulations with HAWCSim is plotted in red.

Figure 4.11 shows different measurements of water absorption length done in a number of external different studies from different years. The wavelength that can be measured with the MPIK device is shown with the green line, and all measurements are adjusted so that they pass through a measurement of  $\lambda = 18$  m at that wavelength (This is the default absorption length used in the HAWCSim simulations). The plot also shows the Quantum Efficiency (QE) of the PMT we commonly use in our WCDs, Hamamatsu R5912 8-inch. It is evident that depending on which spectrum holds true, the signal efficiency is different. For the older measurements of Segelstein 1981 [153], Query 1978 [147], maximum absorption length is reached around 490 nm, while for the newer measurements it is reached at lower wavelengths around 420 nm. David J. Segelstein's master thesis is on the spectrum the complex index of refraction of water as a function of wave number, spanning a wavelength range from 0.1 nm to 10 m. Hence, the Segelstein 1981 spectrum is a compilation of different measurements from literature and theoretical considerations. It also incorporated the measurements by Query et al [147] experimental data that was an attenuation measurement using a split-pulse laser method. Since this is the default used in the HAWCSim simulation software [13] and as it is such a comprehensive study, this spectrum has been used in parts of this thesis as simulation input, in particular for Section 3.3. The more recent studies of Pope & Fry 1997 [143] and Sogandares & Fry 1997 [157], used two independent approaches, namely a photothermal probe beam deflection technique and an integrating cavity technique, which look at different physical quantities. They have used ultra pure water and claim to be providing the most reliable data for

the absorption coefficient of pure water within the spectral range of 380 nm to 700 nm.

For HAWCSim simulations concerning comparison with measured data (Section 4.2.6), therefore, the more recent spectrum from 1997 was used, while the possibility of the 1981 measurements was also considered, informed by the measurements at 410 nm made in our own setup. It should be remembered that the attenuation length of water changes significantly within our wavelengths of interest, even though the measurements were done only for one wavelength.

#### 4.1.4.3 Water Quality Measurement Setup



Figure 4.12: The setup to measure water transmission. The C-star transmissometer is on the left, connected to a power source and a laptop, and on the right are four of the buckets that house materials being tested.

Water quality measurements were carried out by monitoring the evolution of transmissivity and conductivity of highly purified water placed into several barrels that each house a different material sample. The setup, shown in Figure 4.12, includes a transmissometer, a conductivity meter, a laptop to view the outputs, squirt bottles for cleaning and barrels that include the monitored materials immersed in purified water.

The transmissometer that was used is from Seabird Scientific, C-star, CST-2092PV and it uses laser light with wavelength 410 nm, and has a path length of 25 cm [152], similar to the instrument used for onsite water quality tests of HAWC. The device outputs a beam attenuation coefficient  $C$  that is the reciprocal of attenuation length  $\lambda_{att}$ . It first calculates transmittance, from measured corrected signal counts, factory supplied dark offset and factory supplied corrected signal counts for clean water. Then, the beam attenuation coefficient is related to transmittance as

$$\lambda_{att} = \frac{-x}{\ln(T)} = \frac{1}{C} \quad (4.5)$$

The conductivity meter is a device that measures the temperature of the water and its conductivity. It is a commercial device from Greisinger, model G1420 [72]. It has a conductivity range from 0.00 to 20.00  $\mu S$  and a measurement error of

$\pm 1\%$  of measured value. It is operated by simply immersing the sensitive probe into the liquid.

The majority of the barrels are as seen in Figure 4.12, white with a water volume of 30 L each. The barrels are food-safe commercial containers made of polyethylene. The barrels used for PMT testing in water are light tight, 60 L and 30 L barrels made of HDPE. In order to carry out readings, the caps on top of the barrel were taken off and the transmissometer was immersed inside<sup>3</sup>. Afterwards, the sensitive probe of the conductivity meter was immersed into the water inside the barrels.

There are two different types of purified water used in these tests, referred to as reverse osmosis water and filtered water. The reverse osmosis water is produced in small quantities at our institute. This is the water that is inside the muon tagger barrels which are used for the prototyping tests for the lake design in the lake simulation tank of MPIK (see Section 4.2.5.2) [70]. The second type is the filtered water that is produced as described in Section 4.2.2.3. This water is produced through a decalcifier unit and two particle filters. An analysis of these water types was performed by an external company and the main results are in Table 4.2.

Water type	pH	Hardness (°dH)
Tap water	7.47	19.4
Filtered water	7.71	0.4
Reverse osmosis water	5.74	0.2

Table 4.2: The results of an analysis of the two water types used in our water quality measurements, compared with regular tap water from MPIK. The analysis was performed externally.

#### 4.1.5 Summary of Water Quality Measurements

The monitoring of the behavior of eight different kinds of materials inside purified water was started on May 18th 2021. Out of the ten initial barrels in the setup, two functioned as control, one filled with reverse osmosis water and the other filled with filtered water. In the following months, additional barrels were added to the setup to measure water quality for different kinds of materials. All materials that would be expected to come in contact with the water inside the WCD units were monitored, including bladder materials, screws, cables and supports for photosensors. Bladder materials were immersed in filtered water and reverse osmosis water, while other materials were immersed in reverse osmosis water only.

<sup>3</sup> Initially, minimizing contact with water inside the barrels was preferred, hence the preference for the containers with taps. However, trials with the transmissometer using a flow tube were not successful, since a continuous flow is needed and the amount of water sample was not sufficient.

## 4.1.5.1 Bladder Materials

These materials include those used for prototype bladders, the HAWC bladder material, and other candidate materials. Each material was tested using samples of approximately 20 cm<sup>2</sup>.

Figure 4.13 shows the behavior of the PVC used in our very first bladders in purified water. This PVC, supplied by Mayer Luftwerbung [129], caused a significant decrease in attenuation length over time in both types of purified water, reducing it to less than 20 cm. Even after refilling the barrels, water quality continued to degrade rapidly, making this PVC unsuitable for future prototypes.

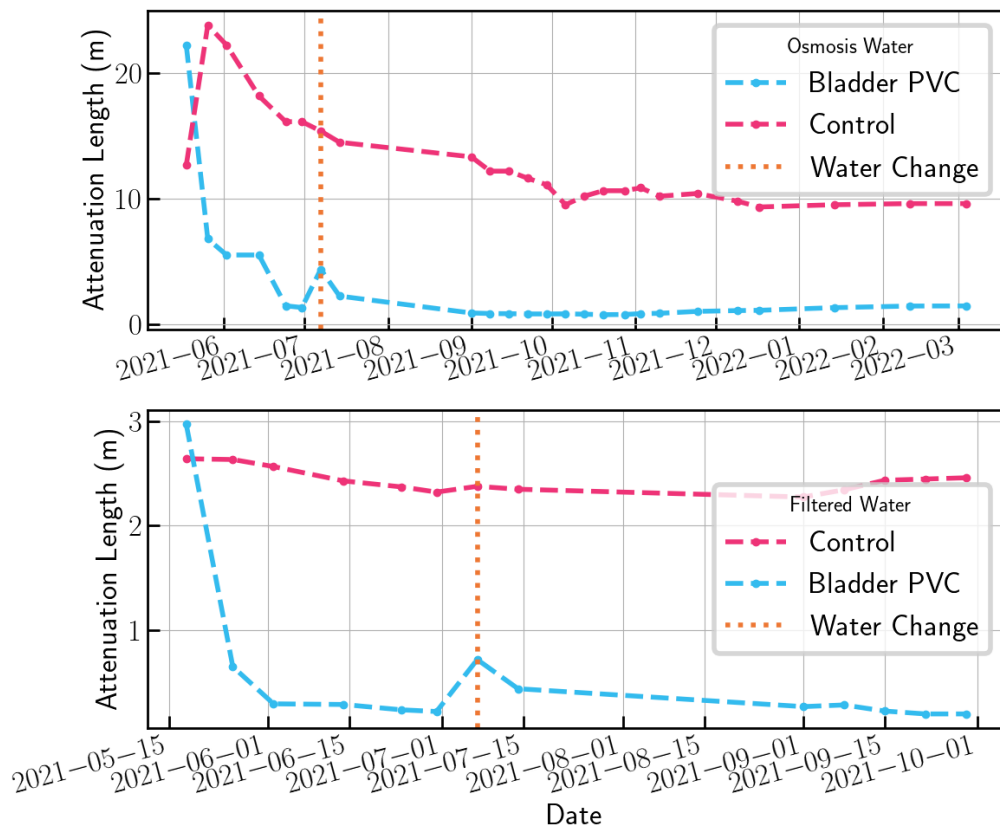


Figure 4.13: Water quality measurements for the PVC bladder material. *Top*: Measurements using reverse osmosis water. *Bottom*: Measurements using filtered water.

The HAWC bladder material, consisting of several LDPE layers as described in Section 3.1, was later tested with filtered and reverse osmosis water. Figure 4.14 shows its behavior over time. While there is a slight degradation in absorption length, most of it occurs within the first month. As previously demonstrated by the HAWC collaboration [3], this material performs well in both water types, achieving an absorption length of about 5.5 m compared to 7.6 m for the control bladder in reverse osmosis water.

Two additional bladder materials were also monitored: Enviro Liner, and GeoFlex, flexible geomembrane liners produced by Layfield [113], which were

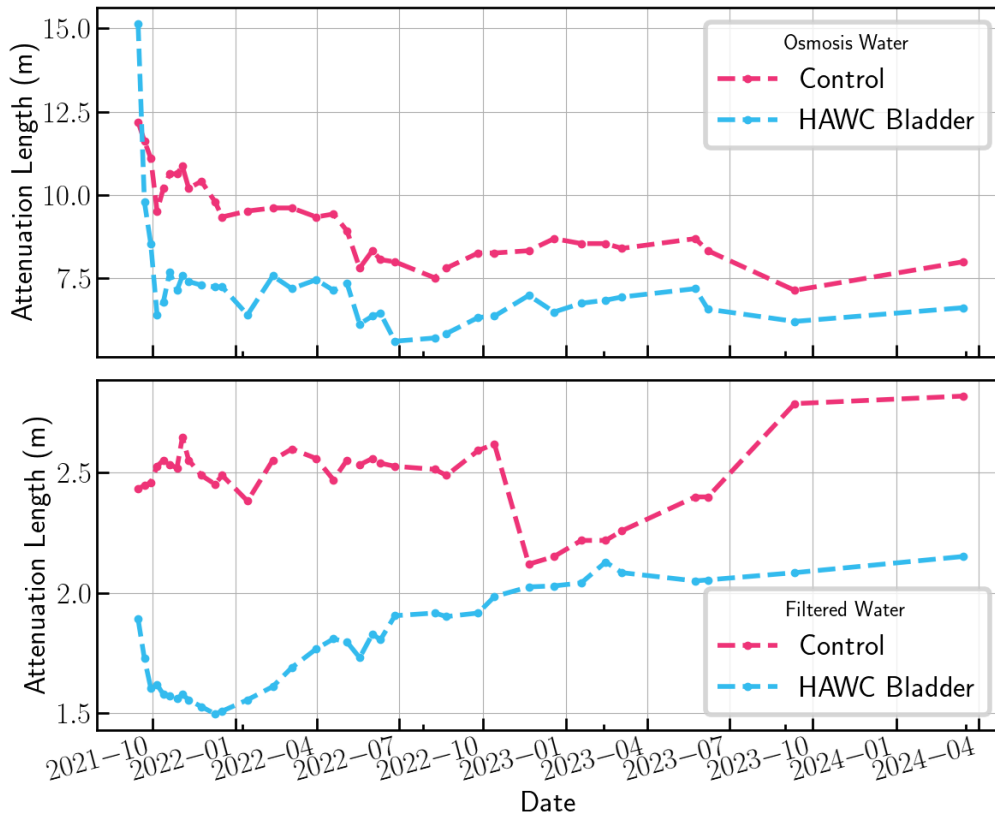


Figure 4.14: Water quality measurements for the HAWC bladder material. *Top*: Measurements using reverse osmosis water. *Bottom*: Measurements using filtered water.

used by the company Aquamate [27] to manufacture prototype bladders for SWGO (More on the bladders in Section 4.2). Their behavior is shown in Figure 4.15. Aquamate GeoFlex material is shown to behave well in water, with an attenuation length of  $\sim 9$  m for the sample with black and white sides, and of  $\sim 11$  m for the sample that is all black.

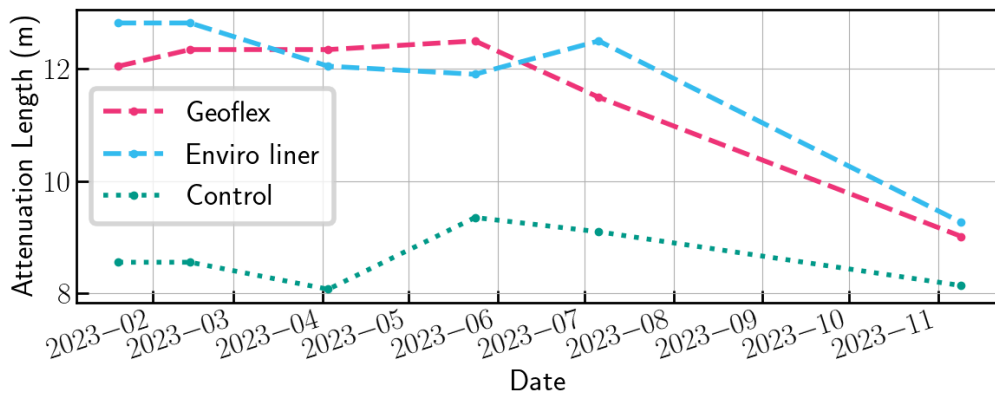


Figure 4.15: Water quality measurements for the GeoFlex and Enviro liners that were produced by the Layfield company. The outer layer of our double-layered WCD prototype is made of GeoFlex (See Section 4.2).

#### 4.1.5.2 Reflective Liners

As explained before, the SWGO unit designs use an all-white muon chamber that is covered with reflective lining, namely, Tyvek. In addition, the prototype tests in MPIK also included small barrels covered with reflective liners that function as muon taggers for coincidence measurements (Section 4.2.5.2). Different samples of Tyvek were monitored over time, as seen in Figure 4.16. These are the same samples whose reflectivity was measured in Section 4.1.3.3. In general we see that the D types degrade water more than the B types, this may be due to the additional surface treatments the D type Tyveks go through in order to make them more adhesive. Tyvek 1082D is shown in a separate plot as it was the first sample we obtained for lining the small muon taggers.

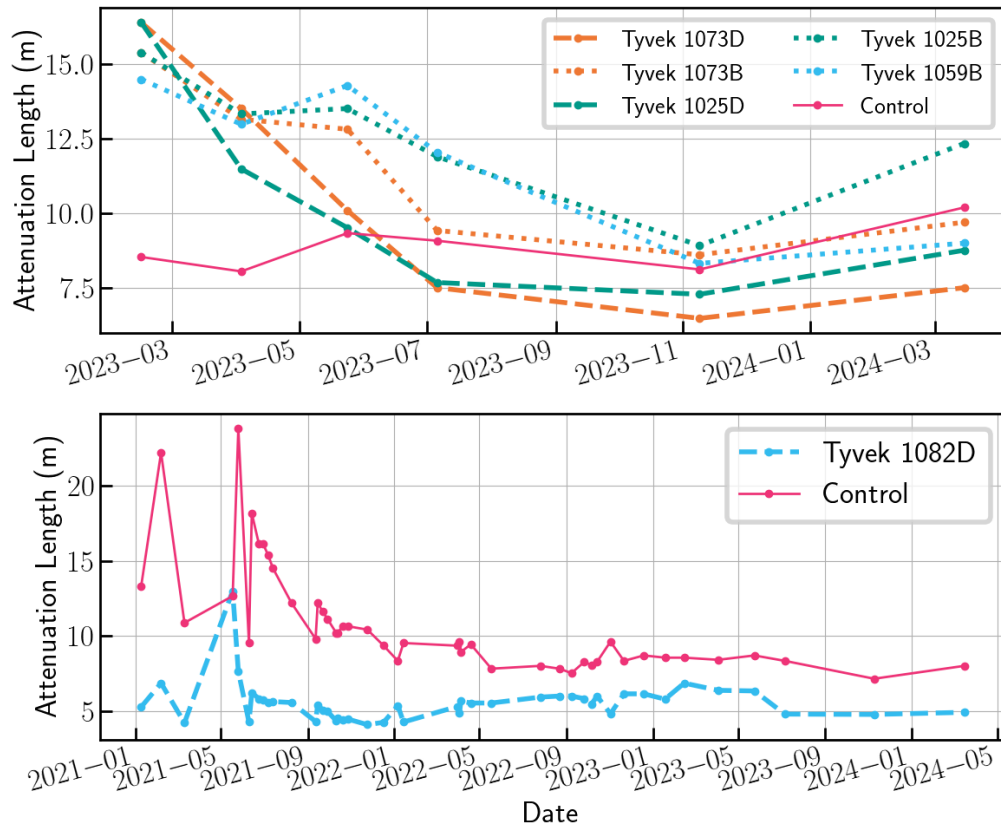


Figure 4.16: *Top*: Water quality measurements of Tyvek samples. *Bottom*: Water quality measurements for Tyvek 1082D, started earlier than the other samples. This is the Tyvek used for the lower chamber for the double-layered WCD prototype (see Section 4.2).

#### 4.1.5.3 Other Materials

Several other materials that would come in contact with purified water are also monitored for their behavior in reverse osmosis water. All of them maintain an attenuation coefficient of less than 0.3, with a drift over time that is comparable to the control barrel. Figure 4.17 shows a monitoring of the screws that would

be used for the PMT supports inside the bladders. Both kinds of materials, A2 (also called 304 or 18/8) and A4 (also called 316 or 18/10) are stainless steel with almost identical chemical compositions [106]. The difference is that A4 has slightly more nickel (10% as opposed to A2's 8%) and has molybdenum. This makes A4 stainless steel more resistant to corrosion, oxidation and is more durable. A4 stainless steel is known to be preferred in marine or chemical environments [163]. Our measurements, done by using six screws of each type, do not show a significant difference between the behavior of the two.

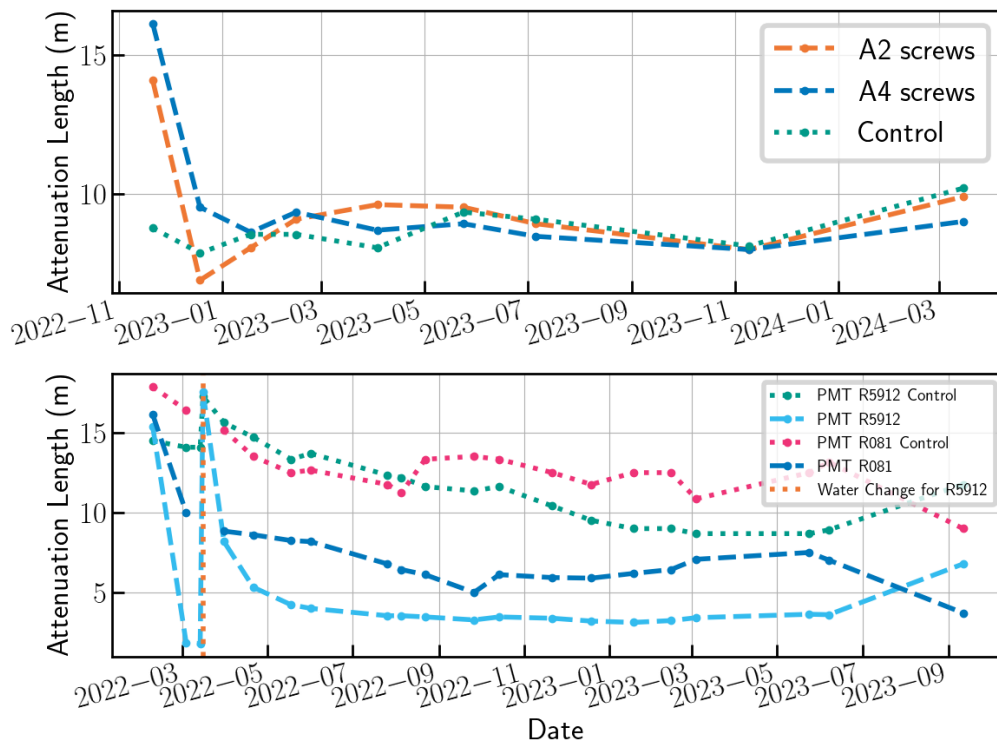


Figure 4.17: *Top*: Water quality measurements for the A4 and A2 stainless steel screws. *Bottom*: Water quality measurements for two different PMTs along with their control barrels.

Moreover, cables, shrinkable tubes, plugs and other components were monitored throughout the years. In addition, four larger and darker barrels are used to monitor the behaviour of the supporting materials for two different PMTs, namely 8-inch R5912 (custom-potted) and a 10-inch R7081 MOD-ASSY PMT recovered from the Double Chooz experiment [33], along with two control barrels. Although the barrel with the Double Chooz PMT seemed to behave better than the self-potted 8-inch R5912 PMT, the last measurement defies this trend.

#### 4.1.5.4 Conductivity Measurements

Conductivity of materials was monitored as well, as this is also a general measure of water quality. When there are changes in salinity and temperature, conductivity changes. Conductivity is caused by impurities in water. When

inorganic chemicals and salts dissolve in water they leave ions which increase conductivity. We were not able to draw strong conclusions from the conductivity monitoring, included in Appendix C.

#### 4.1.6 *Conclusion of Water Quality Tests*

While the monitoring of water quality with the transmissometer served as a guideline for prototyping, this setup is not suitable for future mass use. The results from these measurements are used for comparing different materials over one another, however, measurements done for multiple wavelengths would be desirable.

Overall, the tests show that LDPE materials behave well in water, which is already demonstrated by HAWC, Auger and LHAASO experiments. Moreover, Tyvek is also seen to behave well, while materials such as ropes or certain PVC types contaminate water.

#### 4.1.7 *Future Material Tests*

Regardless of the detector technology option, the WCDs will have bladders holding the water volume that need to fulfill requirements outlined in Section 4.1.1. For this reason, although the material tests outlined here provide guidance, further tests on bladder materials with dedicated setups will need to be pursued in the future:

- **UV resistance tests** may be done by exposing portions of material to UV light. In the lake option this was a much bigger concern as the bladders would be under more direct UV light exposure, however also for the tank options a UV resistance test could provide information on material durability.
- **Stretching/ aging tests** would help evaluate the long-term stability of bladder materials. These may be pursued using a device that continuously bends and stretches the bladder material, most likely to be done by an external company.
- **Water quality monitoring** will need to be pursued using dedicated setups that can measure absorption length in more than one wavelength if possible, improving on the current setup. The attenuation length of water influences the signal as shown in the studies of Section 4.2.6 and the studies by the LHAASO collaboration (see [119, 170] for example).

## 4.2 PROTOTYPING TESTS WITH A LAKE SIMULATION TANK

As a new design option for WCDs, the lake design should be evaluated in detail by the building and testing of prototypes. Starting with the year 2020, prototyping activities for the lake concept were carried out using a lake simulation tank and a full electronics chain that is a candidate electronics option for

SWGO. These activities started with the testing of small scale bladders made of PVC and concluded with the making and testing of the first double-layered prototype detector unit for SWGO.

#### 4.2.1 Small Bladder Tests

The prototyping of bladders began with attempts to manufacture bladders within the institute. In the MPIK workshop, a machine with a plastic wheel that is turn-able via a motor was designed and connected to a hot air welding apparatus, shown in Figure 4.18. A small transparent bladder was made, however this technique proved to be cumbersome and risky. Parts of the PVC material got burnt or stretched, making the bladders very uneven. It was concluded that hot air welding may be a plausible option in general, however it would require bigger and more specialized machines for manufacture.



Figure 4.18: *Left:* The custom hot air welding machine made by MPIK workshop and the first bladder made using it. *Right:* Commercially ordered array of three 60 cm high PVC bladders, attached with floaters.

After these attempts of bladder production by hot air welding, small scale PVC bladders were ordered from a commercial company, called Mayer Luftwerbung [128]. These bladders were roughly 1 : 10 scale, transparent and had a height of 60 cm. An array of three bladders is pictured on Figure 4.18. These were filled with colored water for easier examination, and floaters that are plastic pipes filled with air were connected to them.

Although the bladders were made up of simple PVC and were not to scale, they served to plan the eventual tests with realistic scale bladders. Using an underwater camera, the connections between the bladders were studied, the shape stability of the bladders under impact was examined and weights were added to the bladders. Different filling options were explored. A bladder that is 100% filled results in large stress on the bladder material in case of bladder deformations by waves or impact. A filling of about 90% of the maximal bladder volume was found to be a good compromise. At this fill level, after deformation from impacts or waves, the bladder restores its original shape.

#### 4.2.2 The Test Setup

At the Max-Planck-Institut für Kernphysik (MPIK) a full end-to-end measurement chain exists to make tests. This measurement chain was used to test the bigger scale bladders, making additions after every test.

##### 4.2.2.1 Lake Simulation Tank

A lake simulation tank was prepared at MPIK during the year 2020 to allow the efficient and controlled testing of lake-deployed bladders (Figure 4.19). The lake simulation tank is 7 m in height and 10 m in diameter. Detector signals are routed to a small cabin next to the tank that is equipped with a computer and the FlashCam Data Acquisition (DAQ) system developed at MPIK [172]. In Figure 4.19, this is the cabin in the middle.



Figure 4.19: The test facility at MPIK: A lake simulation tank that is 10m in diameter, 7 m in height, shown with two bladders deployed. Two PhD students are shown for scale.

##### 4.2.2.2 The Data Acquisition System

Throughout the studies, PMT signals are recorded with the FlashCam Data Acquisition (DAQ) system, sampling signals every 4 ns. The FlashCam camera system is a camera designed for the upcoming Cherenkov Telescope Array Observatory (CTAO) and it is the first such camera that has a fully digital signal processing. The FDAQ used in this system digitizes up to 24 channels with 250 MS/s rate and in 12-bit resolution [172]. The readout software used to control the DAQ accepts a number of parameters that allow us to take and adjust the data. Among these is an adjustable baseline (the zero signal level), adjustable readout window size, ability to record data from up to 24 channels into binary files, adjustable event size and time and importantly,

adjustable trigger threshold for every channel. An additional capability is to view the recorded pulses that are higher than our desired threshold in real time. Using this software, the signals coming from the PMTs inside the prototype bladders and other components can be recorded by adjusting a trigger threshold. Moreover, the software enables coincidence triggering via a multiplicity command along with a trigger window, which has enabled the coincidence measurements for the prototype WCDs. The data is recorded in units of least significant bit (LSB), which are used as units for data throughout this thesis prior to calibration. This data can be converted into photoelectrons by recording single photoelectron (SPE) peaks and comparing how many LSB corresponds to a peak, for a given voltage value. Throughout the measurements, the baseline value was typically adjusted to 400 or 200 LSB. The SPE peaks were obtained by adjusting the trigger threshold to a level just above the electronics noise, changing from 4 LSB to 5 LSB.

#### 4.2.2.3 *Water Filtration System*

The bladders that are tested are filled with filtered water. A water filtration system was rented and installed inside a cabin next to the lake simulation tank, shown in Figure 4.19 right next to the lake simulation tank. The decalcifier unit is a duplex water softening unit with co-current regeneration of the ion-exchange resin. It filters below 10 dH continuously, with a speed of up to 2 m<sup>3</sup>/h. There are two particle filters in the unit. One of them filters 0.5 μm as an initial step, which works as a coarse filter, and the other one is 0.1 μm to filter most yeast and bacteria cells. This is the 'filtered water' that was used in the water quality tests of Section 4.1.4.

#### 4.2.3 *Muon Taggers*

The lake simulation tank is equipped with two muon taggers, which consist of an 8-inch Hamamatsu R5912 PMT inside a commercial black barrel of 41 cm diameter and 75 cm length, lined with reflective material (Tyvek 1082D). One muon tagger is located at the bottom of the lake simulation tank and is filled with clean water (reverse osmosis water), while the other is positioned above the bladder under test, filled with two layers of scintillators (each one 4 cm thick), to tag particles crossing the bladder (see Figure 4.20).

The muon taggers were tested for light tightness by placing them into a dark room in the MPIK experimental hall and taking dark count rates inside this room and outside in day light after. The dark count rates inside and outside were comparable, around  $\approx 1.5$  kHz, showing that the barrel used is light tight. Moreover, as shown in Figure 4.20a, coincidence tests were made by inserting the muon taggers between two scintillators, where peak amplitude distributions showed a signal peaking at around 130 p.e..



(a) The muon taggers were tested by being inserted in between two scintillators. (b) The muon tagger later put at the top of the lake simulation tank has two layers of scintillators inside.

Figure 4.20: The muon taggers were used to get known particle paths during the prototyping tests.

#### 4.2.3.1 Single Chamber Bladders

The first full-scale bladders were made of black PVC-coated fabric, with a single volume, and equipped with a single PMT (8-inch Hamamatsu R5912 as with the muon taggers) facing upwards. The very first bladder procured had a hatch at the bottom section, and the upward-looking PMT was directly attached to it. Access to this PMT and deployment of this bladder proved to be difficult, so the next generation bladder was equipped with the hatch at the top. For this bladder, the single upward-looking PMT was hanging via three strings attached to the hatch. Thanks to ease of access to the PMT and ease of bladder deployment, this scheme with a PMT hanging from ropes of a top hatch was adopted for all following bladders (see Figure 4.23).

The two bladders made of 0.9 mm thick black PVC material (which gave poor water quality as shown in Section 4.1.4) were procured from the commercial company Mayer Luftwerbung [128], the same company that made the small transparent bladders. The bladders were  $\approx 2.5$  m high and 3 m in diameter.

The bladders were attached to circular floaters that are dual 90 mm HDPE rings interconnected with clamps, as shown in Figure 4.21. The buoyancy needed to keep bladders afloat was calculated to be around 50 kg (This was done by measuring the specific weight of bladder samples and calculating the weight of our bladders to be around 40 kg). The pipe rings were closed using commercial pipe connectors, and the connection region was filled with foam. An additional ring served to stretch the bottom end of the bladder. (The dual 90 mm floater rings were used since the planned 120 mm rings had longer lead time; later tests confirmed that a single 90 mm floater pipe is sufficient.)

Eventually, bladders with more realistic materials were acquired, manufactured by the company Aquamate, made of Enviro and GeoFlex liners. These liners were previously tested for reflectivity and water quality before (Sec-

tion 4.1). The Enviro bladder had light tightness issues due to the rigidity of the material causing creases during transportation. The GeoFlex bladder was eventually used for the double-layered WCD tests.

#### 4.2.3.2 Single Chamber Prototype Tests

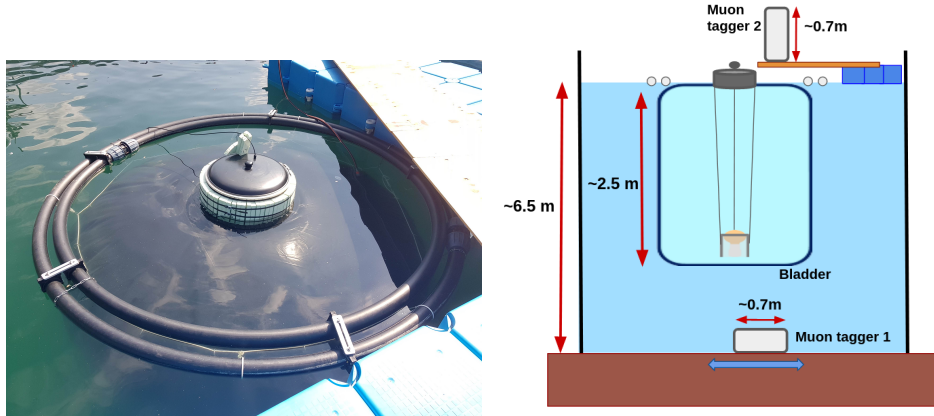


Figure 4.21: *Left:* The first single chamber prototype bladder, made of PVC, with a floating hatch and two floaters attached. *Right:* The sketch of the single-chamber prototype tests. The bladder made of PVC floats in between two muon taggers. The PMT unit is hanging from the hatch at the top of the bladder.

The PVC bladder was deployed inside the lake simulation tank via a crane by partially filling it with air, and then slowly filling it with filtered water using a pipe that utilized the pressure from the drinking water supply at the institute. After deployment of the bladder, the PMT was inserted through the hatch at the top and tied to the hatch with three ropes, as shown in Figure 4.21.

This single-chamber prototype served to test deployment, flotation, filling and other possible mechanical issues. While the PVC bladder material resulted in significant degradation of water quality, it could still be used to detect Cherenkov light, in a two-fold coincidence between the two muon taggers. Figure 4.21 shows the placement of the PVC bladder between the two muon taggers. One muon tagger is placed at the bottom of the lake simulation tank and the other one is placed at the top, named 'bottom tagger' and 'top tagger', so that the bladder is floating in between the two taggers. They provide additional identification and information on the location of muons.

Measurements for the three channels by triggering on the coincidence between the two muon taggers were conducted at night since this bladder was not light-tight. The time window for the measurements was 100 ns with trigger thresholds of 20 LSB for both the top and bottom muon tagger channels. The signal times of the initial coincidence measurements are shown in Figure 4.22. Although there are some outliers, the time correlation between the bladder and top & bottom muon tagger channels are seen in these plots. Quality cuts on the signal amplitudes of the top and bottom muon taggers were made to capture the large amplitude signals, in order to get the hits with direct light as opposed

to reflected light. The bladder channel has no quality cuts. Time differences between the signals are mostly due to different cable lengths, as the bottom muon tagger had a longer cable.

**COINCIDENCE RATES** The expected muon rate at the location of the two-fold coincidence tests can be predicted. The integral intensity of vertical muons above 1 GeV at sea level is given as  $F_0 \approx 70\text{m}^{-2}\text{s}^{-1}\text{sr}^{-1}$  by the Particle Data Group [34]. The overall angular distribution of muons at the ground as a function of zenith angle is given as  $\propto \cos^2\theta$ . The flux of muons on the setup, sketched in Figure 4.21, can be approximated by multiplying  $F_0$  with the solid angle. For the coincidence between the two taggers, the solid angle is approximated as

$$\Omega = \frac{\text{diameter}}{\text{Distance}} = (0.4/7)^2 \approx (1/20)^2$$

using the diameter of vertically placed top muon tagger (0.41 m) and approximating the distance between the two taggers to 7 m. The coincidence rate is found using the relation,  $\text{Rate} = F_0 \times \Omega \times \text{Area}$ . If the area of the top side of the top muon tagger is used for this calculation, the obtained rate is

$$\text{Rate} = 70 \times \frac{1}{400} \times \pi \times 0.2^2 \approx 0.02 \text{ Hz}$$

This approximation can be compared with simulated coincidence rates. HAWC-Sim (see Section 3.3) was used to simulate the three-channel, two-fold coincidence setup and to get coincidence event rates. Input particles were generated for the simulations using EXPACS/PARMA [150], which provides exposure times for each input particle (see Section 4.2.6 for a more detailed description). These simulations gave rates ranging from 0.01 Hz to 0.05 Hz depending on water absorption length. Finally, the measured coincidence rate from our data is  $\sim 0.017 \text{ Hz}$ , which is consistent with both the simulations and the calculations.

The single chamber bladder tests provided us with valuable experience with the deployment of bladders and PMTs. Through these tests, the floaters were tested, bladder filling strategies were explored further and the functionality of the entire electronics chain at MPIK was verified. Hanging PMTs through a hatch at the top was found to be a convenient approach, which was implemented for future prototypes and remains a viable solution for the full-scale array.

#### 4.2.4 Double Chamber Prototype Tests

Once the process of deploying a bladder into the artificial lake setup was optimized thanks to the single-bladder tests, the next step was to make and deploy a double-layered bladder. As described in Section 3.1 and in Kunwar et al. [108], the baseline design for SWGO is a double-layered WCD where the lower chamber functions for background veto. The prototype tests described in this chapter for the lake concept led to the design, building, deployment and testing of such a unit. This double-layered WCD described in this section is the very first double-layered WCD built for SWGO.

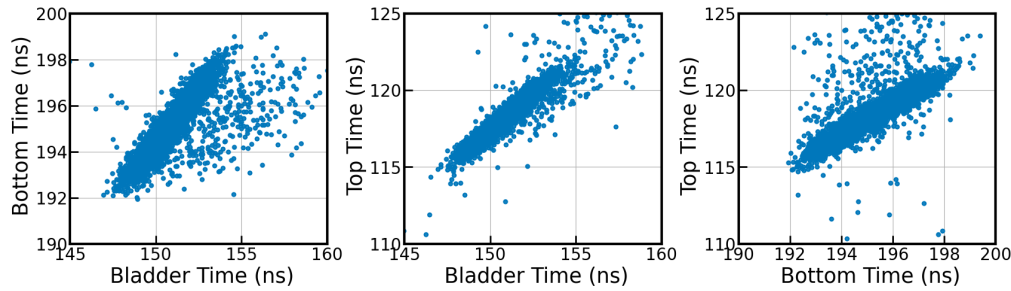


Figure 4.22: The signal times of the three-channel runs taken with the one-chamber PVC bladder, triggering on the coincidence between the top and bottom muon taggers. "Bottom" and "top" denote the bottom and top muon taggers. Time correlation between all channels is seen. The offset in the axis is due to the differences in cable length.

#### 4.2.4.1 Double Chamber Bladders

Different options were considered for the lower chamber as shown in Figure 4.23. In all three cases, a PMT or a pair of PMTs is hung from the access hatch of the WCD located at the top. These three cases are

- A. A single bladder with a divider membrane, such that a pair of PMTs like in Figure 3.1 is lowered into a gap in the membrane.
- B. Two separate bladders that are deployed together, where a separate PMT is already attached to the lower bladder, looking upwards or downwards.
- C. The nested solution, where a reflective inner bladder is deployed inside the larger outer bladder.

Option A) would likely be the easiest to deploy, however requires a specialized bladder with a membrane that is more difficult to manufacture. Option B) offers the flexibility of decoupling the two chambers, which allows the size of the lower unit to be optimized separately, however the deployment and connections between the two bladders are nontrivial. Lastly, option C) allows the usage of a non-specialized outer bladder and eliminates the need to laminate reflective material to the outer bladder liners.

The inner side of the lower chamber needs to be lined with a reflective material such as Tyvek to maximize light collection efficiency for all options<sup>4</sup>. For options A) and B), a Tyvek-coated bladder material is needed. The best material for this is a Tyvek-laminated bladder material, as used for example in the Auger liners. However, this requires specialized bladder manufacturing techniques<sup>5</sup>. For option C), the inner Tyvek bladder does not need to be connected to the outer bladder, and does not need to be light tight.

<sup>4</sup> Option B) offers another possibility: With an upward-looking bottom PMT as in option B, simulations with HAWCSim show that sufficient muon detection can also be achieved for a black lower bladder, provided that the height of the bottom section is significantly increased – up to 1 m

<sup>5</sup> Alternative options could be to spot-weld or spot-glue Tyvek to the bladder material. Tests with Tyvek 1082D showed this to be possible, though somewhat cumbersome.

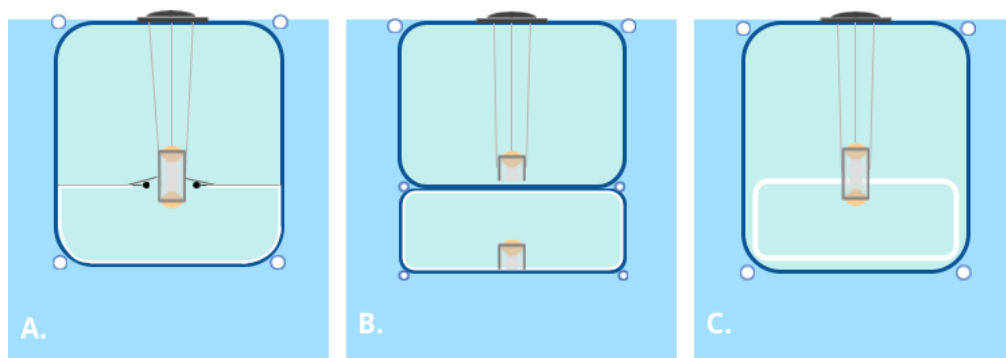


Figure 4.23: The three design options for a double-layered WCD. From left to right: A) Bladder with an internal divider, B) Two independent volumes, C) the matryoshka, or nested bladders

#### 4.2.4.2 The Matryoshka

Option C), the nested solution, nicknamed ‘matryoshka’ after the nested wooden dolls, eliminates the need to connect the reflective liner to the outer bladder altogether. In this option, a bladder is made only using the reflective liner and is inserted along with the double-PMT setup inside the bladder. An octagon-shaped Tyvek bladder was produced at MPIK by welding of Tyvek segments, held via a spider/umbrella structure made up of PVC pipes, as shown in Figure 4.24. The umbrella mechanism is designed such that in its closed position the muon matryoshka is able to go through the hatch of a one-chamber bladder, and then once it is through the hatch, the umbrella structure can be opened via pulleys. The first mechanical tests to see the feasibility of this approach were performed in mid-2023, and are shown in Figure 4.24. The left figure shows that the prototype can go through the hatch of the Aquamate bladder, while the middle and right figures illustrate the closed and open positions of the muon matryoshka<sup>6</sup>. The ‘muon matryoshka’ provides a quick way to test dual-volume bladders in MPIK’s lake simulation tank, without the need of Tyvek lamination.

#### 4.2.5 Tests and Modifications

The matryoshka was seen to go through the bladder’s hatch and open as expected, however more tests were required before deploying the matryoshka inside the Aquamate GeoFlex bladder that was already inside the lake simulation tank. The deployment of the matryoshka was a process involving trial and error and was eventually optimized. Inserting the matryoshka into a single-layer bladder without making extensive tests was not possible, since once inside, the matryoshka cannot be inspected to see whether it opened correctly. Tyvek’s density, varying from  $42 \text{ g/m}^3$  to  $75 \text{ g/m}^3$  depending on type, is much lighter

<sup>6</sup> 1 : 10 scale and a 1 : 3 scale versions of the matryoshka were also made and tested mechanically previously.

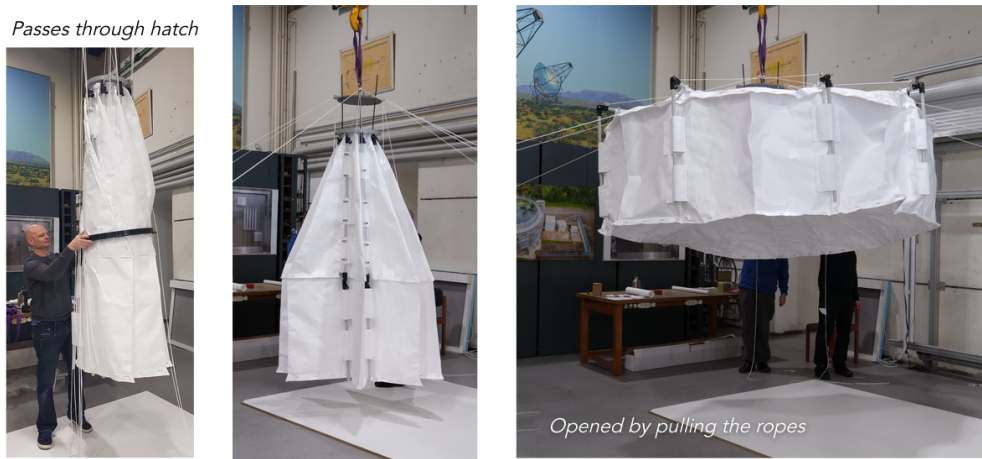


Figure 4.24: The prototyping of a muon matryoshka. *Left:* Muon matryoshka passing through a bladder's hatch. *Middle:* Muon matryoshka in closed position. *Right:* Muon matryoshka in open position, how it would sit inside the larger bladder.

than water, hence it floats inside water, meaning the matryoshka would behave differently in water.

For this reason, a test pool was constructed at MPIK where the hatch of the bladder could be simulated and the behavior of the matryoshka could be examined, as the pool had clear water that allowed underwater inspection. During the first test the matryoshka did not open inside the pool without human interference. The hinges of the umbrella were pushed by the floating Tyvek material in different directions, so they had to be pulled in one direction with additional tools. Furthermore, even after the matryoshka opened, the lighter Tyvek was pulled upwards. In this test, it was seen that the hinges of the umbrella need to be restricted further and that the Tyvek needed to be pulled down with extra weights. The second pool test was more successful, however this time it required too much force to open the umbrella hinges, by several people pulling from separate ropes. A more efficient way to exert enough force for the matryoshka to open inside the bigger bladder was needed. Eventually, the angles of the ropes were modified so that they hang from a cylindrical structure instead of a central point, reducing the force required. The final step for the optimization of the matryoshka was realizing that the weights of the double PMT structure itself could be used to open the matryoshka.

Thanks to the pool tests, the following modifications were made:

- The outer joints of the umbrella mechanism were fixed and restricted so they can only open up to a 90° angle.
- A central weight hanging from the ring around the double PMT support was added, using two steel blocks ( $1 + 0.5 = 1.5$  kg), and three 0.8 m ropes. This ensured the bottom part of the Tyvek of the matryoshka would open at a fixed 0.8 m distance.

- Cylindrical block weights were added to the end of each umbrella joint ( $0.5 \times 16 = 8$  kg total), in order to sink the corners of the matryoshka in water.
- Triangular openings were cut on the Tyvek to fasten the intake of water by the matryoshka.
- The umbrella ropes were suspended from a circular structure, or "ring". The umbrella ropes were connected only to the matryoshka edges and the ring, fixing the distance between the ring and the matryoshka edges.
- The ring was designed to sit inside the hatch, on top of the suspension hooks that are to be used to tie the three ropes of the double-PMT support.
- The ring has a hole in the middle so that the three ropes of the double-PMT support, that would be tied to the matryoshka, can pass through.
- A black foil, cut from the readily available HAWC bladder material, was added to cover the top of the Tyvek bladder for optical isolation.

In this setup, the PMT support's three ropes would be the only element that are to be manually lowered into the larger bladder. Once the ring is fixed into the position just above the hatch of the outer bladder, the matryoshka is expected to open, since the umbrella ropes fix the distance between the ring and the matryoshka edges. The modifications and their expected function are shown in the sketches of Appendix A. A final dry test was performed outside of the pool prior to deployment, to demonstrate the PMT support's weight being able to open the matryoshka.



(a) During the first pool test, the umbrella arms fail to keep the Tyvek stretched.



(b) After all modifications, the matryoshka opens without problems

Figure 4.25: The pool tests for the matryoshka

#### 4.2.5.1 Deployment

The matryoshka was deployed inside the latest Aquamate GeoFlex bag inside the lake simulation tank after all the tests and checks were completed. The process was planned as shown in the sketches of Appendix A and was completed

within half an hour. For insertion into the pre-deployed Aquamate bladder, the Tyvek bladder is collapsed into a packet with diameter just below the hatch opening, and then is lifted with a crane to the top of the water tank, as shown in Figure 4.26. Afterwards, the matryoshka is slowly lowered into the outer bladder via a manual winch, where the crane acts as a pivot point. People near the hatch of the outer bladder ensure that the matryoshka goes through swiftly. The ropes attached to the spokes cause the Tyvek bladder to unfold once fully inside the bladder, as shown in Figure 4.26d.



(a) A large crane was used throughout deployment



(b) During deployment, the wrapped matryoshka is inserted via a manual winch into the larger bladder through its hatch.



(c) The double-PMT unit and the matryoshka are attached to one another.



(d) Underwater image of the top of the opened matryoshka, with the top PMT looking up to view the upper chamber.

Figure 4.26: Deployment of the matryoshka.

#### 4.2.5.2 Data Taking

Two sets of two-fold coincidence data were taken using the full electronics chain and the test setup, recording all four channels. For both sets, the data was taken by triggering on the coincidence between the bottom and top muon

taggers within 80 ns, with a threshold of 20 LSB similar to the coincidence data taken for the single chamber bladder. The runs were taken at a voltage setting of 1500 V. The two muon taggers, as before, are used to get a known geometry for the path of through-going particles.

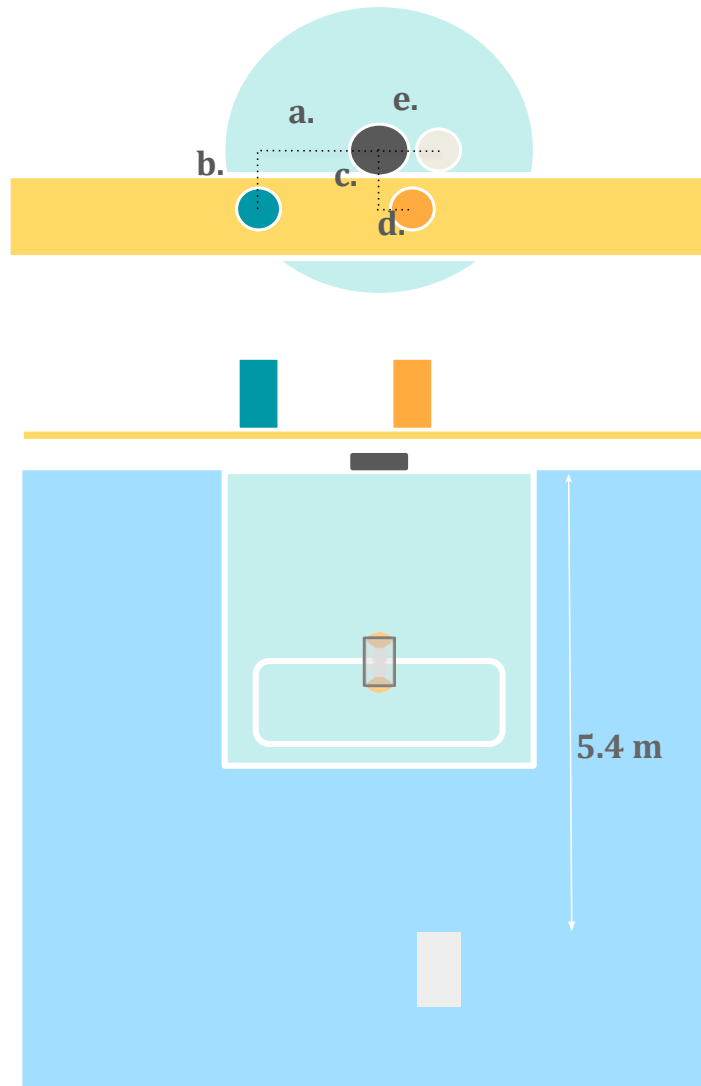


Figure 4.27: The two configurations used while data taking. The setup is shown from the top and from the side. For "Center", the top tagger, shown with orange, was placed close to the hatch. For "Edge", the top tagger was moved to the edge of the bladder, shown in dark green.  $a = 139$  cm.  $b = 64$  cm.  $c = 67$  cm.  $d = 27$  cm.  $e = 55$  cm

Figure 4.27 shows the two geometries used for data taking. First, during the run labeled as "center", the top muon tagger was placed close to the hatch of the bladder, shown with orange. This meant that the particles detected would pass close to the PMTs. For the second set, the top tagger was moved to the position indicated with green in the figure, towards the edge of the bladder, hence the labeling "edge". All of these geometries were measured as indicated in the figure caption.

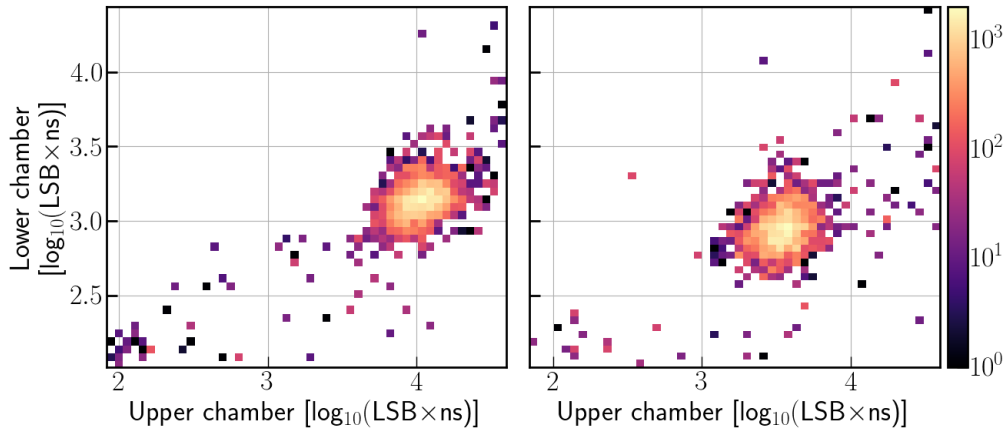


Figure 4.28: The signal in the lower chamber vs the signal in the upper chamber for the two datasets that were obtained by triggering on the coincidence between the two muon taggers, obtained by integrating over the full waveforms after making quality cuts. The left dataset was taken when the top tagger was placed close to the center of the bladder, while the right one was taken when the top tagger was near the edge of the bladder.

The bottom tagger is not visible from the top of the lake simulation tank and ropes of known length were used to determine its position. Still, this gives some uncertainty. Posterior to the measurements, the bottom muon tagger was taken out to measure the rope length for a second time, and the horizontal statistical uncertainty was determined to be around half a meter.

The trigger rate for the center run was 0.025 Hz and it was 0.018 Hz for the edge run, and total number of events was 6658 and 9011 respectively. These coincidence trigger rates are in agreement with the trigger rates of the single-bladder tests. The percentage of saturated pulses, which are not used in the analysis, is around  $\sim 1\%$  for the lower chamber and around  $\sim 6\%$  for the upper chamber.

The data was cleaned up by getting rid of the saturated pulses, and requiring large signals for top and bottom taggers, to ensure that any accidental coincidence triggering is minimized. Figure 4.28 shows the signal distribution, obtained by integrating over the full waveforms for each geometry after the quality cuts, in units of  $\text{LSB} \times \text{ns}$ . In both cases there are only a few outliers to the distributions. In the 'edge' case, the particles pass through a path further away from the PMTs. Since the upper chamber has all black walls, a lower signal is expected for the 'edge' case when the particle path is further way. For the lower chamber the difference is expected to be smaller since the walls are reflective. We see in the plots that the edge case has both the lower and upper chamber signals diminished. The diminished signal for the lower chamber may be due to the top tagger's position causing a smaller path length for the passing particles. This can be investigated further by calibrating the data, and then simulating it using HAWCSim, as shown in Section 4.2.6.

#### 4.2.5.3 Data Calibration

For the calibration of the data that is in units of LSB, or, ADC counts, it is necessary to know how many LSB one photoelectron (p.e.) corresponds to. In other words, the single photoelectron (SPE) peaks need to be found. At the voltages the data was taken, namely 1500 V, the SPE values are too close to the noise level to directly determine (Data at higher voltage settings was not taken as the saturation level was high). Instead of directly determining the SPE peak values, a series of low trigger runs were taken while varying the voltage, which were used for extrapolation. The SPE runs were taken for both PMTs at a threshold of 5 LSB, below which the noise levels get high, and as 10k events each. The voltage settings used were 1.56 kV, 1.61 kV, 1.66 kV, 1.71 kV and 1.76 kV. Some of the individual events with SPE pulses are shown in Figure 4.29.

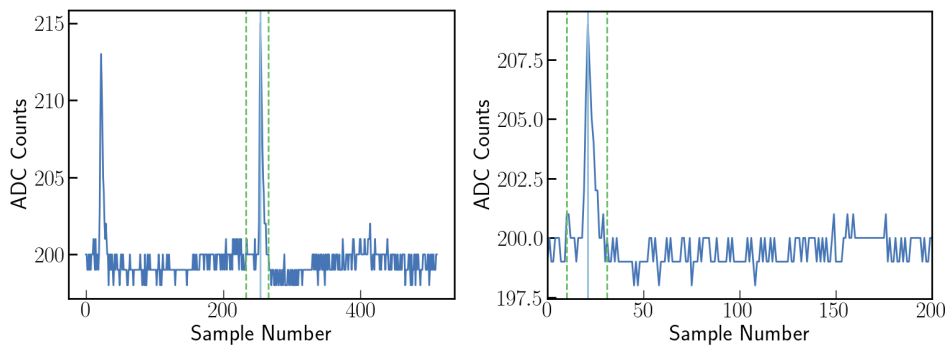


Figure 4.29: Example SPE pulses, for the lower chamber PMT R5912, at a voltage of 1.76 kV

Prior to the double-layered WCD deployment, the data calibration for the single layer bladders and the muon taggers was handled by taking the **maxima** of the highest pulse in each event, and then making a distribution of peak amplitude maxima for each voltage setting. Afterwards, the maxima of each of these distributions were plotted against their corresponding voltage settings, giving a plot of gain.

Once the double-layered WCD data was taken, the approach to integrate around the pulses was adapted, instead of just taking their maxima, as integrating accounts for any wider spread occurring in pulses. Since the lower chamber is lined with the reflective material Tyvek, we expect that the reflections cause a higher spread.

In order to check for this, the two methods are compared, namely taking the maxima of each waveform, as opposed to integrating over the waveforms. Using the two datasets from the previous section, integration is performed around each pulse, and the ratio of the integral of each pulse is compared with its maxima. Figure 4.30 shows that, in case of the lower chamber, which experiences more reflections, the ratio is higher than for the upper chamber. Moreover, we see that in the 'edge' case when we expect more reflections for the lower chamber, the ratio is even higher. The integration approach was adopted in light of these observations.

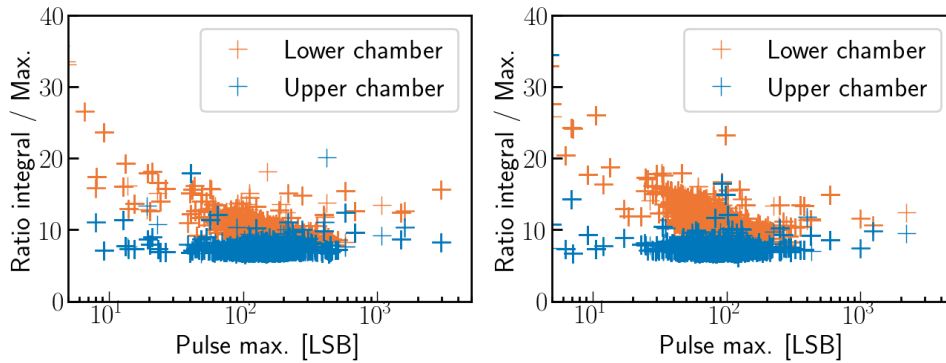


Figure 4.30: Ratio of integrated pulses over pulse maxima. *Left*: Center run. *Right*: Edge run. We see that for smaller pulses, the ratio gets larger for the reflective lower chamber. This effect gets amplified for the edge run where there are more reflections.

The highest pulse of each event in the SPE runs was integrated using the integration boundaries shown light green in Figure 4.29, capturing more information.

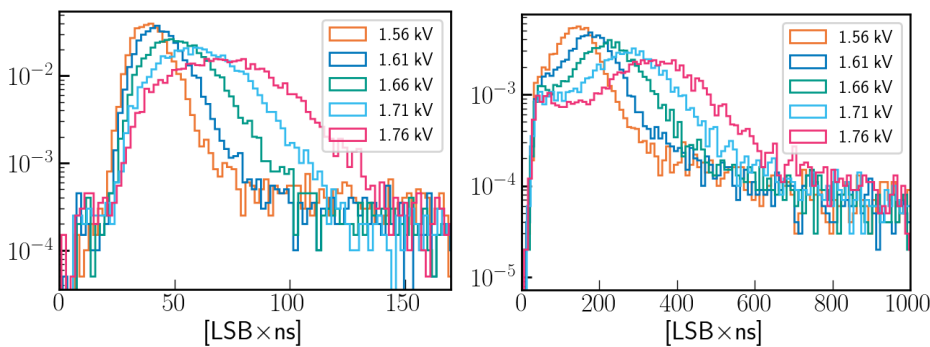


Figure 4.31: The integral distributions of the waveforms for the SPE runs of the lower chamber (*left*) and the upper chamber (*right*)

The data calibration by integrating around the peak was done initially as follows.

- A. A set of five runs with a low threshold of five and ten LSB were taken, for five different voltage settings, each with 10k events, as stated previously. The voltage settings were 1.56, 1.61, 1.66, 1.71 and 1.76 kV.
- B. For each waveform, an integration was done around the highest peak. Integration boundaries were determined by first splitting each waveform into those portions that are above the baseline using a mask, and then finding those samples at which the waveform reaches 2 LSB above the baseline (Integration boundaries shown in green in Figure 4.29). This way, each waveform in a given event was separated, and then the waveform containing the highest peak was used for integration. After the boundaries are determined, baseline was subtracted and then integration was performed. Note that this method does not work well when the local

baseline for the pulse changes largely, then it would be better to determine the baseline locally around each pulse.

- c. An integral distribution for each voltage setting was formed from these integrations of the waveforms, as shown in 4.31. As expected, with increasing voltage the peak of the distribution gets higher and the spread wider.
- d. The maxima of each integral distribution was plotted against the corresponding voltage value as shown in Figure 4.32. Two exponential fits were performed on each. The first fit was taken using all of the values, shown in orange. The second fit (pink) considered only the last three values. This alternative method of using the last three values is checked because we see, especially on the left plot for the lower chamber, that at lower voltage settings the SPE peaks may be laying below the the noise peaks – making them undetectable.
- e. The fit parameters give how many LSB one p.e. corresponds to, for each voltage setting. Hence, the conversion from LSB to p.e. can be done for the two-fold coincidence data.

For the two approaches of using all five runs versus only the last three runs, we see that for the upper chamber there was little difference, however for the lower chamber, shown in the example, the peaks were lower, meaning a higher charge distribution. For the voltage setting of 1500 V that the coincidence runs were taken, the SPE values are shown in Table 4.3. We see that the difference is less than 1% for the upper chamber PMT, while it is around 10% for the lower chamber. The two data sets, the edge and center runs, were divided by the SPE values shown in Table 4.3 and the normalized histograms were plotted as shown in Figure 4.33. We see that for the upper chamber there is no difference, while the lower chamber signal is around 10% higher.

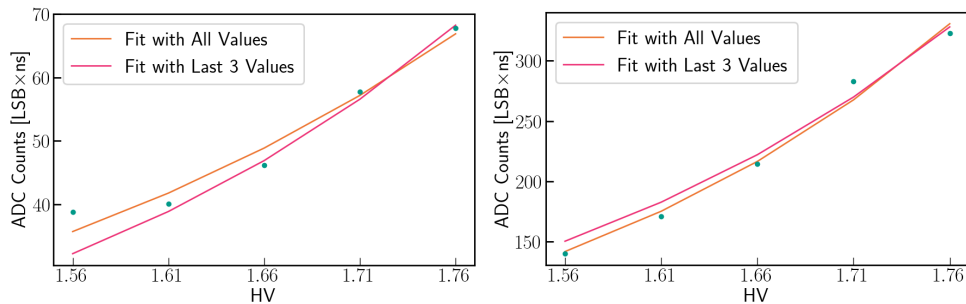


Figure 4.32: Plots of the maxima of the integral distributions from Figure 4.31 vs corresponding voltage settings. *Left*: For the lower chamber. *Right*: For the upper chamber. Two exponential fits are performed for each.

**BIAS FROM TRIGGERED PEAKS** Another factor to consider is that the method of integrating around the region containing the maximum pulse may contain a bias. In the analysis above, for a given waveform, triggered pulses above a

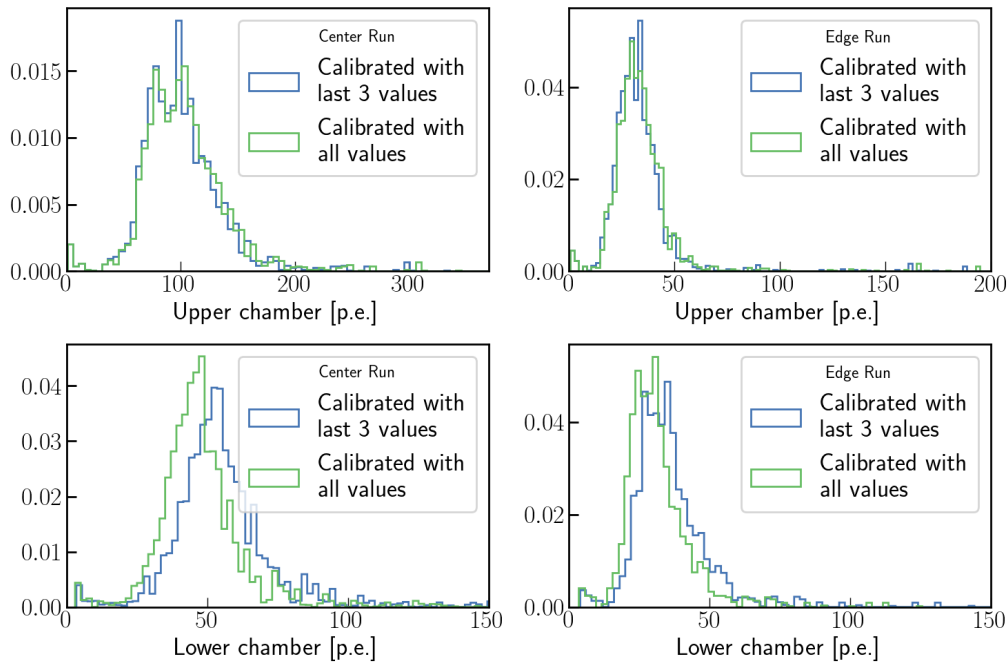


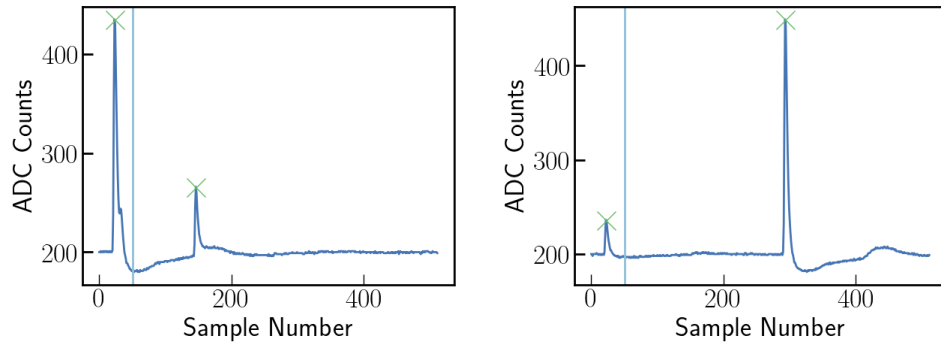
Figure 4.33: Normalized charge distribution histograms for the 'center' and 'edge' case in units of photoelectrons (p.e.). Green shows the calibration that was done with the values from the fit made using all five SPE runs, while blue shows the one made using the three SPE runs with the highest voltages. We see that the lower chamber signal appears higher in the second case, while for the upper chamber there is no difference.

certain threshold (5 LSB or 10 LSB in this case) are considered and the pulse with the highest amplitude is used for integration. As the highest amplitude pulse is considered, the SPE peaks might be over predicted with this method. This effect can be evaluated by examining the distributions of all the peaks that come after the triggered peak (Peaks that come after sample number 50/200 ns). The `scipy.signal.find-peaks()` function is used to look for peaks after sample 50, with parameters `height = 203`, `prominence = 5`, `width = (0, 30)`, `wlen = 20` and `distance = 20`. Figure 4.34a shows the waveforms obtained, with the marked peaks. Initially, the maxima of these peaks are examined to check for a bias (instead of the integrated peaks). The peak amplitude distributions for both chambers are shown in Figure 4.34. "Max pulse only" refers to the original method, and "pulses after trigger" are all the pulses that come after the triggered pulse. The peak amplitude distributions tend to be lower when only the peaks after trigger are considered, especially for the lower chamber, hence this inspection confirms that there seems to be a bias, especially for the lower chamber. At the same time, we see that the statistics is reduced almost to only 20% when only the pulses after the trigger are included, instead of only the maximum pulse.

**BIAS INTEGRATION** Hence, an alternative approach of integrating around every pulse that came after the noise threshold was also tested. Figure 4.35

Chamber	SPE Peak [LSB]
Upper, all values	108
Upper, last 3 values	111
Lower, all values	30
Lower, last 3 values	26

Table 4.3: SPE values acquired using integration around the highest pulses.



(a) Waveforms where all peaks are marked. The peaks with the maxima may not be SPE pulses as seen in the plots.

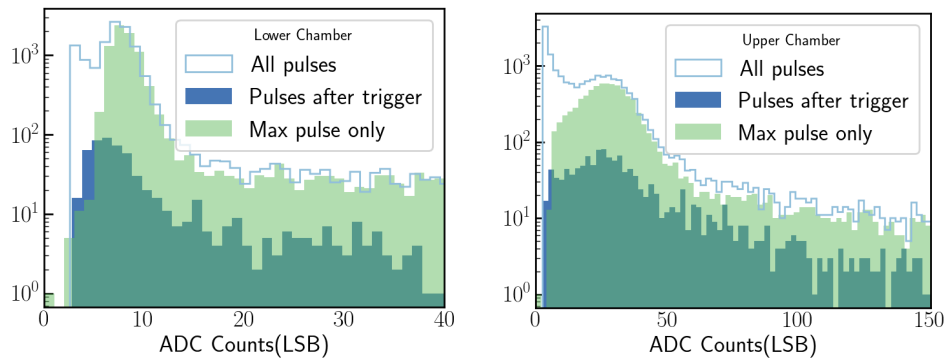
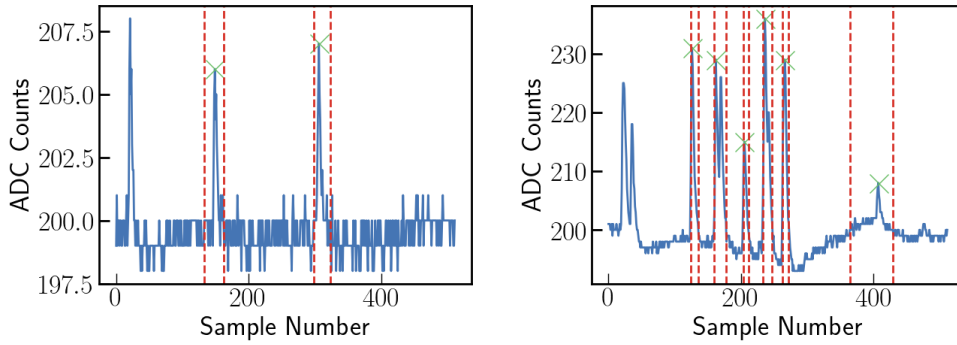
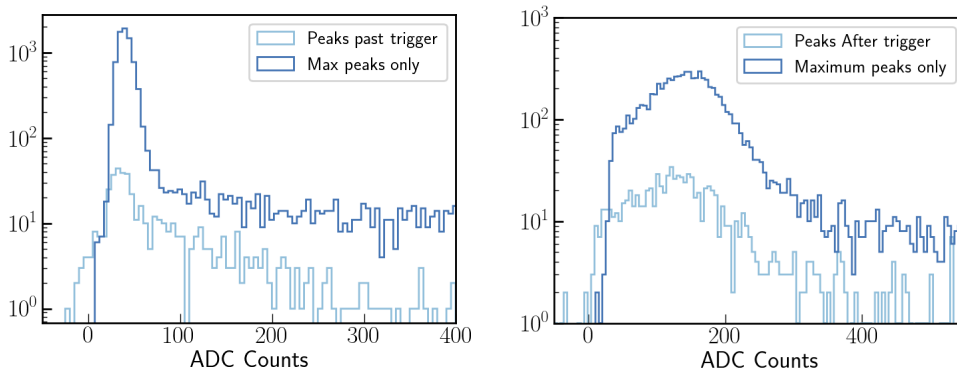
(b) The peak amplitude distributions for the lower chamber (*Left*) and for the upper chamber (*Right*), at 1.56 kV. Taking the largest pulses only makes the distributions peak at higher values, especially for the lower chamber.

Figure 4.34: Peak amplitude distributions obtained by looking at all waveforms, and those that come only after the peak that caused a trigger.

shows the method. As previously, the boundaries for the integrals are found by taking the first and last point at which the waveform containing the local peak is above the baseline; this time for every peak that is after the triggered peak (instead of only the highest peak), and then the peaks are integrated around boundaries after baseline subtraction. Figure 4.35a shows example waveforms along with the integration boundaries. The resulting integral distributions for the case of 1.56 kV are shown in Figure 4.35b. The integral distributions again



(a) Waveforms for the lower chamber (*Left*) and upper chamber (*Right*), integration boundaries in red. For the upper chamber, the baseline is noisier.



(b) The integral distributions for the lower chamber (*Left*) and the upper chamber (*Right*), at 1.56 kV.

Figure 4.35: Integral distributions obtained by looking at all waveforms, and those that come only after the peak that caused a trigger.

show a reduction in statistics of 10% to 20%, and the shapes appear more irregular compared to the previous method.<sup>7</sup>

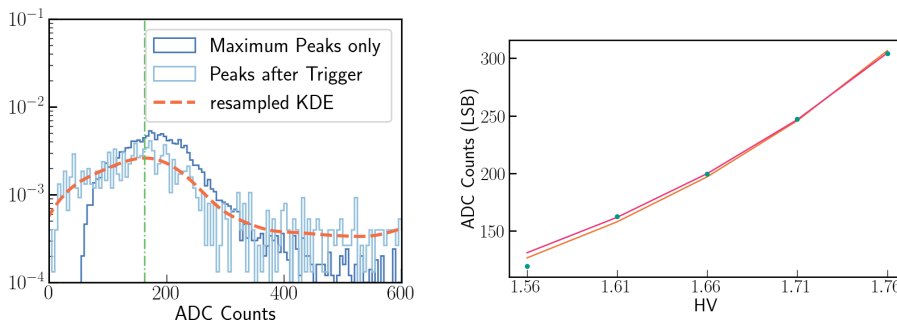


Figure 4.36: *Left*: Example fit performed on an integral distribution of the pulses after the triggered peak, using gaussian-kde. *Right*: The maxima for each fit vs voltage setting for the upper chamber. Two exponential fits are performed as before.

<sup>7</sup> The negative values come from the algorithm which chooses the local baseline for each peak.

The integral distributions obtained this way are more irregular shapes, hence it is more difficult to determine their maxima. Performing fits on these shapes proved difficult, and instead gaussian-kde was used to find the maxima for each kde (kernel density estimation) curve, as shown in Figure 4.36. We see that the noise effect from before is eliminated in this approach. The maxima of the kdes are plotted against the voltage settings as before, and by performing two sets of exponential fits are performed as before. The resulting SPE values are shown in Table 4.4, which are close to values of the previous method. This finding shows that the uncertainty in calibration is around 2% for the upper chamber and around 10% for the lower chamber.

Chamber	SPE Peak [LSB]
Upper, all values	97
Upper, last 3 values	101
Lower, all values	27
Lower, last 3 values	25

Table 4.4: SPE values found by integrating around the pulses that are after the trigger peak to check for bias.

After these investigations, the charge distributions of Figure 4.33 are taken as the final calibrated distributions to compare with simulations.

#### 4.2.6 Comparison of Data with Simulations

The configuration in Figure 4.27 was simulated using HAWCSim in order to make comparisons with the data described in the previous section. The two data configurations of 'edge' and 'center' were simulated using HAWCSim, the same GEANT4 based program used and described in Section 3.3. The simulations were seen to be in general agreement with the data.

The data taking setup sketched in Figure 4.27 was replicated in HAWCSim using two separate bladder volumes, with a smaller lower bladder. Figure 4.37 shows this setup, where a muon traversing the test tank is seen to go through both of the muon taggers and the double-layered WCD in the middle, with tracing of the Cherenkov photons produced in the WCD under test. The lower bladder has a height of 1.8 m and diameter of 3 m, replicating the lower chamber's (matryoshka) measurements. The upper bladder has a height of 1.8 m as measured with the ropes of the double-PMT in the bladder, and a diameter of 3.8 m. The shape of the lower chamber is slightly different from what is replicated in the simulations, as the real lower bladder with the umbrella structure is octagonal and has a weight in the middle of it.

The dimensions of the double-layered WCD and two muon taggers are as measured from the real counterparts. Other inputs to the simulation include reflectivity of the inner walls, and water absorption length. The reflectivity

measurements for Tyvek 1082D and GeoFlex, from Section 4.1.3, were used as inputs in the simulation.

As for water absorption length, the C-star transmissometer from Section 4.1.4 was used to measure the transmissivity of filtered water inside the double-layered WCD, found to be around 5 m at 410 nm, and then after a few weeks 2.5 m. This degradation happened due to the ropes that were used to suspend the matryoshka and the double-PMT setup. The degradation was observed separately as part of those water transmission tests, placing more uncertainty on the water absorption length parameter to be used in the simulation.

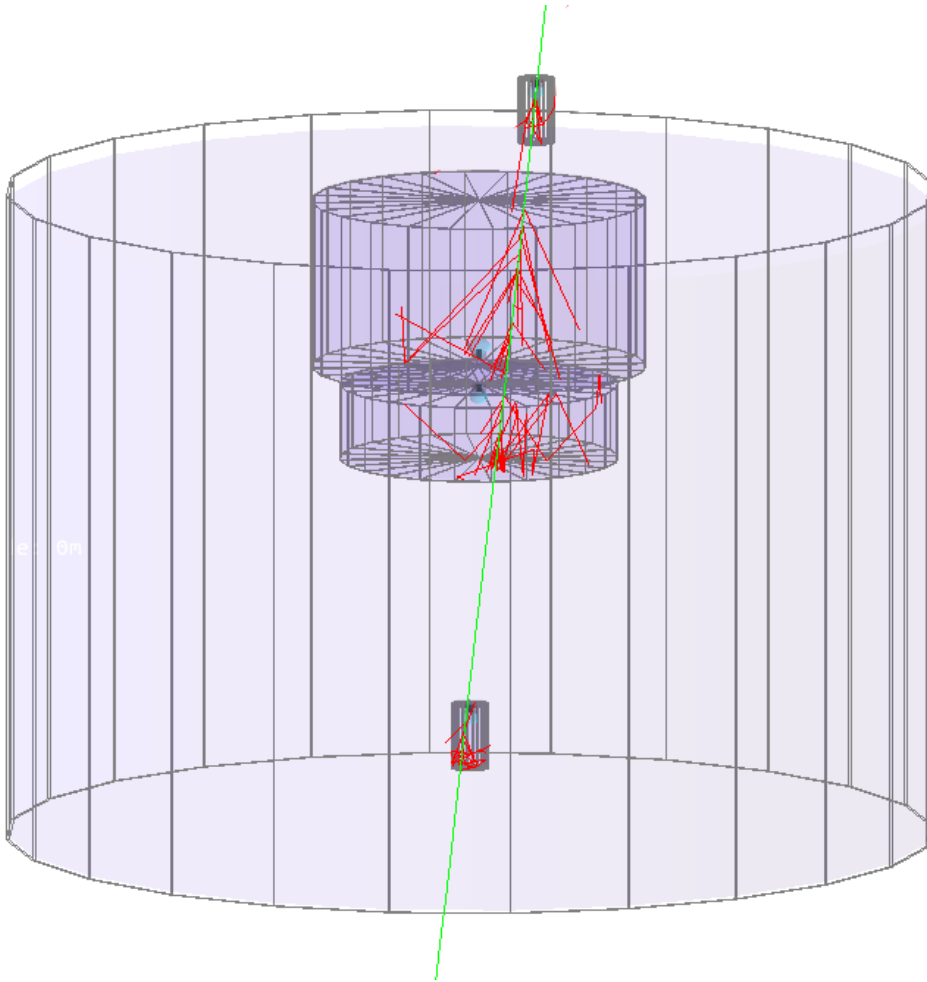


Figure 4.37: Visualisation of a GEANT4 simulation of the test facility in Heidelberg, where the lower chamber that is immersed into the larger bladder is depicted as a separate bladder with a smaller radius.

It is possible to tune these parameters within the uncertainty of each. Extensive simulations of the two setups, varying the parameters, were made to compare with the results from the data. The parameters that can be varied due to uncertainties are as follows.

- The dimensions of the upper and lower chambers have some uncertainty. In particular, the matryoshka has an irregular shape as described. Simulations with an upper chamber of 1.7-1.8-1.9 m height were made and no

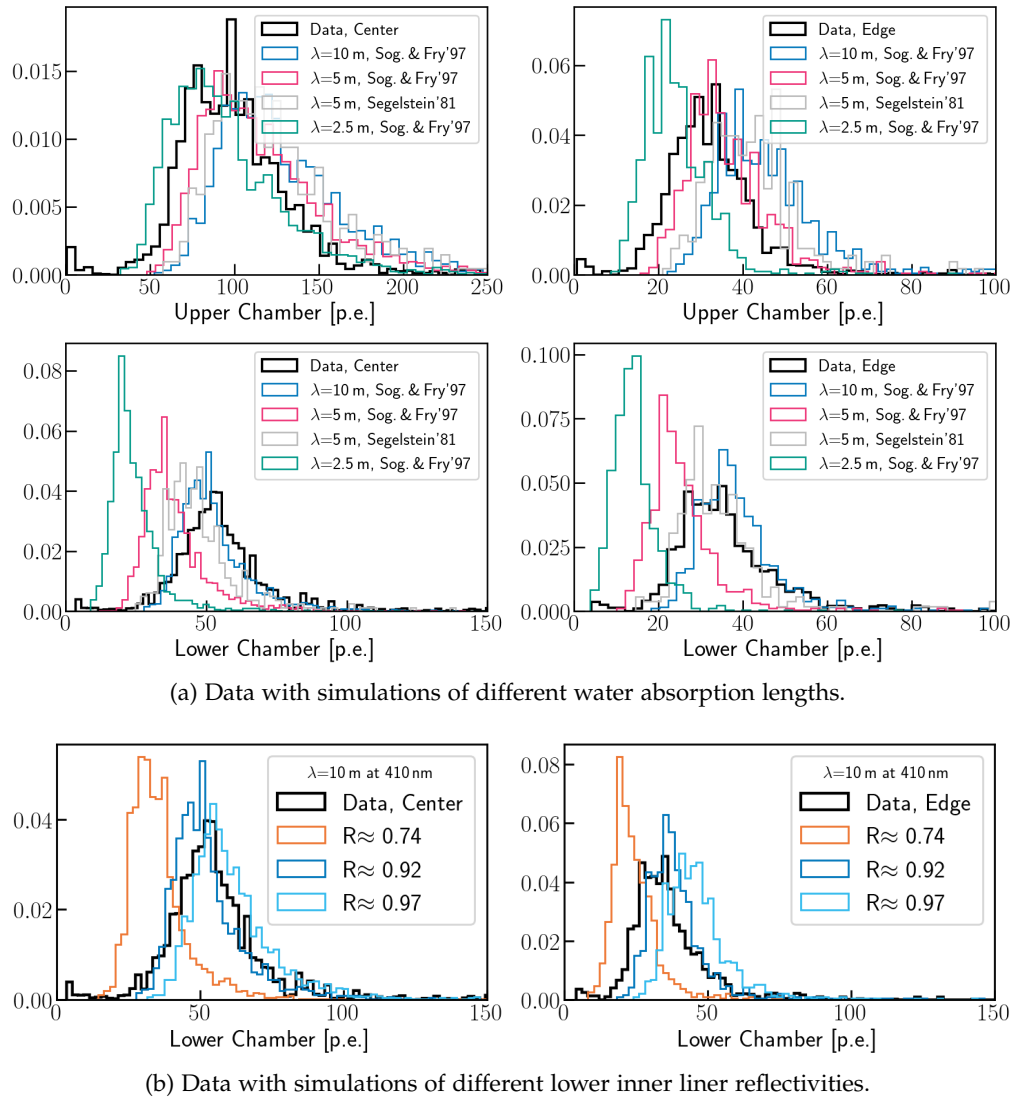
identifiable change was seen. The nominal height of the lower chamber was 0.8 m, and additional simulations with a lower chamber height of 0.5 m and 1 m showed no identifiable change.

- Since the bottom tagger was not visible from the top of the tank and was suspended from two ropes, as described in Section 4.2.5.2, the location of the bottom tagger has an uncertainty of around 50 cm in the axis of the two ropes, hence, three different locations of the bottom tagger were tested. The first case when the bottom tagger is aligned with the bladder's center, the second case when it is 55 cm to the left of the bladder, and the third case when it is 55 cm to the right.
- The water absorption length has considerable uncertainty as described, due to the degradation from the ropes. During the deployment process of the lower chamber, the water inside the larger bladder may have been contaminated further. Moreover, since the transmissometer makes measurements only at the wavelength of 410 nm, there are different absorption spectra possible, as shown in Figure 4.11 (see Section 4.1.4). In light of this, several absorption lengths and spectra were simulated.
- Reflectivity is another parameter that influences the charge and time distribution greatly (see Section 4.1 for the measurements of reflectivity for the lower chamber and upper chamber liners). A case where the reflectivity of Tyvek, the liner of the lower chamber, is lower than expected (down to  $\sim 70\%$ ) and higher than expected were tested. Moreover, a case where the reflectivity of the GeoFlex liner was lower than the measured 10% was also tested and was seen to make no difference.

The input particles for these simulations were created using EXPACS/PARMA [150]. PHITS-based Analytical Radiation Model in the Atmosphere (PARMA) is a model that is able to estimate terrestrial fluxes of cosmic ray particles any time and anywhere on the Earth's atmosphere. PARMA is implemented in the open-access software EXcel-based Program for Calculating Atmospheric Cosmic ray Spectrum (EXPACS).

The inputs of  $\mu^+$  and  $\mu^-$  particles are generated using EXPACS/PARMA. The inputs are aimed at a hemisphere of 1 m radius, centered on the muon tagger at the bottom of the lake simulation tank, with energies ranging from  $1.5 \times 10^3$  MeV to  $5 \times 10^4$  MeV, at an altitude of 303 m and location  $49^\circ 25' \text{ N}$ ,  $08^\circ 43' \text{ E}$ , for Heidelberg, Germany, the location of the lake simulation tank tests. Furthermore, the angles are restricted such that only the particles passing near the vicinity of the top muon tagger are considered, which results with different inputs with slightly different angles for the 'center' and 'edge' cases. The EXPACS/PARMA program provides exposure times for each input, which are used later on to calculate the simulated coincidence rates, and were also used for the single-chamber bladder tests.

The simulations are used to estimate the expected coincidence rate and to predict the time and amplitude response of the double-layered WCD.



(a) Data with simulations of different water absorption lengths.

(b) Data with simulations of different lower inner liner reflectivities.

Figure 4.38: The measured signal distribution (histogram) compared with selected simulations made with HAWCSim.

**EVENT RATES** The calculated coincidence event rates, from Section 4.2.3.2, are around 0.02 Hz. From the previous section, the measured trigger rates are 0.025 Hz and 0.018 mHz for the center and edge cases respectively. Using the EXPACS/PARMA exposure times, the rates of the simulations are found to be of the order of 0.02 Hz, depending on the different parameters that are varied. We see that the event rates for expected, calculated and measured cases are in reasonable agreement— within the same order of magnitude.

**SIGNAL AMPLITUDES** The predicted distribution of signals in the upper and lower chambers of the simulations where the position of the bottom tagger is varied with respect to the double-layered WCD are shown in Figure 4.39 along with the data. A different position for the bottom muon tagger corresponds to a shorter or longer path for the passing muon. All three cases show reasonable agreement with data. The edge case has a somewhat larger difference: The

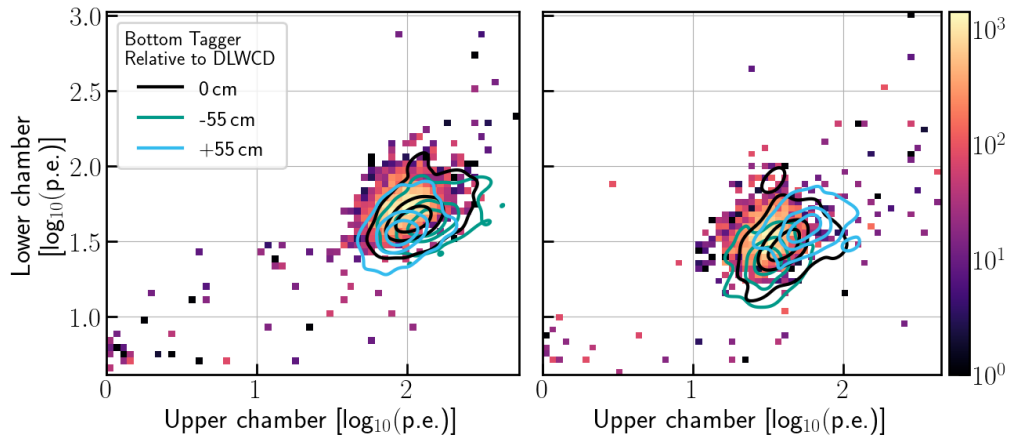


Figure 4.39: Simulations with the bottom tagger's position varied relative to the double-layered WCD.

+55 cm case where the path is the longest has the largest signal. The case where the bottom muon tagger is aligned with the double-layered WCD is chosen as the baseline and used while varying the other parameters.

For reflectivity of the walls and water absorption length, the predicted distribution of signals in the upper and lower chambers of some of the simulations are shown in Figure 4.38, made with the configuration of the bottom tagger aligned with the double-layered WCD. These are normalized histograms of number of photoelectrons (p.e.). The histograms for different reflectivities (Figure 4.38b) shows the measured reflectivity of 0.92 at 400 nm compared to lower and higher possibilities. We see that the measured reflectivity, shown in dark blue, is closest to data.

Meanwhile for different water absorption lengths, (here the spectrum of Sogandares & Fry [157] is assumed as it is the most recent measurement), we see a more complicated result. For the center case, the upper chamber seems to be described well for all of the cases presented, while for the edge case it fits best with the  $\lambda = 5$  m case. However when we consider the lower chamber, we see that both for the center and edge cases the  $\lambda = 10$  m case describes the data best. While the measurements of the water transmission length showed values varying between  $\lambda = 2.5$  m to  $\lambda = 5$  m, we also note that if we are to assume the measurements from Segelstein [153], to interpolate the measured value, a value  $\lambda = 5$  m at 410 nm for Segelstein roughly corresponds to a value  $\lambda = 10$  m at 410 nm for Sogandares and Fry 1997. In that case  $\lambda = 5$  m at 410 nm, assuming the Segelstein spectrum would describe the data well overall (See Figure 4.11 for a reminder).

Overall,  $\lambda = 10$  m at 410 nm for Sogandares & Fry and  $R = 0.92$  seems to have the best agreement with data. More precise measurements of the aspect ratios and a full knowledge of the water absorption length would help better the agreement.

**TIME DISTRIBUTION** An independent cross-check for the simulations is done by looking at the time distribution of the average pulses. The pulse shape

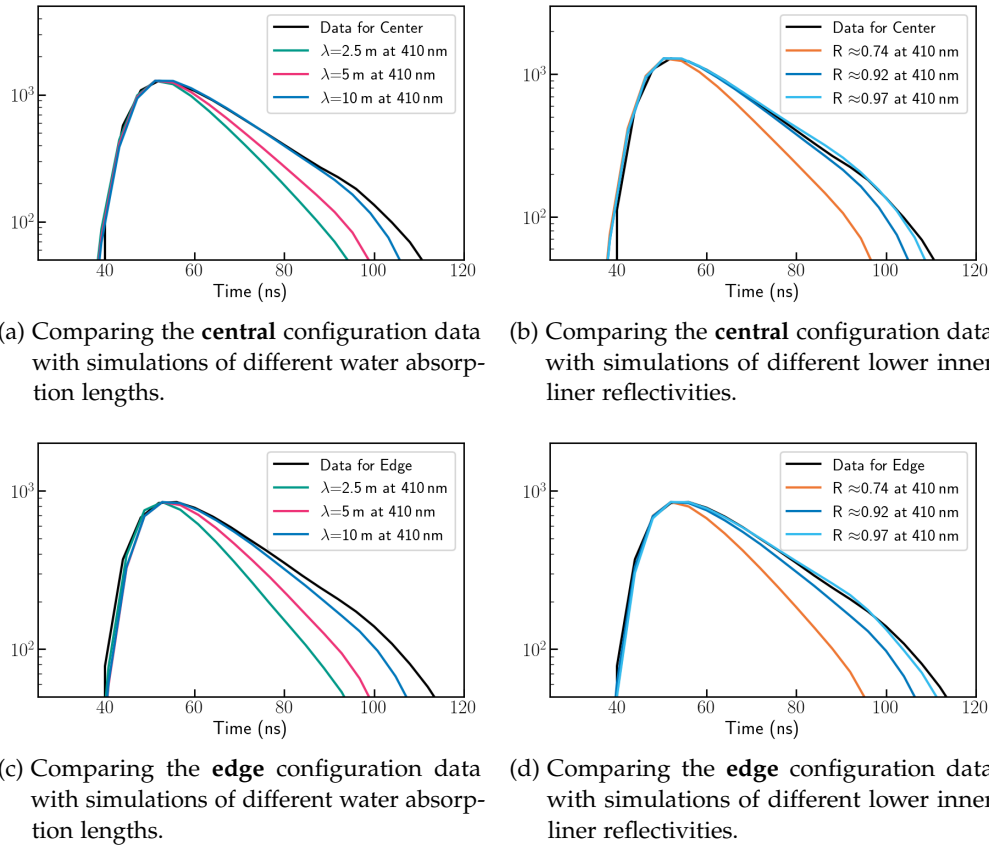


Figure 4.40: Time distributions of data and the simulations with different parameters for the lower chamber. The combination  $\lambda = 10$  m  $R \approx 0.92$  is the most realistic one that matches the data.

of signals from the lower chamber – recorded with 4 ns resolution – provides additional information and handles on wall reflectivity and water transmission.

In order to obtain this, the simulated photoelectron times, which are direct outputs of the HAWCSim simulations described above, are used to simulate the electronics response for each event in order to get simulated pulses. The electronics response was simulated by taking the trace simulations made by Felix Werner and adding the simulated times of the HAWCSim simulations as input. Once the simulated pulses are obtained, the same reconstruction method is applied both on the simulated pulses and the pulses from real data.

The average pulse shapes of the lower chamber are shown in Figure 4.40, for data and simulations. Similar to Figure 4.38, different reflectivity values and water absorption lengths were compared. For water absorption lengths, we see that the simulated average pulse for  $\lambda = 10$  m is closest to the data. A longer water absorption length means that the photoelectrons can travel further within the chamber and thus have more reflections, spending a longer time in the chamber before hitting the PMT. As for reflectivity values, we see that the simulated average pulses for the values  $R \approx 0.97$  and  $R \approx 0.92$  are closest to the average pulse of the data. The simulations confirm that increased Tyvek

wall reflectivity and increased water transmission result in longer signals, with more late (multi-bounce) photons arriving at the PMT.

In general, simulations with good water transmission – around 10 m at 410 nm – and high Tyvek reflectivity describe the data rather well. This analysis shows that the data taken with the first SWGO double-layered WCD can be reproduced with good agreement using simulations.

### 4.3 SUMMARY AND OUTLOOK

This Chapter explained the design, construction, and simulations of a double-layered WCD unit deployed within an artificial lake setup. Initially, the necessary material properties needed for the detector units of SWGO were investigated, and measurements of material reflectivity and performance in water were examined. These measurements served as cross-checks during the prototyping of the detector unit and also served as inputs in simulations. It is important to note that for large-scale measurements, more efficient and dedicated setups will be required.

Furthermore, the process of designing and constructing a double-layered WCD unit was described in detail. The "matryoshka" was built as a practical solution in the absence of bladders with a middle membrane and was demonstrated to function as a lower chamber as expected. It is a unique flexible design that does not require outsourcing to specialized companies. The resulting double-layered WCD unit, created by placing the matryoshka within a larger bladder, was the first of its kind built for SWGO and formed part of the first end-to-end measurement chain, utilizing electronics built by other colleagues at MPIK. The prototyping and analysis described in this chapter demonstrated the capability to collect coincidence data with this setup and accurately predict event rates and signals through simulations.

#### 4.3.1 SWGO Prospects for the lake concept

Building the engineering array in the chosen site of Pampa la Bola will be a big milestone for the SWGO collaboration [25, 149]. While the lake concept was recently discarded as the main array option<sup>8</sup>, the double-layered WCD design was selected as a baseline for SWGO. At the same time, a future ultra-high-energy (UHE) extension to SWGO is under evaluation for energies above 100 TeV, where a lake based solution is planned.

An array for UHE gamma-rays needs a large area and can be at lower altitudes than the SWGO main array since higher energy EAS have shower maxima at lower altitudes (see Figure 2.2). Although still in early development, dedicated groups have been working on simulations, array layout ideas and detector technology options for the UHE extension [86]. In particular colleagues in China have started studying this option (see [118] for a presentation). A layout option is a sparse array of surface detectors accompanied by submerged muon detectors similar to the MD of LHAASO. Prototyping of such an array has

<sup>8</sup> The main array includes the core and the sparser outer array.

been ongoing in an artificial lake at the LHAASO site. In particular, using deep underwater bladders for muon detection is a cost effective alternative to the buried muon detectors of LHAASO (see [123] for images of MD). The surface WCD development work done at MPIK, described throughout this section, will contribute to this work in many ways, including the experience gained with bladder deployment, knowledge of bladder materials and upcoming studies in a wave basin (see Section 3.2.3.4).

Furthermore, geometry calibration for the lake concept, in context of the UHE extension, needs to be evaluated. Data-driven position calibration methods augmented by specific instrumentation are being evaluated within the SWGO collaboration.



## EMISSION FROM PULSAR WIND NEBULA HESS J1825-137 WITH THE HAWC OBSERVATORY

---

### 5.1 INTRODUCTION

HESS J1825-137 is a pulsar wind nebula (PWN) that has a bright core and asymmetric extended emission (see Chapter 1 for a discussion of PWNe). It is located at a right ascension (RA) of  $276.26^\circ$  and a declination (DEC) of  $-13.97^\circ$ , at a distance of  $\sim 4$  kpc [76]. This PWN is the brightest source in that region above an energy of 32 TeV, and is the largest and one of the most luminous PWNe identified within the Milky Way galaxy with a gamma-ray production region of  $\sim 70$  pc [104, 131, 145]. This luminous PWN was the first object in VHE gamma-ray astronomy that was discovered to have energy dependent morphology [17].

The complex region around this PWN has been explored and characterized using several different instruments. In addition to detections in X-ray and gamma-ray regimes, studies of the interstellar medium (ISM) of the region and the studies of energy dependent morphology of the PWN by instruments Fermi-LAT and H.E.S.S., wide field gamma-ray observatories HAWC and LHAASO have also studied this region. Wide field gamma-ray observatories can provide additional information, as they are well suited for extended source detection thanks to their large field-of-view (FOV) compared to IACTs (see Chapter 2 for more details), and furthermore can provide detection at higher energies.

In this section, we give an overview of what is known about this PWN and explore what more can be learned about it using wide field gamma-ray observatories. We first analyse the most recent HAWC data, finding hints of the previously observed energy dependent morphology. We compare this with other instruments such as H.E.S.S. and Fermi-LAT. We furthermore show the potential of the upcoming detector SWGO for this source. A conference contribution in the form of a presentation was made regarding this work in TeVPA 2023 [69].

#### 5.1.1 *The Region*

The region around HESS J1825-137 is rather complex with multiple gamma-ray emitters in the vicinity, which can be seen from Figure 5.1. There are two identified pulsars, one binary system and two extended sources that are identified as PWN, one of which is HESS J1825-137, and structures observed in the ISM.

The pulsar (PSR) J1826-1334 (also known as PSR B1823-13) is a young, Vela-like energetic pulsar. It was detected after a galactic plane survey conducted by the 76-m Lovell radio Telescope at Jodrell Bank, during observations between

1983-84 [50]. It was one of the youngest pulsars detected in the survey with no detectable supernova remnant at the time, with a pulse period of 101 ms and characteristic age of 21.4 kyears. It is at a distance of  $\sim 4$  kpc with a spin-down power  $\dot{E} = 2.8 \times 10^{36} \text{ erg s}^{-1}$  [124].

The extended source HESS J1826-130 is associated to the pulsar J1826-1256. This source was previously considered as part of the extended emission of HESS J1825-137, however the H.E.S.S. galactic plane survey in 2015 revealed it as a distinct source [76]. It is also associated to the "Eel" PWN11 (PWN G18.5-0.4), an X-ray source observed with Chandra. It also spatially coincides with HAWC source J1826-128 [20].

The binary system LS5039 lies in the vicinity as well, to the south of HESS J1825-137. Gamma-ray binaries consist of a young massive star and a compact object. This is a system that was studied and detected numerous times (See, for example [16, 126, 169]).

Furthermore, this is a region with dense molecular clouds as shown by studies of the ISM [168]. In 2021 HAWC discovered ultra-high-energy (UHE) emission from this region, coming from an unidentified source HAWC J1825-134 that is very close to HESS J1825-137 (identified with the HAWC counterpart HAWC J1825-138) [20]. LHAASO similarly detected UHE emission from this region, identified as LHAASO J1825-1326 [46]. A LHAASO study on the energy dependent morphology of this source is in preparation [177]. Studies of energy dependent morphology are also being pursued by the HAWC collaboration, as described in this chapter (see also [69]).

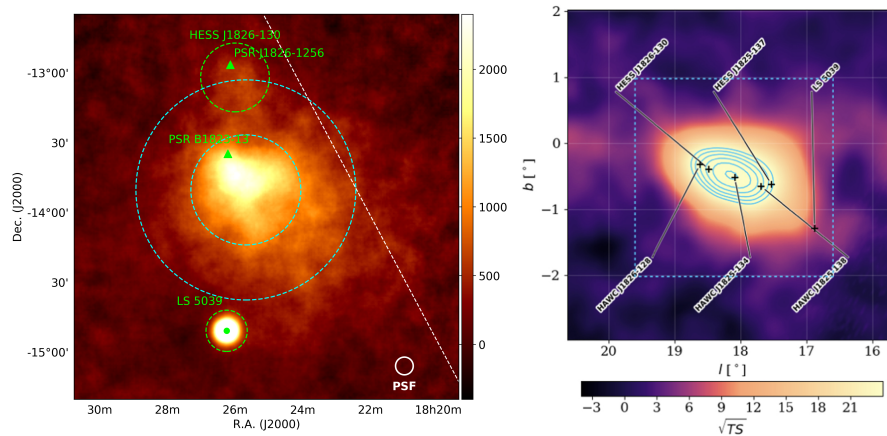


Figure 5.1: *Left:* The excess map from H.E.S.S. paper, taken from [77]. The two PWN (J1826-130 and J1825-137, along with their associated PSR are shown) *Right:* The HAWC detection of the region from 2021, taken from [20]

### 5.1.2 Overview of Observations of the Region

HESS J1825-137 was detected in the gamma-ray regime for the first time by H.E.S.S. during the galactic plane survey of 2005 [15]. The pulsar it is associated with was already a known source detected in radio and X-ray observations, with a PWN identified around it via X-ray observations.

ROSAT X-ray observations around 1996 showed a compact nebula of radius  $\sim 20''$  around PSR J1826-1334 (also known as PSR B1823-13) and an elongated diffuse region of  $\sim 5'$  [65]. Afterwards, in 2003, the extension was revealed to be asymmetric by XMM-Newton observations –with a core component of around  $30''$  surrounded by a more diffuse component, only on the south side of the pulsar and identified as a PWN, G18.0-0.7 [66]. The existence of these two components was confirmed by Chandra observations around 2007 [141] and Suzaku around 2008 [164], where the extension was found to be even larger; up to  $15'$  (or  $0.25^\circ$ ), corresponding to  $\sim 17$  pc from the pulsar. It was argued that this extended emission is synchrotron radiation from the PWN, where the VHE gamma-rays observed with other instruments would come from the inverse Compton scattering of the CMB photons by high energy electrons. A synchrotron intensity with a magnetic field of  $B \sim 7 \mu\text{G}$  was argued to correspond best to the X-ray intensity [164].

In the gamma-ray regime, HESS J1825-137 was discovered during the first H.E.S.S. galactic plane survey as an approximately radially symmetric source near the pulsar PSR B1823-13, as a VHE source, with a flux of VHE gamma-rays of around 17% of that of Crab above 200 GeV [18]. It was discovered by the H.E.S.S. collaboration to have energy-dependent morphology at TeV energies, as a softening of the energy spectrum with increasing distance from the pulsar was observed [17], becoming the first source that was detected to have energy dependent morphology in the gamma-ray regime. This PWN was also detected by Fermi-LAT in the energy range of 1 – 100 GeV in 2011, as a significantly extended source [74]. It was also detected by VERITAS, in 2020 [8]. The particle transport mechanisms of HESS J1825-137 were examined further by the H.E.S.S. collaboration, emphasizing the energy dependent morphology [77]. In this paper, in addition to the shrinking size, the centroid was also found to move closer to the pulsar with increasing energy – in line with the picture of uncooled particles near the pulsar being the source of the high energy emission and then cooling when moving further away, producing TeV emission via IC mechanism. The extension of the nebula emission was found to be  $1.5^\circ$  from the pulsar, (and an intrinsic diameter of  $\sim 100$  pc) making it one of the largest PWNe known (see Figure 5.1). A similar method for finding radial extent was later used in a Fermi-LAT analysis, which showed consistence with the H.E.S.S. analysis [145].

Modeling of particle emission and transport was studied for this PWN by Etten and Romani, Khangulyan et al. [64, 104] and others. Etten and Romani apply a multizone time-dependent modeling, with a pulsar wind termination shock radius of  $R_{TS} \sim 0.03$  pc and Khangulyan et al. postulate that the large size of the PWN is due to significant energy injection from the pulsar at early times. The latest H.E.S.S. and Fermi-LAT publications show a particle transport mechanism of advection and diffusion together may indeed explain this emission and extent, as suggested by these models [77].

An  $\text{H}\alpha$  rim observed in the region at a distance of  $\sim 120$  pc to the south-east of the pulsar J1826-1334, which powers HESS J1825-137, may be an evidence of the supernova remnant (SNR) [168], as it seems consistent with hydrodynamical

simulations that point the expected radius to be four times the size of the PWN [51, 104, 168].

There have also been several studies of the ISM around this region [114, 168]. Extended faint radio emission was detected to the east of PSR J1826-1334 by Jansky Very Large Array (JVLA) observations in 2012, along with a nearby molecular cloud with a density  $\sim 400 \text{ cm}^{-3}$  [49], towards the North of the nebula. Lemièrè et al. identify seven high density molecular regions from a composite survey of CO data, in the vicinity of the PWN [114]. In particular, they find that a molecular cloud laying to the north of the PSR J1826-1334 has spatial correlation with the pulsar.

According to Blondin et al., the interaction of a PWN with the SNR shock with the ISM, in particular with a molecular cloud, can cause a reverse shock that crushes into the PWN, causing it to have an asymmetric morphology [37]. Studies have therefore argued that this may explain the asymmetric, one-sided morphology of the PWN HESS J1825-137. [68, 77].

Furthermore, a region of GeV gamma-ray emission with three peaks were observed by Fermi-LAT, around the region of the H $\alpha$  rim, and it was argued that a combination of high energy electrons diffusing from the PWN and LS5039 could be responsible for this emission [51].

This region was also observed and studied by the HAWC collaboration [20], where the emission from the complex region was described with a three-source model; two of which can be associated to HESS J1825-137 and J1826-130, and a third one, HAWC J1825-134 that was described as a PeVatron candidate. These sources can be seen in the significance maps of Figure 5.1, where the H.E.S.S. counterparts are shown. The authors emphasize that the three source model is favored over the two source model, with the HAWC data and resolution at that time, and argue that the emission from the new source may be coming from PeV cosmic ray protons colliding with the gas in this region.

LHAASO also detected an UHE source from this region, LHAASO J1825-1326, that shows a gradual steepening [46]. The LHAASO angular resolution is unable to resolve the region enough to exclude emission from HESS J1826-130 and a deeper analysis on this region is being pursued [177].

UHE gamma-ray photon detection used to be considered to be evidence of acceleration by protons via pion decay, as the electron Inverse Compton gamma-ray production is suppressed at these energies in Klein-Nishina regime (see Chapter 1). However, recent studies have shown that emission through IC mechanism can dominate if the environment is radiation dominated [42, 179]. The observed energy dependent morphology of this source is further evidence of an IC mechanism, as high energy electrons are not able to travel far distances before cooling and are hence emitting closer to the pulsar.

## 5.2 ANALYSIS

The region of HESS J1825-137 is close to the galactic center, and thus transits through the HAWC FOV with minimum zenith angles of  $32^\circ$ , which makes it challenging to observe. The HAWC publication on this region was done with

Pass 4 data when individual structures could not be resolved around the region, as can be seen on Figure 5.1. Since then there have been improvements in data reconstruction that enable a better point spread function for these angles. Moreover, the analysis presented here uses the open source python package *Gammapy* [58] to analyze HAWC data that complies to the gamma-astro data format.

### 5.2.1 Analysis with *Gammapy*

The analysis in this section is carried out using the *Gammapy* [56, 58] package, although the default tool for HAWC data analysis is the Multi-Mission Maximum Likelihood (3ML) package [166]. 3ML uses plugins that provide an interface between 3ML and the official software of the instrument. Packages like *Gammapy* and *ctools* [105], meanwhile, instead of using the official software of each instrument, provide a single tool to carry out the entire analysis. These open-source tools require data to be delivered following a common format, namely in the gamma-astro-data-format (GADF). While 3ML remains as the official tool for HAWC data analysis, *Gammapy* is increasingly used within the HAWC collaboration. These analyses with open-source tools serve as cross-checks for the HAWC analysis, and provide a window to future gamma-ray analysis combining different instruments like CTAO and SWGO within the same framework.

Analysis of the HESS J1825-137 region is also being pursued in the HAWC Collaboration using 3ML, led by Dezhi Huang (see [89] for more details).

**GAMMA-ASTRO DATA FORMAT (GADF)** The GADF is aimed as a common and standardized model for all gamma-ray instrument high level data. GADF uses the flexible image transport system (FITS) format to provide standardized events lists and instrument response functions (IRFs) for open-source data analysis tools like *Gammapy*. This data format was originally designed for IACTs, however its flexibility allows also data from other instruments like space-based telescopes and ground particle arrays [137]. In fact, recently, the data from ground-particle arrays like HAWC was shown to be compatible with GADF via the reproduction of several published results [21]. The data reduction process is named with 'data levels'(DL), and starts from DL0, which is the raw data coming from the sampled signal from the light sensors of a trigger event. DL1 data is the calibrated data, and DL2 is the data parameterized into observables. DL3 data are selected gamma-ray events, in form of event lists, along with the instrument response functions (IRFs). Finally, science products such as spectra and sky maps are classified as DL4 and catalogs showing observatory results as DL5.

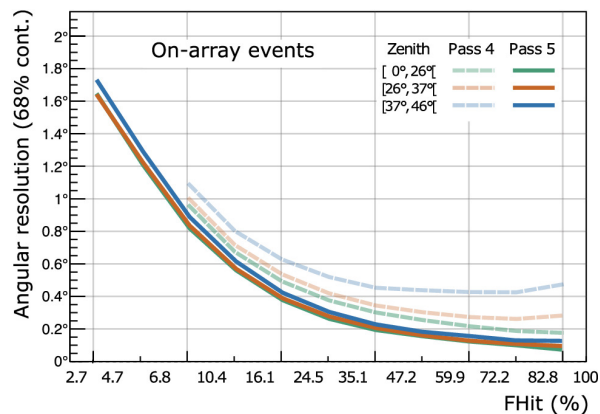
**GAMMAPY PACKAGE** *Gammapy*, an open source Python package using GADF, handles high-level analysis (DL3 to DL5) for gamma-ray data once calibration and gamma-hadron separation are complete (low-level analysis). Up to DL3, data processing is specific to each instrument, however once data is exported to

GADF, the high level data analysis can be handled by *Gammapy*, as the same kind of gamma-ray-like events and IRFs are used. For details in background estimation for ground particle arrays see [21].

*Gammapy* is organized into sub packages. The *gammapy.makers* subpackage is used to perform data reduction from DL3 to DL4, where the information from eventlists and IRFs is projected onto a common physical coordinate system in the form of maps, binned in energy and sky coordinates, which are DL4. These binned maps and data sets are analyzed using subpackages *gammapy.maps* and *gammapy.datasets*. For the modeling, Poisson maximum likelihood fitting is used, with the *gammapy.modeling* and *gammapy.estimators* packages.

### 5.2.2 HAWC Data

HAWC uses a 2D binning scheme, made up of size bins subdivided into energy bins, as shown in Figure 5.3. The size bins, indexed as  $B$ , are determined on the fraction of PMTs in the HAWC array being triggered by an event, where the number of events reduces approximately by half with each bin (also called fHit bins – "fraction of PMTs hit"). They go from 0 to 10, with an increasing size of the event with increasing number. Events in bin 10 have all the PMTs triggered. Initially this was used as the sole energy estimator in HAWC [5], however as described in [7], the energy estimation was later improved, now being done on an event-by-event basis using two algorithms. The first one is Ground Parameter (GP) that is based on the charge density deposited by the shower, and the second one is Neural Network (NN) which uses energy estimation with artificial neural networks (See [7] for more details on the algorithms). Depending on energy, the fhit bins are organized into 12 bins each spanning a quarter decade in  $\log_{10}(E/TeV)$ . The cuts for gamma/hadron separation are optimized for each bin [5, 7], using two parameters called compactness, and PINcness (quantifying the clumpiness of the shower) (For details see [5, 7]).



(b) FHit

Figure 5.2: HAWC angular resolution before (Pass 4) and after (Pass 5) the recent data reconstruction improvements as a function of FHit bin. Plot taken from Albert et al. [22].

**IMPROVEMENTS IN DATA RECONSTRUCTION** The HAWC reconstruction process is being improved every year with a different processing of the data, called "Passes". After the most recent HAWC publication on the region around HESS J1825-137, which used data from Pass 4 [20], there was a revision of data reconstruction called Pass5, which gave a better PSF especially for high zenith angle regions. These revisions included fixing of a shower front curvature correction algorithm and fixing the pointing issues that occurred with increasing zenith angle. These corrections to data reconstruction were implemented to the scripts for producing DL3 data sets for HAWC and verified using the Crab nebula in an earlier study. Figure 5.2 shows the improvement in the angular resolution after these revisions (See [22] for details of the improvements). The poor angular resolution starting with around  $30^\circ$ , and a systematic pointing error more effective in the high zenith regions was fixed after this data revision. At the zenith angles of above  $30^\circ$ , the HAWC angular resolution with Pass 5 is greatly improved compared to Pass 4, to less than  $0.2^\circ$  above 40 TeV. These improvements in HAWC PSF at high zenith angles have enhanced the ability to resolve the HESS J1825-137 region. As this region transits through the HAWC field of view at angles above  $30^\circ$ , the improvements enable the separation of individual structures.

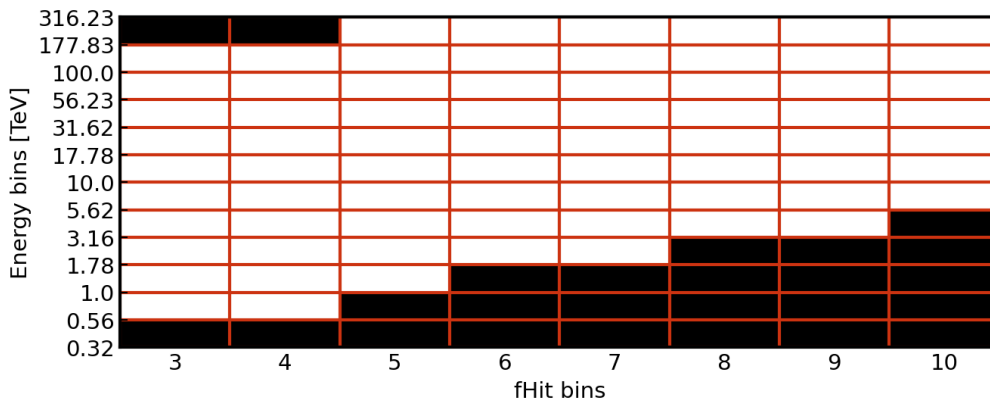


Figure 5.3: The HAWC energy bins. The bins used in this analysis are shown in white.

**DATASET FOR THIS ANALYSIS** The data set used for the analysis encompasses 2460 transits and is from the latest version of Pass 5. The energy reconstruction of this data utilizes the neural network algorithm as described in [7], while the background modeling employs the modified approach for DL3 data, detailed in [21], with modifications to the conventional direct integration method of HAWC analysis.

For the analysis, quality cuts were made based on instrument response functions, considering energy resolution and point spread functions, as shown in 5.3 these eliminate some of the bins used.

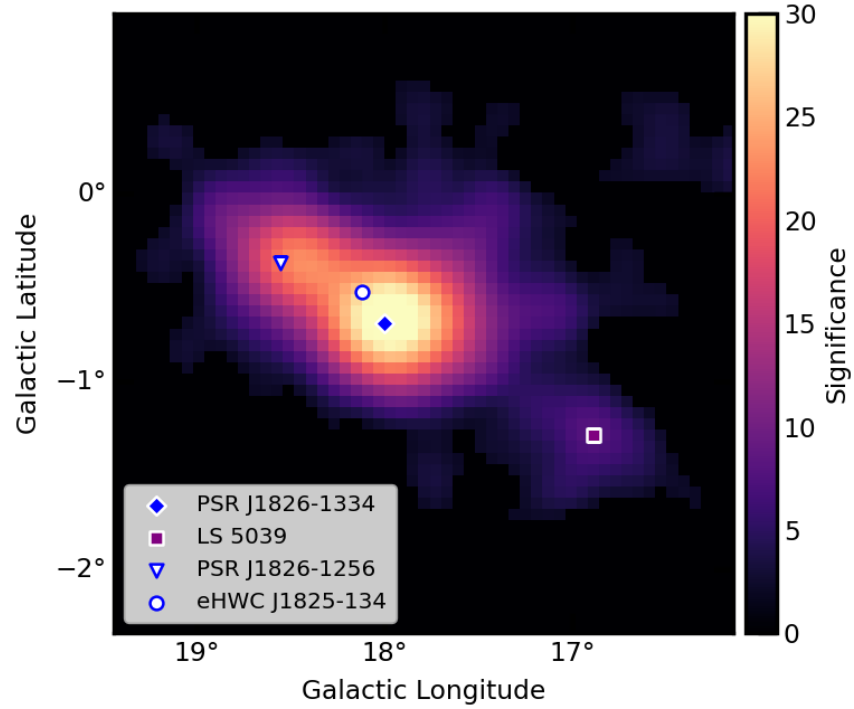


Figure 5.4: Significance map of the region, made by assuming a model and convolving it with the PSF of the instrument. Individual structures are resolved.

### 5.2.3 Significance Maps

Significance maps of the region were made using the data set and *Gammapy*. These are maps that show statistical significance at each pixel, which can be approximated as the square root of the test statistic,  $TS = 2\Delta\log\mathcal{L}$  where  $\mathcal{L}$  is the likelihood function, the product of Poisson probabilities for each data at each pixel.

$$\mathcal{L} = \prod_{ij} p_{ij} \text{ where } p_{ij} = \frac{\theta_{ij}^{n_{ij}} e^{-\theta_{ij}}}{n_{ij}!} \quad (5.1)$$

where  $n_{ij}$  denotes counts observed in pixel  $ij$  and number of predicted counts is  $\theta_{ij}$  [127]. According to the Wilks theorem, under an hypothesis,  $TS = 2\Delta\log\mathcal{L}$  follows asymptotically a  $\chi^2$  distribution with  $n_{dof}$  degrees of freedom where  $n_{dof}$  is the difference between the free parameters of the hypothesis being tested and the null hypothesis. When there is one degree of freedom, statistical significance can be estimated as  $\sigma \approx \sqrt{TS}$ . This is the quantity being plotted on the significance maps, calculated for each pixel.

There are two approaches for estimating significance, both addressed in *Gammapy*. Significance can be calculated in the Li& Ma style [117], where counts in the ON region are compared with counts in the OFF region and the significance of the excess over the background is calculated. In this case all that is needed is a background and a counts map. This approach does not assume any models and is addressed with the class `ExcessMapEstimator`. The

second method is to calculate significance by assuming a model, with a source spectrum and extension, then to apply the IRFs and compute the predicted counts for the model to be compared with the background counts. This method is also named forward folding.

In this analysis, the second method was used, implemented in `TMapEstimator` in *Gammapy*, to make significance maps. This class works based on a model fitting approach. This method allows combining the different bins of the data set into a single map, since a likelihood fit is done for each pixel. When no model is specified, a point spatial model along with a power-law spectral model is assumed as a convention. In this method the model assumed as convolved with the PSF of the instrument, hence it is a more accurate approach.

Figure 5.4 shows the significance map that was made for this analysis using the `TMapEstimator` method. The improvement from the previous publication is clear as individual structures are separated. LS5039, HESS J1826-130 and HESS J1825-137 are clearly separated, with locations of the two PWN coinciding with two pulsars. The Southwest directed asymmetrical nature of HESS J1825-137 observed by previous instruments is also observed.

#### 5.2.4 Modeling the Region

In this analysis, a catalogue pipeline was used as a starting point for models of the three sources, and modifications were made to test different scenarios. As part of the *Gammapy* adaptation work done for HAWC, a catalog pipeline tested on CTA galactic plane survey simulations (see [54]) was adapted to HAWC by Quentin Remy. The pipeline performs bin selection, adds models for diffuse emission and background, and then it finds candidate sources in the excess map using a peak detection algorithm. Afterwards it ranks candidates, performing fits with generalized Gaussian spatial models (equation 5.2.4) and log-parabola spectral models (equation 5.2.4) by default and tests alternative shapes. The interstellar emission model used throughout this analysis comes from this pipeline. The specific model used is noted as "IEM-varmin rescaled", featuring inhomogenous cosmic ray transport [54].

The spatial models from the pipeline for the sources around HESS J1825-137 are generalized Gaussian models for HESS J1825-137 and J1826-130, and a point source model for LS5039.

The generalized Gaussian spatial model is defined as

$$\phi(\text{lon}, \text{lat}) = \phi(r) = N \times \exp \left[ - \left( \frac{r}{r_{\text{eff}}} \right)^{(1/\eta)} \right] \quad (5.2)$$

where the normalization factor is

$$N = \frac{1}{2\pi \sqrt{(1 - e^2)} r_0^2 \eta \Gamma(2\eta)} \quad (5.3)$$

When the  $\eta$  parameter approaches to zero, the shape becomes more disk-like, when it is 1/2, the shape is a Gaussian distribution and when it is  $\eta = 1$  it is a

Laplace distribution. This model was adapted for HESS J1825-137 and HESS J1825-130, and modifications were made.

For spectral modeling, initially, a log-parabola spectral model was used for all three sources, as this was the default from the catalog pipeline.

$$\phi(E) = \phi_0 \left( \frac{E}{E_0} \right)^{-\alpha - \beta \log\left(\frac{E}{E_0}\right)} \quad (5.4)$$

In addition to this model, the exponential cut-off power-law model was also tested, which was the marginally preferred model used for the H.E.S.S. and HAWC publications. We will see that this model is preferred in this analysis as well.

$$\phi(E) = \phi_0 \left( \frac{E}{E_0} \right)^{-\Gamma} \exp(-(\lambda E)^\alpha) \quad (5.5)$$

Both the log-parabola and exponential cut-off power-law models can evolve into the simple power-law model when their curves are adjusted.

$$\phi(E) = \phi_0 \left( \frac{E}{E_0} \right)^{-\Gamma} \quad (5.6)$$

This model is also tested in the analysis, and later used for the spectrum of LS5039.

### 5.2.5 Fitting

The significance map of the region after the addition of the models from the catalogue pipeline shows that the models describe the data well. The residual maps also show good agreement. As the next step, fits were performed, varying different parameters to get a better description of the sources in the region. In particular, the parameter  $\eta = 0.01$  is frozen for HESS J1826-130, making it disk-like, for simplicity. First, a joint fit of the three sources was performed, freezing all parameters except for spatial extent and spectral amplitude. Once this fit converged, an additional fit for HESS J1825-137 was performed, for all of the parameters. For the fitting procedure, the `Fit` class of *GammaPy* was utilized. This class uses the `minuit` backend, which is a numerical minimization software library developed by CERN [94].

The fit quality assessment is done by examining the residual maps and the fit statistic profiles, where the parameter in question is varied while the others are fixed.

The best fit parameters for HESS J1825-137 for different models described in the following section are shown in Table 5.1.

Model	Amplitude	Index	Other
Exponential cut-off power-law	$1.14 \pm 0.06$	$2.33 \pm 0.03$	$E_c = 110 \pm 0.3 \text{ TeV}$
Log-Parabola	$1.07 \pm 0.04$	$2.49 \pm 0.02$	$\beta = 0.02 \pm 0.007$
Power-law	$0.92 \pm 0.03$	$2.51 \pm 0.02$	-

Table 5.1: The best fit parameters for HESS J1825-137 for the three spectral models tested. The amplitude is in units of  $10^{-13} \text{ TeV}^{-1} \text{ s}^{-1} \text{ cm}^{-2}$  with  $E_0 = 10 \text{ TeV}$ .

### 5.2.6 Alternative Models and Fits

For HESS J1825-137, in addition to modeling from the catalogue pipeline; namely with a log-parabola model, fits were performed for every component of the spatial and spectral models. Furthermore, the power-law and exponential cut-off power-law models were also tested.

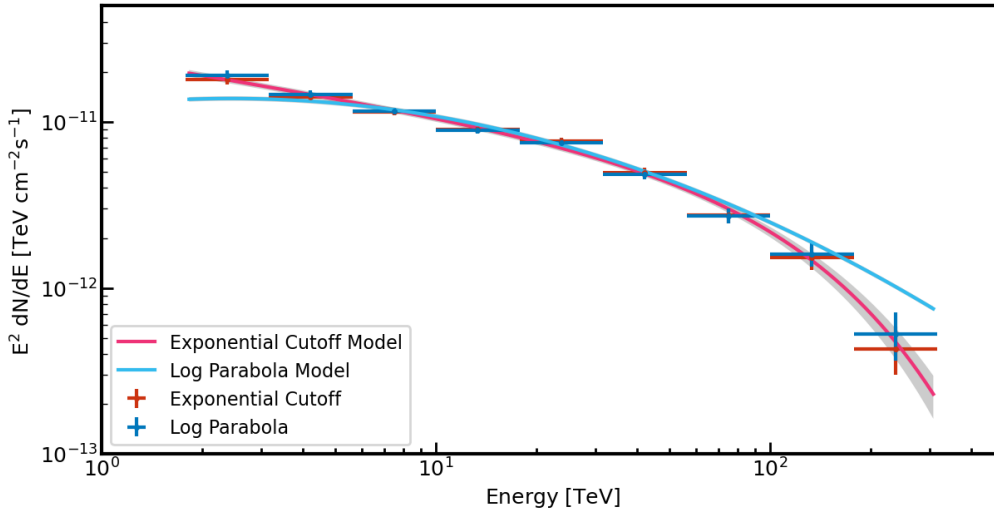


Figure 5.5: The flux points for PWN HESS J1825-137 extracted with a log-parabola model and an exponential cut-off power-law model. There is a marginal preference for the exponential cut-off power-law model.

Firstly, the spectral model for the PWN was changed to the exponential cut-off power-law model (equation 5.2.4) to test it, which was found to be marginally preferred by the earlier H.E.S.S. analysis, although in the Fermi-LAT analysis the log-parabola model was found to be marginally preferred. A fit was performed as before, giving the parameters shown in Table 5.1. In order to compare the two models, a third fit with the power-law model was performed. The power-law model has only one parameter different from the exponential cut-off power-law model (where it is a special case), and likewise the log-parabola model, hence it is possible to compare the  $\sqrt{TS}$  values obtained from this model with the other two models. It was found that the exponential cut-off power-law model is preferred over power-law with  $\Delta\sqrt{TS} \approx 6.2$ , while

log-parabola is  $\Delta\sqrt{TS} \approx 5.6$ . Hence, a marginal preference for the exponential cut-off power-law model is observed.

The modeling and fitting for LS5039 and J1826-130 was done by starting from the catalogue pipeline models and fitting for the spectral amplitudes and size parameters only, instead of fitting for all of the parameters. A power-law model for LS5039 was tested, which was marginally preferred over the log-parabola model (by a preference of  $\sim 0.5$ ). Hence a power-law model for LS5039 was implemented. Moreover, HESS J1826-130 was treated like a disk by fixing  $\eta = 0.1$  in the generalized Gaussian spatial model. The residual maps showed that this gives an acceptable model, and the  $TS$  values over a Gaussian distribution show a marginal preference.

### 5.2.7 Flux Points

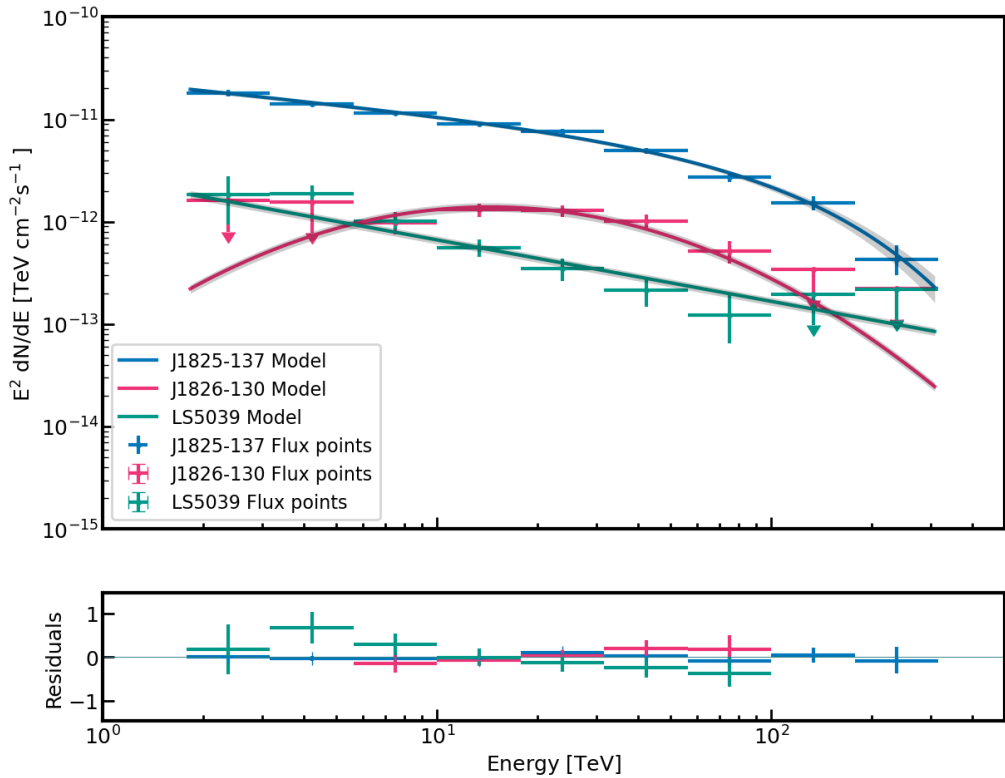


Figure 5.6: The spectra extracted for the three sources in the region. LS5039 has a preferred power-law spectrum, while HESS J1826-130 has log-parabola. The PWN HESS J1825-137 is plotted with the marginally preferred exponential cut-off power-law spectrum.

Flux points are obtained in *Gammapy* by first choosing an energy binning and then doing a one-dimensional likelihood fit profile to compute the flux and flux error for that bin range, so the amplitude is fitted within energy range defined. For this analysis, the energy bins chosen are the logarithmic energy bins of HAWC. The resulting flux points with the log-parabola and exponential cut-off power-law models are shown in Figure 5.5. The spectral models used in the fit

with their best fit parameters, which can be found on Table 5.1, are plotted on top. We see that at the higher and lower energy ends, the exponential cut-off power-law model indeed provides a better description.

The resulting flux points along with the best fit models for the three sources are shown in Figure 5.6. The models used are the exponential cut-off power-law model for HESS J1825-137, log-parabola model for HESS J1826-130, and power-law model for LS5039, as these showed the best agreement with data.

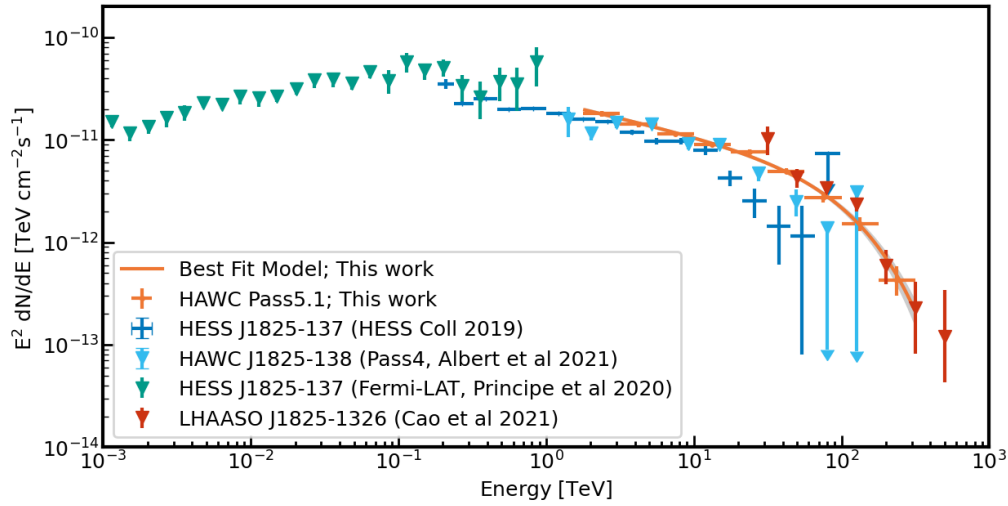


Figure 5.7: Spectral Points taken from Fermi-LAT [145], H.E.S.S. [77], HAWC [20], and LHAASO [46]; compared with our analysis and best fit model.

Next, we look at the spectral energy distributions from other studies that looked at this region with different instruments in the gamma-ray regime. Figure 5.7 shows the spectral energy distributions from studies using Fermi-LAT [145], H.E.S.S. [77], HAWC [20], and LHAASO [46]. For the H.E.S.S. study, the spectrum with the spectral extraction region with the radius of  $0.8^\circ$  was taken, and for the Fermi-LAT study, the data used was taken from a ROI if radius  $15^\circ$ . This figure shows the flux points taken from each publication, spanning an energy range starting around 1 GeV up to hundreds of TeV. The H.E.S.S. study seems to have less flux at higher energies, with cutoff energies around 20 TeV, compared to the flux from the HAWC and LHAASO publications and the HAWC analysis described in this thesis. This could be due to the spatial extent in emission, which is easier to fully take into account for wide FOV instruments, and the decreasing H.E.S.S. sensitivity at these energies. Furthermore, the new HAWC result from the analysis described here appears to be higher than the previous HAWC publication, which may be due to the latest reconstruction process of the HAWC data that enhances the sensitivity and improves the angular resolution at high energy. Additionally, in the previous publication two sources are assumed in this region; HAWC J1825-138, which is plotted in the figure, and HAWC J1825-134 which was argued in that publication to be a new source with a power-law spectrum [20]. The analysis described here seems to be in general agreement with the LHAASO points.

The Fermi-LAT study [145] in GeV energies (1 GeV to 1 TeV) compares a log-parabola model and broken power-law model, finding a preference for the log-parabola model. The broken power-law model returns a break energy of around  $\sim 115$  GeV. In general, comparing the flux points obtained in this analysis for HESS J1825-137 with previous publications, we see they are consistent.

### 5.2.8 Energy Dependent Morphology

PWN HESS J18125-137 was seen to be energy dependent by previous studies using data from H.E.S.S. and Fermi-LAT. The observed energy dependent morphology is in line with the picture that the gamma-ray emission is caused by the IC emission of electrons, with the higher energy ones with shorter cooling times being closer to the pulsar (see Chapter 1). In this section, energy-dependent morphology is also observed using HAWC data.

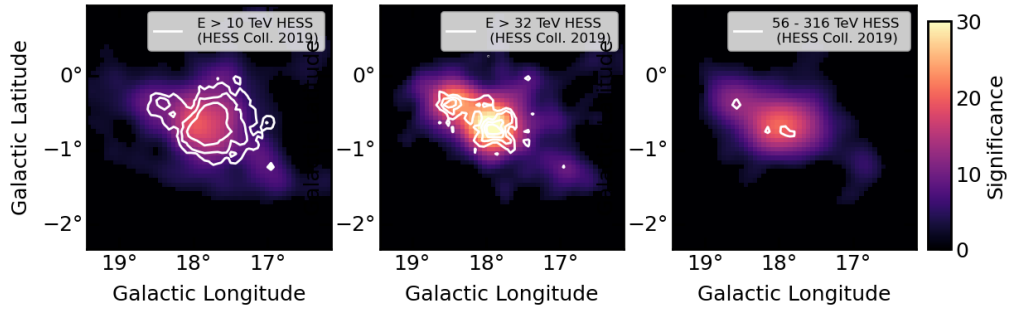


Figure 5.8: Significance maps with different energy bands using HAWC data. Contours from the H.E.S.S. publication [77] are shown in white. *Left*: [1 – 10] TeV. *Middle*: [10 – 56] TeV. *Right*: [56 – 316] TeV.

The PWN was examined in different energy bands as was done in [77]. The energy bands were chosen according to the HAWC energy bins, [1, 10], [10, 56], [56, 316] TeV. Significance maps were made for each energy region, using TsMapEstimator as before. Figure 5.8 shows the resulting significance maps. The H.E.S.S. contours (above 1 TeV, above 32 TeV, and above 56 TeV) from [77] are plotted in white on top of the maps. We see that below 10 TeV the PWN has a size of about  $1^\circ$ , and it gradually shrinks with higher energy bands, following the shrinking of the H.E.S.S. contours.

In order to deduce the radial extent within each energy bands, fits were performed for radial extent of the generalized Gaussian spatial model and spectral amplitude. This was done by slicing the data for each three energy bands. The results of the fits show that the best fit values for the radial extent of the PWN decrease with increasing energy, as shown in Figure 5.9. The bottom plot of the figure shows the size of the PWN as a function of energy, for the results of this analysis, in addition to the results from H.E.S.S. [77] and Fermi-LAT [145]. In the two instruments, they have a different definition of size, where they take a radial profile for each energy band and then fit a polynomial to it. They are also taking into account the asymmetry in the PWN's emission. Hence these two studies are more in-depth compared to the definition of size used

in this analysis, which is simply the radial extent of the generalized Gaussian spatial model. However, despite this difference in the definition of radial extent, we see that the results of this analysis are generally consistent with the trend seen by the two studies.

A separate study using the H.E.S.S. data and the size definition used in this analysis was made and the results were found to be consistent. Hence we see that the PWN HESS J1825-137 has a consistent energy dependent morphology starting from GeV energies up to hundreds of TeV.

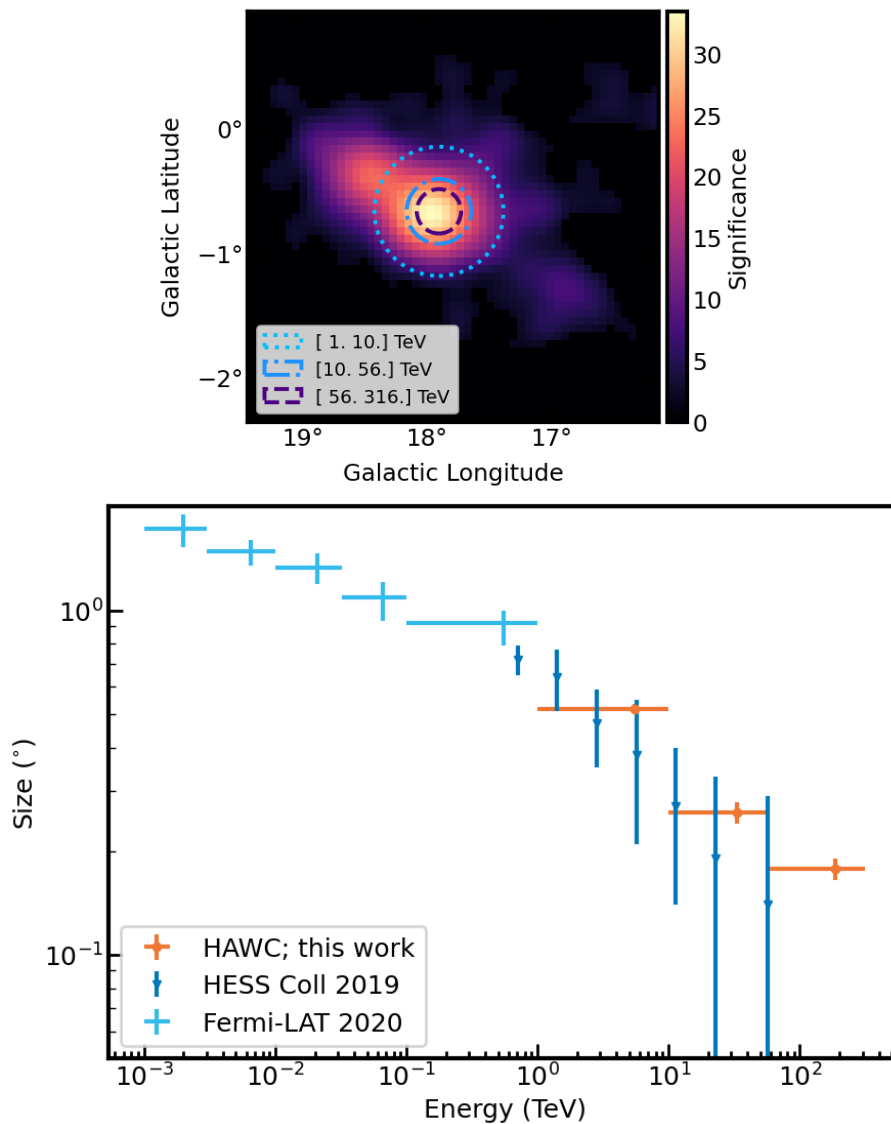


Figure 5.9: The radial extent of the PWN vs energy. The radial extent values for HAWC obtained from the three separate fits are shown in orange. The H.E.S.S. [77] and Fermi-LAT [145] points have a different definition of radial extent. The H.E.S.S. points are taken from Analysis A and include the systematic errors.

### 5.3 DISCUSSION

The energy dependent morphology of HESS J1825-137 observed with HAWC data in this study, confirming the previous findings and reaching up to hundreds of TeV, makes it an interesting PWN for particle acceleration and transport scenarios. The observed emission may be explained with IC emission from high energy electrons, while particle transport mechanisms remain to be studied.

#### 5.3.1 Particle Acceleration Mechanism

The analysis presented in this thesis has shown that the HAWC results with the newest data set are spectrally consistent with the previous findings of HAWC, LHAASO and H.E.S.S.. Moreover, we further see that the shrinking of the PWN with increasing energy, observed with Fermi-LAT and H.E.S.S. data, is confirmed with HAWC up to hundreds of TeV. The analysis shows that as the energy gets higher, the PWN's size gets smaller, and high energy emission is closer to the pulsar site, before particles travel further.

The presence of energy dependent morphology is an indication that the gamma-ray emission comes from electrons. As high energy electrons cool rapidly, they lose their energy before traveling further, unlike lower energy electrons. Hence, while hadronic emission results in energy-independent spatial distribution, leptonic emission is more extended at low energies. At the same time, UHE gamma-ray emission, as observed from HESS J1825-137 and other sources by LHAASO and HAWC, was assumed to have a hadronic origin. This assumption is based on the idea that at these energies, electrons would experience cooling, and not be able to produce gamma-ray at such high energies due to the Klein-Nishina suppression of the IC emission mechanism, as shown in Section 1.2. However, hadronic scenarios need a target material for protons to interact with.

In fact, there are leptonic single-zone models that may be able to explain the UHE emission from HESS J1825-137, without invoking hadronic emission mechanisms. In a recent study, Breuhaus et al. have shown that electrons may be able to reproduce the hard gamma-ray spectra observed by HAWC and LHAASO for this PWN, among others, with IC mechanism [42]. In an earlier study, Breuhaus et al. show that hard IC spectra up to and beyond 100 TeV are possible when IC losses dominate over synchrotron losses in radiation dominated environments, where  $\frac{U_{rad}}{U_B} \gg 1$  where  $U_{rad}$  is the radiation energy density and  $U_B$  is the magnetic energy density [41].

As seen in Section 1.2.2, a softening of the gamma-ray index occurs in the Klein-Nishina regime as the cross section decreases with energy, but at the same time electron cooling gets less efficient. Breuhaus et al. observes that a hardening of the electron spectrum that gives IC emission occurs naturally in a radiation dominated environment [41]. The left panel of Figure 5.10 shows an example electron spectrum in equilibrium between injection and losses, in a radiation dominated environment, where the different cooling processes are seen [41, 43]. At energies around 100 TeV, KN dominated cooling causes a hard-

ening in the electron spectrum which Breuhaus et al. argues can compensate for the softening of the IC emission spectrum. The right panel of Figure 5.10 shows steady-state gamma-ray spectra, with increasing values of  $\Xi = \frac{U_{\text{rad}}}{U_B}$ , meaning an increasingly radiation dominated environment. It is seen that as  $\Xi$  increases, hard gamma-ray spectra are produced due to the increased cooling time of the electrons in KN regime.

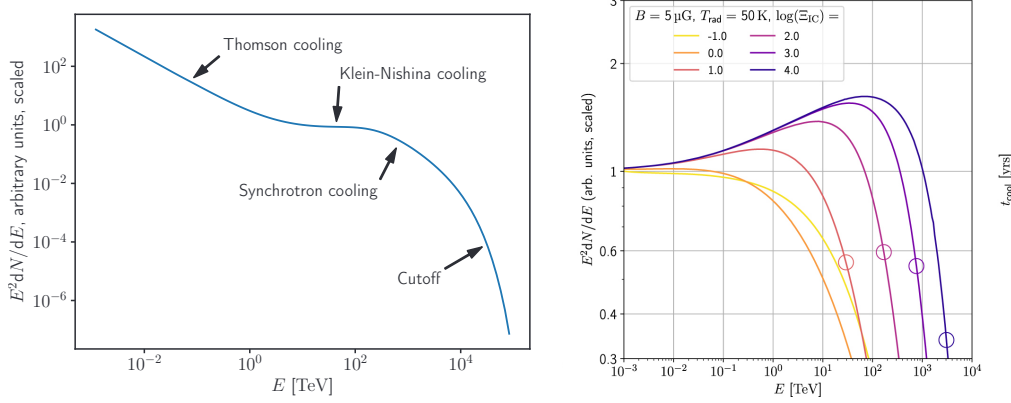


Figure 5.10: *Left*: An example electron spectrum that is in equilibrium between injection and losses, by Breuhaus et al. [43]. *Right*: Steady-state gamma-ray spectra, with increasing values of  $\Xi$ , from an electron spectrum with  $E^{-2}$  with an exponential cutoff at 10 PeV. The IC emission is able to account for higher energy emissions with increasing values of  $\Xi$ . Figure is taken from Breuhaus et al. [41].

In this case, high-power pulsars may be able to account for the observed hard spectrum in UHE sources, such as the UHE emission from the region of HESS J1825-137.

Making these considerations for the IC mechanism in the KN regime, Breuhaus et al. employ a single-zone model where accelerated electron injection time corresponds to the characteristic age of the associated pulsar of that region, with a constant homogeneous magnetic field and isotropic radiation field [42]. Ignoring source evolution, they employ for the injection rate of electrons a power-law distribution with exponential cut-off:  $Q(E) = \dot{N}_0 \left( \frac{E}{1 \text{ erg}} \right)^{-\alpha} \exp\left(-\frac{E}{E_{\text{cut}}}\right)$ , where  $\alpha$  is the injection index,  $E_{\text{cut}}$  is the cut-off energy and  $N_0$  is the normalization. They take into account losses from IC and synchrotron emissions and use the GAMERA package [78] to implement this model. For radiation fields they use a large-scale Galactic emission model and cosmic microwave background (CMB). They perform fits on some UHE emitters detected by LHAASO that are close to pulsars, including the emission around HESS J1825-137, for a fixed magnetic field of  $3 \mu\text{G}$ , fitting for  $\alpha$ ,  $N_0$  and  $E_{\text{cut}}$ , for the two pulsars in the area. They see good agreement with the results of the HAWC and LHAASO publications. In Figure 5.11 we show their fit along with the two publications. Plotting the result of this analysis along with these publications, we see that the result of this analysis is also consistent with this possibility. In light of this and the energy dependent morphology observed, we can say that an IC emission scenario is

very likely. The pulsar J1826-1334 is able to provide necessary power required and the IC emission scenario is plausible. In light of this evidence, we see that high spin down pulsars might be able to accelerate electrons to hundreds of TeV energies, as long as the special conditions are met, the main one being a strong radiation field and/or a low magnetic field.

Moreover, as said before, on the X-ray regime, the spatial extent of the PWN was found to reach up to 17 pc [164], which shows agreement with the smallest size we get, around 14 pc ( $0.17^\circ$ ), at the highest gamma-ray energy band. According to Hinton and Hofmann, the different sizes between gamma-ray PWNe and X-ray PWNe can be attributed to the difference in the energy of the parent electrons [84]. The younger electrons with many tens of TeV energy that are required to produce X-rays would have short cooling times. These electrons would not extend as far as the older electrons with longer cooling times that escape into the surrounding medium, those that may produce TeV gamma-rays with IC emission in the KN regime. Thus, the observed emission may be described using electron populations with different ages and cooling times, as is done by Principe et al. to provide a model for the the H.E.S.S. and Fermi-LAT spectral points for HESS J1825-137 [145].

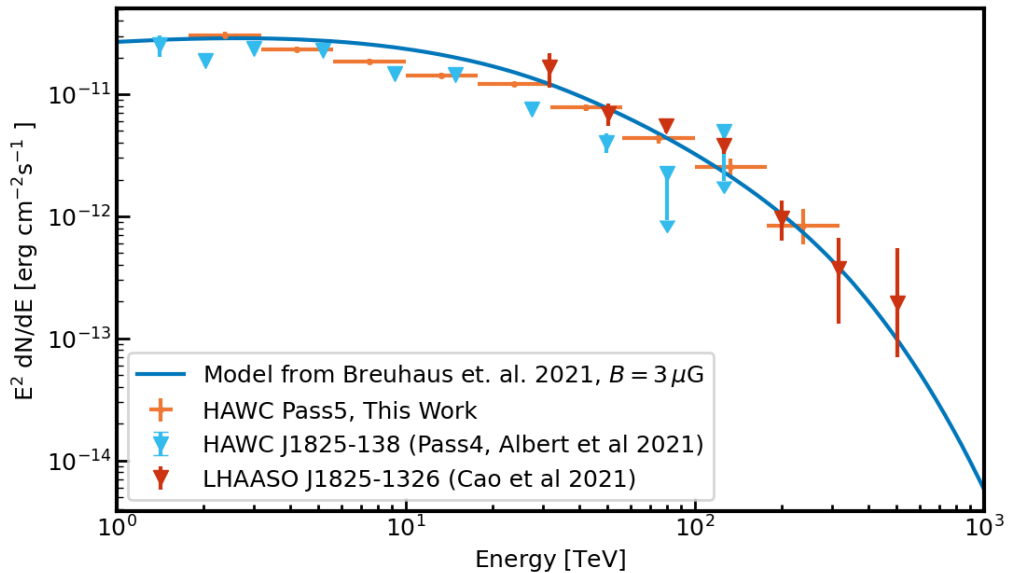


Figure 5.11: The model of IC emission valid in radiation environments from [42], which is able to describe the UHE emission seen from HESS J1825-137 with the HAWC data.

### 5.3.2 PWN Halo

Overall we observe energy dependent morphology of HESS J1825-137 using HAWC data, and are able to incorporate the emission of HAWC J1825-134 PeVatron candidate into this model.

The HAWC 2021 publication [20] suggested a scenario with two separate high energy sources, a PWN, and a PeVatron candidate. The PeVatron candidate

was proposed to be a hadronic source associated with a young star cluster and a molecular cloud in the vicinity that can serve as target material, however association with PSR J1826-1334 was also possible, and the connection with HESS J1825-137 could not be ruled out. Given the number of potential associations in the region and the resolution of HAWC Pass 4 data, it was not possible to draw any conclusion about the nature of this source.

After the revision in data reconstruction described in Section 5.2.2, the structures in this region can be better resolved with HAWC Pass 5 data. The emerging picture for the gamma-ray emission from HESS J1825-137 is now either that of a single energy dependent model accounting for all the emission, or that a separate halo component is necessary to account for the extent of the emission.

Giacinti et al. defines pulsar halos as regions where there is an overdensity of relativistic electrons and the pulsar no longer dominates the dynamics of the system [68]. Remembering the evolutionary stages explained (see Chapter 1 and Figure 1.7), HESS J1825-137 could be transitioning from Stage 2, which accounts for its asymmetric shape, into Stage 3 where a large halo of escaped electrons appears. Either way, the TeV emission can arise entirely from the IC emission of the electrons associated to this source, without any need to introduce another source powered by a hadronic mechanism.

With the IC scenario from Breuhaus et al. [42] and considering its age, HESS J1825-137 could be a hard spectrum UHE IC emitter in an intermediate evolutionary stage, according to the classification done in [68].

The current existing instruments in the UHE energy range see this region at high zenith angles, at the edges of their FOV, except for H.E.S.S. since it is on the southern hemisphere. Thanks to the improvements in data reconstruction described in [22] and 5.2.2, HAWC angular resolution at these angles enabled us to spatially resolve the structures, however the new generation gamma-ray observatories CTAO South and SWGO will deepen our understanding.

#### 5.4 FURTHER ANALYSIS USING HAWC DATA

In the analysis of the energy dependent morphology of the PWN, the radial extent was evaluated in different energy bands. A plausible next step is to check the variations in spectral index with energy, similar to the work of [77] that used H.E.S.S. data. This could allow the evaluation of the spectra for the different electron populations at different stages of cooling that contribute to the overall spectral distribution of the PWN. Furthermore, the spatial analysis can be extended by looking at the variation of the centroid with energy, to see if we also observe the centroid approaching the pulsar that is thought to supply the PWN's energy, as [77] have seen. Another aspect that should be studied is the evaluation of particle transport mechanisms. Models of diffusion and advection mechanisms and their combinations can be tested as was done in the previous studies.

It should also be assessed whether a model with spatial and spectral dependence on energy is preferred over two energy independent models, one of which represents the PWN, and the other an extended TeV halo. In order

to achieve this, the implementation of a truly energy dependent model needs to be achieved, followed by the comparison of fits performed using the two different modeling approaches.

Furthermore, with the introduction and fast spreading usage of the GADF and open source tools like *GammaPy*, multi-instrument analysis of gamma-ray emitters is becoming more common. In case of HESS J1825-137, the observations by Fermi-LAT, H.E.S.S., LHAASO and HAWC may be combined for joint analysis. Studies can be done together with other collaborations, or by performing multi-instrument fits, exploiting the full potential of *GammaPy*.

## 5.5 PROSPECTS OF THE REGION WITH SWGO

This region could be explored further once SWGO is completed and taking data. The region of HESS J1825-137 has been studied in the gamma-ray regime by several instruments, however neither of the ground particle arrays (HAWC, LHAASO) have optimal locations to study this region. Being close to the galactic center, this region is much better viewed from the southern hemisphere, for instruments such as H.E.S.S., and the upcoming instruments CTAO South, and SWGO.

As a water Cherenkov detector (WCD) array in the southern hemisphere, SWGO will be an optimal observatory for studying this region (see Section 2.3.6 for more information). Figure 5.12 shows the number of hours per day HESS J1825-137 spends below a zenith angle of  $45^\circ$  for HAWC and SWGO observatories. The coordinates for SWGO are assumed to be the recently chosen site of Pampa la Bola in Chile, which has a height of 4770 m and coordinates of  $23^\circ$  South,  $68^\circ$  West. The figure shows that SWGO will be able to observe this region more often and efficiently. Moreover, the region passes at a minimum zenith angle of  $32^\circ$  from HAWC, while for SWGO it will reach angles around  $9^\circ$ . This is one of the many interesting sources that will well be within the FOV of SWGO, which presents the possibility to examine this source at a much lower zenith angle, with angular resolution above  $0.1^\circ$  at energies above 10 TeV.

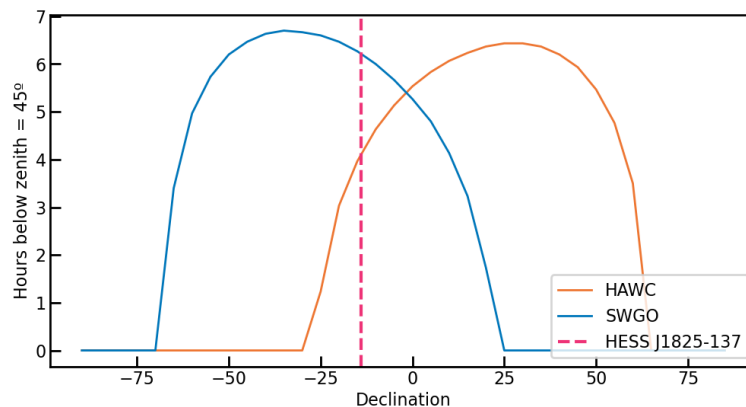


Figure 5.12: The number of hours per day HAWC and SWGO would see sources in the sky depending on their declination. The declination of HESS J1825-137 is shown with pink.

A preliminary study of this region with SWGO was carried out. This study uses the IRFs produced with the efforts of the Analysis & Simulations group of SWGO, and provided by Laura Olivera-Nieto for one year of observation. The energy binning is logarithmic with  $\log_{10}(E_{rec}/\text{GeV})$ , starting from  $\sim 30$  GeV and going up to  $\sim 316$  TeV. As previously, *Gammapy* was used for the analysis. Although SWGO will likely provide reliable measurements above those energies, as shown in Figure 2.11, this preliminary study is limited to energies up to  $\sim 316$  TeV.

For HESS J1825-137 we simulate two data sets with different models :

1. Two components, a smaller component and an extended component.
2. One component that has an energy dependent morphology

For the first option the parameters from the catalog pipeline (see Section 5.2.2), where both models are generalized Gaussian distributions with log-parabola spectra. This model can be seen to represent the idea of a PWN and its separate TeV halo. The second option of a single component model that has an energy dependent morphology is implemented only for the spatial model. The spatial model we use is a Gaussian distribution with

$$\sigma(E) = a \log(E) + b \quad (5.7)$$

where  $E$  is energy and  $a$  and  $b$  are parameters that were determined by performing a fit on the points from Figure 5.9 that showed radial extent as a function of energy. The result of the fit gives  $a = -0.32$  and  $b = 0.75$ . Hence, the radial extent parameter of the spatial model that was simulated for this SWGO study shrinks with higher energies, as observed with HAWC, H.E.S.S. and Fermi-LAT data. For spectral modeling an exponential cut-off power-law model was used, with the HAWC best fit values from Table 5.1.

In order to model the other sources in the region, namely LS5039 and HESS J1826-130, the catalog pipeline modeling was used as previously, with the HAWC analysis fit values. After the modeling was chosen, the data was simulated using *Gammapy*. The full counts maps for the second model (a single model that is energy dependent) can be seen in Appendix D. The energy bins from 1.4 TeV to 317 TeV are used for further analysis as the lower energies are background dominated.

This simulated SWGO data was then analyzed in a manner similar to the HAWC analysis described in Section 5.2, for both of the simulated data sets. The simulated data was fitted by assuming the same models as for the HAWC study, a single component model with exponential cut-off power-law and generalized Gaussian distribution for HESS J1825-137. From this fit, the spectrum shown in Figure 5.13 was obtained. The first simulated data with the two models is shown in red while the second one that assumes one model with energy dependent morphology is shown in black. In this case we can distinguish the two models at energies lower than  $\sim 10$  TeV and at about  $\sim 100$  TeV. SWGO has the potential to separate the halo like part of HESS J1825-137 from the rest.

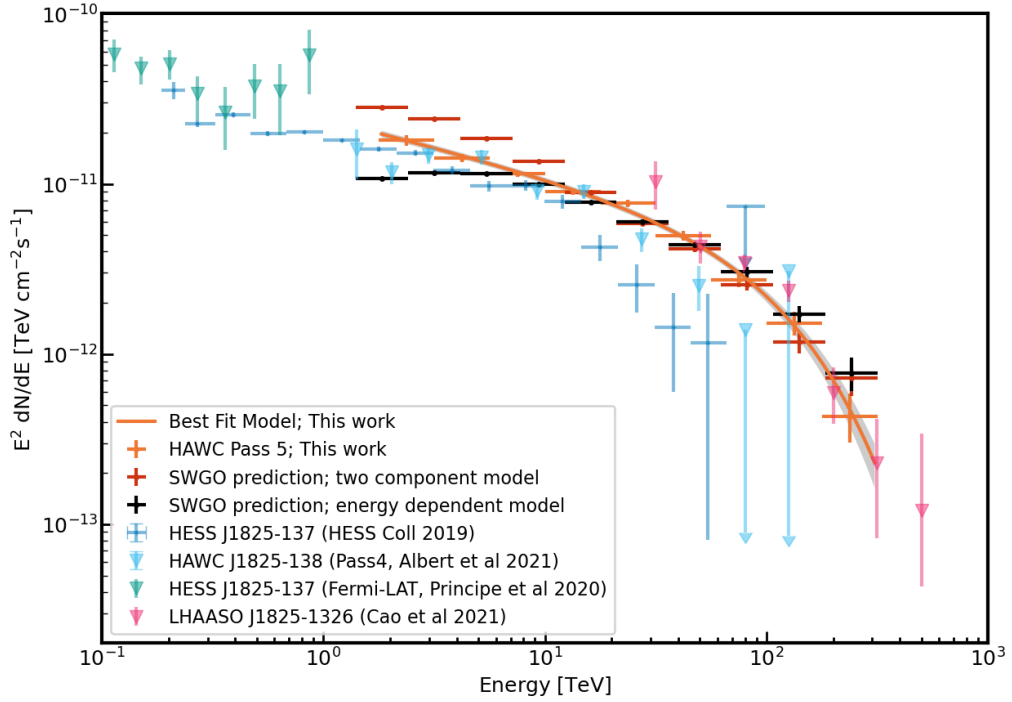


Figure 5.13: The spectral energy distribution of HESS J1825-137 with the two SWGO predictions. Simulating a two component model and fitting with a single component model gives the flux points in dark red, while simulating a single energy dependent component model and fitting with a single model gives the flux points in black.

### 5.5.1 Energy Dependent Morphology

An energy dependent analysis was performed for the simulated data with the energy dependent spatial model. The simulated data was separated into different energy regions as was done before with HAWC, and three separate fits for these regions were performed, for radial extent. The binning [1-4], [4-12], [12-36], [36-100] and [100-316] TeV was used.

The separate fits on these masked regions were performed with *Gammapy* as previously. The resulting radial extent values are plotted along with the HAWC study and the H.E.S.S. publication findings in Figure 5.14. As the PWN was modeled using a Gaussian distribution with a  $\sigma$  that follows equation 5.5, the fitted spatial extent gets smaller with energy.

With SWGO we will be able to observe this region in a wide energy range with a single instrument and get a decent angular resolution at the high energy end, in order to better resolve the structures. This will allow to better probe the energy dependent size at the highest energies. Once the radial extent of the PWN at higher energies can be analyzed with SWGO, particle transport mechanisms may be constrained further. A study similar to H. E. S. S. Collaboration et al. [77] where advection and diffusion models are compared could be conducted.

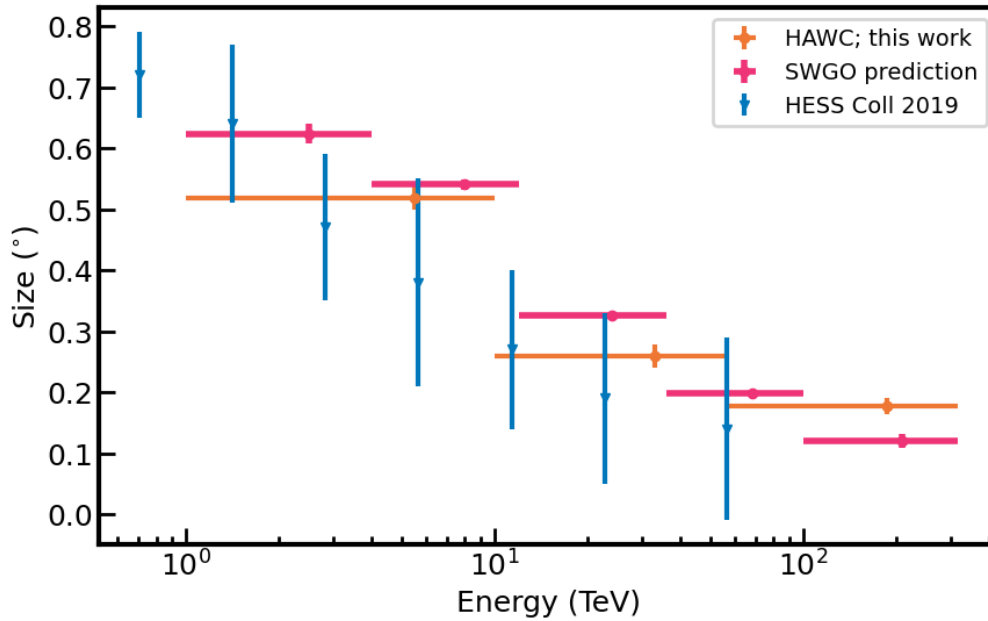


Figure 5.14: The potential for SWGO for seeing the energy dependent size of HESS J1825-137. The radial extent of the nebula was found using simulated data obtained from IRFs that are given up to 317 TeV. SWGO is expected to probe energies higher than shown here.

Even though this is a preliminary study done with simplified models, the motivation to build SWGO and start data taking becomes even clearer when we see how much potential it has.

### 5.5.2 SWGO prospects for PWN HESS J1825-137

The observations of this PWN with SWGO will enable us to probe it with a better angular resolution compared to the current observatories. SWGO's location in Pampa la Bola, Chile, means HESS J1825-137 will transit through its field of view at low zenith angles. The preliminary analysis from Section 5.5 can be repeated with actual data, followed up with the steps described above for HAWC data. Together with CTAO South, structures at low energies can be resolved and then, although CTAO South cannot reach energies as high, consistency checks can be done. Once the region is resolved better at the higher energy end with SWGO, the findings can be used to constrain particle transport mechanism theories further, investigating the change in particle transport mechanisms with distance to the PSR. This way, SWGO can also assist with more realistic models of the region where magnetohydrodynamics processes are included.

In addition to HESS J1825-137, SWGO will be able to probe other TeV bright PWNe and test them for energy dependent morphology, uncovering particle acceleration and transport mechanisms. New detections of PWNe in their Stage three development phase (see Section 1.3), with an extended halo of particles, are possible with an instrument like SWGO [130].

## 5.6 SUMMARY

HESS J1825-137 is one of the brightest UHE gamma-ray sources in the sky situated in a very complex region, that is close enough to be spatially resolvable by current instruments. The understanding of this region and the PWN has been improving in the gamma-ray regime with studies being done using data from different instruments, and new theories to explain its large extent (for example [104]) and its UHE emission (such as [42]) are being put forward. This Chapter described an analysis of the most recent HAWC data using *Gammapy* and showed that HAWC is able to resolve the individual structures in the HESS J1825-137 region. A spectrum consistent with other instruments was found. Furthermore, in this analysis, energy dependent morphology was observed, following the trend of shrinking seen by Fermi-LAT data and H.E.S.S., up to hundreds of TeV with HAWC. Studies regarding the variation of the centroid of emission and spectral index with energy, following the approaches done with other instruments, will be even more informative. The findings described here support the picture of HESS J1825-137 as a large PWN in an intermediate evolutionary stage, able to emit to UHE energies thanks to its radiation dominated environment. Future studies with SWGO will provide an even clearer picture of this region.

## CONCLUSION

---

This thesis describes the evaluation and testing of the first double-layered detector unit prototype for SWGO, in the context of the lake solution. The double-layered water Cherenkov detector (WCD) prototype served to test the lake option and at the same time verified the double-layered WCD concept. The lake option has recently been disfavored for the main array, however it is being pursued in context of the UHE extension developments. The double-layered WCD option, meanwhile, has become the baseline option for the main array.

While the verification of the double-layered WCD concept and the lake concept will continue, the work presented in this thesis helped verify and understand several aspects of prototyping.

The prototyping and evaluation of the lake concept and the double-layered WCD option were done with the following steps:

- Candidate materials were tested for their reflectivity and water contamination properties. These tests served to identify suitable materials, characterize the prototype detectors and provided input for simulations.
- Simulations of double-layered WCDs immersed in water were developed. These simulations evaluated the influence of overburden and the shielding of the lower chamber against the sideways entry of secondary particles. It was seen that when the WCD is not immersed in water, sideways entry to the lower chamber could reach up to 5%, an undesirable effect avoided in the case of the lake option.
- Mechanical tests with small sized and larger sized bladders were carried out in the MPIK workshop and the lake simulation tank facility. The filling of bladders, deployment details and other mechanical aspects of prototyping were tested and optimized in several iterations.
- A custom double-layered WCD was made by designing and testing a separate lower chamber, called the "matryoshka". This is a unique design that was modified based on several tests. The "matryoshka" was built entirely in MPIK and was inserted into a larger commercially made bladder that was already deployed into our lake simulation tank. Thus the first double-layered WCD for SWGO was made.
- Data was taken by triggering on the coincidence signal of two muon taggers, small barrels equipped with PMTs, placed under and above the double-layered WCD prototype. Two different geometries were tested and compared to a full simulation of the lake simulation tank setup, including the double-layered WCD and the two muon taggers. The parameters from material tests were varied within their uncertainties. The data was seen to

be in good agreement with the simulations, completing the verification of the first double-layered WCD prototype.

Furthermore, this thesis presents an analysis of the PWN HESS J1825-137 using the recently reconstructed HAWC data and *GammaPy*. The analysis confirms the energy dependent morphology of the PWN, namely the decrease in size of the PWN with higher energies. This decrease is seen to continue up to hundreds of TeV. A preliminary analysis using simulated SWGO data was also presented, showing that further studies of the morphology of this PWN may be able to uncover particle transport mechanisms. HESS J1825-137 is one of the highest energy and most extended PWN that was seen by HAWC and will also be observed by SWGO. PWNe, as the dominant source population in TeV energies, is a crucial class of galactic accelerators that SWGO will be focused on once it starts operation.

## APPENDIX A: MATRYOSHKA DEPLOYMENT

*The deployment of the matryoshka as planned after several tests*

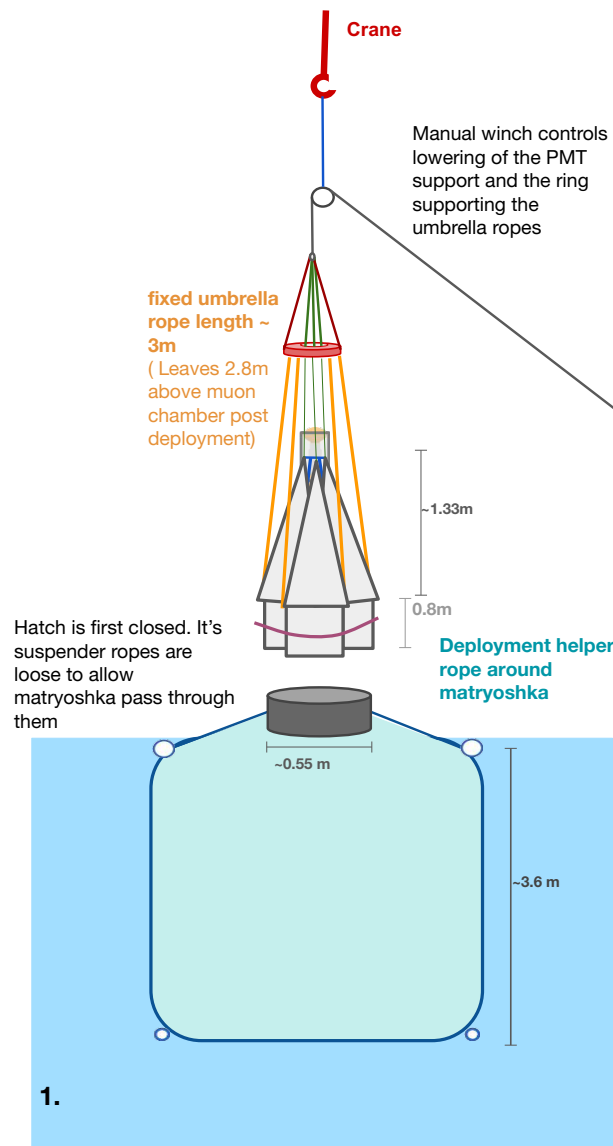


Figure A.1: The matryoshka is attached to a hallow ring via eight ropes, and the PMT support that the matryoshka is attached to has three ropes suspending it. The ropes of the PMT support and the hallow ring are all attached to a pivot point, which is suspended in air via a crane. The ropes shown in orange are not controlled directly by the winch

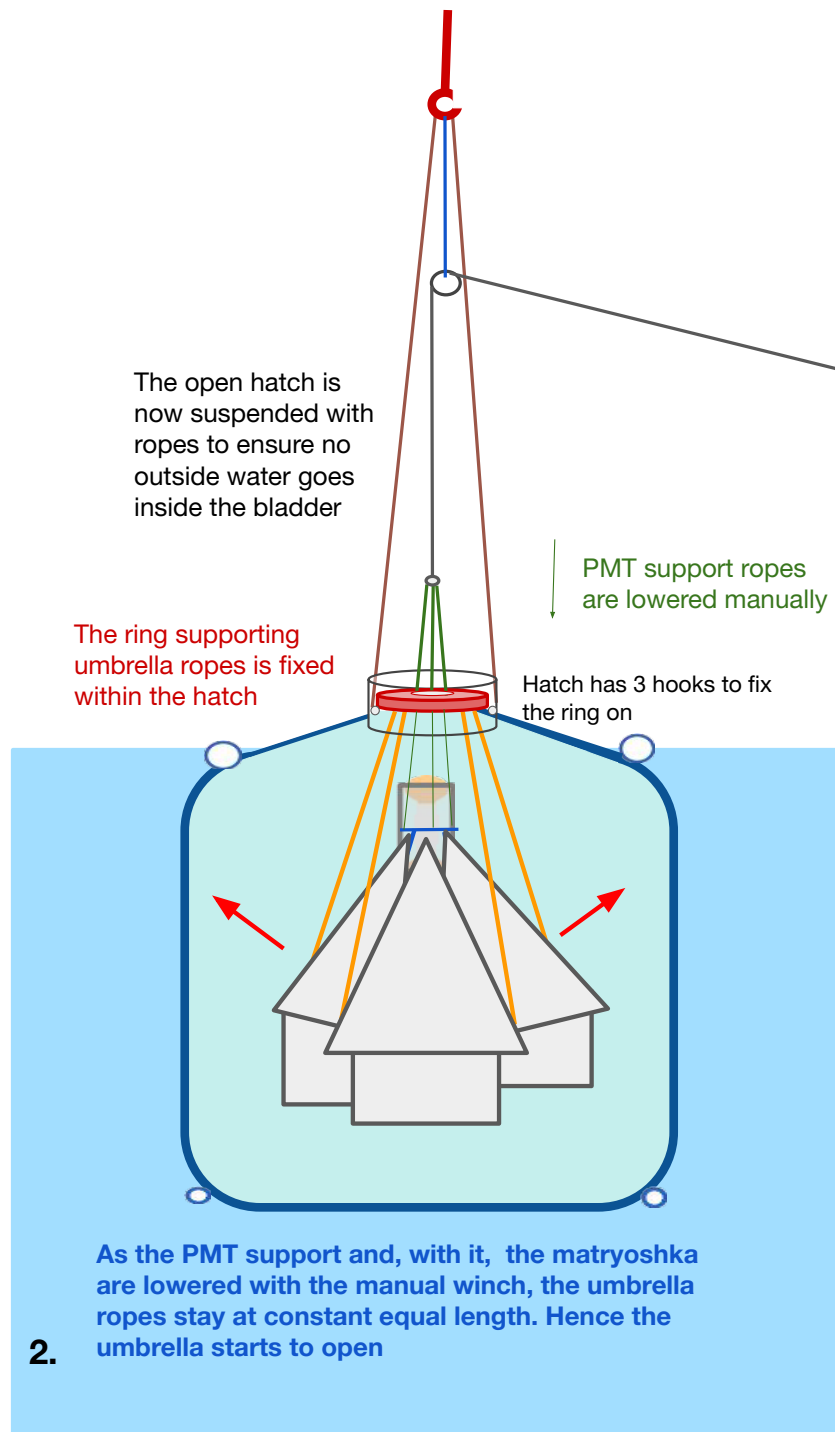


Figure A.2: The matryoshka is lowered into the bladder, two persons waited near the bladder to ensure it went in smoothly.

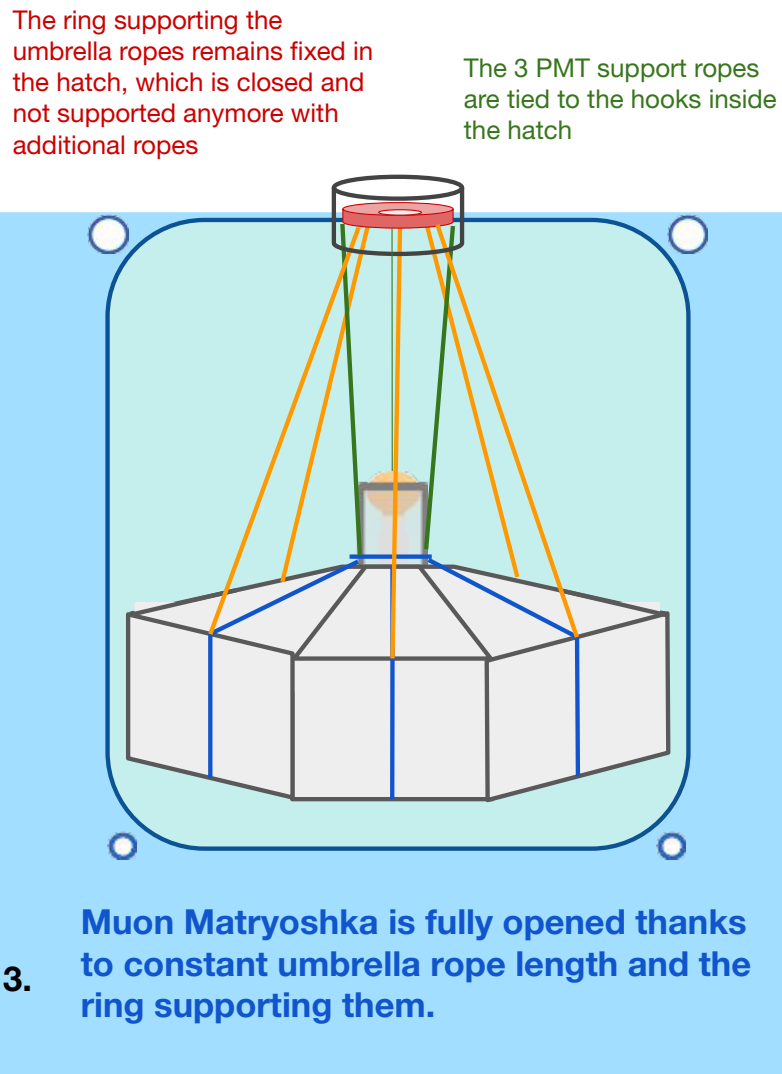


Figure A.3: Fully opened matryoshka inside the larger bladder, SWGO Unit Prototyping ready for data taking.



## REFLECTIVITY MEASUREMENTS

### B.1 INTEGRATING SPHERES AS DEVICES FOR MEASURING REFLECTIVITY

An integrating sphere is a device that spatially integrates radiation that is incident on it. It has a spherical cavity covered with a diffuse reflective coating, with entrance and exit ports. Through multiple reflections on its diffuse spherical surface, it provides a uniform radiance [110].

A fraction of the radiant flux that is received by a region within the sphere is the fractional surface area that the region covers within the sphere [110]. We can use this fact to measure the reflectivity of different materials. We use one port opening to provide an input flux, another port opening for measuring the resulting radiance, and a final larger port opening for placing the material of interest. Figure B.1 shows some of these different ports.  $A_i$  is the input port area,  $\Phi_i$  is the input flux and  $A_e$  is an exit port, which can be used for measurements.

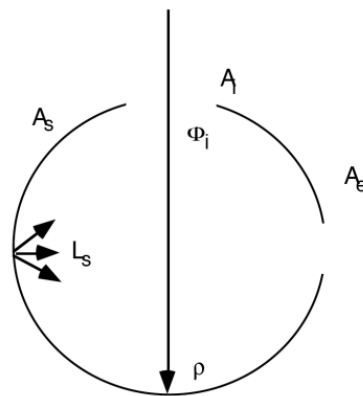


Figure B.1: Input flux hitting the inside of an integrating sphere. Figure taken from [110]

Assuming uniform reflected flux over a solid angle  $\pi$ , the radiance  $L$  (flux density per unit solid angle) of a diffuse surface is

$$L = \frac{\Phi_i \rho}{\pi A} \quad (\text{B.1})$$

where  $\Phi_i$  is the input flux,  $\rho$  is reflectance and  $A$  is the total area illuminated. For an integrating sphere, the port openings cause losses in this total area, and at the same time, there are multiple surface reflections. The total amount of flux incident on the sphere surface is  $\Phi_{received} = \Phi_i \rho F_{sphere}$ . Where  $F_{sphere}$  is the fraction of the flux received on the surface of the sphere:

$$F = \frac{A_s - A_i - A_e}{A_s}$$

where  $A_i$  is the input port area,  $A_e$  is the exit port area, which can be the output or measurement port area, and  $A_s$  is the total area of the inner sphere surface. Below we use the common notation  $F = (1 - f)$  for this term, where  $f$  is the port fraction. After one reflection, the flux incident on the sphere is  $\Phi_{received1} = \Phi_i \rho (1 - f)$ . After several reflections, expanding the equation for the total amount of flux incident on the sphere surface to a power series, we get the radiance of the sphere:

$$L_{sphere} = \frac{\Phi_i \rho (1 - f)}{\pi A (1 - (1 - \rho))} \quad (\text{B.2})$$

The latter term is called "sphere multiplier",  $M$ , and it accounts for the increase in radiance due to multiple reflections.

When the input flux  $\Phi_i$  is not known, comparing the radiance measurements of reference materials with that of the sample of interest can give the reflectance of that sample.

To achieve this, the radiance can be measured three times, where the 'material port' is covered by first the material of interest, then by a reference cap that has the same coating as the inner surface of the integrating sphere, and finally by a material with minimal reflectance (or left open, if the environment is dark). Equation B.2 shows that for each measurement, the reflectance terms and the port openings are absorbed in the sphere multiplier, hence we can compare the sphere multipliers to obtain measurements of reflectivity. The general equation for the sphere multiplier is

$$M = \frac{\rho_0}{1 - \rho_w (1 - \sum f_i) - \sum \rho_i f_i} \quad (\text{B.3})$$

where  $\rho_0$  is the initial reflectance,  $\rho_w$  is the reflectance of the wall of the sphere,  $\rho_i$  is the reflectance of a port  $i$  and  $f_i$  fractional port area of that port.

For the sample material being measured, the sphere multiplier  $M_s$  would be then

$$M_s = \frac{\rho_w}{1 - \rho_w (1 - f_i - f_m - f_s) - \rho_s f_s}$$

where  $f_s$  is the fractional area of the sample port,  $f_i$  is the fractional area of the input port,  $f_m$  is the fractional area of the measurement port, and  $\rho_s$  is the sample reflectance that we are aiming to measure. The reflectance for the input port  $\rho_i$  and for the measurement port  $\rho_m$  are zero.

For the reference measurement, where the sample port is covered with a cap that has the reflectance  $\rho_s = \rho_w$ , we have

$$M_{ref} = \frac{\rho_w}{1 - \rho_w (1 - f_i - f_m)} \quad (\text{B.4})$$

For the measurement that is taken as the zero reflectance reference, called here the "black" measurement, we have

$$M_{black} = \frac{\rho_w}{1 - \rho_w (1 - f_i - f_m - f_{bl})} \quad (\text{B.5})$$

where  $f_{bl}$  is the fractional area of the black measurement port.

For the reference, sample and black materials, we measure the radiance  $L$ , and can get a value for reflectance by comparing the sphere multipliers  $M$ . To get the reflectance of our material sample,  $\rho_s$ , we first derive  $\rho_w$  from the ratio  $M_{black}/M_{ref}$ , and then we plug this expression into the ratio  $M_s/M_{ref}$ .

Firstly, dividing equation B.5 by equation B.4 and solving for  $\rho_w$  gives the expression:

$$\rho_w = \frac{1 - M_{black}/M_{ref}}{(1 - f_i - f_m) - (M_{black}/M_{ref})(1 - f_i - f_m - f_{bl})} \quad (\text{B.6})$$

Then we plug this into the ratio  $M_x/M_{ref}$

$$\frac{M_x}{M_{ref}} = \frac{1 - \rho_w(1 - f_i - f_m)}{1 - \rho_w(1 - f_i - f_m - f_x) - f_x\rho_x}$$

Finally, our final equation to obtain the reflectivity of the material being measured is

$$\rho_x = \rho_w \left( \frac{1 - \frac{M_{black}/M_{ref}}{M_x/M_{ref}}}{1 - (M_{black}/M_{ref})} \right) \quad (\text{B.7})$$



## CONDUCTIVITY MEASUREMENTS OF TEST SAMPLES

### C.1 CONDUCTIVITY MEASUREMENTS

Conductivity of materials was monitored, as this is also a general measure of water quality. When there are changes in salinity and temperature, conductivity changes. Conductivity is caused by impurities in water. When inorganic chemicals and salts dissolve in water they leave ions which increase conductivity.

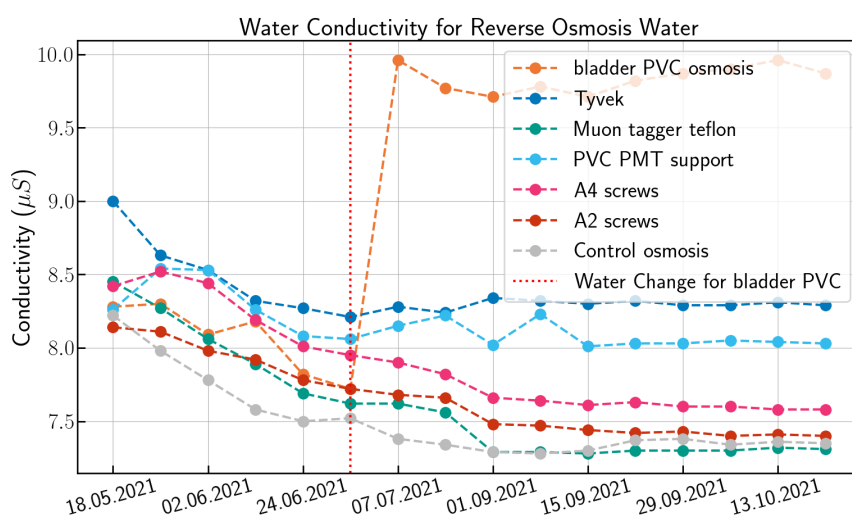


Figure C.1: Some conductivity measurements.

Along with beam transmission coefficients, a conductivity meter was used to measure changes in conductivity, along with regular measurements of temperature, since conductivity is temperature dependent <sup>1</sup>. Filtered water has a conductivity higher than the range of the conductivity meter used, above  $20.00 \mu\text{S}/\text{cm}$ , so its conductivity is not recorded.

Figure C.2 shows the results for liners, bladder PVC and some other materials. For the control barrel, stainless steel screw barrels and the PTFE barrel the conductivity went down below  $7.5 \mu\text{S}/\text{cm}$ . For the PMT support PVC and the Tyvek conductivity went down less, staying at about  $8 \mu\text{S}/\text{cm}$ . The bladder PVC barrel has a sharp change in conductivity due to the water change on July 2021. The decrease in conductivity observed over time is puzzling as this would indicate that the water is getting more pure.

<sup>1</sup> Temperature measurements are not included but can be provided on request.

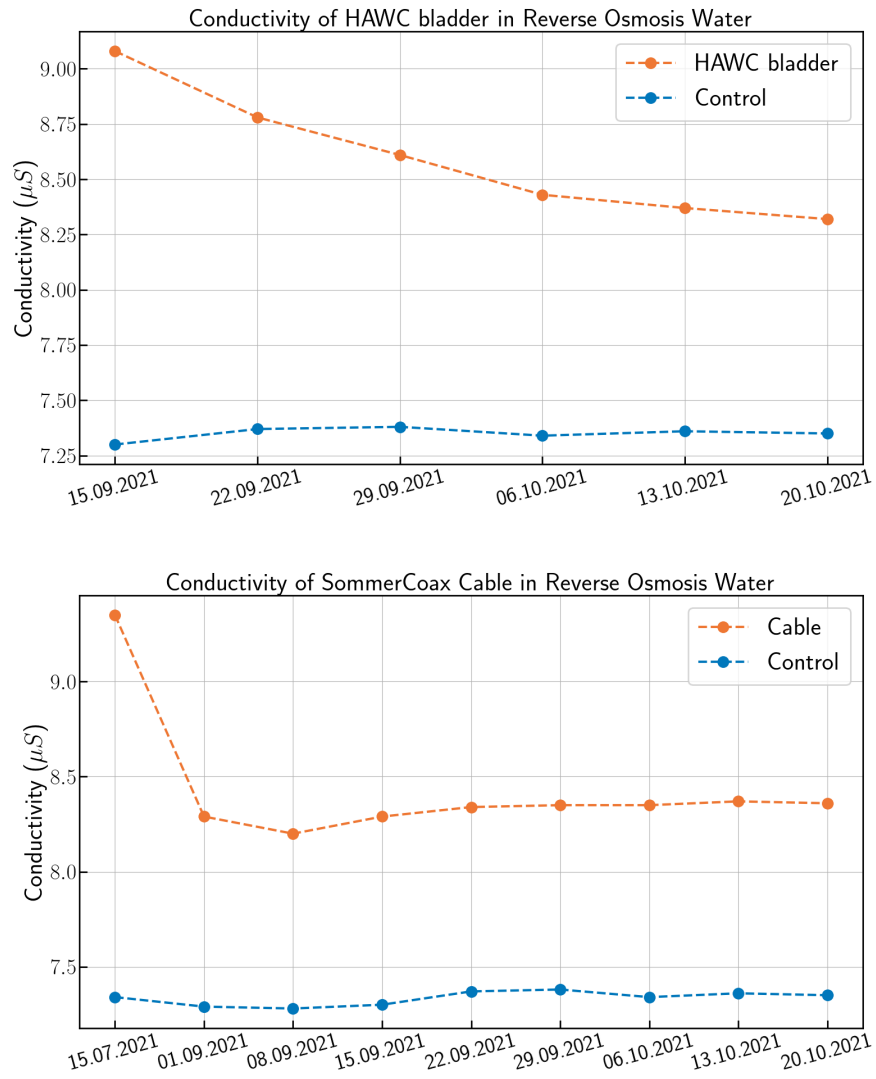


Figure C.2: Some conductivity measurements.

## COUNTS MAPS FOR SWGO SENSITIVITY

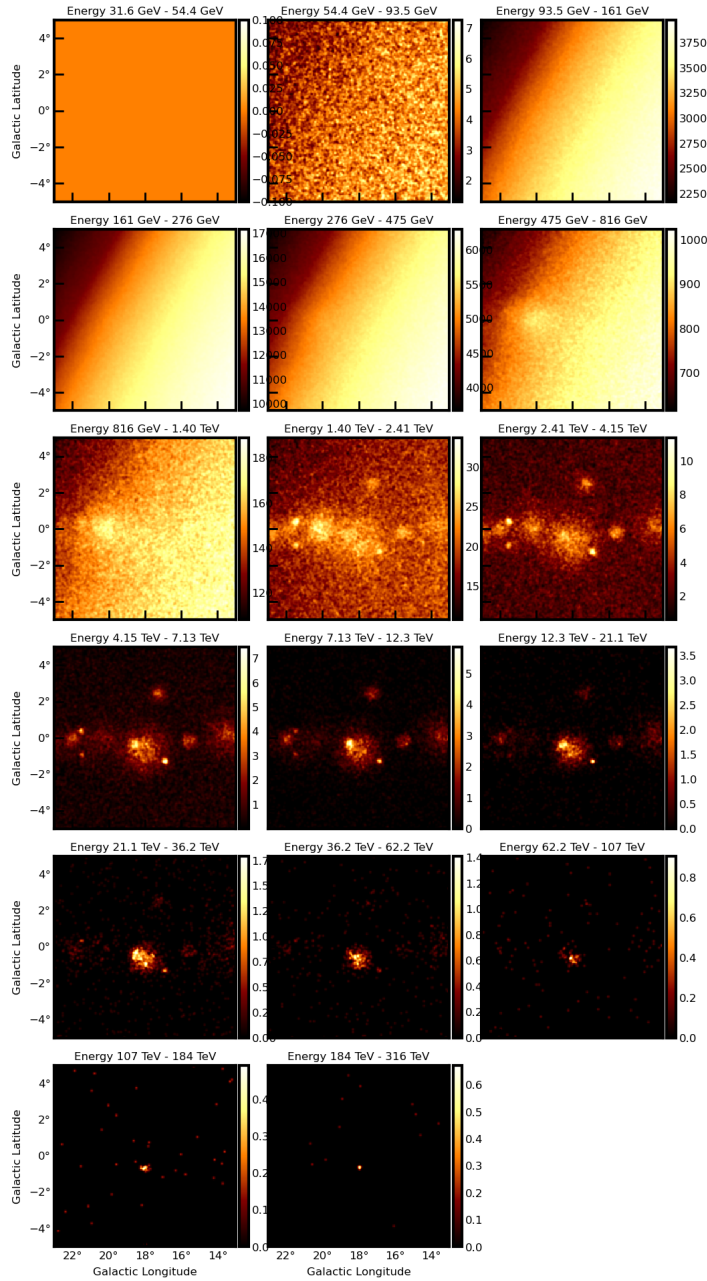


Figure D.1: The counts maps for different energy bins

The sensitivity of SWGO to the HESS J1825-137 region within different energy ranges can be seen from Figure D.1, which shows simulated counts maps, assuming the energy dependent spatial model. The background dominates in the bands below  $\sim 1$  TeV.



## PLANNED TESTS IN A WAVE BASIN

---

The impact of waves on bladders was outlined in Section 3.2.3. In order to evaluate the behaviour of our bladders under wave conditions that may be expected in lakes, we will be making tests in an indoor wave basin in Nantes, France, namely in the Research Laboratory in Hydrodynamics, Energetics and Atmospheric Environment (LHEEA) [91]. The tests will address many aspects of the lake concept, with the monitoring of PMT and bladder positions and motions being one of the key aspects. These tests will also consider the designs for the UHE extension for SWGO that is under evaluation.



Figure E.1: The hydrodynamics and ocean engineering tank at LHEEA, France. The segmented wavemaker is seen in the background. Figure taken from [91].

### E.1 FACILITY

The wave tests will occur in the large (50 m × 30 m) hydrodynamic and ocean engineering tank at LHEEA/Nantes, shown in Figure E.1. The 5 m deep tank is equipped with a segmented wave maker with 48 independent flaps that is able to generate waves covering the entire relevant parameter space for lakes: wave frequencies between 0.5 and 5 Hz and wave heights up to 1 m [91]. The facility is able to provide above-water 3D tracking of makers that can be attached to bladders and additionally below-water 3D tracking of the bladder shapes.

The tank is 5 m deep, has three moveable transverse footbridges and a preparation area next to it. Crucially, this tank is equipped with a segmented wave maker with 48 independent flaps that is able to generate waves covering the entire relevant parameter space for lakes: wave frequencies between 0.5 and 5 Hz and wavemheights up to 1 m [91].

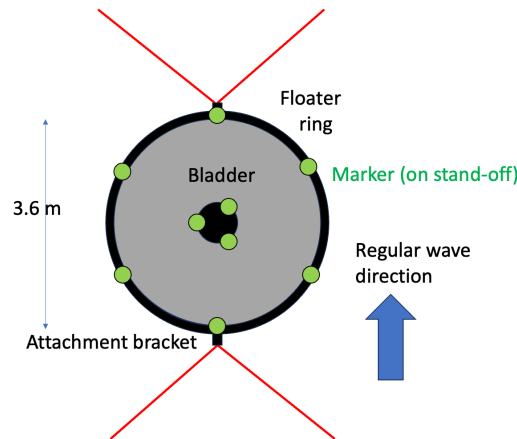


Figure E.2: Sketch of the one-bladder setup for the upcoming wave basin tests in France. Figure credit: Werner Hofmann.

## E.2 TEST SETUP

The tests will take place over a one week period, in early 2025. We will test state-of-the-art Aquamate ([27]) bladders, both in separated and interconnected forms (as originally planned for the lake array). It is also possible that we include bladders from our colleagues from China, for testing of UHE extension technologies.

Once the bladders are anchored into the tank, we will use the segmented wave maker to generate waves of different frequencies and heights, starting from small numbers and reaching up to 1 m. The bladders will have fully-functional PMT units and readout installed to them, and the light tightness of the bladders after enduring strong waves will be monitored via the PMT signals. In addition to what is provided by the facility, we will also equip each bladder with multiple 9-axis inertial sensors that will monitor the motion of PMT units hanging inside the bladders. Furthermore, the anchoring forces on the springs connected to the bladder floaters will also be monitored.

We will have two test setups; one that will consist of a single state-of-the-art Aquamate ([27]) double-layer bladder, and a setup with four interconnected bladders, as was originally planned for the lake array. It is also possible that we include deep muon bladders of our colleagues from China, for testing of UHE extension technologies.

## E.3 TEST PLAN

The plan is to first start with a single bladder. The bladder will be deployed and fixed in position with anchors connected to springs. Once the motion sensors are all fixed in position, the segmented wave maker will be used to generate waves of different frequencies and heights, starting from small numbers and reaching up to 1 m. After these tests, the same procedure will be repeated for the four bladders that are connected. The bladders produced in China, such as

the narrow muon detector bladders, for UHE extension evaluation could also be tested during these wave tests in a similar manner.

The analysis of the data will show us the behavior of the bladders and PMTs inside them depending on the wave conditions. These tests will also enable us to test our scheme as a whole, including deployment and recovery of bladders, interconnections between bladders, anchoring and PMT deployment.



## BIBLIOGRAPHY

---

- [1] A. A. Abdo et al. "TeV Gamma-Ray Sources from a Survey of the Galactic Plane with Milagro." In: *The Astrophysical Journal* 664.2 (2007), p. L91. DOI: [10.1086/520717](https://doi.org/10.1086/520717). URL: <https://dx.doi.org/10.1086/520717>.
- [2] A. Abdul Halim et al. "Constraining the sources of ultra-high-energy cosmic rays across and above the ankle with the spectrum and composition data measured at the Pierre Auger Observatory." In: *Journal of Cosmology and Astroparticle Physics* 2023.5, 024 (May 2023), p. 024. DOI: [10.1088/1475-7516/2023/05/024](https://doi.org/10.1088/1475-7516/2023/05/024). arXiv: [2211.02857](https://arxiv.org/abs/2211.02857) [astro-ph.HE].
- [3] A. U. Abeysekara et al. "Search for Gamma-Rays from the unusually bright GRB 130427A with the HAWC Gamma-ray Observatory." In: *The Astrophysical Journal* 800.2 (2015), p. 78. DOI: [10.1088/0004-637x/800/2/78](https://doi.org/10.1088/0004-637x/800/2/78). URL: <https://doi.org/10.1088/0004-637x/800/2/78>.
- [4] A. U. Abeysekara et al. "Extended gamma-ray sources around pulsars constrain the origin of the positron flux at Earth." In: *Science* 358.6365 (Nov. 2017), pp. 911–914. DOI: [10.1126/science.aan4880](https://doi.org/10.1126/science.aan4880). arXiv: [1711.06223](https://arxiv.org/abs/1711.06223) [astro-ph.HE].
- [5] A. U. Abeysekara et al. "Observation of the Crab Nebula with the HAWC Gamma-Ray Observatory." In: *The Astrophysical Journal* 843.1, 39 (July 2017), p. 39. DOI: [10.3847/1538-4357/aa7555](https://doi.org/10.3847/1538-4357/aa7555). arXiv: [1701.01778](https://arxiv.org/abs/1701.01778) [astro-ph.HE].
- [6] A. U. Abeysekara et al. "Very-high-energy particle acceleration powered by the jets of the microquasar SS 433." In: *Nature* 562.7725 (Oct. 2018), pp. 82–85. DOI: [10.1038/s41586-018-0565-5](https://doi.org/10.1038/s41586-018-0565-5). arXiv: [1810.01892](https://arxiv.org/abs/1810.01892) [astro-ph.HE].
- [7] A. U. Abeysekara et al. "Measurement of the Crab Nebula Spectrum Past 100 TeV with HAWC." In: *The Astrophysical Journal* 881.2, 134 (Aug. 2019), p. 134. DOI: [10.3847/1538-4357/ab2f7d](https://doi.org/10.3847/1538-4357/ab2f7d). arXiv: [1905.12518](https://arxiv.org/abs/1905.12518) [astro-ph.HE].
- [8] A.U. Abeysekara et al. "VERITAS Detection of LS 5039 and HESS J1825-137." In: *Astroparticle Physics* 117 (2020), p. 102403. ISSN: 0927-6505. DOI: <https://doi.org/10.1016/j.astropartphys.2019.102403>. URL: <https://www.sciencedirect.com/science/article/pii/S0927650519302063>.
- [9] HAWC Collaboration Abeysekara A. U. et al. "The High-Altitude Water Cherenkov (HAWC) observatory in México: The primary detector." In: *Nuclear Instruments and Methods in Physics Research A* 1052, 168253 (July 2023), p. 168253. DOI: [10.1016/j.nima.2023.168253](https://doi.org/10.1016/j.nima.2023.168253). arXiv: [2304.00730](https://arxiv.org/abs/2304.00730) [astro-ph.HE].

- [10] Pedro Abreu, Andrea Albert, Ruben Jose Alfaro, Alexander Alfonso, and César et al. Alvarez. “Estimating the potential of SWGO to measure the composition-dependent behaviour of the CR anisotropy.” In: *Proceedings of 38th International Cosmic Ray Conference — PoS(ICRC2023)*. Vol. 444. 2023, p. 486. DOI: [10.22323/1.444.0486](https://doi.org/10.22323/1.444.0486).
- [11] T. Abu-Zayyad, D. Ivanov, C. C. H. Jui, J. H. Kim, J. N. Matthews, J. D. Smith, S. B. Thomas, G. B. Thomson, and Z. Zundel. “The Knee and the Second Knee of the Cosmic-Ray Energy Spectrum.” In: *arXiv e-prints*, arXiv:1803.07052 (Mar. 2018), arXiv:1803.07052. arXiv: [1803.07052](https://arxiv.org/abs/1803.07052) [astro-ph.HE].
- [12] K. H. Ackermann et al. “The Gerda experiment for the search of  $\nu\beta\beta$  decay in  $^{76}\text{Ge}$ .” In: *European Physical Journal C* 73, 2330 (Mar. 2013), p. 2330. DOI: [10.1140/epjc/s10052-013-2330-0](https://doi.org/10.1140/epjc/s10052-013-2330-0). arXiv: [1212.4067](https://arxiv.org/abs/1212.4067) [physics.ins-det].
- [13] S. Agostinelli et al. “GEANT4—a simulation toolkit.” In: *Nucl. Instrum. Meth. A* 506 (2003), pp. 250–303. DOI: [10.1016/S0168-9002\(03\)01368-8](https://doi.org/10.1016/S0168-9002(03)01368-8).
- [14] F. A. Aharonian, S. R. Kelner, and A. Yu. Prosekin. “Angular, spectral, and time distributions of highest energy protons and associated secondary gamma rays and neutrinos propagating through extragalactic magnetic and radiation fields.” In: *Physical Review D* 82.4, 043002 (Aug. 2010), p. 043002. DOI: [10.1103/PhysRevD.82.043002](https://doi.org/10.1103/PhysRevD.82.043002). arXiv: [1006.1045](https://arxiv.org/abs/1006.1045) [astro-ph.HE].
- [15] F. Aharonian et al. “A New Population of Very High Energy Gamma-Ray Sources in the Milky Way.” In: *Science* 307.5717 (Mar. 2005), pp. 1938–1942. DOI: [10.1126/science.1108643](https://doi.org/10.1126/science.1108643). arXiv: [astro-ph/0504380](https://arxiv.org/abs/astro-ph/0504380) [astro-ph].
- [16] F. Aharonian et al. “3.9 day orbital modulation in the TeV  $\gamma$ -ray flux and spectrum from the X-ray binary LS 5039.” In: *Astronomy and Astrophysics* 460.3 (Dec. 2006), pp. 743–749. DOI: [10.1051/0004-6361:20065940](https://doi.org/10.1051/0004-6361:20065940). arXiv: [astro-ph/0607192](https://arxiv.org/abs/astro-ph/0607192) [astro-ph].
- [17] F. Aharonian et al. “Energy dependent  $\gamma$ -ray morphology in the pulsar wind nebula HESS J1825-137.” In: *Astronomy and Astrophysics* 460.2 (Dec. 2006), pp. 365–374. DOI: [10.1051/0004-6361:20065546](https://doi.org/10.1051/0004-6361:20065546). arXiv: [astro-ph/0607548](https://arxiv.org/abs/astro-ph/0607548) [astro-ph].
- [18] F. Aharonian et al. “The H.E.S.S. Survey of the Inner Galaxy in Very High Energy Gamma Rays.” In: *The Astrophysical Journal* 636.2 (Jan. 2006), pp. 777–797. DOI: [10.1086/498013](https://doi.org/10.1086/498013). arXiv: [astro-ph/0510397](https://arxiv.org/abs/astro-ph/0510397) [astro-ph].
- [19] Felix A. Aharonian. *Very High Energy Cosmic Gamma Radiation*. New Jersey: World Scientific, 2004.
- [20] A. Albert et al. “Evidence of 200 TeV Photons from HAWC J1825-134.” In: *The Astrophysical Journal Letters* 907.2 (2021), p. L30. DOI: [10.3847/2041-8213/abd77b](https://doi.org/10.3847/2041-8213/abd77b). URL: <https://dx.doi.org/10.3847/2041-8213/abd77b>.

- [21] A. Albert et al. “Validation of standardized data formats and tools for ground-level particle-based gamma-ray observatories.” In: *Astronomy and Astrophysics* 667, A36 (Nov. 2022), A36. DOI: [10.1051/0004-6361/202243527](https://doi.org/10.1051/0004-6361/202243527). arXiv: [2203.05937](https://arxiv.org/abs/2203.05937) [astro-ph.IM].
- [22] A. Albert et al. “Performance of the HAWC Observatory and TeV Gamma-Ray Measurements of the Crab Nebula with Improved Extensive Air Shower Reconstruction Algorithms.” In: *The Astrophysical Journal* 972.2 (2024), p. 144. DOI: [10.3847/1538-4357/ad5f2d](https://doi.org/10.3847/1538-4357/ad5f2d). URL: <https://dx.doi.org/10.3847/1538-4357/ad5f2d>.
- [23] D.E. Alexandreas et al. “The CYGNUS extensive air-shower experiment.” In: *Nuclear Instruments and Methods in Physics Research Section A: Accelerators, Spectrometers, Detectors and Associated Equipment* 311.1 (1992), pp. 350–367. ISSN: 0168-9002. DOI: [https://doi.org/10.1016/0168-9002\(92\)90883-6](https://doi.org/10.1016/0168-9002(92)90883-6). URL: <https://www.sciencedirect.com/science/article/pii/0168900292908836>.
- [24] U. Barres de Almeida, Pedro Assis, Luis M. Domingues Mendes, Guilherme F. Franco, Borja S. González, Luis F. Mendes, and Gizele L.P. Santos. “The Mercedes water Cherenkov detector: a multi-PMT shallow tank design proposal for ground-based gamma-ray observatories.” In: *Proceedings of 38th International Cosmic Ray Conference — PoS(ICRC2023)*. Vol. 444. 2023, p. 601. DOI: [10.22323/1.444.0601](https://doi.org/10.22323/1.444.0601).
- [25] Ulisses Barres de Almeida. *SWG0: Status Update*. 8th Gamma Symposium Presentation. 2024. URL: [https://indico.ict.inaf.it/event/2661/contributions/19101/attachments/8857/18211/SWG0\\_Gamma2024\\_Milano.pdf](https://indico.ict.inaf.it/event/2661/contributions/19101/attachments/8857/18211/SWG0_Gamma2024_Milano.pdf).
- [26] Rafael Alves Batista et al. “Open Questions in Cosmic-Ray Research at Ultrahigh Energies.” In: *Frontiers in Astronomy and Space Sciences* 6, 23 (June 2019), p. 23. DOI: [10.3389/fspas.2019.00023](https://doi.org/10.3389/fspas.2019.00023). arXiv: [1903.06714](https://arxiv.org/abs/1903.06714) [astro-ph.HE].
- [27] *Aquamate*. 2024. URL: <https://www.aquamate.com.au/water-tanks/> (visited on 07/07/2024).
- [28] Fabrice Ardhuin. *Ocean waves in geosciences*. Tech. rep. Laboratoire d’Océanographie Physique et Spatiale, 2023. DOI: [10.13140/RG.2.2.16019.78888/11](https://doi.org/10.13140/RG.2.2.16019.78888/11).
- [29] P. Assis et al. “The Mercedes water Cherenkov detector.” In: *European Physical Journal C* 82.10, 899 (Oct. 2022), p. 899. DOI: [10.1140/epjc/s10052-022-10857-1](https://doi.org/10.1140/epjc/s10052-022-10857-1). arXiv: [2203.08782](https://arxiv.org/abs/2203.08782) [physics.ins-det].
- [30] R. Atkins et al. “Observation of TeV Gamma Rays from the Crab Nebula with Milagro Using a New Background Rejection Technique.” In: *The Astrophysical Journal* 595.2 (Oct. 2003), pp. 803–811. DOI: [10.1086/377498](https://doi.org/10.1086/377498). arXiv: [astro-ph/0305308](https://arxiv.org/abs/astro-ph/0305308) [astro-ph].

- [31] M. Ave, J. A. Hinton, R. A. Vázquez, A. A. Watson, and E. Zas. “Constraints on the ultrahigh-energy photon flux using inclined showers from the Haverah Park array.” In: *Physical Review D* 65.6, 063007 (Mar. 2002), p. 063007. DOI: [10.1103/PhysRevD.65.063007](https://doi.org/10.1103/PhysRevD.65.063007). arXiv: [astro-ph/0110613](https://arxiv.org/abs/astro-ph/0110613) [astro-ph].
- [32] Nicolai Bailly et al. “Two-year optical site characterization for the Pacific Ocean Neutrino Experiment (P-ONE) in the Cascadia Basin.” In: *European Physical Journal C* 81.12, 1071 (Dec. 2021), p. 1071. DOI: [10.1140/epjc/s10052-021-09872-5](https://doi.org/10.1140/epjc/s10052-021-09872-5). arXiv: [2108.04961](https://arxiv.org/abs/2108.04961) [astro-ph.IM].
- [33] C. Bauer et al. “Qualification tests of 474 photomultiplier tubes for the inner detector of the Double Chooz experiment.” In: *Journal of Instrumentation* 6.6 (June 2011), p. 6008. DOI: [10.1088/1748-0221/6/06/P06008](https://doi.org/10.1088/1748-0221/6/06/P06008). arXiv: [1104.0758](https://arxiv.org/abs/1104.0758) [physics.ins-det].
- [34] J.J. Beatty, J. Matthews, and S.P. Wakely. *Cosmic Rays, PDG*. 2019. URL: <https://pdg.lbl.gov/2019/reviews/rpp2019-rev-cosmic-rays.pdf> (visited on 09/09/2021).
- [35] Jose Bellido and Michael Schneider. “Manufacture Details of a SWGO Double-Layer Tank Design - Water Cherenkov Detector Prototype.” In: *Proceedings of 38th International Cosmic Ray Conference — PoS(ICRC2023)*. Vol. 444. 2021, p. 803. DOI: [10.22323/1.444.0803](https://doi.org/10.22323/1.444.0803).
- [36] I. A. Belolaptikov, Bezrukov, et al. “The Baikal underwater neutrino telescope: Design, performance, and first results.” In: *Astroparticle Physics* 7.3 (Aug. 1997), pp. 263–282. DOI: [10.1016/S0927-6505\(97\)00022-4](https://doi.org/10.1016/S0927-6505(97)00022-4).
- [37] John M. Blondin, Roger A. Chevalier, and Dargan M. Frierson. “Pulsar Wind Nebulae in Evolved Supernova Remnants.” In: *The Astrophysical Journal* 563.2 (Dec. 2001), pp. 806–815. DOI: [10.1086/324042](https://doi.org/10.1086/324042). arXiv: [astro-ph/0107076](https://arxiv.org/abs/astro-ph/0107076) [astro-ph].
- [38] George R. Blumenthal and Robert J. Gould. “Bremsstrahlung, Synchrotron Radiation, and Compton Scattering of High-Energy Electrons Traversing Dilute Gases.” In: *Rev. Mod. Phys.* 42 (2 1970), pp. 237–270. DOI: [10.1103/RevModPhys.42.237](https://doi.org/10.1103/RevModPhys.42.237). URL: <https://link.aps.org/doi/10.1103/RevModPhys.42.237>.
- [39] A. Borione et al. “A large air shower array to search for astrophysical sources emitting gamma-rays with energies  $\geq 10^{14}$  eV.” In: *Nuclear Instruments and Methods in Physics Research Section A: Accelerators, Spectrometers, Detectors and Associated Equipment* 346.1 (1994), pp. 329–352. ISSN: 0168-9002. DOI: [https://doi.org/10.1016/0168-9002\(94\)90722-6](https://doi.org/10.1016/0168-9002(94)90722-6). URL: <https://www.sciencedirect.com/science/article/pii/0168900294907226>.
- [40] J. Bosboom and M.J.F. Stive. *Coastal Dynamics*. Delft University of Technology, 2023.

- [41] M. Breuhaus, J. Hahn, C. Romoli, B. Reville, G. Giacinti, R. Tuffs, and J. A. Hinton. "Ultra-high Energy Inverse Compton Emission from Galactic Electron Accelerators." In: *The Astrophysical Journal Letters* 908.2 (2021), p. L49. DOI: [10.3847/2041-8213/abe41a](https://doi.org/10.3847/2041-8213/abe41a). URL: <https://dx.doi.org/10.3847/2041-8213/abe41a>.
- [42] M. Breuhaus, B. Reville, and J. A. Hinton. "Pulsar wind nebula origin of the LHAASO-detected ultra-high energy  $\gamma$ -ray sources." In: *Astronomy and Astrophysics* 660, A8 (Apr. 2022), A8. DOI: [10.1051/0004-6361/202142097](https://doi.org/10.1051/0004-6361/202142097). arXiv: [2109.05296](https://arxiv.org/abs/2109.05296) [astro-ph.HE].
- [43] Mischa Breuhaus, Joachim Hahn, Carlo Romoli, Brian Reville, Gwenael Giacinti, James Anthony Hinton, and Richard Tuffs. "Ultra-high energy inverse Compton emission from Galactic electron accelerators." In: *European Physical Journal Web of Conferences*. Vol. 280. European Physical Journal Web of Conferences. Sept. 2023, 02001, p. 02001. DOI: [10.1051/epjconf/202328002001](https://doi.org/10.1051/epjconf/202328002001).
- [44] M Bustamante et al. "High-energy cosmic-ray acceleration." In: (2010). DOI: [10.5170/CERN-2010-001.533](https://doi.org/10.5170/CERN-2010-001.533). URL: <https://cds.cern.ch/record/1249755>.
- [45] Joakim Børkja. *Dynamic Analysis of Floating Dock Structures*. 2015.
- [46] Zhen Cao et al. "Ultrahigh-energy photons up to 1.4 petaelectronvolts from 12  $\gamma$ -ray Galactic sources." In: *Nature* 594:7861 (June 2021), pp. 33–36. DOI: [10.1038/s41586-021-03498-z](https://doi.org/10.1038/s41586-021-03498-z).
- [47] David Carreto Fidalgo. "Pulsars and Pulsar Wind Nebulae." In: *Revealing the Most Energetic Light from Pulsars and Their Nebulae*. Cham: Springer International Publishing, 2019, pp. 19–47. ISBN: 978-3-030-24194-0. DOI: [10.1007/978-3-030-24194-0\\_2](https://doi.org/10.1007/978-3-030-24194-0_2). URL: [https://doi.org/10.1007/978-3-030-24194-0\\_2](https://doi.org/10.1007/978-3-030-24194-0_2).
- [48] D.J.T. Carter. "Prediction of wave height and period for a constant wind velocity using the JONSWAP results." In: *Ocean Engineering* 9.1 (1982), pp. 17–33. ISSN: 0029-8018. DOI: [https://doi.org/10.1016/0029-8018\(82\)90042-7](https://doi.org/10.1016/0029-8018(82)90042-7). URL: <https://www.sciencedirect.com/science/article/pii/0029801882900427>.
- [49] G. Castelletti, E. Giacani, and G. Dubner. "First EVLA radio observations towards two TeV sources:HESS J1809-193 and HESS J1825-137." In: *Boletín de la Asociación Argentina de Astronomía La Plata Argentina* 55 (Jan. 2012), pp. 179–183.
- [50] T. R. Clifton, A. G. Lyne, A. W. Jones, J. McKenna, and M. Ashworth. "A high-frequency survey of the galactic plane for young and distant pulsars." In: *Monthly Notices of the Royal Astronomical Society* 254.2 (Jan. 1992), pp. 177–184. ISSN: 0035-8711. DOI: [10.1093/mnras/254.2.177](https://doi.org/10.1093/mnras/254.2.177). eprint: <https://academic.oup.com/mnras/article-pdf/254/2/177/18223663/mnras254-0177.pdf>. URL: <https://doi.org/10.1093/mnras/254.2.177>.

- [51] T Collins, G Rowell, A M W Mitchell, F Voisin, Y Fukui, H Sano, R Alsulami, and S Einecke. “Explaining the extended GeV gamma-ray emission adjacent to HESS J1825-137.” In: *Monthly Notices of the Royal Astronomical Society* 504.2 (Apr. 2021), pp. 1840–1853. ISSN: 0035-8711. DOI: [10.1093/mnras/stab983](https://doi.org/10.1093/mnras/stab983). eprint: <https://academic.oup.com/mnras/article-pdf/504/2/1840/37414921/stab983.pdf>. URL: <https://doi.org/10.1093/mnras/stab983>.
- [52] R. Conceição, B. S. González, A. Guillén, M. Pimenta, and B. Tomé. “Muon identification in a compact single-layered water Cherenkov detector and gamma/hadron discrimination using machine learning techniques.” In: *European Physical Journal C* 81.6, 542 (June 2021), p. 542. DOI: [10.1140/epjc/s10052-021-09312-4](https://doi.org/10.1140/epjc/s10052-021-09312-4). arXiv: [2101.10109](https://arxiv.org/abs/2101.10109) [physics.ins-det].
- [53] Ruben Conceição. “The Southern Wide-field Gamma-ray Observatory.” In: *arXiv e-prints*, arXiv:2309.04577 (Sept. 2023), arXiv:2309.04577. DOI: [10.48550/arXiv.2309.04577](https://doi.org/10.48550/arXiv.2309.04577). arXiv: [2309.04577](https://arxiv.org/abs/2309.04577) [hep-ex].
- [54] CTA Consortium. “Prospects for a survey of the Galactic plane with the Cherenkov Telescope Array.” In: *arXiv e-prints*, arXiv:2310.02828 (Oct. 2023), arXiv:2310.02828. DOI: [10.48550/arXiv.2310.02828](https://doi.org/10.48550/arXiv.2310.02828). arXiv: [2310.02828](https://arxiv.org/abs/2310.02828) [astro-ph.HE].
- [55] Alessandro De Angelis and Mário Pimenta. *Introduction to Particle and Astroparticle Physics*. Springer Cham, 2018.
- [56] C. Deil et al. “Gammapy - A prototype for the CTA science tools.” In: *35th International Cosmic Ray Conference (ICRC2017)*. Vol. 301. International Cosmic Ray Conference. July 2017, 766, p. 766. DOI: [10.22323/1.301.0766](https://doi.org/10.22323/1.301.0766). arXiv: [1709.01751](https://arxiv.org/abs/1709.01751) [astro-ph.IM].
- [57] L. Dirson and D. Horns. “Phenomenological modelling of the Crab Nebula’s broadband energy spectrum and its apparent extension.” In: *Astronomy and Astrophysics* 671, A67 (Mar. 2023), A67. DOI: [10.1051/0004-6361/202243578](https://doi.org/10.1051/0004-6361/202243578). arXiv: [2203.11502](https://arxiv.org/abs/2203.11502) [astro-ph.HE].
- [58] Axel Donath et al. “Gammapy: A Python package for gamma-ray astronomy.” In: *Astronomy & Astrophysics* 678 (2023), A157. DOI: [10.1051/0004-6361/202346488](https://doi.org/10.1051/0004-6361/202346488). URL: <https://doi.org/10.1051/0004-6361/202346488>.
- [59] J. Downing. *Effects of Light Absorption and Scattering in Water Samples on OBS Measurements*. Tech. rep. Campbell Scientific, Inc., 2008.
- [60] DuPont. *Tyvek For greater good*. 2018.
- [61] Michael A. DuVernois and Giuseppe Di Sciascio. “Detecting Gamma-Rays with Moderate Resolution and Large Field of View: Particle Detector Arrays and Water Cherenkov Technique.” In: *Handbook of X-ray and Gamma-ray Astrophysics*. Ed. by Cosimo Bambi and Andrea Santangelo. Singapore: Springer Nature Singapore, 2024, pp. 2575–2605. ISBN: 978-981-19-6960-7. DOI: [10.1007/978-981-19-6960-7\\_64](https://doi.org/10.1007/978-981-19-6960-7_64). URL: [https://doi.org/10.1007/978-981-19-6960-7\\_64](https://doi.org/10.1007/978-981-19-6960-7_64).

- [62] US Army Corps of Engineers. *Coastal Engineering Manual, EM 1110-2-1100 WATER WAVE MECHANICS (Part II)*. US Army Corps of Engineers, 2008.
- [63] Manel Errando and Takayuki Saito. “How to Detect Gamma Rays from Ground: An Introduction to the Detection Concepts.” In: *Handbook of X-ray and Gamma-ray Astrophysics*. Ed. by Cosimo Bambi and Andrea Santangelo. Singapore: Springer Nature Singapore, 2024, pp. 2483–2519. ISBN: 978-981-19-6960-7. DOI: [10.1007/978-981-19-6960-7\\_61](https://doi.org/10.1007/978-981-19-6960-7_61). URL: [https://doi.org/10.1007/978-981-19-6960-7\\_61](https://doi.org/10.1007/978-981-19-6960-7_61).
- [64] Adam Van Etten and Roger W. Romani. “Multi-zone Modeling of the Pulsar Wind Nebula HESS J1825-137.” In: *The Astrophysical Journal* 742.2 (2011), p. 62. DOI: [10.1088/0004-637X/742/2/62](https://dx.doi.org/10.1088/0004-637X/742/2/62). URL: <https://dx.doi.org/10.1088/0004-637X/742/2/62>.
- [65] John P. Finley, Radhika Srinivasan, and Sangwook Park. “The Morphology of Young Neutron Stars: PSR B1823-13, Its Compact Nebula, and Its Interstellar Neighborhood.” In: *The Astrophysical Journal* 466 (Aug. 1996), p. 938. DOI: [10.1086/177564](https://doi.org/10.1086/177564).
- [66] B. M. Gaensler, N. S. Schulz, V. M. Kaspi, M. J. Pivovarov, and W. E. Becker. “XMM-Newton Observations of PSR B1823-13: An Asymmetric Synchrotron Nebula around a Vela-like Pulsar.” In: *The Astrophysical Journal* 588.1 (2003), p. 441. DOI: [10.1086/368356](https://dx.doi.org/10.1086/368356). URL: <https://dx.doi.org/10.1086/368356>.
- [67] Bryan M. Gaensler and Patrick O. Slane. “The Evolution and Structure of Pulsar Wind Nebulae.” In: *Annual Review of Astronomy and Astrophysics* 44. Volume 44, 2006 (2006), pp. 17–47. ISSN: 1545-4282. DOI: <https://doi.org/10.1146/annurev.astro.44.051905.092528>. URL: <https://www.annualreviews.org/content/journals/10.1146/annurev.astro.44.051905.092528>.
- [68] G. Giacinti, A. M. W. Mitchell, R. López-Coto, V. Joshi, R. D. Parsons, and J. A. Hinton. “Halo fraction in TeV-bright pulsar wind nebulae.” In: *Astronomy and Astrophysics* 636, A113 (Apr. 2020), A113. DOI: [10.1051/0004-6361/201936505](https://doi.org/10.1051/0004-6361/201936505). arXiv: [1907.12121](https://arxiv.org/abs/1907.12121) [astro-ph.HE].
- [69] H. Goksu and D. Huang. *Energy-dependent Morphology of J1825-137 with HAWC*. Conference session. Sept. 11, 2023. URL: <https://agenda.infn.it/event/33457/contributions/204980/>. TeVPA, Napoli, Italy.
- [70] Hazal Goksu and Werner Hofmann. “Lake Deployment of Southern Wide-field Gamma-ray Observatory (SWG0) Detector Units.” In: *Proceedings of 37th International Cosmic Ray Conference — PoS(ICRC2021)*. Vol. 395. 2021, p. 708. DOI: [10.22323/1.395.0708](https://doi.org/10.22323/1.395.0708).
- [71] Hazal Goksu and Werner Hofmann. “Updates on Lake Deployment of Southern Wide-field Gamma-ray Observatory (SWG0) Detector Units.” In: *Proceedings of 38th International Cosmic Ray Conference — PoS(ICRC2023)*. Vol. 444. 2023, p. 653. DOI: [10.22323/1.444.0653](https://doi.org/10.22323/1.444.0653).

- [72] Greisinger. *G1420*. 2021. URL: <https://www.greisinger.de/p/neuheiten/g-1420/610007/> (visited on 10/10/2021).
- [73] K.F. Peter Grieder. *Extensive Air Showers: High Energy Phenomena and Astrophysical Aspects: Volume 1*. Springer, 2010.
- [74] M. H. Grondin et al. "Detection of the Pulsar Wind Nebula HESS J1825-137 with the Fermi Large Area Telescope." In: *The Astrophysical Journal* 738.1, 42 (Sept. 2011), p. 42. DOI: [10.1088/0004-637X/738/1/42](https://doi.org/10.1088/0004-637X/738/1/42). arXiv: [1106.0184](https://arxiv.org/abs/1106.0184) [astro-ph.HE].
- [75] C. Grupen, G. Cowan, S. Eidelman, and T. Stroh. *Astroparticle Physics*. SpringerLink: Springer e-Books. Springer Berlin Heidelberg, 2005. ISBN: 978-3-540-27670-8. URL: [https://books.google.fr/books?id=QC-7PZ6m\\_JgC](https://books.google.fr/books?id=QC-7PZ6m_JgC).
- [76] H. E. S. S. Collaboration et al. "The H.E.S.S. Galactic plane survey." In: *Astronomy and Astrophysics* 612, A1 (Apr. 2018), A1. DOI: [10.1051/0004-6361/201732098](https://doi.org/10.1051/0004-6361/201732098). arXiv: [1804.02432](https://arxiv.org/abs/1804.02432) [astro-ph.HE].
- [77] H. E. S. S. Collaboration et al. "Particle transport within the pulsar wind nebula HESS J1825-137." In: *Astronomy and Astrophysics* 621, A116 (Jan. 2019), A116. DOI: [10.1051/0004-6361/201834335](https://doi.org/10.1051/0004-6361/201834335). arXiv: [1810.12676](https://arxiv.org/abs/1810.12676) [astro-ph.HE].
- [78] Joachim Hahn, Carlo Romoli, and Mischa Breuhaus. *GAMERA: Source modeling in gamma astronomy*. Astrophysics Source Code Library, record ascl:2203.007. Mar. 2022.
- [79] K.K. Hamamatsu Photonics. *Photomultiplier Tubes, Basics and Applications, 3rd ed.* 2007.
- [80] Hans Hanson and Magnus Larson. "Implications of extreme waves and water levels in the southern Baltic Sea." English. In: *Journal of Hydraulic Research* 46.2 (2008), pp. 292–302. ISSN: 0022-1686.
- [81] Pat Harding. "Beyond the Standard Model with the Southern Wide-field Gamma-ray Observatory." In: *Proceedings of 38th International Cosmic Ray Conference — PoS(ICRC2023)*. Vol. 444. 2023, p. 1399. DOI: [10.22323/1.444.1399](https://doi.org/10.22323/1.444.1399).
- [82] D. Heck, J. Knapp, J. N. Capdevielle, G. Schatz, and T. Thouw. *CORSIKA: A Monte Carlo code to simulate extensive air showers*. Feb. 1998.
- [83] J. Hinton and SWGO Collaboration. "The Southern Wide-field Gamma-ray Observatory: Status and Prospects." In: *37th International Cosmic Ray Conference*. Mar. 2022, 23, p. 23. DOI: [10.22323/1.395.0023](https://doi.org/10.22323/1.395.0023). arXiv: [2111.13158](https://arxiv.org/abs/2111.13158) [astro-ph.IM].
- [84] J.A. Hinton and W. Hofmann. "Teraelectronvolt Astronomy." In: *Annual Review of Astronomy and Astrophysics* 47. Volume 47, 2009 (2009), pp. 523–565. ISSN: 1545-4282. DOI: <https://doi.org/10.1146/annurev-astro-082708-101816>. URL: <https://www.annualreviews.org/content/journals/10.1146/annurev-astro-082708-101816>.

- [85] Jim A. Hinton, Andrea Albert, Felix Aharonian, Faical Ait-Benkhalil, and Attila et al Alkan. “Galactic Centre with a Southern Wide Field-of-view Gamma-ray Observatory.” In: *Proceedings of 38th International Cosmic Ray Conference — PoS(ICRC2023)*. Vol. 444. 2023, p. 893. DOI: [10.22323/1.444.0893](https://doi.org/10.22323/1.444.0893).
- [86] Jim Hinton. *Gamma-ray from the ground –future perspectives*. <https://indico.ict.inaf.it/event/2661/contributions/19461/attachments/8751/17993/GroundbasedFutureMilanHinton.pdf>. 8th Gamma Symposium Presentation. 2024.
- [87] W. Hofmann and J. Hinton. “Detectors for high-energy messengers from the Universe.” In: *Nuclear Instruments and Methods in Physics Research A* 907 (Nov. 2018), pp. 31–45. DOI: [10.1016/j.nima.2018.03.020](https://doi.org/10.1016/j.nima.2018.03.020). arXiv: [1912.07473](https://arxiv.org/abs/1912.07473) [astro-ph.IM].
- [88] Jamie Holder. “Atmospheric Cherenkov Gamma-ray Telescopes.” In: *arXiv e-prints*, arXiv:1510.05675 (Oct. 2015), arXiv:1510.05675. DOI: [10.48550/arXiv.1510.05675](https://doi.org/10.48550/arXiv.1510.05675). arXiv: [1510.05675](https://arxiv.org/abs/1510.05675) [astro-ph.IM].
- [89] Dezhi Huang and et al. “Revealing Ultra-High-Energy Gamma-Ray Emission from the eHWC J1825-134 Region with HAWC.” In: *Proceedings of 38th International Cosmic Ray Conference — PoS(ICRC2023)*. Vol. 444. 2023, p. 796. DOI: [10.22323/1.444.0796](https://doi.org/10.22323/1.444.0796).
- [90] Petra Huentemeyer, Segev BenZvi, Brenda Dingus, Henrike Fleischhack, Harm Schoorlemmer, and Tom Weisgarber. “The Southern Wide-Field Gamma-Ray Observatory (SWGO): A Next-Generation Ground-Based Survey Instrument.” In: *Bulletin of the American Astronomical Society*. Vol. 51. Sept. 2019, 109, p. 109. arXiv: [1907.07737](https://arxiv.org/abs/1907.07737) [astro-ph.IM].
- [91] Energetics Research Laboratory in Hydrodynamics and Centrale Nantes Atmospheric Environment (LHEEA). *Hydrodynamic and Ocean Engineering Tank*. Online; accessed September 10, 2024. URL: <https://lheea.ec-nantes.fr/test-facilities/ocean-tanks/hydrodynamic-and-ocean-engineering-tank>.
- [92] IceCube Collaboration et al. “Multimessenger observations of a flaring blazar coincident with high-energy neutrino IceCube-170922A.” In: *Science* 361.6398, eaat1378 (July 2018), eaat1378. DOI: [10.1126/science.aat1378](https://doi.org/10.1126/science.aat1378). arXiv: [1807.08816](https://arxiv.org/abs/1807.08816) [astro-ph.HE].
- [93] R Iuppa. “Results from the ARGO-YBJ experiment.” In: *Journal of Instrumentation* 8.08 (2013), T08002. DOI: [10.1088/1748-0221/8/08/T08002](https://doi.org/10.1088/1748-0221/8/08/T08002). URL: <https://dx.doi.org/10.1088/1748-0221/8/08/T08002>.
- [94] F. James and M. Roos. “Minuit - a system for function minimization and analysis of the parameter errors and correlations.” In: *Computer Physics Communications* 10.6 (Dec. 1975), pp. 343–367. DOI: [10.1016/0010-4655\(75\)90039-9](https://doi.org/10.1016/0010-4655(75)90039-9).
- [95] Martin Janecek. “Reflectivity Spectra for Commonly Used Reflectors.” In: *IEEE Transaction on Nuclear Science* (Mar. 2012). DOI: [10.1109/TNS.2012.2183385](https://doi.org/10.1109/TNS.2012.2183385). URL: <https://www.osti.gov/biblio/1184400>.

- [96] Armelle Jardin-Blicq. “The TeV  $\gamma$ -ray emission of the Galactic Plane. HAWC and H.E.S.S. observations of the Galactic Plane and detailed study of the region surrounding 2HWC J1928+177.” Theses. Ruperto-Carola University of Heidelberg, June 2019. URL: <https://hal.science/tel-03347146>.
- [97] J. V. Jelley. “Special Article: Cerenkov radiation and its applications.” In: *British Journal of Applied Physics* 6.7 (July 1955), pp. 227–232. DOI: [10.1088/0508-3443/6/7/301](https://doi.org/10.1088/0508-3443/6/7/301).
- [98] Philip Kaaret. *Lecture notes on Detecting high energy photons*. 2010. URL: <https://homepage.physics.uiowa.edu/~pkaaret/heaastro10s/lectures.html>.
- [99] Ervin Kafexhiu, Felix Aharonian, Andrew M. Taylor, and Gabriela S. Vila. “Parametrization of gamma-ray production cross sections for p p interactions in a broad proton energy range from the kinematic threshold to PeV energies.” In: *Physical Review D* 90.12, 123014 (Dec. 2014), p. 123014. DOI: [10.1103/PhysRevD.90.123014](https://doi.org/10.1103/PhysRevD.90.123014). arXiv: [1406.7369](https://arxiv.org/abs/1406.7369) [astro-ph.HE].
- [100] T. Kaneko et al. “Acoustic and Vlf-Elf Radio Detections of Super Giant Air Showers.” In: *International Cosmic Ray Conference*. Vol. 11. International Cosmic Ray Conference. Aug. 1983, p. 428.
- [101] Oleg Kargaltsev, Blagoy Rangelov, and George Pavlov. “Pulsar-Wind Nebulae as a Dominant Population of Galactic VHE Sources.” In: *The Universe Evolution: Astrophysical and Nuclear Aspects*. Edited by I. Strakovsky and L. Blokhintsev. Nova Science Publishers. 2013, pp. 359–406. DOI: [10.48550/arXiv.1305.2552](https://doi.org/10.48550/arXiv.1305.2552).
- [102] Y. Katayose. *Status of the ALPACA/ALPAQUITA experiment*. Conference session. Aug. 26, 2024. URL: <https://indico.uchicago.edu/event/427/contributions/1376/>. TeVPA, Chicago, United States of America.
- [103] T. Kawashima and The ALPACA Collaboration. “The ALPACA experiment: The project of the first sub-PeV gamma-ray observation in the southern sky.” In: *arXiv e-prints*, arXiv:2208.14659 (Aug. 2022). DOI: [10.48550/arXiv.2208.14659](https://doi.org/10.48550/arXiv.2208.14659). arXiv: [2208.14659](https://arxiv.org/abs/2208.14659) [astro-ph.IM].
- [104] Dmitry Khangulyan, Alexander V. Koldoba, Galina V. Ustyugova, Sergey V. Bogovalov, and Felix Aharonian. “On the Anomalously Large Extension of the Pulsar Wind Nebula HESS J1825-137.” In: *The Astrophysical Journal* 860.1, 59 (June 2018), p. 59. DOI: [10.3847/1538-4357/aac20f](https://doi.org/10.3847/1538-4357/aac20f). arXiv: [1712.10161](https://arxiv.org/abs/1712.10161) [astro-ph.HE].
- [105] J. Knödlseeder et al. “GammaLib and ctools. A software framework for the analysis of astronomical gamma-ray data.” In: *Astronomy and Astrophysics* 593, A1 (Aug. 2016), A1. DOI: [10.1051/0004-6361/201628822](https://doi.org/10.1051/0004-6361/201628822). arXiv: [1606.00393](https://arxiv.org/abs/1606.00393) [astro-ph.IM].
- [106] Curtis W. Kovach. *High-Performance Stainless Steels*. Online. Accessed 05.08.2024. Nickel Institute, 2000. URL: [https://www.nickelinstitute.org/media/1702/highperformancestainlesssteels\\_11021\\_.pdf](https://www.nickelinstitute.org/media/1702/highperformancestainlesssteels_11021_.pdf).

- [107] H.E Krogstad and Ø.A. Artsen. *Linear Wave Theory, Part A., Regular Waves*. Norwegian University of Science and Technology, 2000.
- [108] Samridha Kunwar, Hazal Goksu, Jim Hinton, Harm Schoorlemmer, Andrew Smith, Werner Hofmann, and Felix Werner. “A double-layered Water Cherenkov Detector array for Gamma-ray astronomy.” In: *Nuclear Instruments and Methods in Physics Research A* 1050, 168138 (May 2023), p. 168138. DOI: [10.1016/j.nima.2023.168138](https://doi.org/10.1016/j.nima.2023.168138). arXiv: [2209.09305](https://arxiv.org/abs/2209.09305) [astro-ph.IM].
- [109] *LARGE PHOTOCATHODE AREA PHOTOMULTIPLIER TUBES*. Datasheet for PMT R5912. Hamamatsu Photonics, K.K. 2019.
- [110] Labsphere. *Integrating Sphere Theory and Applications*. 2017.
- [111] Labsphere. *Spectralon Diffuse Reflectance Material*. 2023.
- [112] J. M. Lattimer and M. Prakash. “The Physics of Neutron Stars.” In: *Science* 304.5670 (Apr. 2004), pp. 536–542. DOI: [10.1126/science.1090720](https://doi.org/10.1126/science.1090720). arXiv: [astro-ph/0405262](https://arxiv.org/abs/astro-ph/0405262) [astro-ph].
- [113] *Layfield Flexible Films*. 2024. URL: <https://www.layfieldgroup.com/flexible-films/> (visited on 07/07/2024).
- [114] A. Lemiere, R. Terrier, and A. Djannati-Ataï. “Multi-resolution analysis of the H.E.S.S. Galactic Survey Sources and Search for Counterparts in CO and HI data.” In: *29th International Cosmic Ray Conference (ICRC29), Volume 4*. Ed. by B. Sripathi Acharya, Sunil Gupta, P. Jagadeesan, Atul Jain, S. Karthikeyan, Samuel Morris, and Suresh Tonwar. Vol. 4. International Cosmic Ray Conference. Jan. 2005, p. 105. DOI: [10.48550/arXiv.astro-ph/0602436](https://doi.org/10.48550/arXiv.astro-ph/0602436). arXiv: [astro-ph/0602436](https://arxiv.org/abs/astro-ph/0602436) [astro-ph].
- [115] Cong Li et al. “An apparatus to measure water optical attenuation length for LHAASO-MD.” In: *Nuclear Instruments and Methods in Physics Research A* 892 (June 2018), pp. 122–126. DOI: [10.1016/j.nima.2018.03.029](https://doi.org/10.1016/j.nima.2018.03.029).
- [116] Huicai Li, Mingjun Chen, Bo Gao, Huihai He, Cheng Liu, Kai Li, Bodong Wang, Xiaohao You, and Yuelel Zhang. “Measurement of water quality in LHAASO-WCDA.” In: *Radiation Detection Technology and Methods* 7.2 (2023), pp. 192–199. ISSN: 2509-9930. DOI: [10.1007/s41605-022-00362-0](https://doi.org/10.1007/s41605-022-00362-0). URL: <http://rdtm.ihep.ac.cn/en/article/doi/10.1007/s41605-022-00362-0>.
- [117] T. P. Li and Y. Q. Ma. “Analysis methods for results in gamma-ray astronomy.” In: *The Astrophysical Journal* 272 (Sept. 1983), pp. 317–324. DOI: [10.1086/161295](https://doi.org/10.1086/161295).
- [118] T. Li and Z. Hao. *SWG0 Lake Array Solution Model Planned progress*. Symposium on Frontier Issues in Underground and Space Particle Physics and Cosmic Physics. May 11, 2024. URL: <https://indico-cdex.ep.tsinghua.edu.cn/event/162/contributions/1650/attachments/502/747/SWG0%E6%A8%A1%E6%8B%9F.pdf>. Xichang, China.

- [119] Xiurong Li et al. “Novel methods for measuring the optical parameters of the water Cherenkov detector.” In: *Nuclear Instruments and Methods in Physics Research A* 919 (Mar. 2019), pp. 73–81. DOI: [10.1016/j.nima.2018.10.076](https://doi.org/10.1016/j.nima.2018.10.076). arXiv: [1801.03797](https://arxiv.org/abs/1801.03797) [physics.ins-det].
- [120] Tim Linden, Katie Auchetl, Joseph Bramante, Ilias Cholis, Ke Fang, Dan Hooper, Tanvi Karwal, and Shirley Weishi Li. “Using HAWC to discover invisible pulsars.” In: *Phys. Rev. D* 96 (10 2017), p. 103016. DOI: [10.1103/PhysRevD.96.103016](https://doi.org/10.1103/PhysRevD.96.103016). URL: <https://link.aps.org/doi/10.1103/PhysRevD.96.103016>.
- [121] Malcolm S. Longair. *High Energy Astrophysics*. 2011.
- [122] Lu Lu and Tianlu Yuan. “The use of Cherenkov light in the detection of high-energy cosmic rays and neutrinos: The Pierre Auger and Ice-Cube Observatories.” In: *Nuclear Instruments and Methods in Physics Research Section A: Accelerators, Spectrometers, Detectors and Associated Equipment* 970 (2020). A RICH LEGACY, p. 163678. ISSN: 0168-9002. DOI: <https://doi.org/10.1016/j.nima.2020.163678>. URL: <https://www.sciencedirect.com/science/article/pii/S016890022020302448>.
- [123] Xin-Hua Ma et al. “Chapter 1 LHAASO Instruments and Detector technology.” In: *Chinese Physics C* 46.3, 030001 (Mar. 2022), p. 030001. DOI: [10.1088/1674-1137/ac3fa6](https://doi.org/10.1088/1674-1137/ac3fa6).
- [124] R. N. Manchester, G. B. Hobbs, A. Teoh, and M. Hobbs. “The Australia Telescope National Facility Pulsar Catalogue.” In: *The Astronomical Journal* 129.4 (Apr. 2005), pp. 1993–2006. DOI: [10.1086/428488](https://doi.org/10.1086/428488). arXiv: [astro-ph/0412641](https://arxiv.org/abs/astro-ph/0412641) [astro-ph].
- [125] V. Marandon, A. Jardin-Blicq, and H. Schorlemmer. “Latest news from the HAWC outrigger array.” In: *36th International Cosmic Ray Conference (ICRC2019)*. Vol. 36. International Cosmic Ray Conference. July 2019, 736, p. 736. arXiv: [1908.07634](https://arxiv.org/abs/1908.07634) [astro-ph.IM].
- [126] J. Marti, J. M. Paredes, and M. Ribo. “The system LS 5039: a new massive radio emitting X-ray binary.” In: *Astronomy and Astrophysics* 338 (Oct. 1998), pp. L71–L74.
- [127] J. R. Mattox et al. “The Likelihood Analysis of EGRET Data.” In: *The Astrophysical Journal* 461 (Apr. 1996), p. 396. DOI: [10.1086/177068](https://doi.org/10.1086/177068).
- [128] Mayer Luftwerbung. *Die Manufaktur den Dritten Dimension*. 2021. URL: <https://luftwerbung.de/> (visited on 09/10/2021).
- [129] Mayer Luftwerbung. 2024. URL: <https://luftwerbung.de/> (visited on 07/07/2024).
- [130] A. M. W. Mitchell and J. Gelfand. “Pulsar Wind Nebulae.” In: *Handbook of X-ray and Gamma-ray Astrophysics*. Ed. by Cosimo Bambi and Andrea Sanganelo. 2022, 61, p. 61. DOI: [10.1007/978-981-16-4544-0\\_157-1](https://doi.org/10.1007/978-981-16-4544-0_157-1).

- [131] A. Mitchell, S. Caroff, R. Parsons, J. Hahn, V. Marandon, J. Hinton, and H. E. S. S. Collaboration. "Observations of the Pulsar Wind Nebula HESS J1825-137 with H.E.S.S. II." In: *35th International Cosmic Ray Conference (ICRC2017)*. Vol. 301. International Cosmic Ray Conference. Jan. 2017, 707, p. 707. arXiv: [1708.03126](https://arxiv.org/abs/1708.03126) [astro-ph.HE].
- [132] Alberto Montanari. *Mechanics of sea waves*. 2017. URL: <https://www.albertomontanari.it/node/123> (visited on 07/07/2024).
- [133] Poolla V. Ramana Murthy and Arnold W. Wolfendale. *Gamma-ray Astronomy Second Edition*. Cambridge, Great Britain: Cambridge University Press, 1993.
- [134] NORSK STANDARD NS 9415: *Marine fish farms - Requirements for design, dimensioning, production, installation and operation*. Tech. rep. Oslo, Norway, 2009.
- [135] Mathieu de Naurois. "Very High Energy astronomy from H.E.S.S. to CTA. Opening of a new astronomical window on the non-thermal Universe." Habilitation à diriger des recherches. Université Pierre et Marie Curie - Paris VI, Mar. 2012. URL: <https://theses.hal.science/tel-00687872>.
- [136] Vu Giang Nguyen, Hoang Thai, Duc Huynh Mai, Huu Trung Tran, Dai Lam Tran, and Manh Tuan Vu. "Effect of titanium dioxide on the properties of polyethylene/TiO<sub>2</sub> nanocomposites." In: *Composites Part B: Engineering* 45.1 (2013), pp. 1192–1198. ISSN: 1359-8368. DOI: <https://doi.org/10.1016/j.compositesb.2012.09.058>. URL: <https://www.sciencedirect.com/science/article/pii/S1359836812006087>.
- [137] Cosimo Nigro, Tarek Hassan, and Laura Olivera-Nieto. "Evolution of Data Formats in Very-High-Energy Gamma-Ray Astronomy." In: *Universe* 7.10, 374 (Oct. 2021), p. 374. DOI: [10.3390/universe7100374](https://doi.org/10.3390/universe7100374). arXiv: [2109.14661](https://arxiv.org/abs/2109.14661) [astro-ph.IM].
- [138] Pourya Omidvar. "Wave loading on bodies in free surface using smoothed particle hydrodynamics (SPH)." PhD thesis. The University of Manchester, 2010.
- [139] Particle Data Group (PDG). *Atomic and nuclear properties of air (dry, 1 atm)*. Online; accessed 10.08.2024. URL: [https://pdg.lbl.gov/2014/AtomicNuclearProperties/HTML/air\\_dry\\_1\\_atm.html](https://pdg.lbl.gov/2014/AtomicNuclearProperties/HTML/air_dry_1_atm.html).
- [140] J.C. Pang, S.X. Li, Z.G. Wang, and Z.F. Zhang. "General relation between tensile strength and fatigue strength of metallic materials." In: *Materials Science and Engineering: A* 564 (2013), pp. 331–341. ISSN: 0921-5093. DOI: <https://doi.org/10.1016/j.msea.2012.11.103>. URL: <https://www.sciencedirect.com/science/article/pii/S0921509312016553>.
- [141] G. G. Pavlov, O. Kargaltsev, and W. F. Brisken. "Chandra Observation of PSR B1823–13 and Its Pulsar Wind Nebula." In: *The Astrophysical Journal* 675.1 (2008), p. 683. DOI: [10.1086/525842](https://doi.org/10.1086/525842). URL: <https://dx.doi.org/10.1086/525842>.

- [142] Pierre Auger Collaboration et al. "The surface detector system of the Pierre Auger Observatory." In: *Nuclear Instruments and Methods in Physics Research A* 586.3 (Mar. 2008), pp. 409–420. DOI: [10.1016/j.nima.2007.12.016](https://doi.org/10.1016/j.nima.2007.12.016). arXiv: [0712.2832](https://arxiv.org/abs/0712.2832) [astro-ph].
- [143] R.M. Pope and E.S. Fry. "Absorption spectrum (380-700 nm) of pure water. II. Integrating cavity measurements." In: *Appl. Opt.*, 36, 8710-8723 (1997).
- [144] Matsusada Precision. *Photomultiplier Tube (PMT)*. 2023. URL: [https://www.matsusada.com/application/ps/photomultiplier\\_tubes/](https://www.matsusada.com/application/ps/photomultiplier_tubes/).
- [145] G. Principe, A. M. W. Mitchell, S. Caroff, J. A. Hinton, R. D. Parsons, and S. Funk. "Energy dependent morphology of the pulsar wind nebula HESS J1825-137 with Fermi-LAT." In: *Astronomy and Astrophysics* 640, A76 (Aug. 2020), A76. DOI: [10.1051/0004-6361/202038375](https://doi.org/10.1051/0004-6361/202038375). arXiv: [2006.11177](https://arxiv.org/abs/2006.11177) [astro-ph.HE].
- [146] *Properties of Metals*. Online; accessed 10.09.2024. The page provides chapters from "DOE Fundamentals Handbook: Material Science," DOE-HDBK-1017/1-93, U.S. Department of Energy, Jan 1993. URL: <https://engineeringlibrary.org/reference/properties-of-metals-doe-handbook>.
- [147] M.R. Querry, P.G. Cary, and R.C. Waring. "Split-pulse laser method for measuring attenuation coefficients of transparent liquids: application to deionized filtered water in the visible region." In: *Appl. Opt.* 17, 3587-3592 (1978).
- [148] Michael Richmond. *Highest-energy gamma rays: ground based telescopes, sources*. [Online; accessed September 14, 2024]. 2021. URL: [http://spiff.rit.edu/classes/ast613/lectures/gamma\\_high/gamma\\_high.html](http://spiff.rit.edu/classes/ast613/lectures/gamma_high/gamma_high.html).
- [149] *SWG0 Site Selection*. 2024. URL: [https://www.swgo.org/SWGOWiki/doku.php?id=site\\_press\\_release](https://www.swgo.org/SWGOWiki/doku.php?id=site_press_release).
- [150] Tatsuhiko Sato. "Analytical Model for Estimating the Zenith Angle Dependence of Terrestrial Cosmic Ray Fluxes." In: *PLOS ONE* 11.8 (Aug. 2016), pp. 1–22. DOI: [10.1371/journal.pone.0160390](https://doi.org/10.1371/journal.pone.0160390). URL: <https://doi.org/10.1371/journal.pone.0160390>.
- [151] Harm Schoorlemmer, Jim Hinton, and Rubén López-Coto. "Characteristics of extensive air showers around the energy threshold for ground-particle-based Gamma-ray observatories." In: *European Physical Journal C* 79.5, 427 (May 2019), p. 427. DOI: [10.1140/epjc/s10052-019-6942-x](https://doi.org/10.1140/epjc/s10052-019-6942-x). arXiv: [1905.06816](https://arxiv.org/abs/1905.06816) [astro-ph.HE].
- [152] SeaBird Scientific. *Transmissometer C-Star User's Guide*. 2016.
- [153] D. J. Segelstein. *The Complex Refractive Index of Water*. 1981.
- [154] *Shore Protection Manual*. Online; accessed 12.07.2024. 1984. URL: <https://usace.contentdm.oclc.org/digital/collection/p16021coll11/id/1934/>.

- [155] Gus Sinnis. "Water Cherenkov technology in gamma-ray astrophysics." In: *Nuclear Instruments and Methods in Physics Research Section A: Accelerators, Spectrometers, Detectors and Associated Equipment* 623.1 (2010). 1st International Conference on Technology and Instrumentation in Particle Physics, pp. 410–412. ISSN: 0168-9002. DOI: <https://doi.org/10.1016/j.nima.2010.03.019>. URL: <https://www.sciencedirect.com/science/article/pii/S0168900210005838>.
- [156] Andrew J. Smith. "The MILAGRO Gamma Ray Observatory." In: *29th International Cosmic Ray Conference (ICRC29), Volume 10*. Ed. by B. Sripathi Acharya, Sunil Gupta, P. Jagadeesan, Atul Jain, S. Karthikeyan, Samuel Morris, and Suresh Tonwar. Vol. 10. International Cosmic Ray Conference. Jan. 2005, p. 227.
- [157] F.M. Sogandares and E.S. Fry. "Absorption spectrum (340- 640 nm) of pure water. I. Photothermal Measurements." In: *Appl. Opt.*,36, 8699-8709 (1997).
- [158] Christian Spiering. "Neutrino Detectors Under Water and Ice." In: *Particle Physics Reference Library: Volume 2: Detectors for Particles and Radiation*. Ed. by Christian W. Fabjan and Herwig Schopper. Cham: Springer International Publishing, 2020, pp. 785–822. ISBN: 978-3-030-35318-6. DOI: [10.1007/978-3-030-35318-6\\_17](https://doi.org/10.1007/978-3-030-35318-6_17). URL: [https://doi.org/10.1007/978-3-030-35318-6\\_17](https://doi.org/10.1007/978-3-030-35318-6_17).
- [159] R.H. Stewart. *Introduction to Physical Oceanography*. Texas A & M University, 2000.
- [160] Martin Alfonso Subieta Vasquez. "Overview status of the ALPACA experiment." In: *Proceedings of 38th International Cosmic Ray Conference — PoS(ICRC2023)*. Vol. 444. 2023, p. 767. DOI: [10.22323/1.444.0767](https://doi.org/10.22323/1.444.0767).
- [161] Masato Takita. "Highlights from the Tibet AS-gamma experiment." In: *PoS ICRC2023* (2023), p. 213. DOI: [10.22323/1.444.0213](https://doi.org/10.22323/1.444.0213).
- [162] David J. Thompson. "Space detectors for gamma rays (100 MeV–100 GeV): From EGRET to Fermi LAT." In: *Comptes Rendus Physique* 16.6 (2015). Gamma-ray astronomy / Astronomie des rayons gamma, pp. 600–609. ISSN: 1631-0705. DOI: <https://doi.org/10.1016/j.crhy.2015.07.002>. URL: <https://www.sciencedirect.com/science/article/pii/S1631070515001280>.
- [163] *Types Of Stainless Steel: A2 vs A4 or 304 vs 316*. 2018. URL: <https://www.goebelfasteners.com/types-of-stainless-steel-a2-vs-a4-or-304-vs-316/>.
- [164] Hideki Uchiyama, Hironori Matsumoto, Takeshi Go Tsuru, Katsuji Koyama, and Aya Bamba. "Suzaku Observation of HESS J1825-137: Discovery of Largely-Extended X-Rays from PSR J1826-1334." In: *Publications of the Astronomical Society of Japan* 61 (Jan. 2009), S189. DOI: [10.1093/pasj/61.sp1.S189](https://doi.org/10.1093/pasj/61.sp1.S189). arXiv: [0808.3436 \[astro-ph\]](https://arxiv.org/abs/0808.3436).

- [165] Vittoria Vecchiotti, Giulia Pagliaroli, and Francesco Lorenzo Villante. “The contribution of Galactic TeV pulsar wind nebulae to Fermi large area telescope diffuse emission.” In: *Communications Physics* 5.1, 161 (Dec. 2022), p. 161. DOI: [10.1038/s42005-022-00939-7](https://doi.org/10.1038/s42005-022-00939-7). arXiv: [2107.03236](https://arxiv.org/abs/2107.03236) [astro-ph.HE].
- [166] Giacomo Vianello, Robert J. Lauer, Patrick Youngk, Luigi Tibaldo, James M. Burgess, Hugo Ayala, Patrick Harding, Michelle Hui, Nicola Omodei, and Hao Zhou. “The Multi-Mission Maximum Likelihood framework (3ML).” In: *arXiv e-prints*, arXiv:1507.08343 (July 2015), arXiv:1507.08343. DOI: [10.48550/arXiv.1507.08343](https://doi.org/10.48550/arXiv.1507.08343). arXiv: [1507.08343](https://arxiv.org/abs/1507.08343) [astro-ph.HE].
- [167] Jacco Vink. “Radiation Processes.” In: *Physics and Evolution of Supernova Remnants*. Cham: Springer International Publishing, 2020, pp. 379–457. ISBN: 978-3-030-55231-2. DOI: [10.1007/978-3-030-55231-2\\_13](https://doi.org/10.1007/978-3-030-55231-2_13). URL: [https://doi.org/10.1007/978-3-030-55231-2\\_13](https://doi.org/10.1007/978-3-030-55231-2_13).
- [168] F. Voisin, G. Rowell, M. G. Burton, A. Walsh, Y. Fukui, and F. Aharonian. “ISM gas studies towards the TeV PWN HESS J1825-137 and northern region.” In: *Monthly Notices of the Royal Astronomical Society* 458.3 (Mar. 2016), pp. 2813–2835. ISSN: 0035-8711. DOI: [10.1093/mnras/stw473](https://doi.org/10.1093/mnras/stw473). eprint: <https://academic.oup.com/mnras/article-pdf/458/3/2813/8006507/stw473.pdf>. URL: <https://doi.org/10.1093/mnras/stw473>.
- [169] Igor Volkov, Oleg Kargaltsev, George Younes, Jeremy Hare, and George Pavlov. “NuSTAR Observation of LS 5039.” In: *The Astrophysical Journal* 915.1, 61 (July 2021), p. 61. DOI: [10.3847/1538-4357/abfe0e](https://doi.org/10.3847/1538-4357/abfe0e). arXiv: [2103.04403](https://arxiv.org/abs/2103.04403) [astro-ph.HE].
- [170] Hui Wang et al. “Measuring the optical parameters for LHAASO-MD.” In: *Nuclear Instruments and Methods in Physics Research Section A: Accelerators, Spectrometers, Detectors and Associated Equipment* 956 (2020), p. 163416. ISSN: 0168-9002. DOI: <https://doi.org/10.1016/j.nima.2020.163416>. URL: <https://www.sciencedirect.com/science/article/pii/S016890022030022X>.
- [171] A. A. Watson. “A Brief History of the Study of High Energy Cosmic Rays using Arrays of Surface Detectors.” In: *European Physical Journal Web of Conferences*. Vol. 283. European Physical Journal Web of Conferences. Oct. 2023, 01002, p. 01002. DOI: [10.1051/epjconf/202328301002](https://doi.org/10.1051/epjconf/202328301002). arXiv: [2303.05133](https://arxiv.org/abs/2303.05133) [physics.hist-ph].
- [172] F. Werner et al. “Performance verification of the FlashCam prototype camera for the Cherenkov Telescope Array.” In: *Nuclear Instruments and Methods in Physics Research A* 876 (Dec. 2017), pp. 31–34. DOI: [10.1016/j.nima.2016.12.056](https://doi.org/10.1016/j.nima.2016.12.056). arXiv: [1612.09528](https://arxiv.org/abs/1612.09528) [astro-ph.IM].
- [173] Felix Werner and Lukas Nellen. “Technological options for the Southern Wide-field Gamma-ray Observatory (SWGGO) and current design status.” In: *PoS(ICRC2021)*. 2021, p. 714.

- [174] Alan Wood. *Extractables and leachables analysis of pharmaceutical products*. Online; accessed 10.08.2024. URL: <https://www.outsourcing-pharma.com/News/Promotional-features/Extractables-and-leachables-analysis-of-pharmaceutical-products>.
- [175] R.L. et. al. Workman. "Passage of Particles Through Matter." In: (*Particle Data Group*), *Prog. Theor. Exp. Phys.* 083C01 (2022).
- [176] Gaurang B. Yodh. "The MILAGRO gamma ray observatory." In: *Nuclear Physics B - Proceedings Supplements* 52.3 (1997), pp. 264–268. ISSN: 0920-5632. DOI: [https://doi.org/10.1016/S0920-5632\(96\)00902-4](https://doi.org/10.1016/S0920-5632(96)00902-4). URL: <https://www.sciencedirect.com/science/article/pii/S0920563296009024>.
- [177] Xiaohao You, Shicong Hu, and Shaoxiang Xi. "Updated analysis of the brightest UHE Gamma-ray Source LHAASO J1825-1326." In: *Proceedings of 38th International Cosmic Ray Conference — PoS(ICRC2023)*. Vol. 444. 2023, p. 643. DOI: [10.22323/1.444.0643](https://doi.org/10.22323/1.444.0643).
- [178] A. de Angelis, O. Mansutti, and M. Persic. "Very-high energy gamma astrophysics." In: *Nuovo Cimento Rivista Serie* 31.4 (Apr. 2008), pp. 187–246. DOI: [10.1393/ncr/i2008-10032-2](https://doi.org/10.1393/ncr/i2008-10032-2). arXiv: [0712.0315](https://arxiv.org/abs/0712.0315) [astro-ph].
- [179] Emma de Oña Wilhelmi, Rubén López-Coto, Elena Amato, and Felix Aharonian. "On the Potential of Bright, Young Pulsars to Power Ultrahigh Gamma-Ray Sources." In: *The Astrophysical Journal* 930.1, L2 (May 2022), p. L2. DOI: [10.3847/2041-8213/ac66cf](https://doi.org/10.3847/2041-8213/ac66cf). arXiv: [2204.09440](https://arxiv.org/abs/2204.09440) [astro-ph.HE].



## PERSONAL BIBLIOGRAPHY

---

The publications, presentations and proceedings articles that I have worked on during my doctoral studies, where I am a corresponding author, are listed below.

### PUBLICATIONS

- Samridha Kunwar, Hazal Goksu, Jim Hinton, Harm Schoorlemmer, Andrew Smith, Werner Hofmann, and Felix Werner. "A Double-Layered Water Cherenkov Detector Array for Gamma-ray Astronomy." In: *Nuclear Instruments and Methods in Physics Research A* 1050, 168138 (May 2023), p. 168138. doi: 10.1016

### IN COLLABORATION REVIEW

- Hazal Goksu, Werner Hofmann, Felix Werner, Fabian Haist and Jim Hinton. "Instrumenting a Lake as a Wide-Field Gamma-ray Detector." *Prepared for submission to: Nuclear Instruments and Methods in Physics Research A*

### CONFERENCE PROCEEDINGS

- Hazal Goksu and Werner Hofmann. "Lake Deployment of Southern Wide-field Gamma-ray Observatory (SWGGO) Detector Units." In: *Proceedings of 37th International Cosmic Ray Conference — PoS(ICRC2021)*. Vol. 395. 2021, p. 708. doi: 10.22323/1.395.0708.
- Hazal Goksu and Werner Hofmann. "Updates on Lake Deployment of Southern Wide-field Gamma-ray Observatory (SWGGO) Detector Units." In: *Proceedings of 38th International Cosmic Ray Conference — PoS(ICRC2023)*. Vol. 444. 2023, p. 653. doi: 10.22323/1.444.0653.

### CONFERENCE CONTRIBUTIONS

- H. Goksu and D. Huang. "Energy-dependent Morphology of J1825-137 with HAWC". Conference session. Sept. 11, 2023. TeVPA, Napoli, Italy.
- Hazal Goksu. "SWGGO Unit Prototyping." Invited talk in a Workshop. June 11, 2023. 3rd GCOS Workshop. Brussels, Belgium.
- H. Goksu. "Wide-field Gamma-ray Observations in a Natural Lake". Conference Poster contribution. July 2022. 7th Heidelberg International Symposium on High-Energy Gamma-Ray Astronomy. Barcelona, Spain.



## COLOPHON

This document was typeset using the typographical look-and-feel `classicthesis` developed by André Miede and Ivo Pletikosić. The style was inspired by Robert Bringhurst's seminal book on typography "*The Elements of Typographic Style*". `classicthesis` is available for both  $\text{\LaTeX}$  and  $\text{\LyX}$ :

<https://bitbucket.org/amiede/classicthesis/>

*Final Version* as of October 28, 2024 (`classicthesis v4.6`).